



MINISTÉRIO DA CIÊNCIA, TECNOLOGIA, INOVAÇÕES E COMUNICAÇÕES
INSTITUTO NACIONAL DE PESQUISAS ESPACIAIS

sid.inpe.br/mtc-m21b/2017/04.12.00.58-TDI

**ANGLE-OF-ATTACK IMPACT IN THE
AEROTHERMODYNAMICS OF A HYPERSONIC
VEHICLE WITH SURFACE DISCONTINUITY-LIKE A
CAVITY**

Daimer Mauthsud Leovan Ospina Contreras

Master's Dissertation of the
Graduate Course in Engineering
and Space Technology, guided by
Dr. Wilson Fernando Nogueira dos
Santos, approved in April 19, 2017.

URL of the original document:

<<http://urlib.net/8JMKD3MGP3W34P/3NMDH2S>>

INPE
São José dos Campos
2017

PUBLISHED BY:

Instituto Nacional de Pesquisas Espaciais - INPE

Gabinete do Diretor (GB)

Serviço de Informação e Documentação (SID)

Caixa Postal 515 - CEP 12.245-970

São José dos Campos - SP - Brasil

Tel.:(012) 3208-6923/6921

E-mail: pubtc@inpe.br

**COMMISSION OF BOARD OF PUBLISHING AND PRESERVATION
OF INPE INTELLECTUAL PRODUCTION (DE/DIR-544):**

Chairperson:

Maria do Carmo de Andrade Nono - Conselho de Pós-Graduação (CPG)

Members:

Dr. Plínio Carlos Alvalá - Centro de Ciência do Sistema Terrestre (CST)

Dr. André de Castro Milone - Coordenação de Ciências Espaciais e Atmosféricas (CEA)

Dra. Carina de Barros Melo - Coordenação de Laboratórios Associados (CTE)

Dr. Evandro Marconi Rocco - Coordenação de Engenharia e Tecnologia Espacial (ETE)

Dr. Hermann Johann Heinrich Kux - Coordenação de Observação da Terra (OBT)

Dr. Marley Cavalcante de Lima Moscati - Centro de Previsão de Tempo e Estudos Climáticos (CPT)

Silvia Castro Marcelino - Serviço de Informação e Documentação (SID) **DIGITAL LIBRARY:**

Dr. Gerald Jean Francis Banon

Clayton Martins Pereira - Serviço de Informação e Documentação (SID)

DOCUMENT REVIEW:

Simone Angélica Del Ducca Barbedo - Serviço de Informação e Documentação (SID)

Yolanda Ribeiro da Silva Souza - Serviço de Informação e Documentação (SID)

ELECTRONIC EDITING:

Marcelo de Castro Pazos - Serviço de Informação e Documentação (SID)

André Luis Dias Fernandes - Serviço de Informação e Documentação (SID)



MINISTÉRIO DA CIÊNCIA, TECNOLOGIA, INOVAÇÕES E COMUNICAÇÕES
INSTITUTO NACIONAL DE PESQUISAS ESPACIAIS

sid.inpe.br/mtc-m21b/2017/04.12.00.58-TDI

**ANGLE-OF-ATTACK IMPACT IN THE
AEROTHERMODYNAMICS OF A HYPERSONIC
VEHICLE WITH SURFACE DISCONTINUITY-LIKE A
CAVITY**

Daimer Mauthsud Leovan Ospina Contreras

Master's Dissertation of the
Graduate Course in Engineering
and Space Technology, guided by
Dr. Wilson Fernando Nogueira dos
Santos, approved in April 19, 2017.

URL of the original document:

<<http://urlib.net/8JMKD3MGP3W34P/3NMDH2S>>

INPE
São José dos Campos
2017

Cataloging in Publication Data

Ospina Contreras, Daimer Mauthsud Leovan.
Os6a Angle-of-attack impact in the aerothermodynamics
of a hypersonic vehicle with surface discontinuity-like a
cavity / Daimer Mauthsud Leovan Ospina Contreras. – São
José dos Campos : INPE, 2017.
xxviii + 172 p. ; (sid.inpe.br/mtc-m21b/2017/04.12.00.58-TDI)

Dissertation (Engineering and Space Technology) – Instituto
Nacional de Pesquisas Espaciais, São José dos Campos, 2017.
Guiding : Dr. Wilson Fernando Nogueira dos Santos.

1. Computational study. 2. DSMC method. 3. Hypersonic
rarefied flow. 4. Aerothermodynamic. 5. Angle of attack. I.Title.

CDU 629.7.015:004



Esta obra foi licenciada sob uma Licença [Creative Commons Atribuição-NãoComercial 3.0 Não Adaptada](https://creativecommons.org/licenses/by-nc/3.0/).

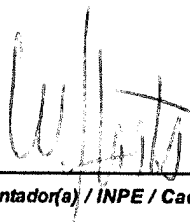
This work is licensed under a [Creative Commons Attribution-NonCommercial 3.0 Unported License](https://creativecommons.org/licenses/by-nc/3.0/).

Aluno (a): **Dalmer Mauthsud Leovan Ospina Contreras**
"ANGLE-OF-ATTACK IMPACT IN THE AEROTHERMODYNAMICS OF A HYPERSONIC VEHICLE WITH SURFACE DISCONTINUITY-LIKE CAVITY"

Aprovado (a) pela Banca Examinadora
em cumprimento ao requisito exigido para
obtenção do Título de **Mestre** em

Engenharia e Tecnologia
Especiais/Combustão e Propulsão

Dr. **Wilson Fernando Nogueira dos Santos**



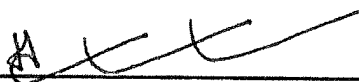
Presidente / Orientador(a) / INPE / Cachoeira Paulista - SP

Dr. **Jerônimo dos Santos Travelho**



Membro da Banca / INPE / São José dos Campos - SP

Dr. **Hélcio Francisco Villa Nova**



Convidado(a) / UNIFEI / Itajubá - MG

Este trabalho foi aprovado por:

maioria simples

unanimidade

São José dos Campos, 19 de Abril de 2017

“Failure is simply the opportunity to begin again, this time more intelligently”.

HENRY FORD

*To my grandparents **Manuel Ospina** and **Pabla Contreras**, To my mother **Amalia Ospina** and my brother **Juan David Pajoi***

ACKNOWLEDGEMENTS

Firstly, to my grandparents Manuel Ospina and Pabla Contreras, for their help in this process, for their teachings and support me always.

To my mother Amalia Ospina, for her understanding and help me in everything becoming my base of support.

To my advisor, Dr. Wilson F. N. Santos, who supervised this thesis. I acknowledge with gratitude his support, guidance and advice for all these years.

To my friends, Luis Carlos Roldan Torres, Luis Thiago Lucci Correa, Maycol Vargas, Paulo Henrique Mineiro Leite.

I also express my gratitude to Roldan and Lucci's family that supported me and helped me during this time.

Finally, I want to thank to Coordenação de Aperfeiçoamento de Pessoal de Nível Superior - CAPES for the financial support during my Masters course.

ABSTRACT

The study described in this dissertation was undertaken with the purpose to investigate the impact of discontinuities present on the surface of hypersonic space vehicles. With this perspective in mind, computational simulations of a non-reacting rarefied hypersonic flow over a flat plate with a cavity have been performed by using the Direct Simulation Monte Carlo method. Simulations provided a comprehensive description about the nature of the flowfield structure and the aerodynamic surface properties on the cavity resulting from changes in the length-to-depth (L/H) ratio and changes in the angle of attack of the oncoming flow. A detailed description of the flowfield properties (velocity, density, pressure and temperature) and aerodynamics surface properties (number flux, heat transfer, pressure and skin friction) were obtained by a numerical method that properly account for non-equilibrium effects in the transition flow regime. Results for a cavity defined by L/H ratio of 1, 2, 3 and 4, and flow with angle of attack of 10, 15 and 20 degrees, were compared to those of a flat plate without a cavity with zero-degree angle of incidence and with a flat plate at incidence. The analysis showed that the flow topology inside the cavity, composed by recirculation regions, depended on the L/H ratio as well as on the angle of attack, for the conditions investigated. For $L/H < 3$ a single vortex core was formed, and filled entirely the cavity. In contrast, for L/H of 3 and 4, two vortices were formed inside the cavity, at the vicinity of the backward and forward faces. The analysis also showed that, for the $L/H = 4$ case, the flow topology inside the cavity corresponds to that of a “closed cavity” in the continuum flow regime for 10-degree angle of incidence, and similar to an “open cavity” for the others angles of attack investigated. In addition, it was found that the maximum values for the heat transfer, pressure and skin friction coefficients inside the cavity took place on the cavity forward face. It was also found that, maximum values for heat transfer coefficient inside the cavities increased with increasing the angle of attack α . However, it was observed that these maximum values are smaller than those observed in a flat-plate without a cavity for the corresponding angle of attack. Consequently, in terms of pressure, the presence of the cavity on the vehicle surface can not be ignored in the vehicle design.

Keywords: Computational study. DSMC method. Hypersonic rarefied flow. Aerothermodynamic. Cavity. Angle of attack.

IMPACTO DO ÂNGULO DE ATAQUE NA AEROTERMODINÂMICA DE UM VEÍCULO HIPERSÔNICO COM DESCONTINUIDADES NA SUPERFÍCIE COMO UMA CAVIDADE.

RESUMO

O estudo descrito nesta dissertação foi realizado com o propósito de investigar o impacto de descontinuidades presentes na superfície de veículos espaciais hipersônicos. Em busca deste propósito, simulações computacionais de um escoamento hipersônico rarefeito não-reativo sobre uma cavidade foram realizadas usando-se o método Direct Simulation Monte Carlo. As simulações forneceram informações detalhadas sobre a natureza da estrutura do escoamento, propriedades primárias e propriedades aerodinâmicas, em função de mudanças na razão comprimento-profundidade (L/H) da cavidade, e mudanças no ângulo de ataque do escoamento incidindo sobre a cavidade. Uma descrição detalhada, das propriedades primárias (velocidade, massa específica, pressão e temperatura) e das quantidades aerodinâmica na superfície (transferência de calor, pressão e atrito), foi obtida por um método numérico que leva em conta adequadamente os efeitos de não-equilíbrio no regime de transição. Os resultados, para cavidades definidas por L/H de 1, 2, 3 e 4, com ângulos de ataque do escoamento de 10, 15 e 20 graus, foram comparados com os de uma placa plana sem/com a presença de cavidade sem/com incidência. A análise mostrou que a topologia do escoamento dentro da cavidade, composta por regiões de recirculação, dependeu da razão L/H bem como do ângulo de ataque do escoamento, para as condições investigadas. Para $L/H < 3$, observou-se a formação de um único vórtice ocupando inteiramente a cavidade. Para cavidade com $L/H = 3$ e 4, dois vórtices foram formados dentro da cavidade, nas vizinhanças das faces a montante e a jusante da cavidade. A análise também mostrou que, para uma cavidade com $L/H = 4$ e 10 graus de incidência, a estrutura do escoamento dentro da cavidade correspondeu aquela de uma “cavidade fechada”, conforme definido para um escoamento no regime do contínuo. Por outro lado, para $L/H = 4$ e maiores ângulos de incidência, a estrutura do escoamento correspondeu aquela de uma “cavidade aberta”, para os ângulos de ataque investigados. Outrossim, verificou-se que os valores máximos para os coeficientes de transferência de calor, pressão e coeficiente de atrito ocorreram na superfície a montante do escoamento dentro da cavidade. Verificou-se também que, os valores máximos para o coeficiente de transferência de calor dentro da cavidade aumentaram com o aumento do ângulo de ataque α . Todavia, esses valores máximos foram menores do que aqueles observados sobre uma placa plana sem cavidade com incidência. Como resultado, em termos de pressão, a presença da cavidade sobre a superfície do veículo não pode ser ignorada no projeto do veículo.

Palavras-chave: Estudo computacional. Metodo DSMC. Fluido hipersônico enrarecido. Aerotermodinâmica. Cavidade. Ângulo de ataque.

LIST OF FIGURES

	<u>Page</u>
1.1 (a) Thermal Protection System of Space Shuttle Discovery, (b) Space Vehicle X-37B, (c)TPS Assembly, (d)TPS Tiles.	2
1.2 Drawing illustrating the (a) location, (b) the on-orbiter photograph of D-118-RPM-600_2-001 damage site and (c) the final condition.	4
1.3 Flow regimes as a function of the Knudsen number.	6
1.4 Flowfield structure in cavities.	10
1.5 Streamline traces inside the cavities for L/H ratio of 1, 2, 3 and 4.	11
2.1 Validity of the conventional mathematical models as function of local Knudsen number.	16
2.2 Flowchart of the DSMC method.	22
2.3 Typical intermolecular force field.	24
2.4 Frames of references for the analysis of binary collisions.	33
2.5 Maxwell model of reflection.	37
3.1 Drawing illustrating the cavity.	39
3.2 Illustration of the computational domain.	42
4.1 Drawing illustrating the flat-plate computational domain.	51
4.2 Effect of the variation on a cell size (x -direction) on pressure (top), skin friction (middle) and heat transfer (bottom) coefficients.	54
4.3 Effect of changing the cell size (y -direction) on pressure (top), skin friction (middle) and heat transfer (bottom) coefficients.	55
4.4 Effect of changing the number of molecules on pressure (top), skin friction (middle) and heat transfer (bottom) coefficients.	56
4.5 Effect of changing the plate length on pressure (top), skin friction (middle) and heat transfer (bottom) coefficients.	57
4.6 Density ratio (ρ/ρ_∞) profiles normal to the plate surface for three locations along the plate surface.	59
4.7 Overall kinetic temperature ratio (T_O/T_∞) profiles normal to the plate surface for three locations along the plate surface.	59
4.8 Tangential velocity ratio ($u/U_\infty \cos\alpha$) profiles normal to the plate surface for three locations along the plate surface.	60
4.9 Density ratio (ρ/ρ_∞) profile at section $x/L = 1.5$ along the flat plate surface.	61
4.10 Wall pressure (p_w/p_∞) distribution along the flat plate surface.	62

4.11	Translational (T_T/T_∞) and rotational (T_R/T_∞) temperature distribution along the flat plate surface.	62
4.12	Effect of variation in the cell size in the x -direction on skin friction coefficient for $L/H = 1$ and $\alpha = 10$ deg.	66
4.13	Effect of variation in the cell size in the x -direction on pressure coefficient for $L/H = 1$ and $\alpha = 10$ deg.	67
4.14	Effect of variation in the cell size in the x -direction on heat transfer coefficient for $L/H = 1$ and $\alpha = 10$ deg.	68
4.15	Effect of variation in the cell size in the y -direction on skin friction coefficient for $L/H = 1$ and $\alpha = 10$ deg.	69
4.16	Effect of variation in the cell size in the y -direction on pressure coefficient for $L/H = 1$ and $\alpha = 10$ deg.	70
4.17	Effect of variation in the cell size in the y -direction on heat transfer coefficient for $L/H = 1$ and $\alpha = 10$ deg.	71
4.18	Effect of variation in the number of molecules on skin friction coefficient for $L/H = 1$ and $\alpha = 10$ deg.	72
4.19	Effect of variation in the number of molecules on pressure coefficient for $L/H = 1$ and $\alpha = 10$ deg.	73
4.20	Effect of variation in the number of molecules on heat transfer coefficient for $L/H = 1$ and $\alpha = 10$ deg.	74
4.21	A Drawing illustrating the cell distribution.	75
5.1	Tangential velocity ratio (u/U_∞) profiles for three sections along surface S1 parameterized by the cavity L/H ratio. Left and right columns correspond to angle of attack α of 10 and 20 degrees, respectively.	78
5.2	Tangential velocity ratio (u/U_∞) profiles for three sections along surface S1 parameterized by the angle of attack. Left and right columns correspond to cavity L/H ratio of 1 and 4, respectively.	80
5.3	Tangential velocity ratio (u/U_∞) profiles for three sections along surface S3 parameterized by the cavity L/H ratio. Left and right columns correspond to angle of attack α of 10 and 20 degrees, respectively.	81
5.4	Tangential velocity ratio (u/U_∞) profiles for three sections along surface S3 outside the cavity parameterized by the cavity L/H ratio. Left and right columns correspond to angle of attack α of 10 and 20 degrees, respectively.	82
5.5	Tangential velocity ratio (u/U_∞) profiles for three sections along surface S3 parameterized by the angle of attack α . Left and right columns correspond to cavity L/H ratio of 1 and 4, respectively.	83

5.6	Normal velocity ratio (v/U_∞) profiles inside the cavity for three transversal sections as a function of the dimensionless length X'_L . Left and right columns correspond to angle of attack α of 10 and 20 degrees, respectively.	85
5.7	Normal velocity ratio (v/U_∞) profiles inside the cavity for three transversal sections as a function of the dimensionless length X'_L . Left and right columns correspond to cavity L/H ratio of 1 and 2, respectively.	87
5.8	Normal velocity ratio (v/U_∞) profiles inside the cavity for three transversal sections as a function of the dimensionless length X'_L . Left and right columns correspond to cavity L/H ratio of 3 and 4, respectively.	88
5.9	Distribution of streamline traces inside the cavities for L/H ratio of 1, 2, 3, and 4 with 10-degree angle of attack.	89
5.10	Distribution of streamline traces inside the cavities for L/H ratio of 1, 2, 3, and 4 with 15-degree angle of attack.	90
5.11	Distribution of streamline traces inside the cavities for L/H ratio of 1, 2, 3, and 4 with 20-degree angle of attack.	91
5.12	Tangential velocity ratio (u/U_∞) profiles for three sections along surface S5 parameterized by the L/H ratio. Left and right columns correspond to angle of attack α of 10 and 20 degrees, respectively.	93
5.13	Tangential velocity ratio (u/U_∞) profiles for three sections along surface S5 parameterized by the angle of attack α . Left and right columns correspond to cavity L/H ratio of 1 and 4, respectively.	94
5.14	Distribution of Mach number along with streamline traces inside the cavity for L/H ratio of 1 (top), 2, 3, and 4 (bottom), with angle of attack $\alpha = 10$ degrees.	95
5.15	Distribution of Mach number along with streamline traces inside the cavity for L/H ratio of 1 (top), 2, 3, and 4 (bottom), with angle of attack $\alpha = 15$ degrees.	96
5.16	Distribution of Mach number along with streamline traces inside the cavity for L/H ratio of 1 (top), 2, 3, and 4 (bottom), with angle of attack $\alpha = 20$ degrees.	97
5.17	Density ratio (ρ/ρ_∞) profiles for three sections along surface S1 parameterized by the cavity L/H ratio. Left and right columns correspond to angle of attack α of 10 and 20 degrees, respectively.	99
5.18	Density ratio (ρ/ρ_∞) profiles for three sections along surface S1 parameterized by the angle of attack α . Left and right columns correspond to cavity L/H ratio of 1 and 4, respectively.	101

5.19	Density ratio (ρ/ρ_∞) profiles for three sections along surface S3 parameterized by the cavity L/H ratio. Left and right columns correspond to angle of attack α of 10 and 20 degrees, respectively.	102
5.20	Density ratio (ρ/ρ_∞) profiles for three sections along surface S3 outside the cavity parameterized by the cavity L/H ratio. Left and right columns correspond to angle of attack α of 10 and 20 degrees, respectively.	103
5.21	Density ratio (ρ/ρ_∞) profiles for three sections along surface S3 parameterized by the angle of attack α . Left and right columns correspond to cavity L/H ratio of 1 and 4, respectively.	105
5.22	Density ratio (ρ/ρ_∞) profiles for three sections along surface S5 parameterized by the L/H ratio. Left and right columns correspond to angle of attack α of 10 and 20 degrees, respectively.	106
5.23	Density ratio (ρ/ρ_∞) profiles for three sections along surface S5 parameterized by the angle of attack α . Left and right columns correspond to cavity L/H ratio of 1 and 4, respectively.	107
5.24	Distribution of density ratio (ρ/ρ_∞) along with streamline traces inside the cavity for L/H ratio of 1 (top), 2, 3, and 4 (bottom), with angle of attack $\alpha = 10$ degrees.	108
5.25	Distribution of density ratio (ρ/ρ_∞) along with streamline traces inside the cavity for L/H ratio of 1 (top), 2, 3, and 4 (bottom), with angle of attack $\alpha = 15$ degrees.	109
5.26	Distribution of density ratio (ρ/ρ_∞) along with streamline traces inside the cavity for L/H ratio of 1 (top), 2, 3, and 4 (bottom), with angle of attack $\alpha = 20$ degrees.	110
5.27	Pressure ratio (p/p_∞) profiles for three sections along surface S1 parameterized by the cavity L/H ratio. Left and right columns correspond to angle of attack α of 10 and 20 degrees, respectively.	112
5.28	Pressure ratio (p/p_∞) profiles for three sections along surface S1 parameterized by the angle of attack α . Left and right columns correspond to cavity L/H ratio of 1 and 4, respectively.	113
5.29	Pressure ratio (p/p_∞) profiles for three sections along surface S3 parameterized by the cavity L/H ratio. Left and right columns correspond to angle of attack α of 10 and 20 degrees, respectively.	114
5.30	Pressure ratio (p/p_∞) profiles for three sections along surface S3 outside the cavity parameterized by the cavity L/H ratio. Left and right columns correspond to angle of attack α of 10 and 20 degrees, respectively.	116

5.31	Pressure ratio (p/p_∞) profiles for three sections along surface S3 parameterized by the angle of attack α . Left and right columns correspond to cavity L/H ratio of 1 and 4, respectively.	117
5.32	Pressure ratio (p/p_∞) profiles for three sections along surface S5 parameterized by the L/H ratio. Left and right columns correspond to angle of attack α of 10 and 20 degrees, respectively.	118
5.33	Distribution of pressure ratio (p/p_∞) along with streamline traces inside the cavity for L/H ratio of 1 (top), 2, 3, and 4 (bottom), with angle of attack $\alpha = 15$ degrees.	120
5.34	Distribution of pressure ratio (p/p_∞) along with streamline traces inside the cavity for L/H ratio of 1 (top), 2, 3, and 4 (bottom), with angle of attack $\alpha = 10$ degrees.	121
5.35	Distribution of pressure ratio (p/p_∞) along with streamline traces inside the cavity for L/H ratio of 1 (top), 2, 3, and 4 (bottom), with angle of attack $\alpha = 20$ degrees.	122
5.36	Kinetic temperature ratio (T/T_∞) profiles for three sections along surface S1 parameterized by the cavity L/H ratio. Left and right columns correspond to angle of attack α of 10 and 20 degrees, respectively.	124
5.37	Kinetic temperature ratio (T/T_∞) profiles for three sections along surface S1 parameterized by the angle of attack α . Left and right columns correspond to cavity L/H ratio of 1 and 4, respectively.	125
5.38	Kinetic temperature ratio (T/T_∞) profiles for three sections along surface S3 parameterized by the cavity L/H ratio. Left and right columns correspond to angle of attack α of 10 and 20 degrees, respectively.	128
5.39	Kinetic temperature ratio (T/T_∞) profiles for three sections along surface S5 parameterized by the L/H ratio. Left and right columns correspond to angle of attack α of 10 and 20 degrees, respectively.	129
5.40	Kinetic temperature ratio (T/T_∞) profiles for three sections along surface S5 parameterized by the angle of attack α . Left and right columns correspond to cavity L/H ratio of 1 and 4, respectively.	130
5.41	Distribution of overall temperature ratio (T/T_∞) along with streamline traces inside the cavity for L/H ratio of 1 (top), 2, 3 and 4 (bottom), with angle of attack $\alpha = 10$ degrees.	131
5.42	Distribution of overall temperature ratio (T/T_∞) along with streamline traces inside the cavity for L/H ratio of 1 (top), 2, 3 and 4 (bottom), with angle of attack $\alpha = 15$ degrees.	132

5.43	Distribution of overall temperature ratio (T/T_∞) along with streamline traces inside the cavity for L/H ratio of 1 (top), 2, 3 and 4 (bottom), with angle of attack $\alpha = 20$ degrees.	133
5.44	Dimensionless number flux (N_f) distribution along the cavity surfaces parameterized by the cavity L/H ratio for 10-degree angle of attack.	135
5.45	Dimensionless number flux (N_f) distribution along the cavity surfaces parameterized by the cavity L/H ratio for 20-degree angle of attack.	136
5.46	Dimensionless number flux (N_f) distribution along the cavity surfaces parameterized by the angle of attack α for the L/H ratio of 1.	138
5.47	Dimensionless number flux (N_f) distribution along the cavity surfaces parameterized by the angle of attack α for the L/H ratio of 4.	139
5.48	Heat transfer coefficient (C_h) distribution along the cavity surfaces parameterized by the cavity L/H ratio for for 10-degree angle of attack.	141
5.49	Heat transfer coefficient (C_h) distribution along the cavity surfaces parameterized by the cavity L/H ratio for for 20-degree angle of attack.	142
5.50	Heat transfer coefficient (C_h) distribution along the cavity surfaces parameterized by the angle of attack α for the cavity L/H ratio of 1.	144
5.51	Heat transfer coefficient (C_h) distribution along the cavity surfaces parameterized by the angle of attack α for the cavity L/H ratio of 4.	145
5.52	Pressure coefficient C_p distribution along the cavity surfaces parameterized by the L/H ratio for 10-degrees angle of attack.	148
5.53	Pressure coefficient C_p distribution along the cavity surfaces parameterized by the L/H ratio for 20-degrees angle of attack.	149
5.54	Pressure coefficient (C_p) distribution along the cavity surfaces parameterized by the angle of attack α for the cavity L/H ratio of 1.	150
5.55	Pressure coefficient (C_p) distribution along the cavity surfaces parameterized by the angle of attack α for the cavity L/H ratio of 4.	151
5.56	Skin friction coefficient (C_f) distribution along the cavity surfaces parameterized by the cavity L/H ratio for 10-degrees angle of attack.	154
5.57	Skin friction coefficient (C_f) distribution along the cavity surfaces parameterized by the cavity L/H ratio for 20-degrees angle of attack.	155
5.58	Skin friction coefficient (C_f) distribution along the cavity surfaces parameterized by the angle of attack α for the cavity L/H ratio of 1.	157
5.59	Skin friction coefficient (C_f) distribution along the cavity surfaces parameterized by the angle of attack α for the cavity L/H ratio of 4.	158

LIST OF TABLES

	<u>Page</u>
3.1 Geometric characteristics for the cavities.	40
3.2 Characteristics of simulated air for DSMC calculations.	41
3.3 Freestream flow conditions.	43
4.1 Freestream conditions (LENGRAND et al., 1992).	49
4.2 Freestream conditions (DOGRA et al., 1989).	50
4.3 Number of cells in the (x -direction) and the [y -direction] for the flat plate case.	52
4.4 Number of cells in the (x -direction) and the [y -direction] for the cavity case.	64

NOMENCLATURE

A	Area, m^2
a	Speed of sound, m/s
C_f	Skin friction coefficient, $\tau_w/(\frac{1}{2}\rho_\infty U_\infty^2)$
C_h	Heat transfer coefficient, $q_w/(\frac{1}{2}\rho_\infty U_\infty^3)$
C_p	Pressure coefficient, $(p_w - p_\infty)/(\frac{1}{2}\rho_\infty U_\infty^2)$
\mathbf{c}	Molecular velocity vector, m/s
\mathbf{c}'	Thermal molecular velocity, m/s
e	Specific molecular energy, J/kg
d	Molecular diameter, m
D	Diffusion coefficient, m^2/s
F	Force, N
F_n	Intermolecular force potential
F_N	Real molecules represented by a single DSMC molecule
H	Cavity depth, m
Kn	Knudsen number, λ/l
k	Molecular characteristic constant; Boltzmann constant, $1.3806488 \times 10^{-23} \text{ Js}$
L	Cavity length, m
l	Characteristic length, m
M	Mach number, $ U /a$
m	Molecular mass, kg
N	Number of particles
N_{coll}	Number of collisions
N_f	Dimensionless number flux
n	Number density, m^{-3}
p	Pressure, N/m^2
P	A probability
q	Heat flux, W/m^2
R	Ordinary gas constant, $J/Kmol$
Re	Reynolds number
R_F	Random number between 0 and 1
r	Position vector; Intermolecular separation, m
T	Temperature, K
t	Time, s
U	Velocity, m/s
u	Tangential velocity, m/s
V_C	Cell volume, m^3

v	Normal velocity, m/s
X	Dimensionless length, x/λ_∞
X''_L	Dimensionless length, $(X - L_u - L)/L_d$
X'_L	Dimensionless length, $(x - L_u)/L$
Y	Dimensionless height, y/λ_∞
Y_H	Dimensionless height, y/H
Z	Relaxation collision number

GREEK SYMBOLS

α	Accommodation coefficient; Angle of attack, degree
Δ	Increment
δt	Time counter
η	Molecular characteristic constant; Power law
λ	Mean free path, m
μ	Viscosity coefficient, $kg/m.s$
ω	Viscosity-temperature index
ϕ	Potential energy of interaction; Average probability
φ	Gas property
ρ	Gas density, kg/m^3
σ	Collision cross-section, m
σ_T	Total collision cross-section
τ	Relaxation time, s ; Shear stress, N/m^2
τ_c	Mean collision time, s
Θ	Characteristic temperature, K
ζ	Number of degrees of freedom

SUBSCRIPTS AND SUPERSCRIPTS

d	Refers to downstream
H	Refers to cavity depth
i	Refers to incident
L	Refers to cavity length
m	Refers to centre of mass
n	Refers to normal
O	Refers to overall
R	Refers to rotational

<i>r</i>	Refers to rotational; reduced; relative; Reflect
<i>ref</i>	Refers to reference values
<i>T</i>	Refers to translational
<i>t</i>	Refers to translational
<i>u</i>	Refers to upstream
<i>V</i>	Refers to vibrational
<i>v</i>	Refers to vibrational
<i>w</i>	Refers to wall conditions
<i>x, y, z</i>	Refers to x-, y-, and z- cartesian axes
1, 2	Refers to species
∞	Refers to the freestream
*	refers to post-collision

CONTENTS

	<u>Page</u>
1 INTRODUCTION	1
1.1 Motivation	1
1.2 Reentry Flow Regimes	4
1.3 Review of Previous Work	6
1.4 Problem Definition and Scope of Current Work	12
2 COMPUTATIONAL METHOD	15
2.1 Methods for Modeling Transition Flows	15
2.2 Direct Simulation Monte Carlo (DSMC) Method	19
2.2.1 DSMC Methodology	21
2.2.2 Molecular Model	23
2.2.3 Collision Model	28
2.2.4 Binary Elastic Collision	30
2.2.5 Internal Degrees of Freedom	34
2.2.6 Boundary Conditions	35
3 COMPUTATIONAL PROCEDURE	39
3.1 Geometry Definitions	39
3.2 Computational Conditions	40
3.3 Freestream and Flow Conditions	43
4 VERIFICATION AND VALIDATION PROCESSES	45
4.1 Computational Requirements	45
4.2 Computational Mesh Generation	47
4.3 Computational Mesh Adaptation	47
4.4 DSMC Test Case	48
4.4.1 Effect of Mesh Resolution	51
4.4.2 Effect of the Variation in the Number of Molecules	52
4.4.3 Effect of Downstream Boundary Condition	53
4.5 Experimental and Numerical Comparisons	58
4.5.1 First Test Case	58
4.5.2 Second Test Case	60
4.6 Cavity test case	63

5	COMPUTATIONAL RESULTS AND DISCUSSIONS	77
5.1	Flowfield Structure	77
5.1.1	Velocity Field	77
5.1.2	Density Field	98
5.1.3	Pressure Field	111
5.1.4	Kinetic Temperature Field	119
5.2	Aerodynamics Surface Quantities	134
5.2.1	Number Flux	134
5.2.2	Heat Transfer Coefficient	140
5.2.3	Pressure Coefficient	146
5.2.4	Skin Friction Coefficient	152
6	CONCLUSIONS	159
6.1	Concluding Remarks	159
6.2	Future Work	160
	REFERENCES	161

1 INTRODUCTION

1.1 Motivation

Hypersonic vehicles, such as space vehicles, hypersonic aircrafts, missiles and projectiles are exposed to severe aerodynamics and aerothermodynamics loads that can perturb the aerodynamics of the vehicle as well as result in heating of the surface. In this way, the knowledge of factors affecting the thermal and mechanical loads acting on the vehicle is one of the key issues in the design of hypersonic vehicles for future space systems. Usually, in the thermal loads calculation, the analysis assumes that the vehicle has a smooth surface. However, discontinuities are present in the aerospace vehicles surfaces. Large discontinuities are observed due to sensor installations, mechanical connections and open gates, while small discontinuities are present as features of design and fabrication (BERTRAM; WIGGS, 1963; BERTRAN et al., 1967; HAHN, 1969; NESTLER et al., 1969; NESTLER, 1982; MORGENSTERN JR.; CHOKANI, 1994; SILTON; GOLDSTEIN, 2000; SARAVANAN et al., 2009; THOMPSON et al., 2009; HUANG et al., 2011; HAIBO; WEIQIANG, 2012; HAIBO; WEIQIANG, 2013). Small discontinuities can be divided in two types, distributed and discrete. Distributed discontinuities are generally small and abundant such as cavities, gaps, steps and protuberances. This type of discontinuities is present on the surfaces due to fabrication tolerances and space between tiles in the Thermal Protection System (TPS) of Space Shuttle Orbiter. Discrete discontinuities are typically unintentional such as damages from launch in the form of cavities or gaps, and differential expansion or ablation rates between nonsimilar materials (BERRY; HORVATH, 2008).

The TPS of reentry vehicles, such as that in the space shuttle orbiter or in the space vehicle X-37B (Figure 1.1(a),(b).) usually consist in tiles of silica foam with 6 X 6 inches squares, with variable depth that depends on the tile location on the surface. These tiles require cavities or gaps between the junctions in order to compensate the thermal expansion of the material. In this context, it is necessary a detailed prediction of the flow conditions and the thermal loads due the presence of cavities or gaps in the thermal protection system (SCOTT; MARAIA, 1979).

The flow inside gaps and cavities can be complex due to pressure gradients (EVERHART et al., 2006), to the flow-structure interaction (HINDERSKIS; RADESPIEL, 2006), and others factors. Moreover, the flow configuration become more complex if the structure of the vehicle is deformed by thermal or mechanical loads. These mechanical or thermal loads may cause significant changes in the dimensions of the gaps or cavities between the thermal protection tiles located in the vehicle surface.

Figure 1.1 - (a) Thermal Protection System of Space Shuttle Discovery, (b) Space Vehicle X-37B, (c)TPS Assembly, (d)TPS Tiles.



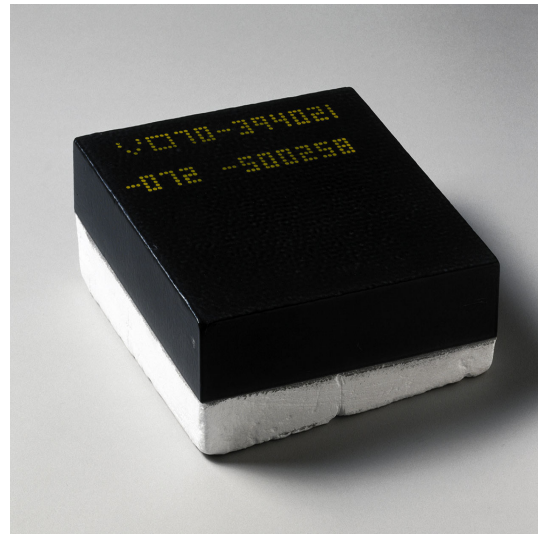
(a)



(b)



(c)



(d)

SOURCE: (a)National Aeronautics and Space Administration NASA (2009),(b)The Boeing company (2010), (c)Science Museum London / Science and Society Picture Library (1986), (d)DAZZI, F. (2005).

Consequently, these modifications in the geometry of the vehicle can lead to the appearance of stagnation points, hot spots and affect the boundary layer transition (BERRY; HORVATH, 2008).

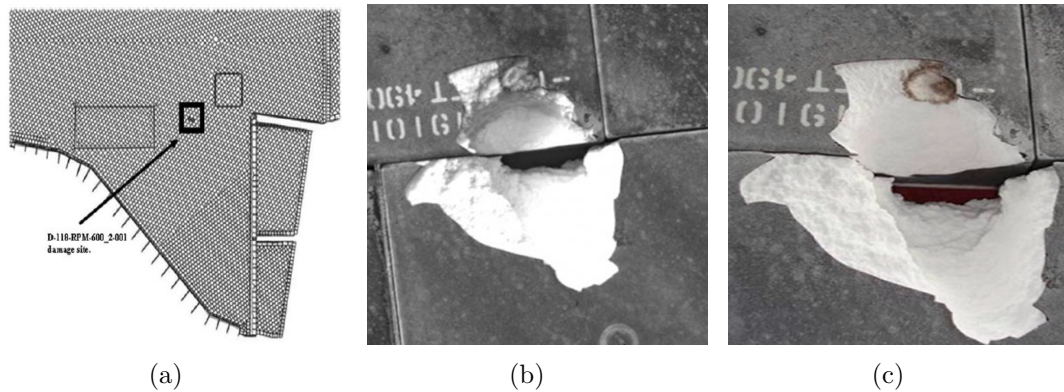
Defects in the TPS can cause serious accidents such as that occurred with the Space Shuttle Orbiter Columbia, during its reentry from orbit on February 1, 2003. According to the final report of the Columbia Accident Investigation Board (CAIB), a piece of insulating foam produced a breach in the TPS of the leading edge of the left wing. It is believed that this small breach in the TPS resulted in a local increase of the heating and eventual burn through of the structure due to the severe aerothermodynamic environment in the reentry trajectory of the Columbia during its mission STS-107 (EVERHAT *et al.*, 2011).

Similar to the accident of the Space Shuttle Orbiter Columbia, a piece of foam insulation was released from the external tank of the Space Shuttle Endeavour during the vehicle ascent in its mission STS-118 in August 2007 (PALMER *et al.*, 2009). The impact of the foam in the TPS tile caused a defect like a cavity, 0.076 m long by 0.051 m wide, designated as damage site D-118-RPM-600_2-001, as illustrated in the Figure 1.3(a). The photograph shown in the Figure 1.3(b) was produced during the damage site inspection performed when the Orbiter Endeavour was docked to the International Space Station (ISS). In these sense, a group of analysts, scientists from the NASA Ames and NASA Langley Research Centers, known as the Damage Assessment Team (DAT), performed computational fluid dynamic (CFD) simulations in order to provide insight into the flow structures and flow physics in the interior of the cavity. Based on the detailed CFD solutions generated by the DAT, it was decided not to perform a spacewalk to repair the damage site but rather to fly Space Shuttle Endeavour back to Earth with the damage site. Fortunately, the Space Shuttle Endeavour successfully entered to the Earth atmosphere and landed on August 21, 2007. The final condition of the piece of insulation is shown in the Figure 1.3(c).

These examples emphasizes the importance of the flow over gaps or cavities and indicate that a precise investigation in the aerothermodynamic loads is needed in design of space vehicles .

In the development of space vehicles, the modeling of the reentry aerothermodynamics is one of the key issues. The precise knowledge of the aerodynamics of the vehicles along the trajectory on reentry allows a better understanding of the vehicles performance, possibly resulting in increased payload as well as a reduction in the thickness of the thermal protection system of the space vehicle.

Figure 1.2 - Drawing illustrating the (a) location, (b) the on-orbiter photograph of D-118-RPM-600_2-001 damage site and (c) the final condition.



SOURCE: PALMER et al. (2009).

1.2 Reentry Flow Regimes

Space vehicles reentering into the Earth atmosphere go through different velocity and flow conditions. In the descent phase during reentry, space vehicle enters the upper atmosphere where the air density is significantly low, and as the vehicle approaches the surface of the Earth, the air density increases. In this phase, space vehicles undergo not only different velocity regimes - hypersonic, supersonic and subsonic - but also different flow regimes (free molecular, transition and continuum flow)(see Figure 1.3). Therefore, the vehicle flight trajectories transverse a wide range of Mach, Reynolds and Knudsen numbers that may difficult the aerodynamic design.

During the descent phase, important physical interactions arise between the space vehicle and the environment. At high altitudes, the interaction between the vehicle and the atmospheric air is characterized by the free molecular flow regime. In this regime, molecules collide with the surface of the vehicle, interact with the surface and then are reflected from the surface. However, collisions of reflected molecules with incoming molecules from the freestream are not frequently in this flow regime. As a result, these collisions are ignored.

As the space vehicle enters a little deeper into the dense atmosphere, the mean free path between incoming molecules decreases, and collisions between molecules reflected from the vehicle surface and the molecules incoming from the freestream can no longer be ignored. As a result, the flow in this condition defines the transition

flow regime, i.e., transition between the collisionless flow regime and the continuum flow regime. In the transition flow regime, the contribution of aerodynamic forces and heat flux to the vehicle surface increases rapidly with decreasing altitude, causing large changes in the aerodynamic characteristic of the vehicle when compared with those observed in the free molecular flow.

As the space vehicle continues to enter into the atmosphere, it finally reaches the continuum flow regime. In this regime, the flow around the space vehicle is treated by a macroscopic model that considers the air as a continuum, and the description of the flow is made in terms of spatial and temporal variations of the primary properties, such as velocity, pressure, density and temperature.

The basic criterion that determines the flow regimes, as collisionless, transition or continuum flow regime, is determined by a nondimensional parameter called Knudsen number, defined as:

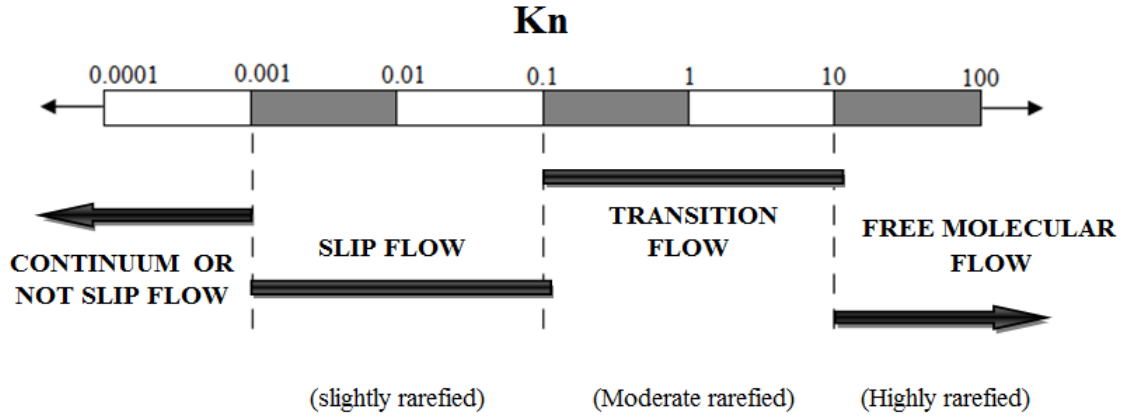
$$Kn = \frac{\lambda}{l} \quad (1.1)$$

where λ is the molecular mean free path, the distance travelled by molecules between collisions, and l is the characteristic length of the body. The mean free path λ varies by orders of magnitude between high altitudes and sea-level. In addition, l can be larger for object such as meteors and blunt spacecraft, or can be small for space debris and sharp leading edge on hypersonic vehicles.

A flow is defined in the free molecular flow when the Knudsen number tends to infinity. On the other hand, the flow is defined in the continuum regime when the Knudsen number goes to zero. Figure 1.3 presents the classification of flow regimes as a function of the local Knudsen number. It should also be mentioned that these limits are just indicative values and do not represent a general rule.

For flows around reentry vehicles in the range from 120 *km* to 60 *km* of altitude, the mean free path λ may be of the order of the dimensions of the discontinuities on the vehicle surface. In such a circumstance, the Knudsen number, which indicates the degree of rarefaction, may be in the range of the transition flow regime, i.e., between the continuum flow regime and the collisionless flow regime. For example, the depth H and the length L for gaps or cavities are usually on the order of 3 to 12 *mm* (WEINSTEIN et al., 1975; GAI; MILTHORPE, 1995; EVERHART et al., 2006). Therefore, as a base of comparison, for 90, 80, 70, and 60 *km* of altitude, the mean

Figure 1.3 - Flow regimes as a function of the Knudsen number.



SOURCE: GAD-EL-HAK (1999).

free path λ is 26.03, 4.11, 0.929 and 0.265 *mm*, respectively. As a result, for $H(ou L)$ of 3 *mm*, the overall Knudsen number is the order of 8.67, 1.37, 0.31 and 0.088, for altitudes of 90, 80, 70 and 60 *km*, respectively. By considering $H(ou L)$ of 12 *mm*, the overall Knudsen number is reduced by quarter. In this scenario, the Knudsen number is in the transition flow regime, usually defined by the range $0.1 < Kn < 10$. In the transition flow regime, the concepts of the continuum hypothesis can not be applied and the molecular structure of the gas must be considered.

1.3 Review of Previous Work

Flows on gaps, cavities and steps, which are found in many engineering applications, have been investigated for several decades. In the aerospace engineering, gaps, cavities or steps appear as design features in modern aerodynamics configurations. Several experimental and numeric studies (BERTRAM; WIGGS, 1963; NICOLL, 1964; BERTRAN et al., 1967; HAHN, 1969; NESTLER et al., 1969; NESTLER, 1982; MORGENSTERN JR.; CHOKANI, 1994; GAI; MILTHORPE, 1995; GROTHOWSKY; BALLMANN, 2000; SHANKAR; DESHPANDE, 2000; ESTEVE et al., 2000; JACKSON et al., 2001; HOZUMI et al., 2004; ZDANSKI et al., 2004; NARIS; VALOUGEORGIS, 2005; EVERHART et al., 2006; HINDERSKS; RADESPIEL, 2006; LEE; CHANDRA, 2006; ROWLEY; WILLIAMS, 2006; MIZZI et al., 2007; PALHARINI, 2010; OHMACHI; SUSUKI, 2011) have been conducted with the purpose of investigating the impact of these surface discontinuities on the flowfield structure of supersonic/hypersonic flows over the aerospace

vehicles. For the purpose of this introduction, only a few of these studies will be discussed below.

Bertram and Wiggs (BERTRAM; WIGGS, 1963) have investigated experimentally the effect of distortions, consisting of small steps and slots on the wing of a hypersonic vehicle. The effect of distortions in the pressure on and heat flux to the surface was investigated for Mach number in the range of 7 to 10 and angle of attack up to 20 degrees. According to the results, the distortions in the surface had a much smaller influence in the pressure distribution than on the heat flux. The study showed that all distortions investigated caused at least high local increased in the aerodynamic heating.

Nicoll (NICOLL, 1964) investigated experimentally the effect of the cavity length-to-depth (L/H) ratio on pressure and heat transfer coefficient, and on the reattachment region. The investigation was based on cones with annular cavities with L/H ratio between 2 and 20, using a helium flow at freestream Mach number of 11. For the flow condition investigated, he found that the region of influence of significant disturbance due the presence of cavity extended about one cavity length downstream of reattachment zone. The pressure over the cavity floor for $L/H < 7$ is constant over the first 90% of the cavity length and increases to the last 10%. For cavities with $L/H > 7$, the pressure increases gradually over all cavity floor. In addition, the heat transfer coefficient on the floor of the cavity is about 10 to 20% of the value for the attached flow heat transfer coefficient.

Nestler et al. (NESTLER et al., 1969) conducted an experimental investigation on cavities and steps in a hypersonic turbulent flow. For the flow conditions investigated, they found that the pressure distributions in the cavity presented a typical behavior of closed cavity flow in the sense that the flow expands into the cavity, reattaches to the floor, and separates as it approaches the downstream corner.

Unsteady hypersonic flow over cavities was investigated numerically by Morgenstern Jr. and Chokani (MORGENSTERN JR.; CHOKANI, 1994). The objective of the study was to examine the effects of Reynolds number and the cavity L/H ratio. It was found a significant increase in the heat transfer rate and variations in the static pressure at the rear part of the cavity. In addition, flow oscillations were observed for high Reynolds number flows. Results also showed that the amplitude of these oscillations increased with the cavity L/H ratio.

Flowfield characterization inside cavities was investigated experimentally by Esteve

et al. (ESTEVE *et al.*, 2000). The objective of their study was to analyze the flow-field structure inside a cavity with high (L/H) ratio for a low Reynolds number. The investigation showed that there is no reattachment point at the bottom of the cavity, but a sub-layer with negative axial mean velocity appeared. The sub-layer appeared 2 *mm* above the bottom wall and stopped the shear layer giving rise to a stagnation point. The investigation compared results for a cavity with those for a rearward-facing step, and determined that the influence of the rearward facing step was insignificant. In addition, an important increase of the turbulence level was observed downstream from the stagnation point due the second recirculation zone.

Everhart *et al.* (EVERHART *et al.*, 2006) investigated experimentally the effect of a pressure gradient on the local heating disturbance of rectangular cavities in a hypersonic flow at Mach 10. This experimental study showed that for open cavities, pressure gradient has a minimal effect on the average floor augmentation. Conversely, for closed cavities, pressure gradient increased the average heating by a factor of 50% above the zero gradient conditions, which was approximately 0.3. An assessment of the maximum increasing on the end wall revealed no apparent effect for the short or open cavity. However the analysis was inconclusive for the long or closed cavity.

Ohmichi and Susuki (OHMICHI; SUSUKI, 2011) investigated numerically and experimentally a hypersonic flow over a shallow cavity. The objective of the study was to analyze the heat transfer flux inside the cavity and the flowfield structure. The computational study was based on a three-dimensional cavity with different length-to-width (L/W) ratio and L/H of 50. The results showed that longitudinal vortices are generated inside and outside downstream the cavity. These vortices increases the heat transfer to the cavity sidewalls. Similarly, near the cavity back face, two ascendent vortices are generated, which increase the pressure and the heat transfer on the wall. For the experimental study, two configurations of cavity were tested. One configuration is a flat plate with a shallow cavity in the flow direction and the other configuration is a flat plate with H-shaped cavity. For the test, it was used oil flow at Mach number equal to 7, pressure and temperature of stagnation equal to 950 kPa and 650 K, respectively, and 10-degree angle of attack. The study confirmed the presence of the longitudinal vortices inside and outside of the cavities. In addition, for the H-shaped cavity, two shock or compression waves were generated from the lateral channels.

Based on studies available in the current literature (EVERHART *et al.*, 2006), the flow topology over cavities in the continuum flow regime may be generally identified

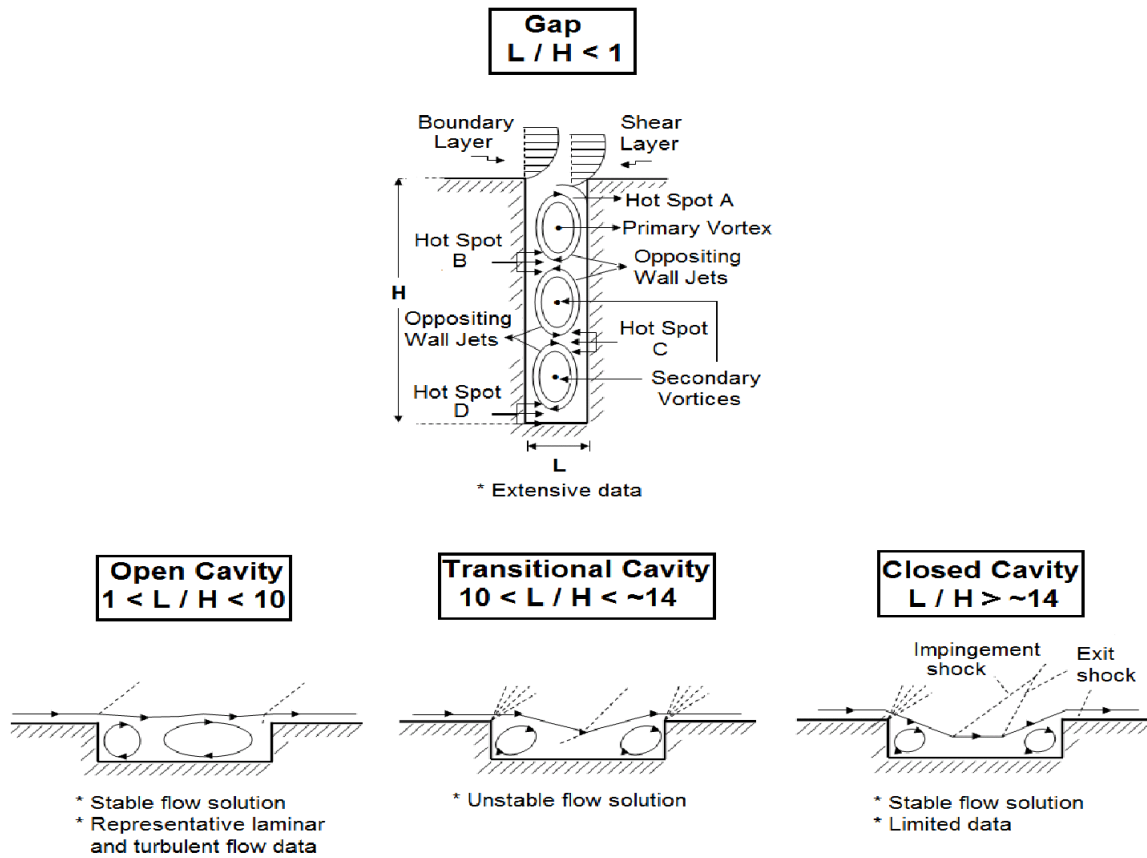
by the length-to-depth (L/H) ratio. Figure 1.4 illustrates the flow regimes through cavities as a function of the L/H ratio. The main cases may be defined as following:

- $L/H < 1$: deep cavities are defined as gaps. The gap flow topology is usually defined by the development of a column of counter-rotating vortices within the gap caused by the main stream flow, where the number of vortices is approximately given by H/L ratio.
- $1 < L/H < 10$: defined as open cavities. In this range, the flow conditions are stable. The mainstream flow does not enter into the cavity directly. The pressure in the cavity is typically above that of the environment and reaches a peak at the corner of the cavity forward face.
- $10 < L/H < 14$: defined as transitional cavities. Cavities in this range are considered as unsteady, since the flow alternates between open and closed cavity. These cavities are avoided in experimental tests due to the complexity of instrumentation and test time necessary to observe the transient process.
- $L/H > 14$: defined as closed cavities; The flow conditions are stable, similar to those in open cavities. In this configuration, three distinct types of flow can occur if the cavity is sufficiently long: (1) the upstream flow is able to penetrate into the cavity and to reach the bottom surface, similar to the flow on a backward-facing step, (2) the boundary layer on the bottom surface may develop and reach the outside, and (3) as the flow reaches the cavity forward face, it turns outward in a similar way like the flow in a forward-facing step.

It is important to mention that different investigations (SOLTANI; HILLIER, 1994; ESTEVE et al., 2000; THOMPSON et al., 2009; ATVARIS et al., 2009; LADA; KONTIS, 2010) have found different ranges of L/H ratio for open, transitional and closed cavity flows.

Finally, Palharini (PALHARINI, 2010) investigated a hypersonic rarefied flow over cavities by employing the Direct Simulation of Monte Carlo (DSMC) method. The study was motivated by the interest in investigating the L/H ratio effect in the flowfield structure and in the aerodynamic proprieties on the surface. In this study,

Figure 1.4 - Flowfield structure in cavities.

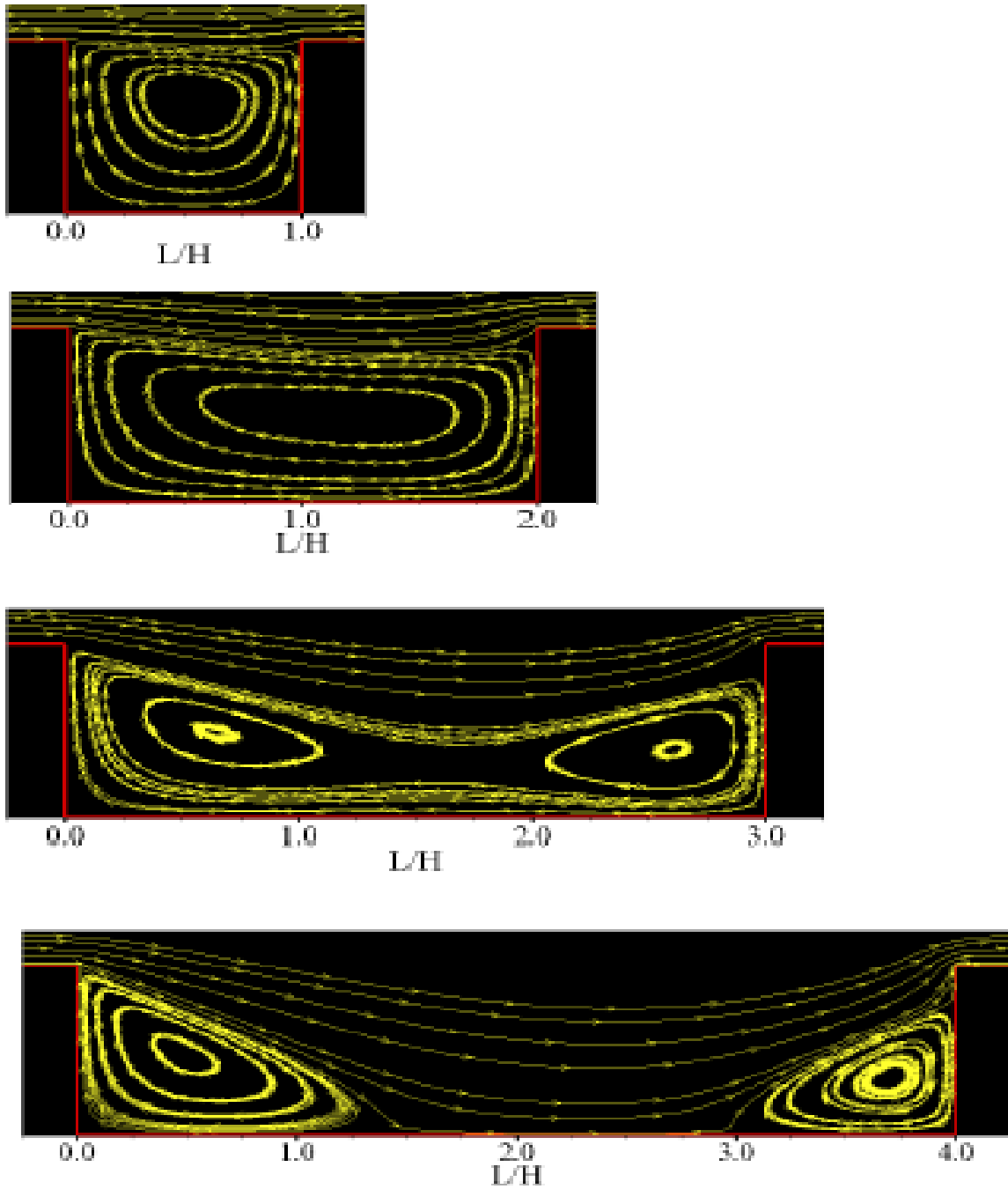


SOURCE: Everhart et al. (2006).

the major emphasis was to examine the behavior of the primary properties, such as velocity, density, pressure and temperature, together with the aerodynamics surface quantities for L/H ratio of 1, 2, 3, and 4. The analysis showed that for L/H ratio of 1 and 2 the flow structure was characterized by a primary recirculation region system, with the recirculation region filling the entire cavities. In contrast, for L/H of 3 and 4, it was observed the formation of two recirculation regions. However, the external stream reached the cavity bottom surface only for the L/H ratio of 4. Therefore, for the conditions investigated, the flow topology corresponded to that of an “open cavity” for L/H ratio of 1 and 2, and a “close cavity” for L/H ratio of 4, as defined in the continuum flow regime. For convenience and later reference, Figure 1.5 illustrates the flow structure inside the cavities for L/H ratio of 1, 2, 3

and 4 obtained by Palharini (PALHARINI, 2010).

Figure 1.5 - Streamline traces inside the cavities for L/H ratio of 1, 2, 3 and 4.



SOURCE: Palharini (2010).

1.4 Problem Definition and Scope of Current Work

The majority of the available research studies on surface discontinuities, as pointed out in the previous subsection, has gone into considering laminar or turbulent flow in the continuum flow regime. Nevertheless, there is little understanding of the physical aspects of a rarefied hypersonic flow past to these surface discontinuities related to the severe aerothermodynamic environment associated to a reentry space vehicle. In this fashion, the purpose of this dissertation is to investigate the effect of the angle of attack on discontinuities present on the surface of a reentry vehicles. The primary emphasis is to examine the sensibility of the flowfield structure and of the aerodynamic surface quantities due to angle of attack variation of a hypersonic flow in the transition flow regime. In the present work, the flowfield structure is defined by the distribution of the primary properties, such as velocity, density, pressure, and the kinetic temperature, adjacent to the vehicle surfaces. Aerodynamic surface quantities are identified by the heat flux, and the normal and tangential forces acting on the vehicle surface.

In the present account, surface discontinuities are modeled by cavities, usually present in the TPS of hypersonic reentry vehicles, in a sufficiently high altitude where the mean free path becomes large, as compared to the cavity dimensions, for the use of continuum hypothesis but not large enough for applying free molecular concept. At high altitudes, and therefore, low density, the molecular collision rate is low and the energy exchange occurs under non-equilibrium conditions. In such a circumstance, the conventional continuum gas dynamics that are based on the concept of local equilibrium is inappropriate, and an approach based on molecular gas dynamics is required.

In order to assess the overall performance of these cavities, a parametric study related to the effects of the length-to-depth (L/H) ratio and angle of attack will be explored. In an attempt to assess such effects, a two-dimensional flat plate with a cavity in a hypersonic flow will be investigated by employing the Direct Simulation Monte Carlo (DSMC) method.

The research behind the contribution of this work is described in detail in the remainder of this dissertation. In order to guide the reader, a breakdown of the purpose and contents of the following chapters is provided below.

Chapter 2: In this chapter, a description of the appropriate computational method is presented. Particular emphasis is placed on the DSMC methodology, molecular

model, collision model, internal degrees of freedom and boundary conditions.

Chapter 3: The computational procedure is explored in this chapter. It includes the simulation conditions, the definition of the geometry analyzed in this research as well as the important geometric parameters.

Chapter 4: This chapter outlines the procedure for the verification and validation processes of the DSMC code employed in the simulations. This procedure is applied in a test case defined by a two-dimensional cavity in a flat plate. The DSMC code is validated with simulation of a hypersonic flow over a flat plate at incidence and comparisons with previous experimental and numerical results are presented.

Chapter 5: The purpose of this chapter is to present the computational results and discussion. In this chapter, the major features of the primary properties, velocity, density, pressure and kinetic temperatures, are discussed in details. Moreover, the aerodynamic surface quantities, number flux to the surface, heat transfer, pressure, and shear stress, expressed in a coefficient form, are carefully examined.

Chapter 6: The final chapter of this dissertation contains a summary of the results obtained throughout the course of this work, and the conclusions that were drawn from them. Recommendations are made regarding further computational work that should be undertaken on the topic of this dissertation.

2 COMPUTATIONAL METHOD

2.1 Methods for Modeling Transition Flows

The resurgence of interest in the last decades toward developing concepts for future hypersonic transportation systems has witnessed incredible advancements in the technology and scientific knowledge base. Hypersonic systems are complex due to a lack in the physical understanding of the involved flow regimes. High temperature gas effects is one of the key issues that deserve a better understanding in order to improve the technology level for future space systems. High temperature gas effects have a great influence on the forces present in the flows (pressure, shear stress), on the energy flux (radiative and convective heating), and on the mass flux (ablation). As the flow density decreases, the complexity of these problems becomes more representative, making more difficult to find experimental studies for hypersonic flow of high enthalpy and low density, where several physical and chemical processes are relevant. The rapid and significant advances in computational power in recent decades have identified computational fluid dynamics as an important and indispensable tool for research in this field. In this way, the development of various numerical methods to simulate these flows has increased. As result, nowadays there are many numerical methods which are accurate and capable of solving hypersonic problems in a rarefied environment. The characteristic length of the problem, degree of flow rarefaction and the presence of the real gas effects are important items when choosing the appropriate method.

Aerothermodynamic flows are characterized by a variety of dimensionless quantities. For the purpose of this work, the Reynolds number, Re , the Mach number, M , and the Knudsen number, Kn , are the most important. The overall Knudsen number defined by Equation 1.1 expresses the degree of rarefaction of the flow. By considering that the mean free path λ is inversely proportional to the density of the flow, then it seen from Equation 1.1 that it is not the density alone that determines the degree of rarefaction of a flow, but the ratio of this property to the characteristic dimension of the problem. When the Knudsen number tends to zero, $Kn < 0.001$, the flow is considered as continuum and the continuum hypothesis is valid. In this flow regime, the microscopic structure can be disregard, and the macroscopic properties such as density, velocity, pressure or temperature are considered. Conversely, when the Knudsen number tends to infinity, $Kn > 10$, the flow is defined as free molecular. In this flow regime, intermolecular collisions can not be ignored and the collisions of the particles with the body surface become important. The region between the

two extremes, i.e., $0.1 < Kn < 10$, corresponds to the transition flow regime. In this regime, not only the intermolecular collisions but also the gas-surface collisions are important. Also, viscosity, heat conduction, chemical relaxation and diffusion processes are important in this flow regime. In this way, the velocity distribution function may deviate from the Maxwell distribution function, which results in a thermodynamic non-equilibrium gas flow.

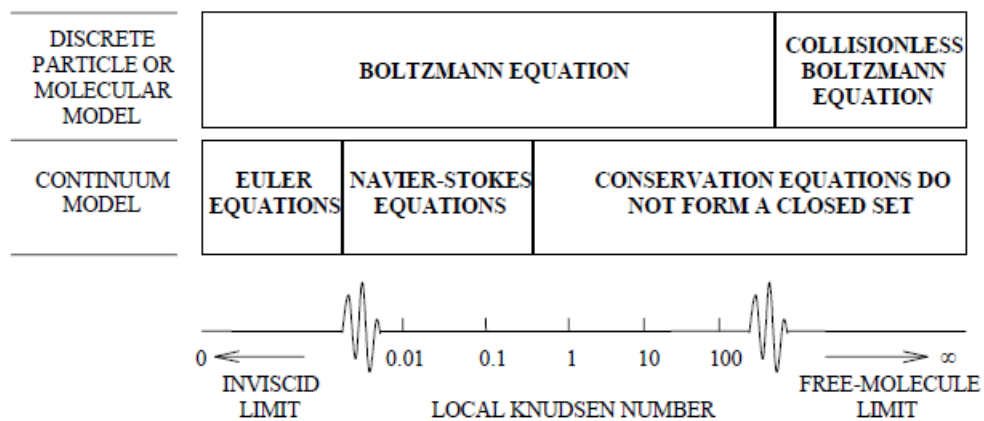
Sometimes, the characteristic length l is not easily recognizable, whereby, the local Knudsen number is used instead of the overall Knudsen number. The local Knudsen number is the ratio of the local mean free path λ , to the characteristic length l defined by any macroscopic gradient, given by the following expression:

$$l = \frac{\varphi}{\left| \frac{\partial \varphi}{\partial x} \right|} \quad (2.1)$$

where φ may be the density, velocity, pressure or temperature.

Ranges of validity of the conventional mathematical formulations as a function of the local Knudsen number are illustrated in Figure 2.1.

Figure 2.1 - Validity of the conventional mathematical models as function of local Knudsen number.



SOURCE: BIRD (1986)

In the macroscopic model or continuum flow model, the general expressions of the fundamental conservation principles that govern the motion of gases are valid for all flow regimes. For the applications of conservation equations, it becomes imperative to have a detailed information about the heat flux vector and the shear stress tensor. When these two constitutive relationships are equal to zero, the conservation equations are called as Euler equations. The Euler equations are used for inviscid and isentropic flow. It means that the velocity distribution function at any point is equal to the Maxwellian distribution function and the flow is in local thermodynamic equilibrium.

In the following, Navier-Stokes equations are assumed to be valid when the Knudsen number is very small in comparison with unity. In this case, the velocity distribution function departs from the Maxwellian distribution. However, the transport coefficients, obtained from the Chapman-Enskog theory (CHAPMAN; COWLING, 1970), are still valid, since the departure is still sufficiently small. When the transition regime is introduced from the continuum flow regime, the first failure of the continuum theory occurs at the fluid-surface interface. The boundary condition of the continuity of the tangential velocity and temperature at the surface break down, leading to slip and temperature jump boundary conditions. This region is called the slip flow region given when $0.001 < Kn < 0.1$.

Boyd et al. (BOYD et al., 1995) have shown that for the local Knudsen number $Kn > 0.05$, the departure from the Maxwellian distribution becomes important, indicating that both the Chapman-Enskog theory and the Navier-Stokes equations are no longer valid. The Chapman-Enskog expansion to higher order may be one alternative approach to the problem of the failure of the Navier-Stokes equations, obtaining the Burnett equations (BURNETT, 1936). Each level of approximation implies a different distribution function that deviates from the Maxwellian distribution. In the last decades the interest in the use of Burnett equations, based on the second order of the Chapman-Enskog expansion for calculating rarefied hypersonic flows, have increased (TANNEHILL; EISLER, 1976; FISCKO; CHAPMAN, 1988; FISCKO; CHAPMAN, 1989; LUMPKIN III; CHAPMAN, 1992; ZHONG et al., 1993; LEE, 1994; COMEAUX et al., 1995; KEON-YOUNG et al., 2001; ZHAO et al., 2014). However, for flows with small disturbances, the application of Burnett equations present additional difficulties related to the instability and the correct formulation of the boundary conditions. Furthermore, the differential equations that govern momentum and heat transport in the gas increases their order when the Burnett equations are used. These equations are more difficult to solve numerically, and fail when the degree of rarefaction

is sufficiently high. Finally, the Burnett equations can also lead to second-law impossibilities in certain situations, such as a negative dissipation function or a heat flux in an isothermal gas (COMEAUX et al., 1995). Cheng and Emanuel (CHENG; EMANUEL, 1995) present a more detailed description of the use of Burnett equations for rarefied hypersonic flows.

In the microscopic model or molecular flow model, the gas is treated as a collection of molecules whose positions and velocities are individually tracked. Such system requires the solution of the Boltzmann equation (CERCIGNANI, 1988). Nevertheless, only when the Knudsen number tends to infinity, analytical solutions of the Boltzmann equations are possible to be obtained. However, when the Knudsen number tends to finite values, analytical solutions are more difficult to be obtained. The Boltzmann equation is an integro-differential equation with the velocity distribution function as the only dependent variable. In contrast, the flow velocity and macroscopic thermodynamic properties are dependent variables in the Navier-Stokes equations. The reduction in the number of dependent variables is made at the expense of increasing the number of independent variables from those of physical space to those of phase space. Thereby, an one-dimensional steady flow of a monatomic gas has an axially symmetric velocity distribution function so that the problem is three-dimensional in phase space.

Analytical solutions are generally limited to flows involving a simple molecular model, one independent macroscopic variable and small disturbances. In addition, rarefied hypersonic flow problems often involve physical effects that have not yet been incorporated into the Boltzmann formulation, such as chemical reactions and thermal radiation. Consequently, physically-based numerical methods have been developed to solve mathematical difficulties associated with the direct solution of the Boltzmann equation. The Boltzmann equation may be solved numerically by the following approaches: molecular dynamics method (ALDER; WAINWRIGHT, 1957; ALDER; WAINWRIGHT, 1958; DOMINIK; JÜRG, 2009; AKIRA, 2011), test-particle method (HAVILAND; LAVIN, 1962; HAVILAND, 1965; FRENKEL; SMIT, 2009), direct numerical integration method (YEN, 1971; YEN, 1984) and the Direct Simulation Monte Carlo method (BIRD, 1976; BIRD, 1994; BIRD, 2013). For the purpose of this dissertation only the Direct Simulation Monte Carlo method will be discussed, since it has become a powerful tool for practical calculations.

2.2 Direct Simulation Monte Carlo (DSMC) Method

The Direct Simulation Monte Carlo method, introduced by Bird in 1963 (BIRD, 1976; BIRD, 1994; BIRD, 2013), is a numerical method that provides a probabilistic physical simulation of a gas flow by simultaneously following the motion of simulated molecules in physical space. It is based on the physical concepts of rarefied gases and on physical assumptions that form the basis for the phenomenological derivation of the Boltzmann equation. However, it is not derived from the Boltzmann equation itself. Similar to the Boltzmann equation, the DSMC method is derived from the classical kinetic theory, and for this reason, both are subjected to the same restrictions. The restriction of dilute gas is one of the assumptions of the DSMC method. It means that average molecular diameter is much smaller than the average spacing between molecules in the gas. Nevertheless, Alexander et al. (ALEXANDER et al., 1995) demonstrated that the DSMC is also a potential method for investigating dense gases. Another assumption is the molecular chaos, in which the velocities of colliding particles are uncorrelated, and independent of position.

The method has been tested in the transition flow regime in the last 50 years, and has shown excellent results when compared with experimental data (HARVEY, 1986; MOSS et al., 1995; HARVEY; GALLIS, 2000; HARVEY, 2003; HOLDEN; WADHAMS, 2003). Comparisons with experimental data have given credibility to the method, which has been vital in the receptivity of it. Some advantages of the method that make it useful in the engineering applications are: (1) the comparative simplicity of work with 1-D, 2-D or 3-D problems; (2) complex models of gas-surface interaction, including the models of internal degrees of freedom and chemical reactions, which can be included without substantial complications in the computational algorithm, and (3) the parallelization of the code that may result in significant reduction in the computational time.

The DSMC method models the flow as a collection of particles or molecules, each one has a position, velocity and internal energy. The state of the simulated molecules is stored and modified with the time as the molecules move, collide and interact with the surface in the simulated physical domain. One approximation of the DSMC is to uncouple the molecular motion from molecular collision process over very small time steps. The molecular motion is modeled deterministically, while collisions are treated statistically. A small number of simulated molecules is used in order to represent a larger number of real molecules due to the difficulty of simulating the real number of molecules in the computational domain. Simulations can vary from thousands for

millions of molecules in rarefied-flow problems.

A computational cell network, representing the physical space to be investigated, is required for the method execution. The cells provide a convenient reference for the sampling of the macroscopic gas properties and for the choice of potential collision pairs (XUE et al., 2000). The simulated molecules in the cell are considered as representative of the real molecules at the position of the cell, and the relative position of the molecules within the cell is ignored in the collision process of molecules. The dimension of the cells must be such that changes in flow properties across each cell be small. The linear dimensions of the cells should be small in comparison with the mean free path λ in the direction of primary gradients (BIRD, 1994). Meiburg (MEIBURG, 1986) and Bird (BIRD, 1987) showed that the violation of cell dimension restriction leads to erroneous results. According to Alexander et al. (ALEXANDER et al., 1998; ALEXANDER et al., 2000) significant errors occur when the cell dimensions are larger than the mean free path λ . Since local mean free path λ is inversely proportional to flow density, high density flows demand more computational cells. This means that more molecules are simulated and more collisions are computed.

An additional requirement of the DSMC method is related to the number of simulated molecules per cell. As mentioned earlier, the DSMC method uses the cell system for the sampling of the macroscopic properties and for the selection of collision partners. Both the collision rate and the number of collision partners are a function of the number of molecules in the cells. For the collision rate is desirable that each cell has the largest possible number of molecules. However, for the number of collision partner, it is desirable to have the number of molecules per cell as small as possible. Bird (BIRD, 1987) solved this conflict by introducing the option of subdividing the cells into an arbitrary number of sub-cells for the selection of collision pairs. This procedure improves the accuracy of the method by ensuring that collisions occur only between near neighbor molecules. In addition, it is desirable that the number of simulated molecules per cell is around 20 to 30 molecules (BIRD, 1994).

Another requirement in the DSMC method is a proper time step Δt . The paths of the simulated molecules are traced out in physical space by decoupling intermolecular collisions from molecular motion. The size of the time step may represent two problems for the molecular motion and the intermolecular collisions. The size of the time step should be chosen to be significantly smaller than the mean time between collisions (XUE et al., 2000). A very small time step results in that the molecules

will need many time steps to cross a given cell. This represents that the same group of molecules will be involved in several time steps due to that almost no molecules leaving or entering the cell. Also, a large time step allows the molecules to move too far without the opportunity to participate in a collision, resulting in inaccurate or non-physical results. In this way, the time step should be chosen such that a typical molecule moves about one fourth the cell dimension at each time step (LIU; YIN-KWEENG, 2002). It should be remarked in this context that stability problems are completely absent in the DSMC method.

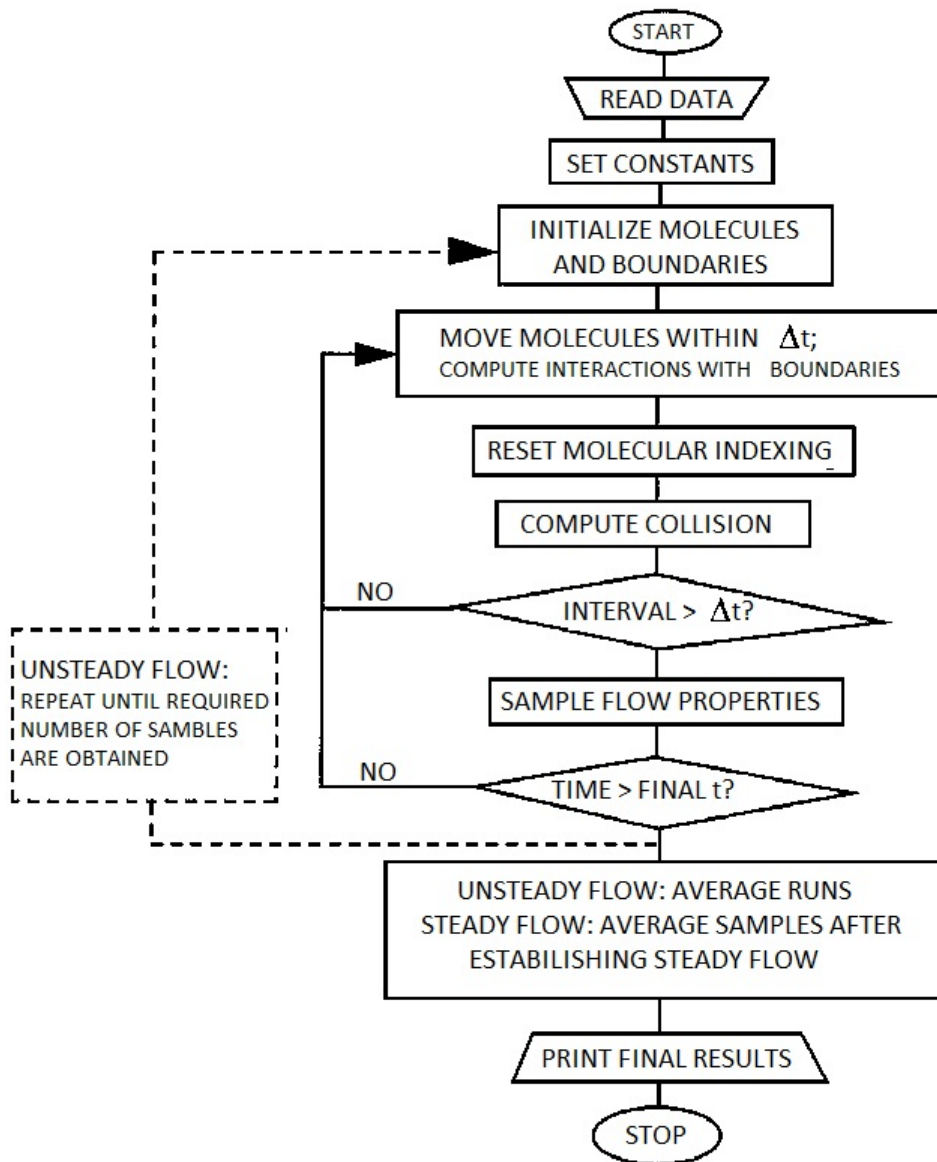
2.2.1 DSMC Methodology

The main steps related to the application of the DSMC method are illustrated in Figure 2.2. The DSMC algorithm may be divided into four individual steps: (1) movement of molecules, (2) indexing of molecules, (3) calculation of the molecular collisions and (4) sampling of molecules properties.

The freestream conditions in the physical space are represented in the computational domain by a uniform equilibrium gas condition. Known boundary conditions are specified by the velocity, temperature, density and internal energy of the molecules entering to the computational domain during each time step. The linear combination of the freestream velocity and the thermal velocity can represent the velocity of a simulated molecule. Boundary conditions corresponding to the desired flow are imposed at time zero. Boundary conditions should be such that a steady flow is established at a sufficient large time, and the desired steady result is a time average of all values calculated after reaching the steady state

Once the velocity and position of each simulated molecule are defined, all molecules are moved through distances appropriate to the size of the time step and their velocity components. After the particle has been moved, the new location in the computational domain is determined. This can be obtained in different ways. For cartesian grids, Bird (BIRD, 1994) defined the indexing scheme, it is used for determining the new particle position and the destination cell. Dietrich (DIETRICH, 1990), Laux (LAUX, 1997), and Usami and Nakayama (USAMI; NAKAYAMA, 2003) outlined particle location schemes for structured and unstructured grids. For more complex computational grids, such as hexahedral or tetrahedral, ray-trading techniques can be used to determine the particle position (NANCE et al., 1997; WILMOTH et al., 1996). After defining the location of simulated molecules, it is important to define the appropriate actions for molecules crossing boundaries representing solid surfaces, lines or surfaces of symmetry or the outer boundary of flow. New simulated

Figure 2.2 - Flowchart of the DSMC method.



SOURCE: ORAN et al. (1998).

molecules are introduced to the computational domain from the outer boundaries for freestream boundary conditions or from within the domain from sources. Molecule-surface interactions can be treated as being either fully diffuse, fully specular or a combination of the two. The conservation laws are applied to individual simulated molecules for modeling molecule-surface interactions instead of using the velocity distribution function. Such application allows the DSMC method to be extended to

include physical effects such as radiation effects, chemical reactions, ionized flows, catalytic walls and three-body collisions without major modifications in the basic algorithm.

After determining the location of the simulated molecules, they should be indexed by cell location for the two subsequent steps: calculation of collisions and sampling the flowfield. For the selection and calculation of intermolecular collisions, each cell must be given a base index from which all other simulated molecules in the cell can be reached through a cross-reference list. Bird (BIRD, 1976) proposed a fast indexing scheme in the original version of the DSMC algorithm. For the calculation of intermolecular collisions, molecular interactions are treated probabilistically rather than deterministically. Several different collision modeling schemes have been formulated and applied in the DSMC method. Among them, one has the time-counter (TC) technique (BIRD, 1976), Nanbu scheme (NANBU, 1986), null-collision (NC) technique (KOURA; MATSUMOTO, 1991), no-time-counter (NTC) technique (BIRD, 1989) and the generalized scheme (ABE, 1993) of the no-time-counter technique. The NTC scheme and the sub-cell approach proposed by Bird (BIRD, 1989; BIRD, 1987) are the preferred models currently used.

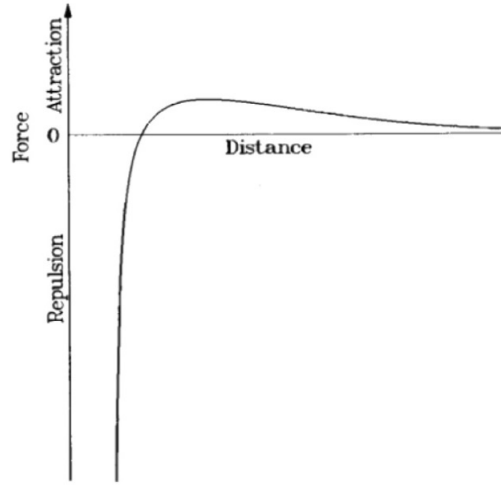
The collision procedure takes place on a cell-by-cell basis. Therefore, the candidates of collision pairs that will be evaluated in the collision process are determinate by the time step, the cell volume and the number of simulated molecules resident in the cell. The collision partners are randomly selected with the restriction that the molecular mean separation be a fraction of the molecular mean free path. This restriction is enforced by selecting collision pairs from the list of simulated molecules in the same subcell. The DSMC method evaluates individual collision in a probabilistic basis, conserving momentum and energy.

Finally, the sampling process of the macroscopic flow properties density, velocity, temperature and pressure is made. These properties are computed by average of the microscopic state of particles in each cell.

2.2.2 Molecular Model

The behavior of molecules during a simulated collision process depends on the choice of the intermolecular force field. This force field is assumed to be spherically symmetric and the general form of the force between two molecules is a function of the distance between their nuclei, as shown in Figure 2.3.

Figure 2.3 - Typical intermolecular force field.



SOURCE: BIRD (1994).

According to this figure, the force is zero when the distance between the molecular nuclei is very large. Slightly attractive when the molecules are closed enough to the point of initiating the interaction. Finally, this attractive force decays and becomes strongly repulsive as the molecules are very close one to each other (BIRD, 1994).

A simple molecular model that is accurate enough for the majority of hypersonic calculations is the inverse power potential. The intermolecular force potential is modeled as the inverse of the repulsive power force by,

$$F_n = \frac{k}{r^\eta} \quad (2.2)$$

where r is the distance between the nuclei of the colliding molecules, and k and η are constants characterizing the molecule. The molecular force model of Equation 2.2 corresponds to a Maxwellian gas for $\eta = 5$. The hard sphere (HS) model is obtained by setting $\eta \rightarrow \infty$.

In general, in engineering simulations, millions or billions of collisions are considered. Therefore, a simple interaction model should be employed. In this case, the simplest model is that corresponding to a hard sphere. In the HS model, the collision cross section is invariant for a single gas species. The scattering angle is isotropic, and the

post-collision relative velocity is sampled from a uniform solid angle distribution. However, such a model is not realistic, because its total collision cross-section σ_T does not depend on the relative velocity of the colliding molecules. When the intermolecular force law is given by Equation 2.2, the Chapman-Enskog theory yields a direct relationship between the coefficient of viscosity and the gas temperature given by,

$$\mu \propto T \left(\frac{1}{2} + \frac{2}{\eta - 1} \right) \propto T^s \quad (2.3)$$

According to the Equation 2.3, the coefficient of viscosity has a fixed temperature exponent of 1 for Maxwellian model and 0.5 for hard sphere models. The Maxwellian and hard sphere models are theoretical gases that can be viewed as the limiting cases for the behavior of a real gas, since for almost real gases the exponent s is generally in the range 0.6 to 0.9.

Alternative versions based on the hard sphere model have been proposed. These alternative versions have proved to be very successful at reproducing the macroscopic behavior of a gas yet remain computationally efficient. The first alternative model was defined as the variable hard sphere (VHS) model introduced by Bird (BIRD, 1981). The VHS molecular model treats the molecules as “hard spheres” as far as the scattering angle distribution is concerned, i.e., all directions are equally possible for the post-collision velocity in the center-of-mass frame of reference. Moreover, the total collision cross section σ_T is allowed to vary with the relative speed of colliding molecules.

The VHS model has a molecular diameter d well defined and follows the classical scattering law used in the HS model. This diameter is the inverse power law function of the relative translational energy in the molecular collision, so,

$$\sigma \equiv \pi d^2 \propto \left(\frac{1}{2} m_r c_r^2 \right)^{-\omega} \quad (2.4)$$

where m_r is the reduced mass, c_r is the relative speed of the colliding molecules.

The collision cross section σ varies with the collision relative speed and the temperature as follows,

$$\sigma \propto c_r^{-4(\eta-1)} \propto T^{\frac{-2}{\eta-1}} \quad (2.5)$$

A comparison of Equations 2.4 and 2.5 shows that ω is related to the exponent of the inverse power law force by

$$\omega = \frac{2}{\eta-1} \quad (2.6)$$

Therefore ω is equal to 0, 1/4, or 1/2 for the HS model, the inverse power law model and the Maxwell model, respectively. The mean collision energy in an equilibrium gas at temperature T is,

$$\frac{1}{2}m_r c_r^2 = 2 \left(\frac{\eta-2}{\eta-1} \right) kT = (2-\omega)kT \quad (2.7)$$

where k is the Boltzmann constant.

For an equilibrium gas, the collision cross section σ is inversely proportional to the temperature to the power $-\omega$, defined by,

$$\sigma = \sigma_{ref} \left(\frac{T}{T_{ref}} \right)^{-\omega} \quad (2.8)$$

The reference value of the cross section σ_{ref} is based on a reference temperature T_{ref} . For a non-equilibrium gas, the collision energy should be employed, and Equation 2.4 may be written as:

$$\sigma = \sigma_{ref} \left(\frac{c_r^2}{c_{rref}^2} \right)^{-\omega} \quad (2.9)$$

The reference value for the square of relative collision speed can be chosen as the mean value of c_r^2 in an equilibrium gas at the reference temperature T_{ref} . Therefore Equations 2.7 and 2.9 can be combined as follows:

$$\sigma = \sigma_{ref} \left(\frac{m_r c_r^2}{2(2-\omega)kT_{ref}} \right)^{-\omega} \quad (2.10)$$

The DSMC code sets d_{ref} , T_{ref} and ω as constant, and Equation 2.10 is used to obtaining σ as a function of c_r .

In the variable hard sphere (VHS) model, the mean free path λ may be written as:

$$\lambda = \frac{(T/T_{ref})}{(2 - \omega)^\omega \Gamma(2 - \omega) 2^{(1/2)} n \sigma_{ref}} \quad (2.11)$$

At this way, the mean free path decreases with cross section and increases with temperature according to the same power law.

The viscosity coefficient μ in a real gas is given in terms of temperature by:

$$\mu \propto T^\zeta \quad (2.12)$$

where ζ usually varies from 0.6 to 0.9. The mean cross section for a gas in thermodynamic equilibrium is given by :

$$\bar{\sigma} \propto T^{-\omega} \quad (2.13)$$

According the Chapman-Enskog theory, the viscosity coefficient is given by:

$$\mu = \frac{(15m/8)(\pi kT)^{1/2}}{(2 - \omega)^\omega \Gamma(4 - \omega) \bar{\sigma}} \quad (2.14)$$

where k is the Boltzmann constant and m the molecular mass. Comparing Equations 2.12, 2.13 and 2.14, one has

$$\zeta = \frac{1}{2} + \omega \quad (2.15)$$

At this way, by combining Equations 2.11 and 2.15 is obtained the mean free path as a function of the variable ζ

$$\lambda = \frac{(2\mu/15)(7 - 2\zeta)(2 - 2\zeta)(2\pi kT)^{(1 - 1/2)}}{\rho} \quad (2.16)$$

Koura and Matsumoto (KOURA; MATSUMOTO, 1991; KOURA; MATSUMOTO, 1992) further improved the VHS model and introduced the Variable Soft Sphere (VSS) molecular model. The VSS model considers the post-collision scattering as anisotropic. The second free parameter introduced by the post-collision scattering dynamics in the VSS model is chosen in order to reproduce correctly the real viscosity and diffusion coefficients of the gases. Hassan and Hash (HASSAN; HASH, 1993) introduced the generalized hard sphere (GHS) molecular model. The GHS model accounts for both repulsive and attractive parts of the interaction between particles. In this model, molecules scatter like hard sphere, as was considered in the VHS model. Since the GHS model can reproduce the effects of attractive portion of an interaction potential, then the molecular model is appropriate to simulate low temperature flows that are dominated by the attractive collisions (HASH et al., 1993; KUNC et al., 1995)

2.2.3 Collision Model

A few different collision-modeling schemes appropriated for DSMC method were presented in the subsection 2.2.1. For instance, the time-counter (TC) technique (BIRD, 1976), the Nanbu scheme (NANBU, 1986), null-collision (NC) technique (KOURA; MATSUMOTO, 1991), no-time-counter (NTC) (BIRD, 1989) and the generalized scheme (ABE, 1993) of the NTC technique. For the purpose of this work, only the Time-counter TC and the no-time-counter NTC will be described.

The procedures for the establishment of the correct collision rate are based on the cells, while individual collision pairs are selected from the subcells. The time step Δt , the number of molecules N resident in the each cell and the cell volume V_c will determine the number of candidate collision pairs that will be evaluated. From kinetic theory, it may be shown that the number of collisions that must be simulated over a time step Δt is given by,

$$N_{coll} = \frac{1}{2} N \Delta t n \overline{\sigma_T c_r} \quad (2.17)$$

where n is the number density (BIRD, 1994).

In order to determine the correct total number of collisions during the time step Δt , it would be necessary to compute the average product of the relative speed c_r and the collision cross section σ_r for all possible pairs of molecules. An algorithm that uses this procedure would have a computational time proportional to N^2 , where

N is the total number of simulated molecules. In order to overcome this difficulty, Bird (BIRD, 1976) introduced the parameter $(\sigma_{Tc_r})_{max}$, where the subscript *max* denotes the largest value for the cell, and it should be updated during a binary collision if the real product σ_{Tc_r} were greater than $(\sigma_{Tc_r})_{max}$. Furthermore, the parameter $(\sigma_{Tc_r})_{max}$ is used to determine a real collision according to the following three operations:

- (1) Two molecules are randomly selected in the cell. The probability that these molecules collide is then given by

$$P = \frac{\sigma_r c_r}{(\sigma_r c_r)_{max}} \quad (2.18)$$

if this probability P is larger than R_f , where R_f is a uniform random number in the range 0 to 1, then the pair of molecules is accepted for collision. Otherwise, a new pair is randomly selected and the procedure is repeated. This is the acceptance-rejection method described by Bird (BIRD, 1994) to select collision pair of molecules.

- (2) If the pair of molecules is accepted for collision, then a time counter for the current cell is advanced by the amount,

$$\delta t = \frac{2}{N n \sigma_{Tc_r}} \quad (2.19)$$

- (3) A number of collisions is calculated in the cell until the sum of a number of Δt 's is just greater than the time step σ_t . This is the time-counter (TC) scheme proposed by Bird (BIRD, 1976).

In the time-counter scheme, the total number of collision within the given time step Δt depends on the product σ_{Tc_r} related to the collision pairs, which are randomly select. In addition to that, it is not possible to calculate the total number of collisions at the beginning of the iteration time step. Consequently, a complete vectorization of the collision process is not possible. The difficulty in treating the TC scheme is due to the vector dependency associated with the implementation of summing several values of δt given by Equation 2.19 (BAGANOFF; MCDONALD, 1990)

In the no time counter scheme, the time increment related to a randomly chosen pair of molecules is independent of the real product σ_{Tc_r} . The parameter $(\sigma_{Tc_r})_{max}$ is fixed during a time interval Δt and modified after performing all collisions. The idea

of a time counter is replaced with the expression for the total number of collisions N_{coll} to be sampled in each cell by,

$$N_{coll} = \frac{1}{2} \frac{N \bar{N} F_N (\sigma_T c_r)_{max}}{V_c} \quad (2.20)$$

where F_N is the number of real molecules represented by a single simulated molecule, N is a fluctuating quantity and \bar{N} is an average value. The probability of collision for each pair sampled is again given by Equation 2.18.

The no time counter scheme was introduced to alleviate difficulties found with the time counter scheme in regions where the flows is not in equilibrium such as strong shock waves. The problem is related to the acceptance of an unlikely collision pair with a relatively small collision probability (one with a very small value for $\sigma_T c_r$). Under such conditions, the time increment determined by Equation 2.19 may substantially exceed the decoupled time step Δt .

2.2.4 Binary Elastic Collision

It was mentioned in the previous subsections that DSMC method is subjected to the assumption of dilute gases. For dilute gases, the intermolecular collision are considered as being binary collisions. Also, an elastic collision is defined as one in which there is no interchange of translational and internal energy.

The pre-collision velocities for two molecules may be denoted by \mathbf{c}_1 and \mathbf{c}_2 . By knowing the orientation of trajectories of the molecules and their physical properties, the post-collision velocities \mathbf{c}_1^* and \mathbf{c}_2^* may be determined. At the same time the energy and the momentum must be conserved in the collision process. In this manner, one has,

$$m_1 \mathbf{c}_1 + m_2 \mathbf{c}_2 = m_1 \mathbf{c}_1^* + m_2 \mathbf{c}_2^* = (m_1 + m_2) \mathbf{c}_m \quad (2.21)$$

$$m_1 \mathbf{c}_1^2 + m_2 \mathbf{c}_2^2 = m_1 \mathbf{c}_1^{*2} + m_2 \mathbf{c}_2^{*2} \quad (2.22)$$

Where m_1 and m_2 are the molecular masses of the molecules 1 and 2, and the \mathbf{c}_m is the velocity of the center of mass of the pair of molecules. The Equation 2.21 shows that the velocity of the centre of mass is not affected by the collision process. The values of pre- and post-collision of relative velocity between the two molecules can

be defined by:

$$\mathbf{c}_r = \mathbf{c}_1 - \mathbf{c}_2 \quad (2.23)$$

$$\mathbf{c}_r^* = \mathbf{c}_1^* - \mathbf{c}_2^* \quad (2.24)$$

Combined the Equations 2.23 and 2.24 with the Equation 2.21, one obtains the following expressions:

$$\mathbf{c}_1 = \mathbf{c}_m + \frac{m_2}{m_1 + m_2} \mathbf{c}_r \quad (2.25)$$

$$\mathbf{c}_2 = \mathbf{c}_m - \frac{m_1}{m_1 + m_2} \mathbf{c}_r \quad (2.26)$$

similarly, the post-collision velocities are defined by:

$$\mathbf{c}_1^* = \mathbf{c}_m + \frac{m_2}{m_1 + m_2} \mathbf{c}_r^* \quad (2.27)$$

$$\mathbf{c}_2^* = \mathbf{c}_m - \frac{m_1}{m_1 + m_2} \mathbf{c}_r^* \quad (2.28)$$

The conservation of angular momentum requires that the projected distance between the post-collision velocities be equal to the projected distance between the pre-collision velocities. Equations 2.25, 2.26, 2.27 and 2.28 show that:

$$m_1 \mathbf{c}_1^2 + m_2 \mathbf{c}_2^2 = (m_1 + m_2) \mathbf{c}_m^2 + m_r \mathbf{c}_r^2 \quad (2.29)$$

$$m_1 \mathbf{c}_1^{*2} + m_2 \mathbf{c}_2^{*2} = (m_1 + m_2) \mathbf{c}_m^2 + m_r \mathbf{c}_r^{*2} \quad (2.30)$$

where m_r is the reduced mass and is given by:

$$m_r = \frac{m_1 m_2}{m_1 + m_2} \quad (2.31)$$

Comparing Equations 2.29 and 2.30 with the Equation 2.22, it is seen that the magnitude of relative velocity does not change in the collision, i.e.,

$$\mathbf{c}_r^* = \mathbf{c}_r \quad (2.32)$$

Since \mathbf{c}_m and \mathbf{c}_r can be calculated from the pre-collision velocities, then the determination of post-collision velocity is reduced to calculating the change in direction of the relative velocity vector. If \mathbf{F} is the force between two spherically symmetric points, and \mathbf{r}_1 and \mathbf{r}_2 their position vectors, then the equations of motion of the molecules are defined by:

$$m_1 \ddot{\mathbf{r}}_1 = \mathbf{F} \quad (2.33)$$

$$m_2 \ddot{\mathbf{r}}_2 = -\mathbf{F} \quad (2.34)$$

By combining the last two equations, one has,

$$m_1 m_2 (\ddot{\mathbf{r}}_1 - \ddot{\mathbf{r}}_2) = (m_1 + m_2) \mathbf{F} \quad (2.35)$$

If $\dot{\mathbf{r}}$ denoted the relative velocity vector, then one obtains,

$$m_r \ddot{\mathbf{r}} = \mathbf{F} \quad (2.36)$$

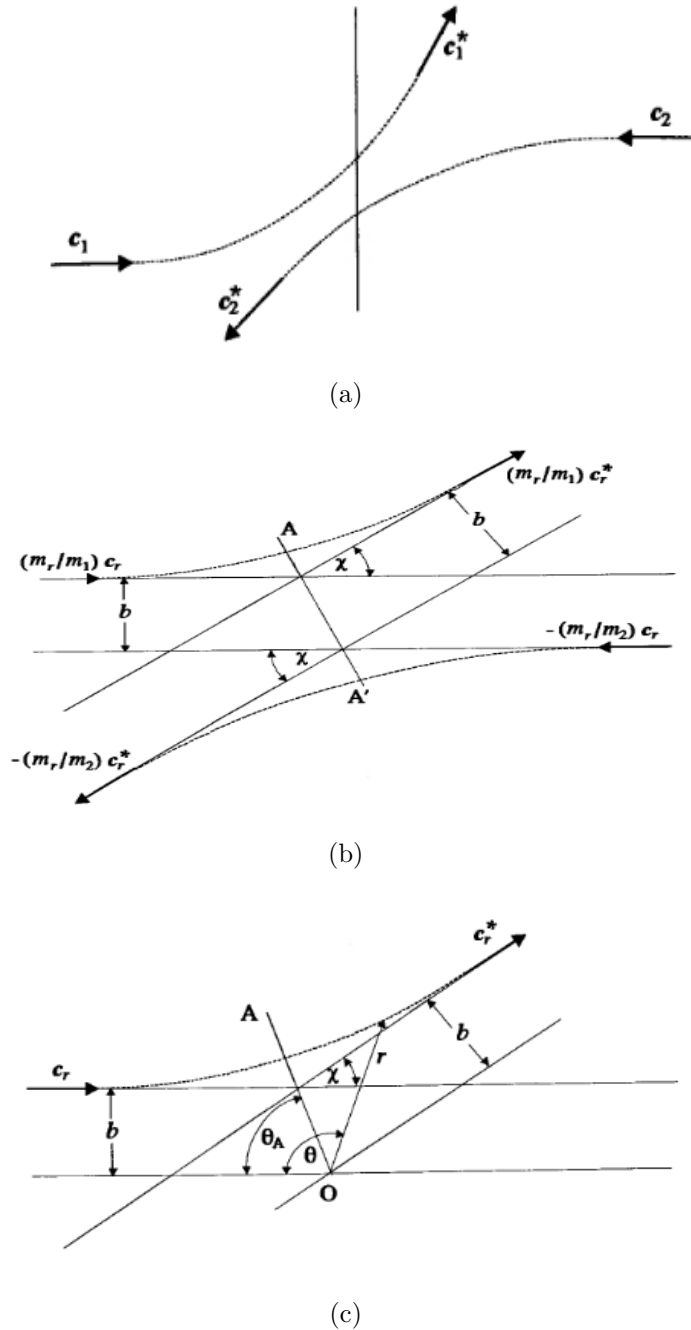
Therefore, the motion of the molecule of mass m_1 relative to the molecule of mass m_2 is equivalent to the movement of the molecule of mass m_r relative to a fixed center of force.

For completeness, the results mentioned above are illustrated in Figure 2.4. According to these plots, the transformation from the centre of mass coordinate system changes to two-dimensional trajectory from a three-dimensional trajectory, which is symmetric about the apse line AA'. The two trajectories are reduced to one in the further transformation to the reduced mass frame of reference, and this trajectory remains symmetrical about the transformed apse line, which passes through the scattering centre O.

This symmetry reflects the symmetry of the equation with respect to pre- and post-collision velocities. Another consequence of this symmetry is that the distance b between the trajectories of two molecules with velocities \mathbf{c}_1 and \mathbf{c}_2 is conserved in

the collision process.

Figure 2.4 - Frames of references for the analysis of binary collisions.



a) Planar representation of a collision in the laboratory frame of reference. (b) binary collision in the center of mass frame of reference. (c) Interaction of the reduced mass particle with a fixed scattering center.

SOURCE: BIRD (1994)

2.2.5 Internal Degrees of Freedom

The presence of a large degree of non-equilibrium between the various internal energy modes of the gas is one of the most significant effects observed in rarefied flows. For polyatomic gases, the transfer of energy to and from the internal modes has to be considered. However, energy transfer between translational, rotational and vibrational degrees of freedom can not be accurately predicted using simple collision models.

Borgnakke and Larsen (BORGNAKKE; LARSEN, 1975) introduced the phenomenological model, which is usually implemented into the DSMC model, in order to transfer internal energy between the various modes. The main feature of this model is that a fraction ϕ of translational collisions are assumed to be inelastic, and the remaining $(1 - \phi)$ collisions are considered as elastic. The fraction ϕ can be interpreted as the average probability of vibrational or rotational energy exchange for translational collisions. This average probability can be determined from measured relaxation times. The relaxation time is a function of the local flow properties and can be related to a relaxation number (or collision number) Z . The relaxation or collision number Z is usually defined by,

$$Z = \frac{\tau}{\tau_c} \quad (2.37)$$

where τ is the relaxation time and τ_c is the mean collision time.

The relaxation or collision number is the average number of molecular collisions that are required for a particular mode to attain equilibrium energy. Therefore, once this number is determined, the average probability ϕ for each mode in a given collision is conveniently defined as,

$$\phi = \frac{1}{Z} \quad (2.38)$$

Usually, DSMC calculations use the rotational collision number Z_R^{DSMC} on the order of 5. This means that, on average, a molecule rotationally relaxes once every five collisions. This is generally a good approximation in engineering problems. However, Boyd (BOYD, 1990a; BOYD, 1990c; BOYD, 1990d) has proposed more realistic models for rotational collision number as a function of the translational temperature or translational energy.

The mechanisms of energy transfer employed in the DSMC calculation affect the rate of energy transfer. According to Lumpkin et al. (LUMPKIN et al., 1991), the value of the collision number used in DSMC will be approximately half of that determined experimentally and employed in a continuum computation. As a result, the following equation should be applied:

$$Z_R^{DSMC} = \frac{Z_R^{cont}}{\left(1 + \frac{\zeta_R}{\zeta_T}\right)} \quad (2.39)$$

where ζ_R and ζ_T are the rotational and translational degrees of freedom, respectively.

The Borgnakke-Larsen method can be applied to the vibrational modes through either a classical or quantum procedure. In the classical procedure, the number of vibrational degrees of freedom ζ_V described the vibrational energy is treated as a continuous distribution, this number of degrees is fixed. In the quantum procedure, the discrete nature of vibrational spectrum is taken into account, since the vibrational spectrum of real molecules is characterized by large gaps between the neighboring energy levels. The quantum procedure allows sampling of post-collision vibrational energy levels from the discrete form of the Simple Harmonic Oscillator (SHO). This procedure does not require the value of ζ_V to be estimated for the whole flowfield. Instead, ζ_V varies according to the local energy content of the flow. Both procedures are discussed at length by Bird (BIRD, 1994). Vibrational relaxation number as a function of the collision energy is presented by Boyd and Bergemann (BOYD, 1990b; BOYD, 1991; BERGEMANN; BOYD, 1994) and as a function of temperature by Hash and Hassan (HASH; HASSAN, 1993).

2.2.6 Boundary Conditions

There are two basic types of boundary conditions in the gas dynamic problems: those at a solid surface where molecules interact or reflect directly and those specified by quantities given in the undisturbed freestream.

The first boundary condition depends on the treatment of gas-surface interactions. The influence of the model of gas-surface interactions on the aerodynamic forces and heat transfer increases substantially as the gas rarefaction increases. The second boundary condition is easily represented as a gas in equilibrium is moving with an imposed velocity. The molecular velocity distribution can be defined as Maxwellian with an imposed velocity. This distribution holds for any ideal gas independently of

the type of forces between molecules. Therefore, the correct choice of the model for calculating hypersonic rarefied flows plays an important role.

Three models of gas-surface interactions may be employed in the DSMC method: (1) specular reflection, (2) diffuse reflection, and (3) a combination of these two methods. In a specular reflection, molecules are reflected as a perfectly elastic sphere with reversal of the normal component of velocity and no change in either the tangential components of velocity and energy. In a diffuse reflection, the molecules are reflected equally in any directions with a complete thermal accommodation. The final velocity components of the reflected molecules are independent of their incident velocity and direction. The Maxwell model combines the diffuse reflection with specular reflection and introduces a single parameter f to indicate the fraction of those molecules reflected diffusely in a completely accommodated fashion according to a Maxwellian distribution based on the wall temperature, the remaining fraction, $(1-f)$, is assumed to reflect specularly.

The Maxwell model describes the degree of accommodation of the incident normal momentum, tangential momentum and kinetic energy to the surface, by using accommodation coefficients. A variety of definitions for accommodation coefficients exist in the literature. The traditional definition is usually expressed as being,

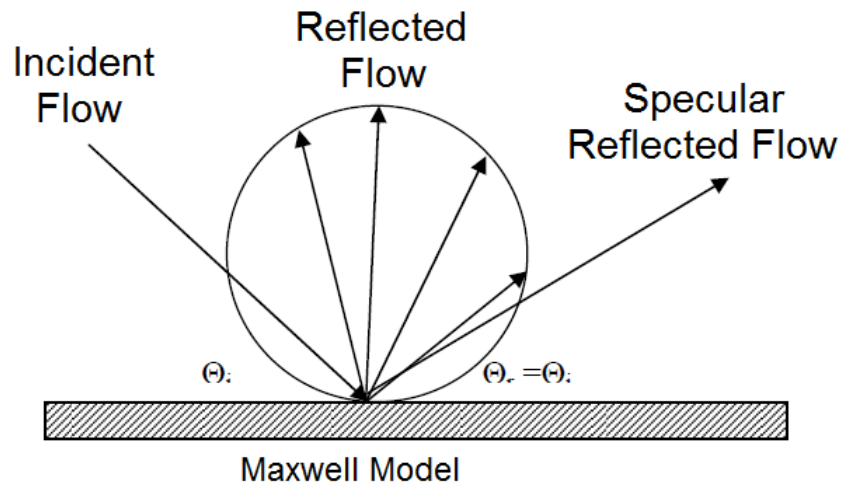
$$\alpha_n = \frac{p_i - p_r}{p_i - p_w} \quad (2.40)$$

$$\sigma_t = \frac{\tau_i - \tau_r}{\tau_i} \quad (2.41)$$

$$\alpha_r = \frac{e_i - e_r}{e_i - e_w} \quad (2.42)$$

where e_i , τ_i and p_i are flux of energy, tangential and normal momentum, respectively, incident on the surface, e_r , τ_r and p_r , are the fluxes of these quantities reflected from the surfaces, and e_w and p_w ($\tau_w = 0$), are the flux that would be reflected by a gas in a complete Maxwellian equilibrium with the surface. The model of Maxwell reflection is showed in Figure 2.5.

Figure 2.5 - Maxwell model of reflection.



SOURCE: Palharini (2010)

3 COMPUTATIONAL PROCEDURE

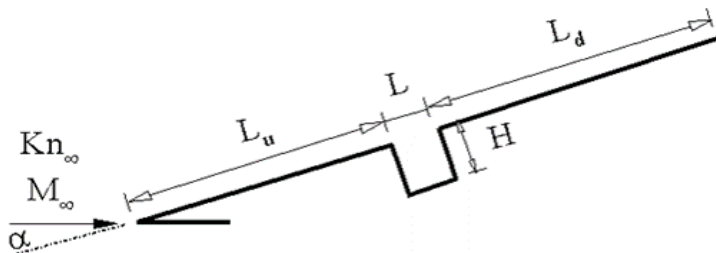
3.1 Geometry Definitions

The present work was undertaken in an attempt to investigate the angle-of-attack effects on the flowfield structure and on the aerodynamic surface properties of a hypersonic flow on a cavity, which represents a discontinuity on the surface of reentry vehicles.

By considering that the nose radius R of a reentry vehicle is orders of magnitude larger than the cavity depth H or the cavity length L , then one has that H/R or $L/R \ll 1$. In this context, a discontinuity on the vehicle surface may be modeled by a cavity with depth H and length L on a flat plate. In addition, an understanding of the angle-of-attack effect on the flowfield structure can be gained by comparing the flowfield behavior of a flat-plate with a cavity to that of a flat-plate without a cavity.

A schematic drawing of the model employed and the main parameters related to the hypersonic flow are illustrated in Figure 3.1. According to this figure, Kn_∞ stands for the Knudsen number, M_∞ represents the freestream Mach number, α the angle of attack, L_u the length of the cavity upstream surface, L the cavity length, H the cavity depth and L_d the length of the cavity downstream surface. It was considered that the flat-plate is infinitely long but only the total length $L_u + L + L_d$ is investigated. In this context, for the cases investigated in this work L_u , L , L_d and H are tabulated in Table 3.1. The length L of 3, 6, 9 and 12 mm correspond to length L of $3.23\lambda_\infty$, $6.46\lambda_\infty$, $9.69\lambda_\infty$ and $12.92\lambda_\infty$, where λ_∞ is the freestream mean free path for an altitude of 70 km, defined in the subsequent subsection.

Figure 3.1 - Drawing illustrating the cavity.



SOURCE: PALHARINI and SANTOS (2011).

Table 3.1 - Geometric characteristics for the cavities.

Cases	$L_u(mm)$	$L_d(mm)$	$L(mm)$	$H(mm)$	L/H
A	46.43 ($50\lambda_\infty$)	46.43 ($50\lambda_\infty$)	3	3	1
B	46.43 ($50\lambda_\infty$)	46.43 ($50\lambda_\infty$)	6	3	2
C	46.43 ($50\lambda_\infty$)	46.43 ($50\lambda_\infty$)	9	3	3
D	46.43 ($50\lambda_\infty$)	46.43 ($50\lambda_\infty$)	12	3	4

3.2 Computational Conditions

The DSMC method has been considered as one of the alternative approaches for solving the Boltzmann equation (CERCIGNANI, 1988) by simulating the behavior of individual simulated molecules. It has been considered as the appropriate choice for problems involving complex multidimensional flows of rarefied hypersonic aerothermodynamics.

In this study, the molecular collisions are modeled by using the variable hard sphere (VHS) model and the non-time-counter (NTC) method as a collision-sampling technique. The Borgnakke-Larsen phenomenological model (BORGNAKKE; LARSEN, 1975) is employed in order to control the energy exchange between internal and kinetic modes. The simulations are performed using a non-reactive air as working fluid with two chemical species, O_2 and N_2 . An outline of the Borgnakke-Larsen phenomenological model in a form that is compatible with a gas mixture of VHS molecules is given by Bird (BIRD, 1989).

The rate at which energy is transferred between the translational and internal modes after an inelastic collision is determinate by the probability of a collision of this type. For a given collision, the probabilities are designated by the inverse of the relaxation numbers, which correspond to the number of collisions necessary, on average, for a molecule to relax. The relaxation numbers for rotation Z_R and vibration Z_V employed in this work were assumed to have a temperature dependence. The Borgnakke-Larsen approach is use to compute the mechanics of vibrational energy exchange using the post-collision vibrational energy levels sampled from the discrete form of the simple harmonic oscillator (SHO) (BIRD, 1994).

The rotational and vibrational relaxation numbers used in this simulation were assumed to have a temperature dependence as defined by Boyd (BOYD, 1990a) for rotation and Bird (BIRD, 2008) for vibration.

Table 3.2 - Characteristics of simulated air for DSMC calculations.

properties	Values	Unity
Working fluid	$N_2 + O_2$	
Molecular weight	28.96	<i>kg/kgmole</i>
Molecular mass of N_2	4.650×10^{-26}	<i>kg</i>
Molecular mass of O_2	5.312×10^{-26}	<i>kg</i>
Molecular diameter of N_2	4.170×10^{-10}	<i>m</i>
Molecular diameter of O_2	4.070×10^{-10}	<i>m</i>
Mole fraction of N_2	0.763	
Mole fraction of O_2	0.237	
viscosity index of N_2	0.74	
viscosity index of O_2	0.77	
Degrees of freedom of N_2	5 to 7	
Degrees of freedom of O_2	5 to 7	

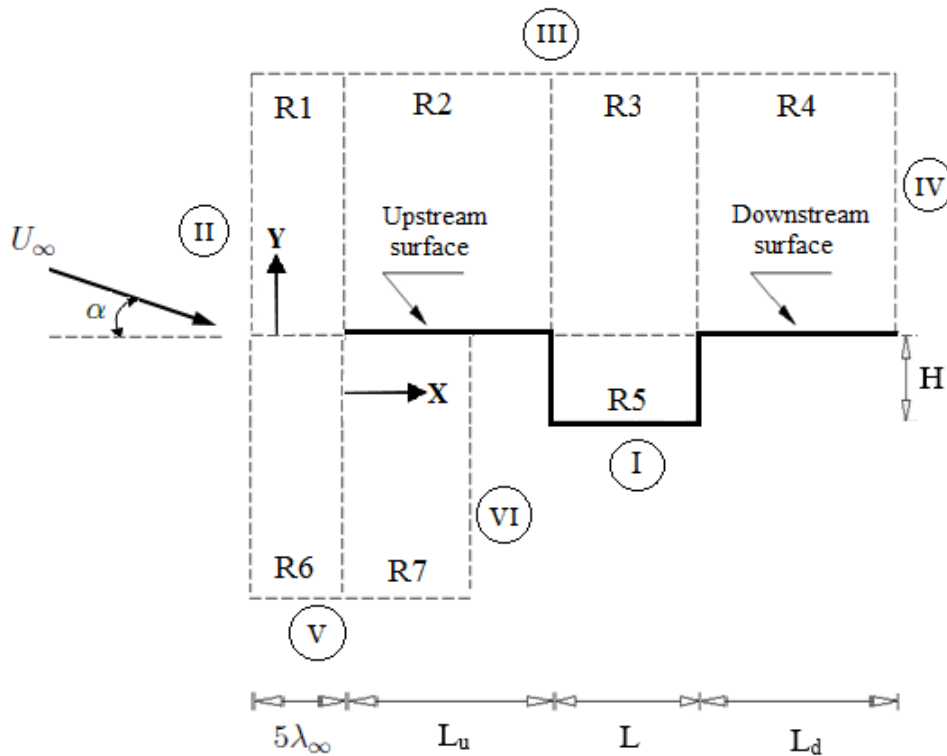
SOURCE: BIRD (1994).

The coefficient of viscosity μ_∞ and the mean free path λ_∞ of the freestream are evaluated from a consistent definition (BIRD, 1983) by using the VHS collision model with the temperature exponent s (Equation 2.3) equal to 0.74 and 0.77 for N_2 and O_2 , respectively. The Table 3.2 summarizes the air characteristics used in the DSMC calculations.

The computational domain used for the calculations is large enough so that body disturbances do not reach the upstream and side boundaries, where freestream conditions are specified. In order to implement the particle collisions, the computational domain around the cavity is divided into an arbitrary number of regions, and each one of them has a separate value of time step Δt and scale factor F_N , which represents the ratio of real molecules to the number of simulated molecules. The ratio of these two quantities, F_N and Δt , is the same in every region. The cell dimensions must be such that the change in flow properties across each cell is small; hence, the cell dimension is less than the local mean free path. Each cell is divided into four subcells where the collision partners are selected for the establishment of the collision rate. Also, time is advanced such that each time step is small in comparison with the mean collision time. A view of the computational domain is depicted in Figure 3.2.

According to Figure 3.2, the side I corresponds to the cavity surface. Diffuse reflection with complete thermal accommodation is the condition applied to this side.

Figure 3.2 - Illustration of the computational domain.



SOURCE: Author Production.

Sides II and III are freestream sides through which simulated molecules can enter and exit. Finally, the flow at the downstream outflow boundary, sides IV, V, and VI are predominantly supersonic and vacuum condition is specified. At this boundary, simulated molecules can only exit. The choice of vacuum is normally used when the velocity of the gas through the boundary is supersonic. For flows with Mach number equal to or greater than three (BIRD, 1994), the molecules entering to the computational domain through the boundary can be neglected.

The mesh generation procedure, the effect of the mesh resolution, and the verification and validation process employed in the present work are discussed in the next chapter.

Table 3.3 - Freestream flow conditions.

properties	Values	Unity
Velocity (U_∞)	7546.5	m/s
Temperature (T_∞)	219.69	K
Pressure (p_∞)	5.582	N/m^2
Density (ρ_∞)	8.752×10^{-5}	kg/m^3
Number density (n_∞)	1.819×10^{21}	m^{-3}
Viscosity (μ_∞)	1.455×10^{-5}	Ns/m^2
Mean free path (λ_∞)	9.285×10^{-4}	m

3.3 Freestream and Flow Conditions

Freestream conditions employed in this investigation are those given by Palharini (PALHARINI, 2010), tabulated in Table 3.3. These conditions represent those experienced by a reentry vehicle at an altitude of 70 km .

The freestream velocity U_∞ is assumed constant as 7546.5 m/s , which corresponds to a freestream Mach number M_∞ of 25. The cavity surface temperature T_W was assumed as a constant value of 880 K . Diffuse reflection with complete thermal accommodation was assumed for the gas-surface interaction.

By assuming the cavity length L as the characteristic length, the overall Knudsen number Kn_∞ corresponds to 0.3095, 0.1548, 0.1032 and 0.0774 for length L of 3, 6, 9 and 12 mm , respectively. In addition, the Reynolds number Re_∞ is around 121.7, 243.4, 365.1 and 486.8 for L of 3, 6, 9 and 12 mm , respectively, also based on conditions in the undisturbed stream. Finally, in order to account for the angle-of-attack effects, simulations were conducted by assuming α of 10, 15, and 20 degrees. It is important to remark that simulations with zero-degree angle of attack were investigated earlier by Palharini (PALHARINI, 2010).

4 VERIFICATION AND VALIDATION PROCESSES

Before presenting and discussing the computational results, it proves convenient to first examine the verification and validation processes. Related to the computational code, the DSMC verification and validation processes consist of four basic steps: (1) to verify the appropriate number of computational cells, (2) to verify the appropriate number of simulated molecules, (3) to verify the time step, and (4) to compare DSMC results with analytic or experimental results available in the current literature. In this fashion, the purpose of this chapter is to discuss in detail these steps.

4.1 Computational Requirements

Nowadays, the DSMC method is the appropriate computational technique used for modeling complex transitional flows in engineering. This method models a gas flow by using a computational mesh to track the trajectory of simulated molecules. Each simulated molecule represents a fixed number of real gas molecules. The simulated molecules are allowed to move and collide, while the computer store their position coordinates, velocities and energies. In order to do that, a computational mesh is used as a reference in the selection process of the collision pairs, and for sampling and averaging macroscopic flowfield properties. Currently, several methods of mesh generation have been used for different body shapes, each with its complexity and computational cost. For instance, the body-fitted coordinate system implemented by Abe (ABE, 1989), the transfinite interpolation method made by Olynick et al. (OLYNICK et al., 1989), the adaptive rectangular mesh implemented by Babovsky et al. (BABOVSKY et al., 1989), the “Point reference” scheme implemented by Bird (BIRD, 1976), the multi-level Cartesian mesh proposed by Rault (RAULT, 1994), and other mesh generation process as the simple rectangular grid, the “General” scheme, and the rectangular multi-level sub-cells with adaptive body-fitted cells described by Bird (BIRD, 1994).

Traditionally, three schemes of mesh generation may be employed in DSMC code: (1) a uniform cartesian mesh, (2) a structured body-fitted mesh, and (3) an unstructured body-fitted mesh. Each of these schemes has advantages and disadvantages such as a low cost during the movement of simulated molecules, the use of cells with non-uniform size in regions where the gradients are more intense, and application in simulation of complex geometries. Wilmoth et al. (WILMOTH et al., 1996) and Nance et al. (NANCE et al., 1997) discuss in details the advantages of each scheme, in terms of accuracy, computational efficiency and ease of use.

Once defined the mesh generation scheme, three primary constraints must be considered in order to evaluate the DSMC computational requirements: (1) the cell size must be smaller than the local mean free path, (2) the number of simulated molecules per cell should be approximately constant in order to preserve collision statistics, and (3) the simulation time step must be less than the local mean collision time. As mentioned earlier, an important assumption in the DSMC method is that the gas is dilute, meaning that the molecular diameter is much smaller than the spacing between molecules in the gas. This assumption allows that the molecular motion be decoupled from the molecular collisions over a small local time interval. Thus, the successful application of the DSMC method requires that the time step must be a fraction of the mean collision time, as well as the cell dimensions should be of the order of one third of the local mean free path λ , becoming even smaller than λ in the directions in which the gradients are more intense (BIRD, 1994).

The cell size requirement is because in certain regions, such as the vicinity of adiabatic surfaces, flowfield gradients must be very small, and the cell size must be small enough to adequately capture flowfield physics near the body surface. Otherwise, if the cell size near the body surface are too large, then the most energetic molecules so close to the far edge of the cell could transfer energy and momentum to molecules located immediately adjacent to the body surface. Moreover, such molecules adjacent to the surface could transfer energy and momentum to the body surface. This leads to over-prediction of heat flux and the aerodynamic forces acting on the body surface. This type of error can be minimized by reducing the cell size relative to the local mean free path of molecules near the surface. As a result, the cell size should be small in regions within the flowfield where the physical properties vary rapidly, such as the regions where the density is large. In these regions, the cell size should be reduced in order to limit not only the number of molecules in each cell but also the number of collisions in a given time step.

In order to adequately model the physics of interest, the number of simulated molecules in each cell must be greater than a certain number. To obtain accurate collision statistics, it is desirable to have 20 - 30 simulated molecules in each cell (ALEXANDER et al., 2000; FALLAVOLLITA et al., 1993). However, it is very difficult to maintain this requirement when the density distribution is no longer uniform in the computational domain. As pointed out by Kannenberg and Boyd (KANNENBERG; BOYD, 2000), the number of simulated molecules in the cell varies inversely with the gas density. Therefore, high-density regions will tend to have few molecules, while low-density regions will have a large number of molecules, resulting in over resolu-

tion in the flow domain. In order to overcome this difficulty, a variable scaling factor F_N is used to control the distribution of simulated molecules within the cells. The scaling factor F_N is the ratio of the number of real molecules and the number of simulated molecules.

In this scenario, the computational effort is substantially reduced by subdividing the flowfield into an arbitrary number of regions where the scaling factor F_N and the time step Δt remain constant within a region, but they can vary from one region to another. The combination of subdividing the computational domain into regions along with the use of variable cell sizes provides the flexibility to a substantial reduction in the total number of simulated molecules used in the simulation, and contributes to improve the mesh resolution in those regions where the gradients are more intense. It is important to remark that although Δt and F_N can vary from region to region, the ratio $F_N/\Delta t$ must be the same for all regions in order to conserve mass across region boundaries in the flow.

More details for estimating the computational requirements of DSMC simulations are presented at length by Rieffel (RIEFFEL, 1999) and Shu et al. (SHU et al., 2005).

4.2 Computational Mesh Generation

The mesh generation scheme used in this study was based on the procedure presented by Bird in his algorithm called DS2G (BIRD, 1999). Proceeding in a manner analogous to the Bird treatment, the physical domain is divided into a number of arbitrary four-sided regions, as shown in Figure 3.2. Along the boundaries, point distributions are generated in such way that the number of points on each side is the same. The cell structure is defined by joining the corresponding points on each side by straight lines and then dividing each of these lines into segments which are joined to form the system of quadrilateral cells. The distribution can be controlled by a number of different distribution functions which allow the concentration of points in areas where high flow gradients or small mean free paths are expected. In addition, the point distributions may be chosen independently for each region.

4.3 Computational Mesh Adaptation

In order to improve the solution accuracy and the mesh efficiency, a mesh adaptation technique is employed in the present study. The procedure for the adaptation of the computational mesh is threefold: (1) initially, the computational mesh structure is generated based on the freestream conditions, (2) the values of F_N are defined for

each region, and the time step Δt is then estimated based on the condition that the ratio $F_N/\Delta t$ be the same for all regions, (3) these parameters are iteratively modified until an acceptable number of simulated molecules, cell size distribution and simulation time step are obtained.

4.4 DSMC Test Case

In order to validate the two-dimensional version of the DSMC code employed in this work, the problem of a hypersonic flow over a flat plate was selected as a test case. The flat-plate model has been selected for comparison because experimental data and numerical simulations on this subject are available in the current literature. In doing so, it becomes instructive to examine two different flat plates as DSMC test cases in the present work. One of them corresponds to experimental and numerical investigations carried out by Lengrand et al. (LENGRAND et al., 1992) for a hypersonic flow over a sharp flat plate. The other one corresponds to a numerical study conducted by Dogra et al. (DOGRA et al., 1989) for a rarefied flow past a flat plate at incidence.

The experimental work conducted by Lengrand et al. (LENGRAND et al., 1992) considered a flat plate of 100 *mm* of length with 100 *mm* of width and sharp leading edge. Two angle of incidence, 0 and 10 degrees, were considered to perform the experiments. Nitrogen, used as the working gas, was generated by the freejet expansion from a distance of the flat plate resulting in a freestream Mach number of 20.2, temperature of 13.32 *K* and pressure of 0.06831 *N/m*². The flat-plate surface temperature, T_w , was 290 *K*. The flow conditions were chosen among those that could be obtained in the SR3 wind tunnel of Centre National de la Recherche Scientifique (CNRS). Table 4.1 presents the freestream conditions.

In addition to this experimental work, Lengrand et al. (LENGRAND et al., 1992) also investigated numerically this hypersonic flat-plate flow by employing the DSMC method. In their simulations, molecular collisions were treated by the VHS model associated with the Larsen-Borgnakke model for rotation-translation energy exchange. By considering the temperature level, vibration mode was neglected. In addition, the gas-surface interaction was treated by the Maxwell's model with a single accommodation coefficient.

Also of great significance in the present validation process is the numerical investigation of a hypersonic flat-plate flow conducted by Tsuboi et al. (TSUBOI et al., 2004). Tsuboi et al. examined a hypersonic flow over a flat plate with 100 *mm* of

Table 4.1 - Freestream conditions (LENGRAND et al., 1992).

Properties	Value	Unity
Mach number (M_∞)	20.2	
Velocity (U_∞)	1,503	m/s
Temperature (T_∞)	13.32	K
Stagnation temperature (T_0)	1,100	K
Pressure (p_∞)	0.06831	N/m^2
Number density (n_∞)	3.716×10^{20}	m^{-3}
Mean free path (λ_∞)	2.35×10^{-3}	m
Angle of attack (α)	0 and 10	deg

SOURCE: LENGRAND et al. (1992).

length and 100 mm of width. The plate had a leading-edge angle of 20 degrees and thickness of 5 mm . Simulation conditions are those employed in the experimental work conducted by Legrand et al. (LENGRAND et al., 1992). Simulations were performed by employing the DSMC method, along with the dynamic molecular collision (DMC) model (TOKUMASU; MATSUMOTO, 1999) for gas-gas collisions, the diffuse reflection for gas-surface interactions, and the null collision technique for collision frequency. According to Tsuboi et al. (TSUBOI et al., 2004), the DMC model for nitrogen molecules is able to capture the non-equilibrium characteristics in the rarefied gas flow below 2000 K .

In the same framework, Dogra et al. (DOGRA et al., 1989) conducted DSMC simulations of a rarefied flow past a flat plate at 40-degree of incidence. Their study considered a flat plate with 1 m of length and zero thickness. The flow conditions simulated were those experienced by the Shuttle Orbiter during re-entry at 7.5 km/s . These conditions correspond to an altitude of 90 km , freestream Mach number of 27.2, freestream temperature of 188 K and density of $3.418 \times 10^{-6} kg/m^3$. The flat-plate surface temperature, T_w , was 1000 K . The flat-plate surface was assumed to be diffused with full thermal accommodation and to promote recombination of the oxygen and nitrogen atoms. In addition, the freestream Knudsen number was 0.023. The Table 4.2 summarizes the freestream conditions.

In order to assess the overall performance of the DSMC code employed in this work, the freestream flow conditions and the geometric parameters, used for the test cases, are those given by the experimental and numerical investigations conducted by Lengrand et al. (LENGRAND et al., 1992), as shown in Table 4.1 It is

Table 4.2 - Freestream conditions (DOGRA et al., 1989).

Properties	Values.	Unity
Altitude	90	<i>km</i>
Velocity (U_∞)	7500	<i>m/s</i>
Temperature (T_∞)	188	<i>K</i>
Density (ρ_∞)	3.418×10^{-6}	<i>kg/m³</i>
Angle of attack (α)	40	<i>deg</i>

SOURCE: DOGRA et al. (1989).

important to recall that this investigation was numerically reproduced by Tsuboi et al. (TSUBOI et al., 2004) by employing the DSMC method. In the computational solution reproduced in this work, it was assumed that the flat plate is immersed in a uniform stream flowing to the plate at 20-degree of incidence. The flat plate was modeled as one with zero thickness and length of $100\lambda_\infty$.

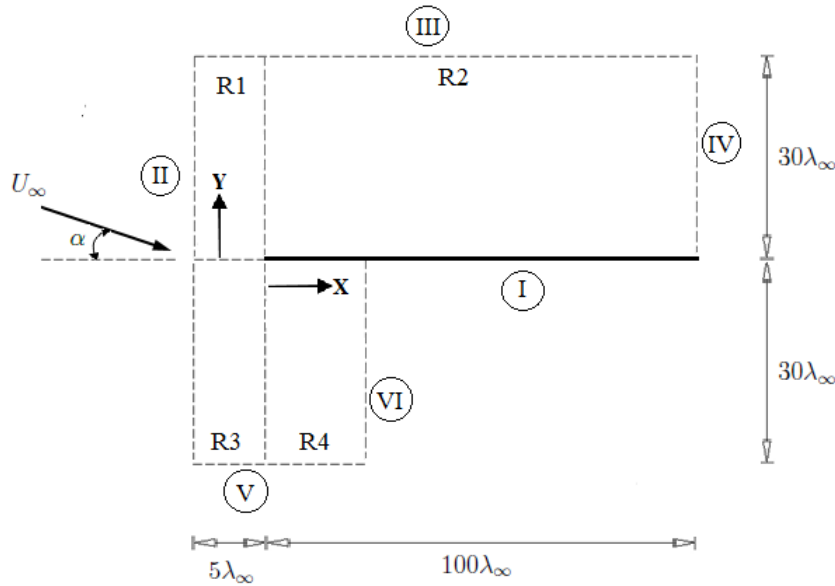
In doing so, the computational domain used for the simulation was made large enough so that flat-plate disturbances did not reach the upstream and side boundaries, where simulation conditions were specified. The undisturbed freestream boundary conditions were imposed at $5\lambda_\infty$ upstream of the plate leading edge, and the boundaries normal to the plate extended to a distance of $30\lambda_\infty$ from the plate surface. This computational domain was divided into four regions, which were subdivided into computational cells, more precisely, quadrilateral cells. The cells were subdivided into subcells, two subcells/cell in each coordinate direction. A schematic view of the computational domain around the flat plate used for the DSMC test case is displayed in Figure 4.1.

Referring to Figure 4.1, side I corresponds to the flat-plate surface. Diffuse reflection with complete thermal accommodation is the condition applied to this side. Sides II, III, and V are freestream sides through which simulated molecules can enter and exit. The uniform flow is entering the left boundary, side II, at a freestream Mach number of 27.2. The flow at the downstream outflow boundaries, sides IV and VI, are predominantly supersonic and vacuum condition was specified. As a result, simulated molecules can only exit at these boundaries.

Still referring to Figure 4.1, region 1 consisted of 30 cells along x -direction (side III) 70 cells along y -direction (side II). Region 2 consisted of 320 cells by 100 cells along x - and y -directions, respectively. Similarly, region 3 and region 4 have 30 cells

by 70 cells and 50 cells by 70 cells along the x - and y -directions, respectively. This computational mesh was defined as being the standard case. In addition to this mesh, two other meshes, defined by coarse and fine, were used to study the sensitivity of the computations to the mesh resolution.

Figure 4.1 - Drawing illustrating the flat-plate computational domain.



SOURCE: Author Production.

4.4.1 Effect of Mesh Resolution

It is usually accepted without questions that the computational results are affected by the mesh resolution. Insufficient mesh resolution near the body surface can reduce significantly the accuracy of predicted aerodynamic heating and forces acting on the body surface. Hence, heat transfer, pressure and skin friction coefficients, are used as the representative parameters for the mesh sensitivity study.

The effect of altering the mesh resolution in the x - and y -direction was investigated for three different computational mesh, defined by coarse, standard, and fine. The coarse and fine meshes correspond, respectively, to 50% less and 100% more cells with respect to the standard mesh. As a base of comparison, Table 4.3 tabulates the number of cells employed for each region in these meshes. It is important to remark that each mesh was made up of non-uniform cell spacing in both coordinate direc-

tions. In addition, the effect of altering the mesh resolution was examined separately for each coordinate direction.

Table 4.3 - Number of cells in the (x -direction) and the [y -direction] for the flat plate case.

	Coarse	Standard	Fine
Region 1	(15 x 70)[30 x 35]	30 x 70	(60 x 70)[30 x 140]
Region 2	(160 x 100)[320 x 50]	320 x 100	(640 x 100)[320 x 200]
Region 3	(15 x 70)[30 x 35]	30 x 70	(60 x 70)[30 x 140]
Region 4	(25 x 70)[50 x 35]	50 x 70	(100 x 70)[50 x 140]
Cells	19,850	39,700	79,400

The effect of changing the number of cells in the x -direction on pressure C_p , skin friction C_f and heat transfer C_h coefficients is illustrated in Figure 4.2. In this group of plots, the dimensionless length X corresponds to the length x normalized by the freestream mean free path λ_∞ . Based on these plots, it is clearly observed that the calculated results are not affected by the range of cell spacing considered for the x -direction in the cases defined by coarse, standard and fine meshes.

A similar examination was made in the y -direction. The influence of the calculated results to cell size variations in the y -direction is demonstrated in Figure 4.3. In this set of plots, a new series of three simulations, with mesh in the region 2 of 320 cells fixed in the x -direction, and 35, 70 and 140 cells in the y -direction, are compared. The cell spacing in both directions is again nonuniform. According to this set of plots, the results for three independent meshes are approximately the same, indicating that the standard mesh is essentially grid independent. For the standard case, the cell size in the y -direction is always less than the local mean free path in the vicinity of the surface. The comparison shows that the influence of cell variations over these quantities was negligible for the cases investigated in the present work, indicating that the standard mesh is essentially independent of the cell size.

4.4.2 Effect of the Variation in the Number of Molecules

Proceeding in a manner analogous to the cell size treatment, an examination was made for the number of simulated molecules. The effect of the calculated results to variations in the number of molecules is illustrated in Figure 4.4. The standard

mesh corresponds to a total of 672,000 molecules. Two new cases using the same mesh were investigated. These new cases correspond to, on average, 336,000 and 1,344,000 molecules in the entire computational domain. The number of molecules was increased by changing the scaling factor F_N defined earlier. It is clearly seen that the results are the same for the three cases investigated, indicating that the number of simulated molecules for the standard mesh, 672,000 molecules, is enough for the code validation process.

4.4.3 Effect of Downstream Boundary Condition

As mentioned earlier in Chapter 3, vacuum was defined as the boundary condition on sides IV and VI (see Figure 4.1) in the computational domain. The vacuum option is usually adopted when the gas velocity through the boundary condition is supersonic, more precisely, for a flowfield with a Mach number equal to or greater than three (BIRD, 1994). As a result, the flux of molecules across the boundary condition into the computational domain can be neglected. It is important to remark that, close to the wall, molecules may not be moving at supersonic speed. Consequently, in this subsonic region close to the wall, there is an interaction between the flow and the downstream boundary. In order to determine the extend of the upstream effect of this imposed downstream vacuum boundary conditions, simulations were made for two other plates with different lengths, i.e., 80 and 120 λ_∞ . Figure 4.5 displays a comparison of the aerodynamic surface quantities calculated for these three different flat-plate sizes.

Based on Figure 4.5, it is seen that the vacuum boundary condition presents a minor effect in the heat transfer coefficient, followed by the skin friction coefficient, and, finally, for the pressure coefficient. Based on the distribution for the skin friction and pressure coefficients, it is clearly noticed that the upstream disturbance imposed by the vacuum condition is around $30\lambda_\infty$.

Figure 4.2 - Effect of the variation on a cell size (x -direction) on pressure (top), skin friction (middle) and heat transfer (bottom) coefficients.

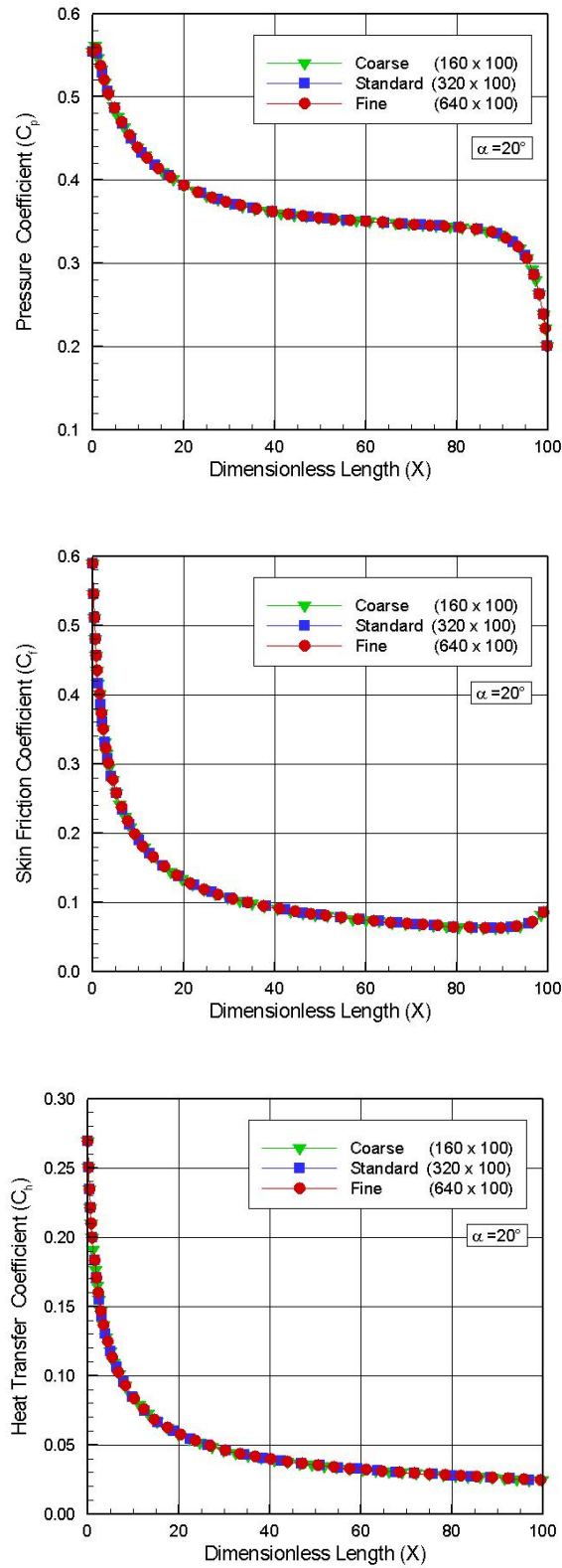


Figure 4.3 - Effect of changing the cell size (y -direction) on pressure (top), skin friction (middle) and heat transfer (bottom) coefficients.

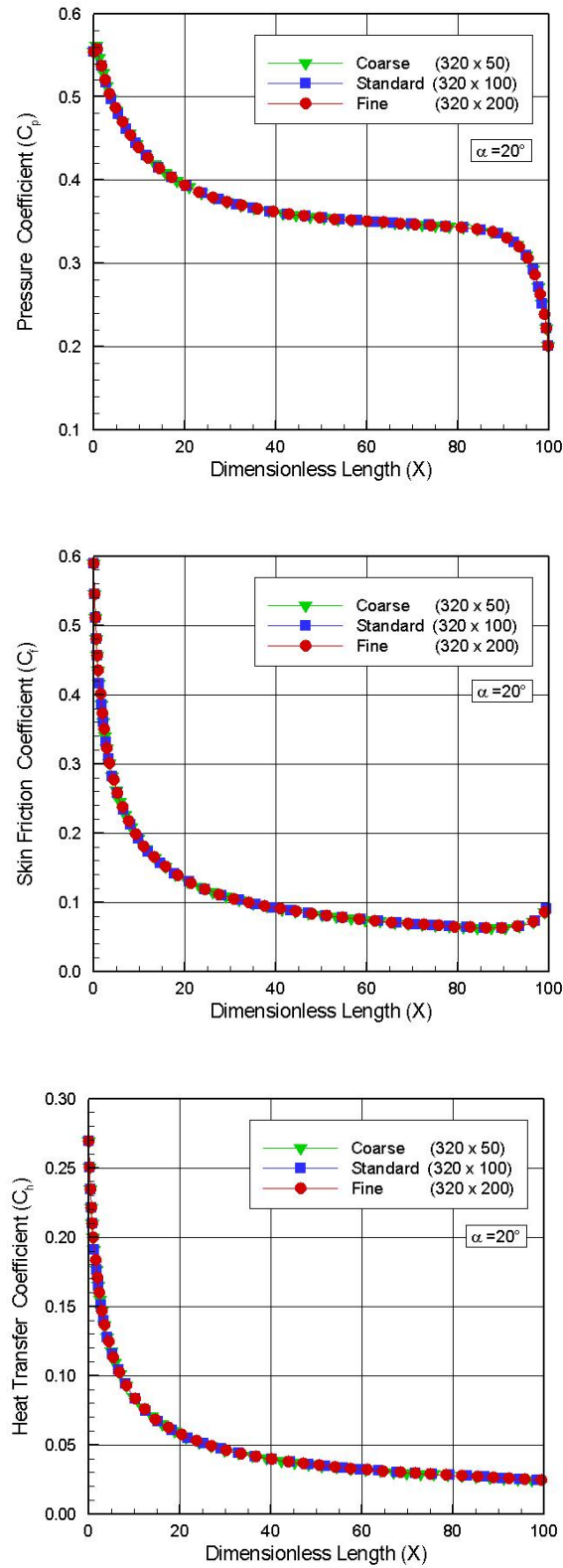


Figure 4.4 - Effect of changing the number of molecules on pressure (top), skin friction (middle) and heat transfer (bottom) coefficients.

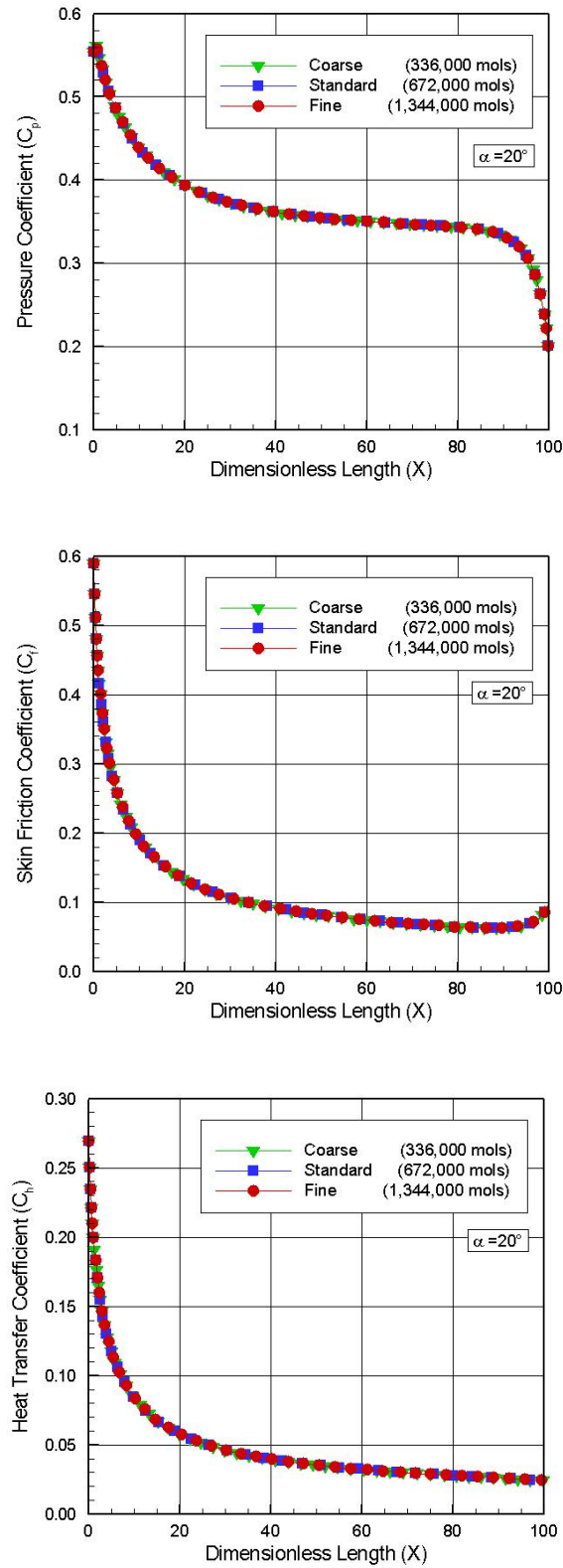
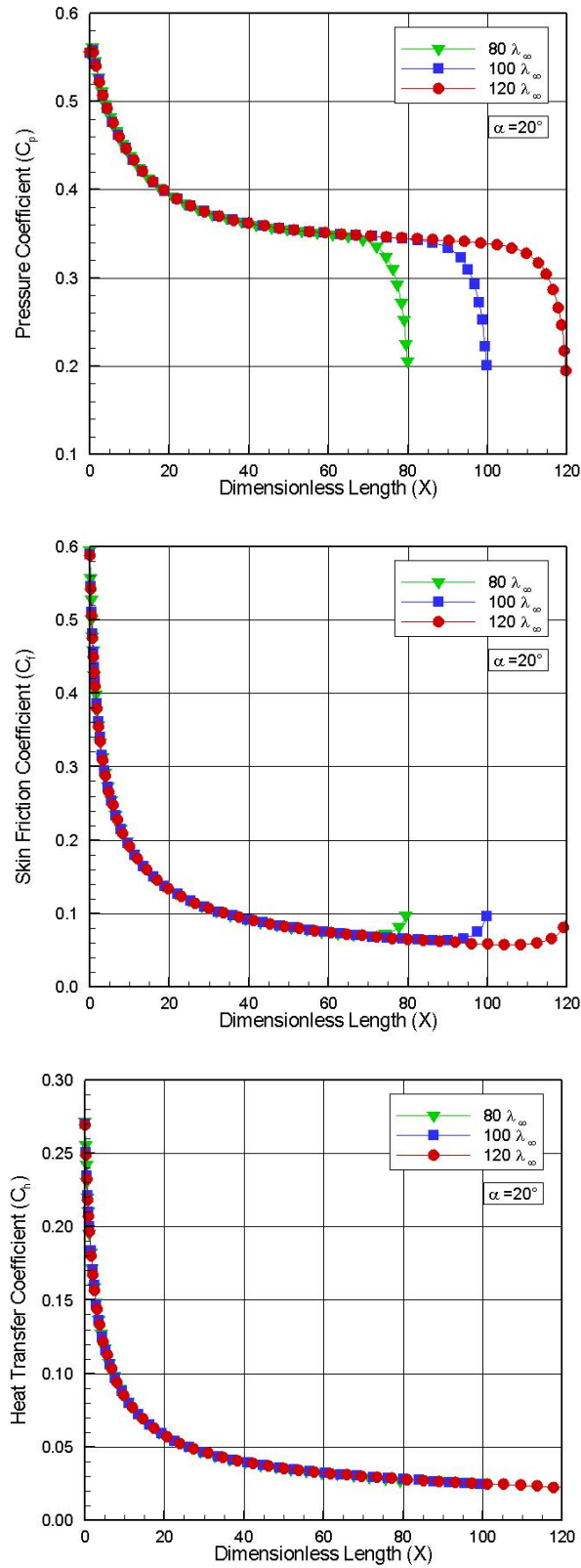


Figure 4.5 - Effect of changing the plate length on pressure (top), skin friction (middle) and heat transfer (bottom) coefficients.



4.5 Experimental and Numerical Comparisons

After completing the discussion of verification process, the attention is turned to the validation process. In this manner, this section presents comparisons of two test cases with experimental and numerical results for a flat-plate given by (1) a numerical study conducted by Dogra et al. (DOGRA et al., 1989) for a rarefied flow past a flat plate at incidence, and by (2) Lengrand et al. (LENGRAND et al., 1992), that was numerically reproduced by Tsuboi et al. (TSUBOI et al., 2004) by using the DSMC method. For comparison purpose, freestream flow conditions employed in the DSMC code for the two cases are those tabulated in Tables 4.1 and 4.2.

4.5.1 First Test Case

The first test case, a rarefied hypersonic flow over a flat-plate at 40-degree of incidence, was simulated in order to reproduce the DSMC results obtained by Dogra et al. (DOGRA et al., 1989), as defined earlier in section 4.4. Results for three different locations along the flat-plate surface are presented for density, overall kinetic temperature and tangential velocity.

Profiles perpendicular to the flat-plate surface for density, overall kinetic temperature, and tangential velocity are illustrated in Figures 4.6, 4.7, and 4.8 for three sections along the flat-plate surface. In these plots, density ρ is normalized by the freestream density ρ_∞ , the overall kinetic temperature T_O is normalized by freestream temperature T_∞ , and tangential velocity u is normalized by $U_\infty \cos\alpha$, where α is the angle of attack, 40 degrees. In addition, empty symbols correspond to the present DSMC results and filled symbols represent DSMC results obtained by Dogra et al. (DOGRA et al., 1989). Also, it is important to mention that overall kinetic temperature T_O is defined for a nonequilibrium gas as the weighted mean of the translational and internal temperatures, as given by Equation (5.1), Chapter 5.

According to these plots, it is observed that results obtained in this work present a good agreement as compared to numerical DSMC results obtained by Dogra et al. (DOGRA et al., 1989) for stations x/L of 0.1 and 0.5. However, for station x/L of 0.9, significant differences are observed in the overall kinetic temperature (small difference for density and tangential velocity) inside the shock layer. These differences are attributed to two effects: (1) the vacuum condition assumed as the downstream boundary condition, as explained in subsection 4.4.3, where the upstream disturbance seems to be larger than 10% of the plate length; (2) differences in the simulations conditions between the present DSMC simulations and those conducted

by Dogra et al. (DOGRA et al., 1989), for instance, the recombination of Nitrogen and Oxygen atoms promoted by the flat-plate surface.

Figure 4.6 - Density ratio (ρ/ρ_∞) profiles normal to the plate surface for three locations along the plate surface.

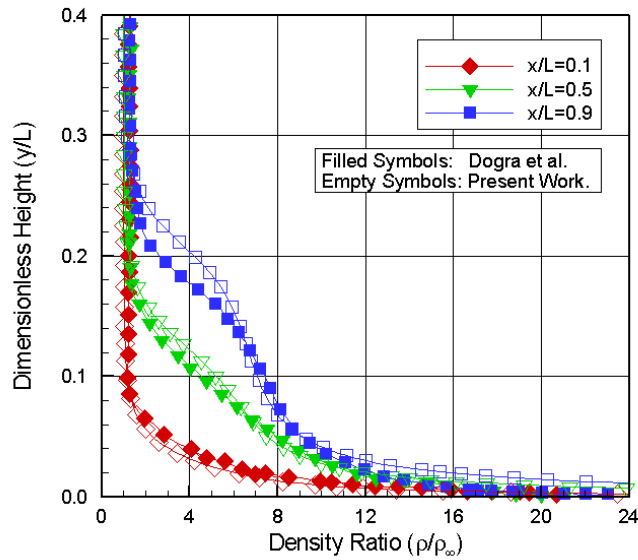


Figure 4.7 - Overall kinetic temperature ratio (T_o/T_∞) profiles normal to the plate surface for three locations along the plate surface.

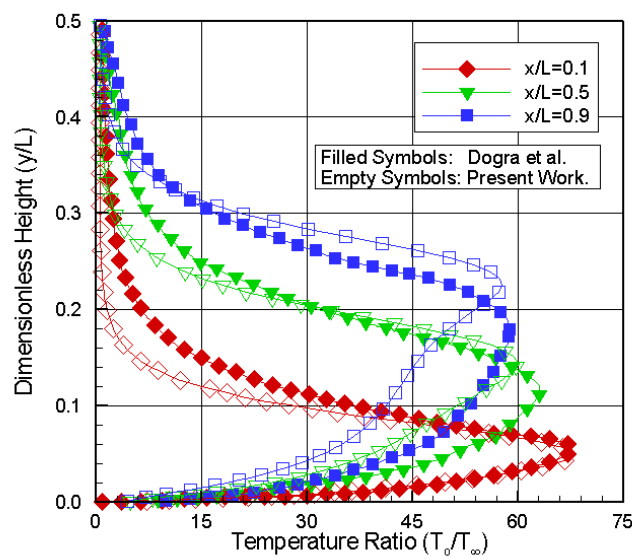
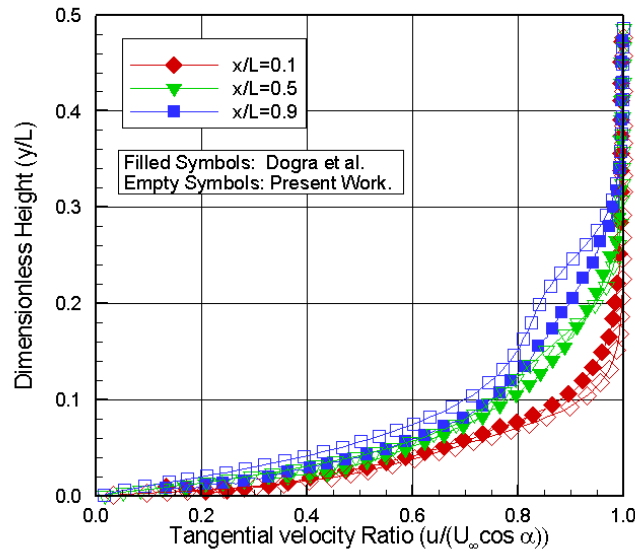


Figure 4.8 - Tangential velocity ratio ($u/U_\infty \cos \alpha$) profiles normal to the plate surface for three locations along the plate surface.



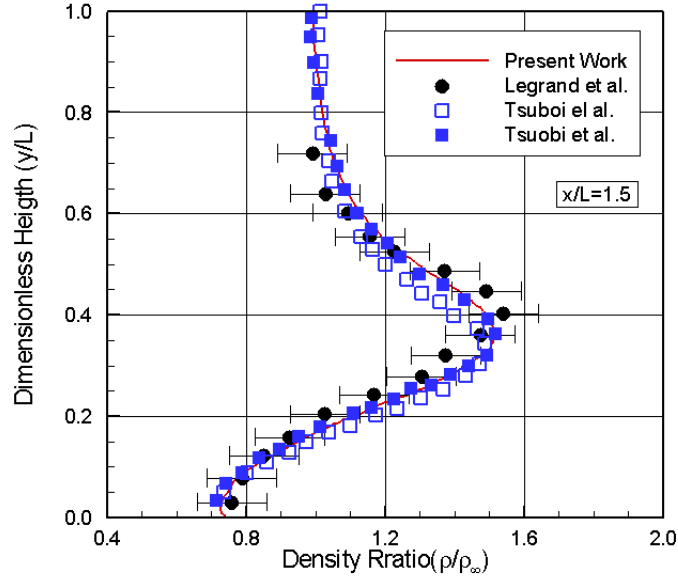
4.5.2 Second Test Case

The second test case was simulated in order to reproduce the results for a rarefied hypersonic flow over a flat-plate that was investigated experimentally by Lengrand et al. (LENGRAND et al., 1992) and reproduced numerically by Tsuboi et. al (TSUBOI et al., 2004), as defined earlier in subsection 4.4.

Density ratio, ρ/ρ_∞ , profile normal to the flat plate surface is demonstrated in Figure 4.9 for section $x/L = 1.5$ along the flat plate surface. In this plot, solid line correspond to the present DSMC results, filled and empty square symbols represent numerical data for 0-degree and 20-degree leading-edge bevel angle, respectively, obtained by Tsuboi et al. (TSUBOI et al., 2004), and filled circle symbol represents experimental data obtained by Lengrand et al. (LENGRAND et al., 1992) with uncertainty of 10%. According to this figure, it is observed that results obtained in this work present an excellent agreement as compared to experimental and numerical DSMC results obtained by Lengrand et al. (LENGRAND et al., 1992) and by Tsuboi et al. (TSUBOI et al., 2004).

In the results that follow, Figure 4.10 illustrates the wall pressure distribution along the flat plate. In this plot, wall pressure p_w is normalized by the freestream pressure

Figure 4.9 - Density ratio (ρ/ρ_∞) profile at section $x/L = 1.5$ along the flat plate surface.

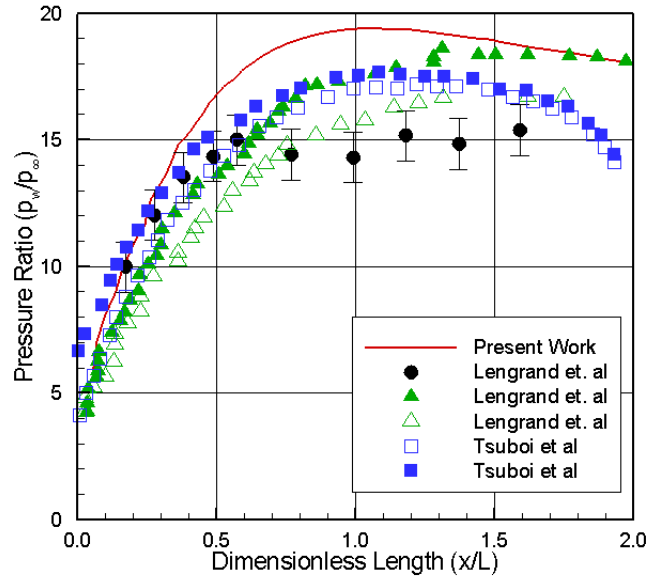


Filled circle: experimental data; filled square: 0-degree leading-edge bevel angle; empty square: 20-degree leading-edge bevel angle.

p_∞ , and the distance x along the plate is normalized by the plate length L . Again, solid line corresponds to the present DSMC results, filled and empty square symbols stand for numerical data for 0-degree and 20-degree leading-edge bevel angle, respectively, obtained by Tsuboi et al. (TSUBOI et al., 2004), and filled circle symbol represents experimental data obtained by Lengrand et al. (LENGRAND et al., 1992). In addition, filled and empty triangles correspond to DSMC results by considering the fraction f of inelastic collisions of 0.5 and 1.0, respectively, also simulated by Lengrand et al. (LENGRAND et al., 1992). Also, it is important to mention that wall pressure definition is given by Equation (5.8), Chapter 5.

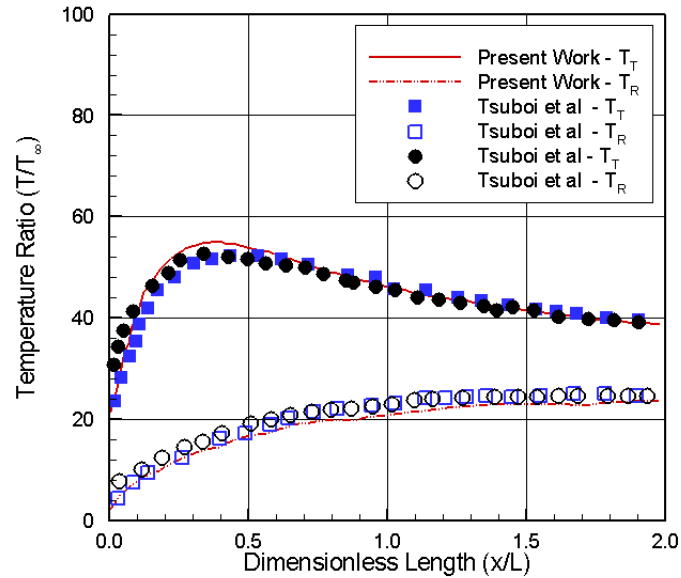
Referring to Figure 4.10, it is clearly seen that the DSMC results present a good agreement only at the vicinity of the flat-plate leading edge, as compared to the experimental data. Far from the flat-plate leading edge, DSMC results overpredict the experimental data for wall pressure. These differences are attributed to different numerical conditions, such as, molecular collision model, energy exchange model, and gas-surface interaction model, used between the current DSMC test case, the numerical data given by Lengrand et al. (LENGRAND et al., 1992), and the numerical DSMC investigation given by Tsuboi et al. (TSUBOI et al., 2004).

Figure 4.10 - Wall pressure (p_w/p_∞) distribution along the flat plate surface.



Filled circle: experimental data; filled square: 0-degree leading-edge bevel angle; empty square: 20-degree leading-edge bevel angle; filled triangle: $f = 0.5$; empty triangle: $f = 1.0$.

Figure 4.11 - Translational (T_T/T_∞) and rotational (T_R/T_∞) temperature distribution along the flat plate surface.



Square symbols: 0-degree leading-edge bevel angle; circle symbols: 20-degree leading-edge bevel angle.

In the following, Figure 4.11 displays the translational and rotational temperature distribution along the flat plate for the first row of cells immediately adjacent to flat plate. In this plot, translational temperature T_T and rotational temperature T_R are normalized by the freestream pressure T_∞ , and the distance x along the plate is normalized by the plate length L . In addition, solid and dashed lines stand for the present DSMC results, square and circle symbols represent numerical data for 0-degree and 20-degree leading-edge bevel angle, respectively, obtained by Tsuboi et al. (TSUBOI et al., 2004). Based on this plot, it is seen a good agreement of the present DSMC results with DSMC simulations given Tsuboi et al. (TSUBOI et al., 2004).

4.6 Cavity test case

The procedure for the verification process employed previously in the DSMC Test Case, section 4.4, was also employed to the cavity geometry, defined in Figure 3.1. In this fashion, simulations were performed with computational meshes that met the general requirements for the DSMC method already presented in sections 4.1 to 4.3.

Under the aforementioned procedure, this section presents the analysis in order to verify the mesh resolution and the impact of the number of simulated particles on the aerodynamic surface quantities, such as heat transfer, pressure, and skin friction coefficients, for a cavity defined by L/H ratio of 1 and 10-degree angle of incidence. A similar procedure was employed in the mesh independence study for the other cavity L/H ratio.

As discussed earlier, cell dimensions are more critical in the direction with high gradients. For a cavity, as illustrated in Figure 3.2, gradients are important in the direction normal to the cavity surfaces and inside of it. Therefore, computer simulations were performed by considering computational meshes containing cells distributed in seven regions. In this framework, the number of cells employed in the seven regions for a coarse, a standard, and a fine mesh for a cavity, defined by L/H ratio of 1 and 10-degree angle of attack, is tabulated in Table 4.4.

Table 4.4 - Number of cells in the (x -direction) and the [y -direction] for the cavity case.

	Coarse	Standard	Fine
Region 1	(15 x 70)[30 x 35]	30 x 70	(60 x 70)[30 x 140]
Region 2	(75 x 100)[150 x 50]	150 x 100	(300 x 100)[150 x 200]
Region 3	(25 x 100)[50 x 50]	50 x 100	(100 x 100)[50 x 200]
Region 4	(75 x 100)[150 x 50]	150 x 100	(300 x 100)[150 x 200]
Region 5	(25 x 50)[50 x 25]	50 x 50	(100 x 50)[50 x 100]
Region 6	(15 x 70)[30 x 35]	30 x 70	(60 x 70)[30 x 140]
Region 7	(25 x 70)[50 x 35]	50 x 70	(100 x 70)[50 x 140]
Cells	22,600	45,200	90,400

The impact of altering the cell size in the x -direction was investigated for a coarse and a fine mesh with, respectively, 50% less and 100% more cells with respect to the standard mesh. Figures 4.12, 4.13, and 4.14 illustrate the cell size impact on skin friction, pressure, and heat transfer coefficients, respectively. In this set of plots, X is the length x normalized by the freestream mean free path λ_∞ , and Y_H is the height y normalized by the cavity height H . In addition, the left-column plots correspond to the distribution of the surface quantities along the cavity upstream and downstream surfaces, i.e., surfaces S1 and S5, while the right-column plots correspond to the distribution on the surfaces inside the cavity, i.e., surfaces S2, S3, and S4. Based on this set of plots, the impact of altering the cell size in the x -direction on the aerodynamic surface quantities was rather insensitive to the range of cell spacing considered for the standard and fine meshes.

In analogous fashion, an investigation was made in the y -direction with a coarse and a fine mesh with, respectively, 50% less and 100% more cells with respect to the standard mesh, as shown in Table 4.4. Figures 4.15, 4.16, and 4.17 exhibit the cell size effects on skin friction, pressure, and heat transfer coefficients, respectively, due to changes on the cell size in the y -direction only. According to these plots, it is observed that the effect of changing the cell size in the y -direction on the aerodynamic surface quantities was also insensitive to the range of cell spacing considered for the standard and fine meshes.

A similar examination was made for the dependence of the standard mesh on the number of molecules. The standard mesh for the cavity $L/H = 1$ case corresponds to a total of 949,200 molecules. Two new cases using the same mesh were investigated. These two new cases correspond to 474,600 and 1,898,400 molecules in the

entire computational domain, i.e, cases with 50% less and 100% more cells with respect to the standard mesh. The effect of the number of molecules on skin friction, pressure, and heat transfer coefficients is illustrated in Figures 4.18, 4.19, and 4.20, respectively. As these cases presented the same results for the aerodynamic surface quantities, hence the standard mesh with a total of 949,200 molecules is considered enough for the computation of the flowfield properties. For the purpose of illustration, Figure 4.21 displays the standard mesh for the cavity $L/H = 1$ case. In these plots, X and Y are the length x and height y normalized by the freestream mean free path λ_∞ .

Figure 4.12 - Effect of variation in the cell size in the x -direction on skin friction coefficient for $L/H = 1$ and $\alpha = 10$ deg.

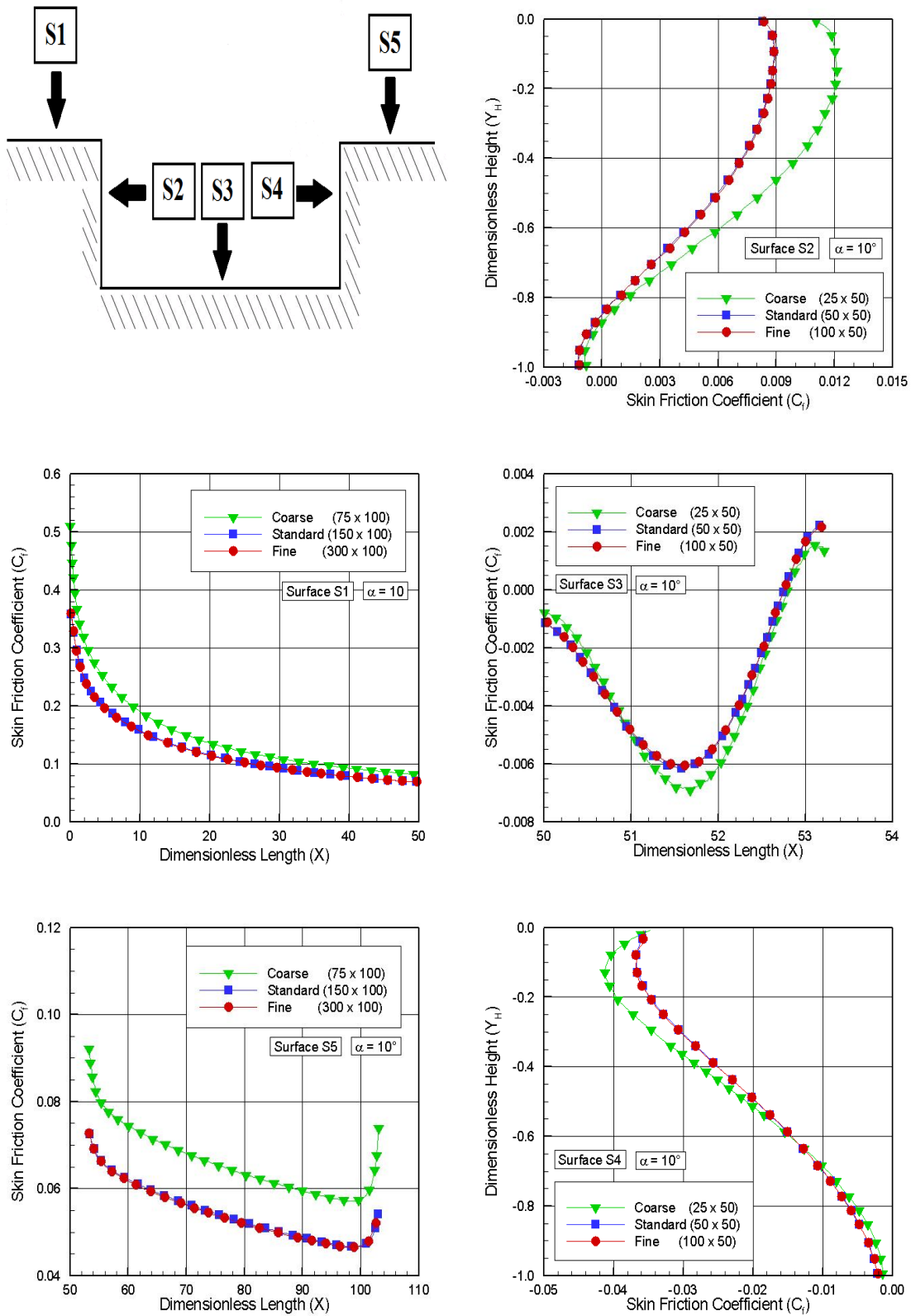


Figure 4.13 - Effect of variation in the cell size in the x -direction on pressure coefficient for $L/H = 1$ and $\alpha = 10$ deg.

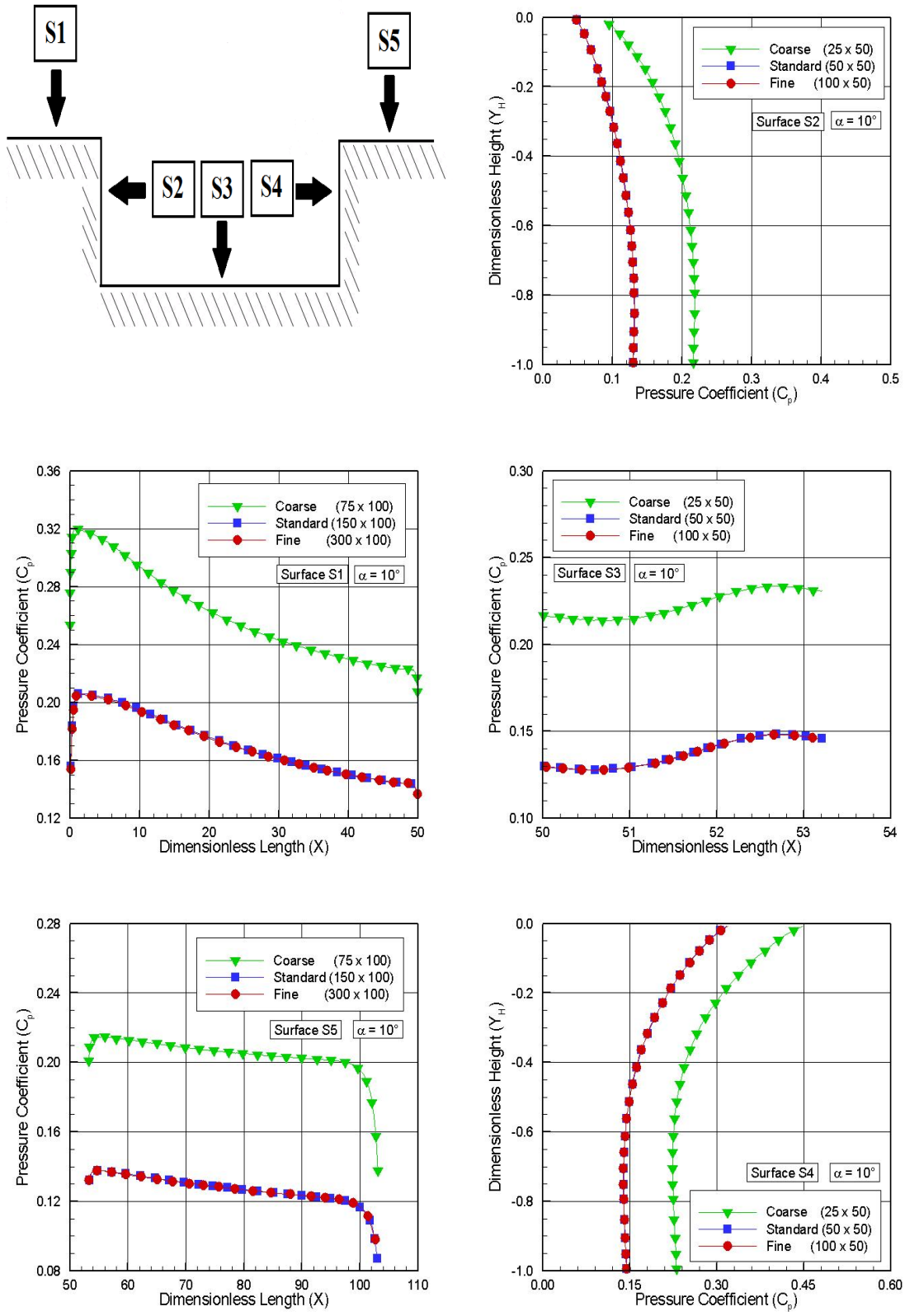


Figure 4.14 - Effect of variation in the cell size in the x -direction on heat transfer coefficient for $L/H = 1$ and $\alpha = 10$ deg.

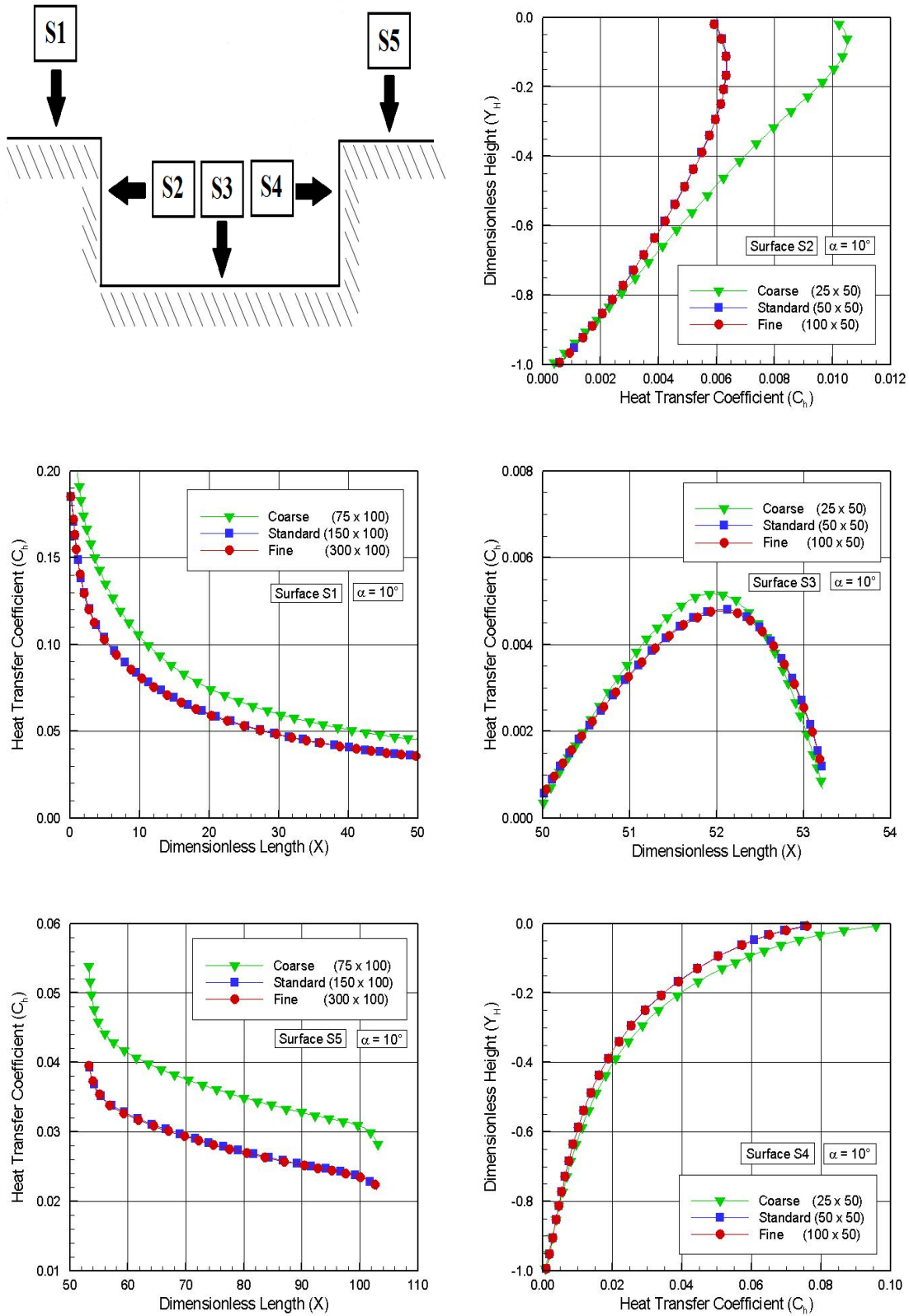


Figure 4.15 - Effect of variation in the cell size in the y -direction on skin friction coefficient for $L/H = 1$ and $\alpha = 10$ deg.

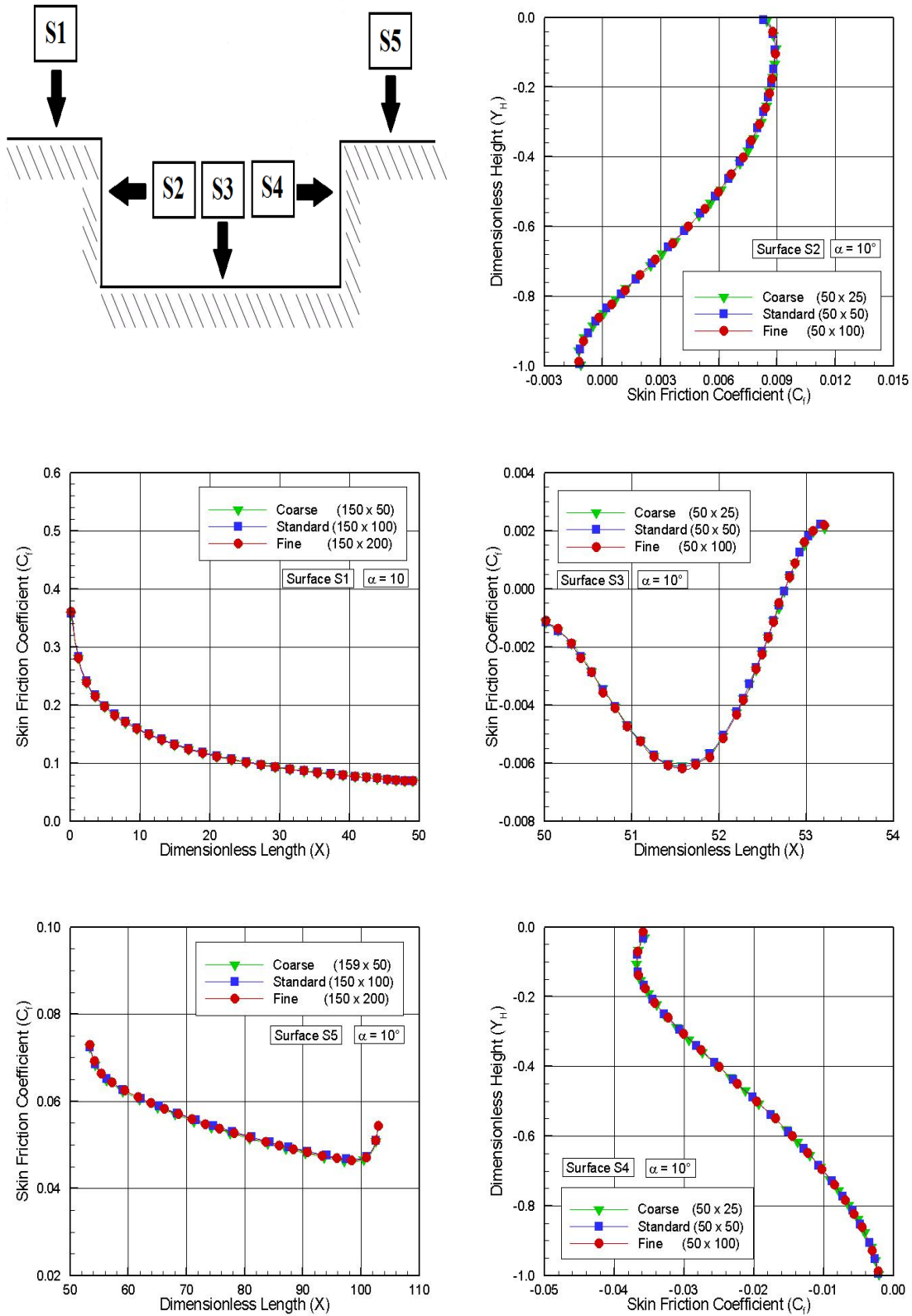


Figure 4.16 - Effect of variation in the cell size in the y -direction on pressure coefficient for $L/H = 1$ and $\alpha = 10$ deg.

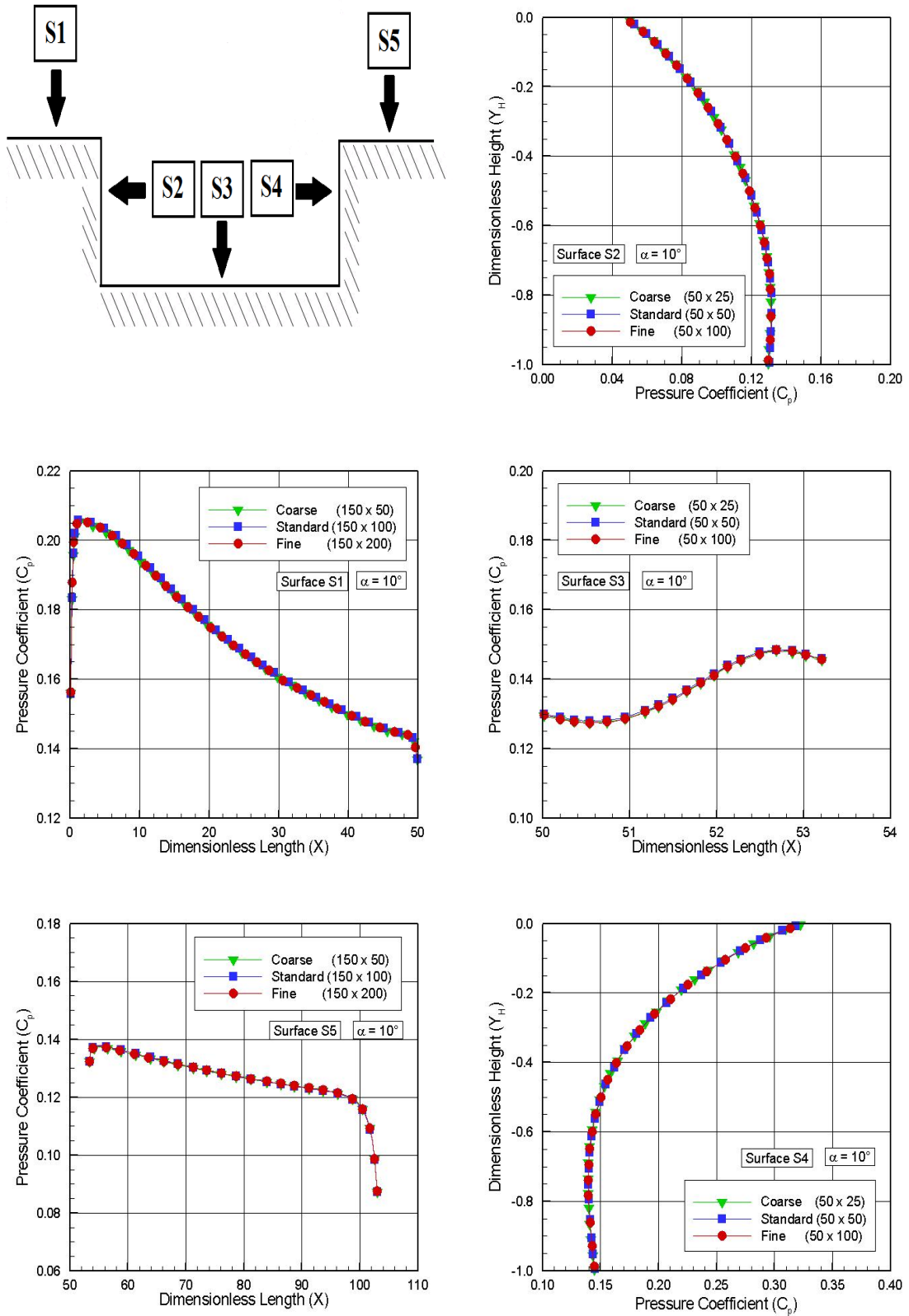


Figure 4.17 - Effect of variation in the cell size in the y -direction on heat transfer coefficient for $L/H = 1$ and $\alpha = 10$ deg.

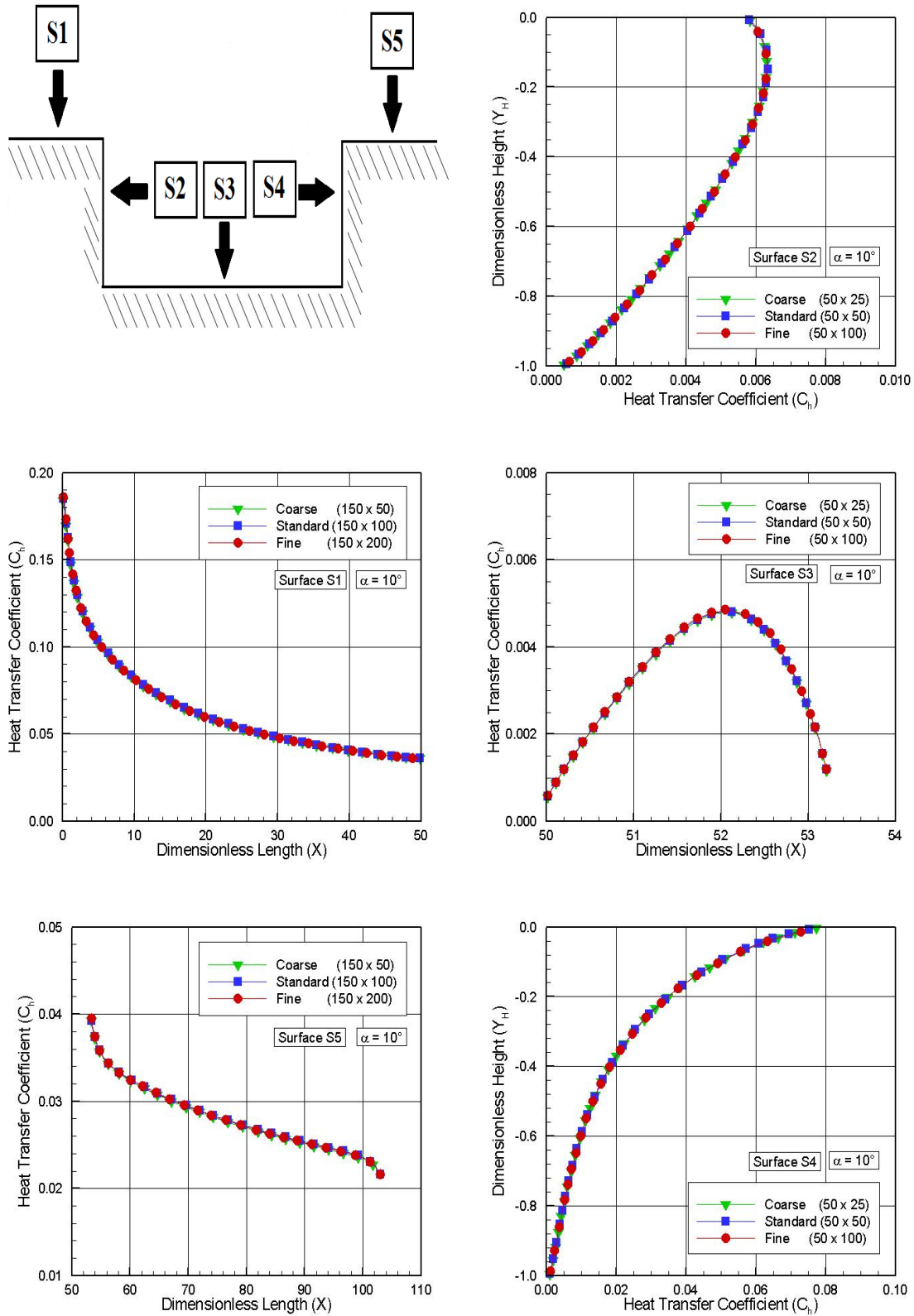


Figure 4.18 - Effect of variation in the number of molecules on skin friction coefficient for $L/H = 1$ and $\alpha = 10$ deg.

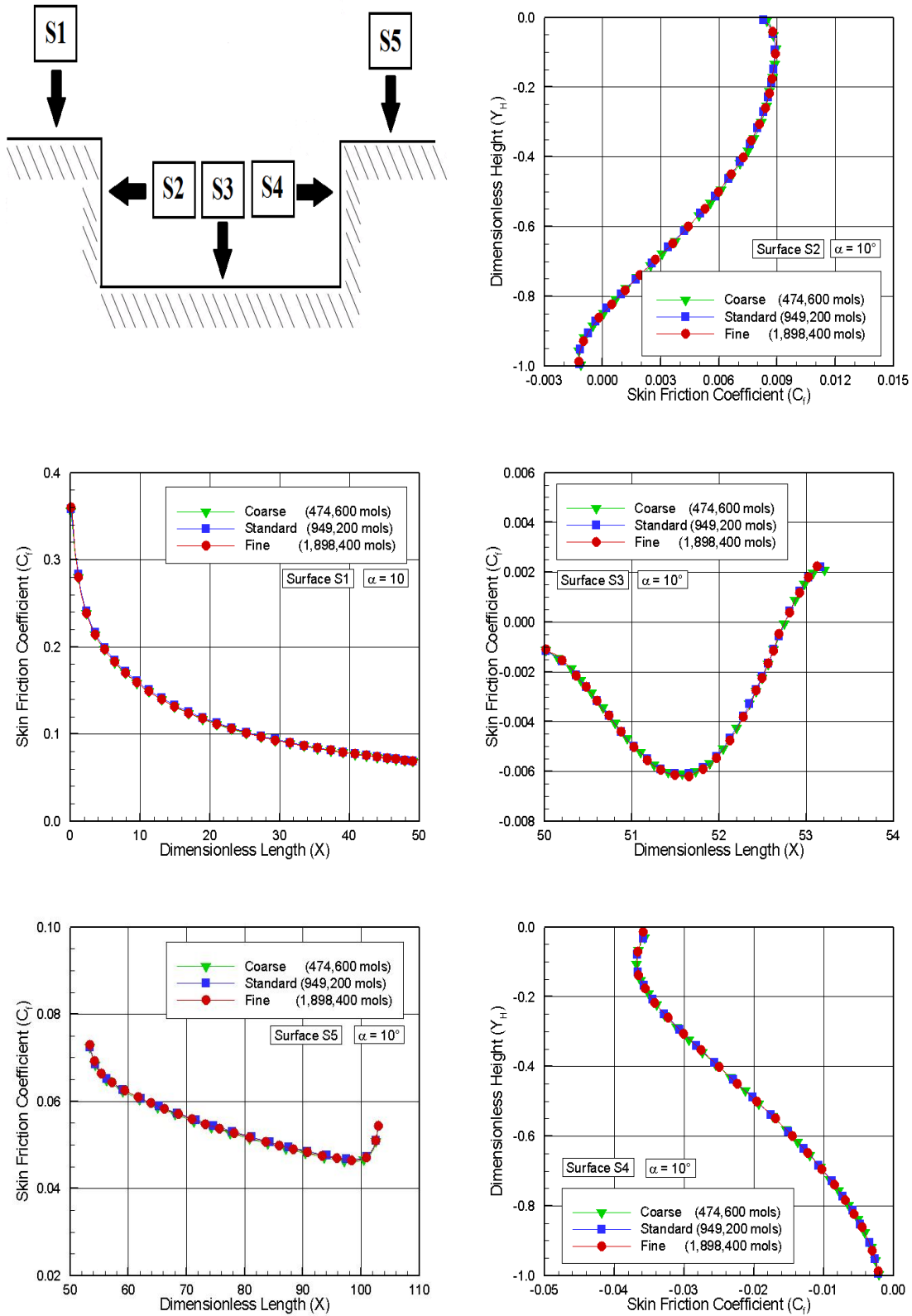


Figure 4.19 - Effect of variation in the number of molecules on pressure coefficient for $L/H = 1$ and $\alpha = 10$ deg.

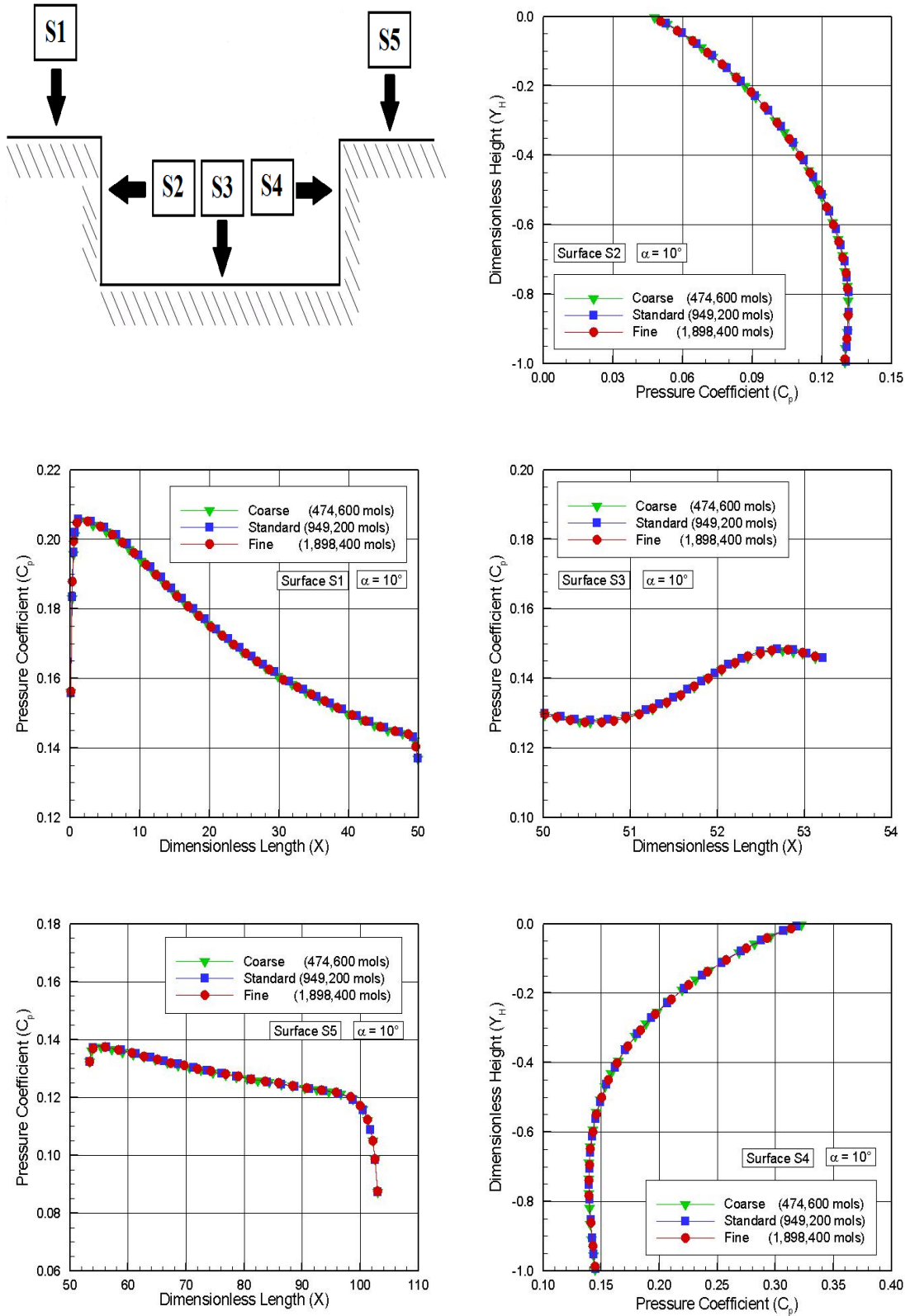


Figure 4.20 - Effect of variation in the number of molecules on heat transfer coefficient for $L/H = 1$ and $\alpha = 10$ deg.

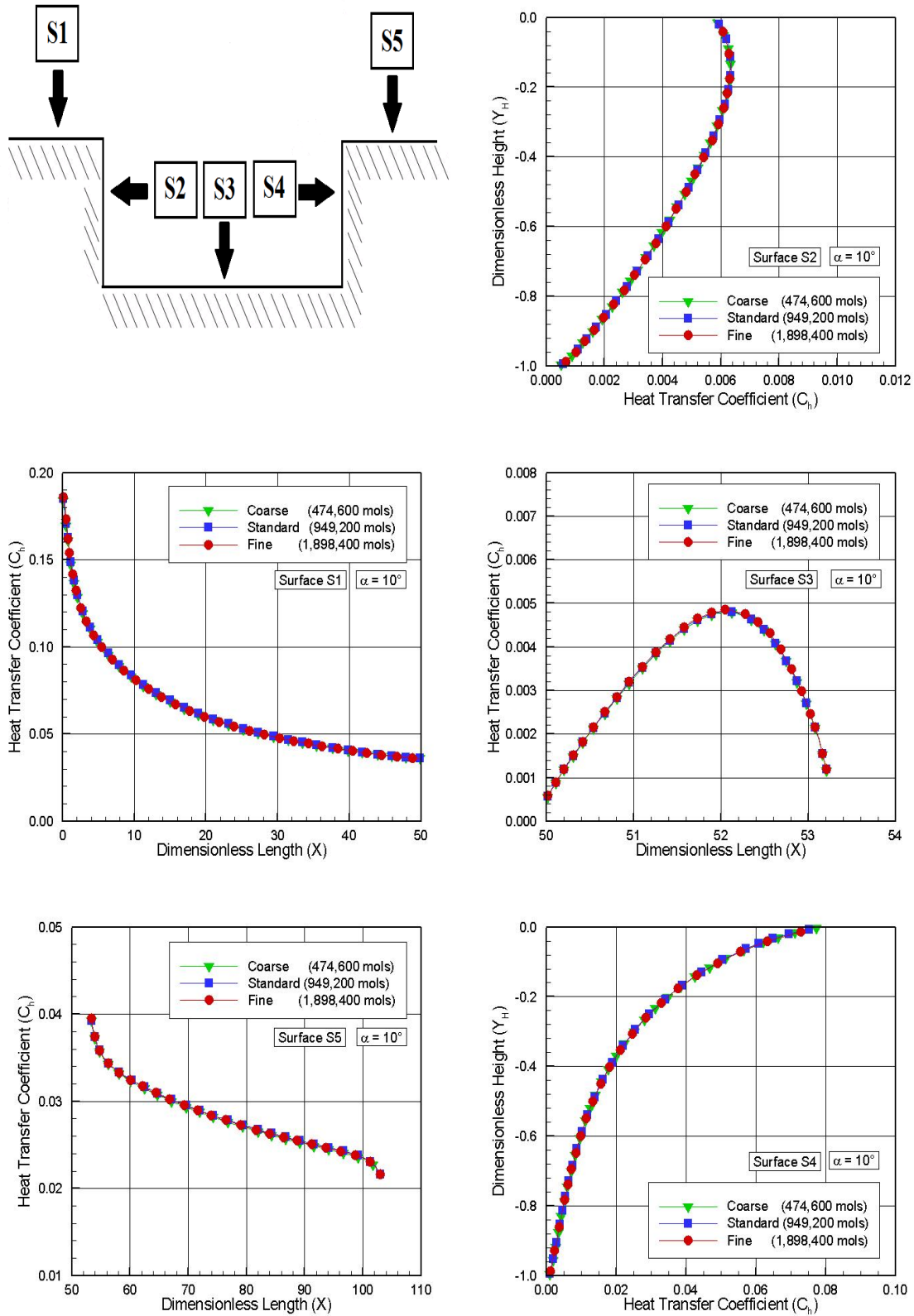
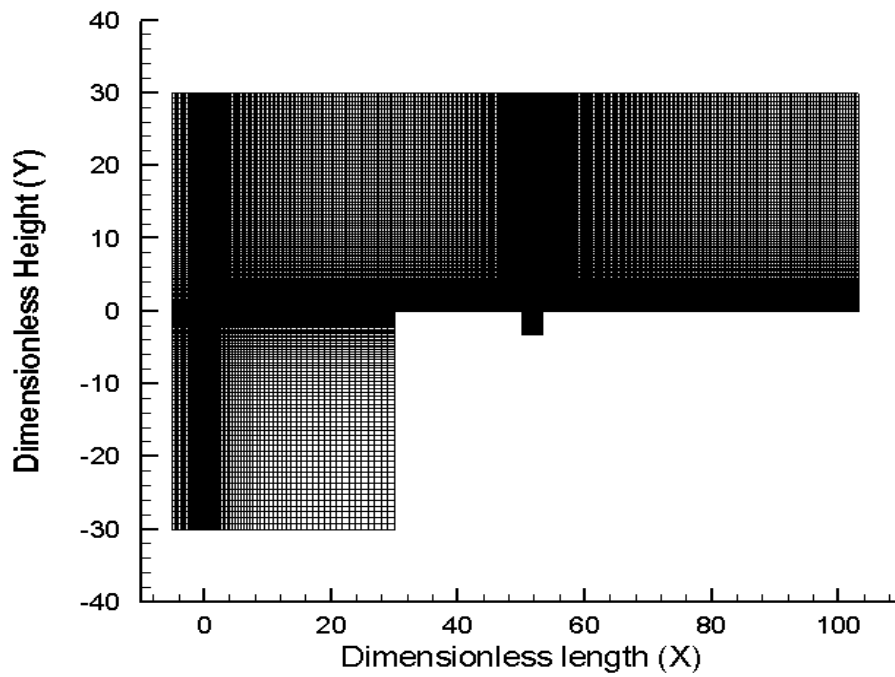
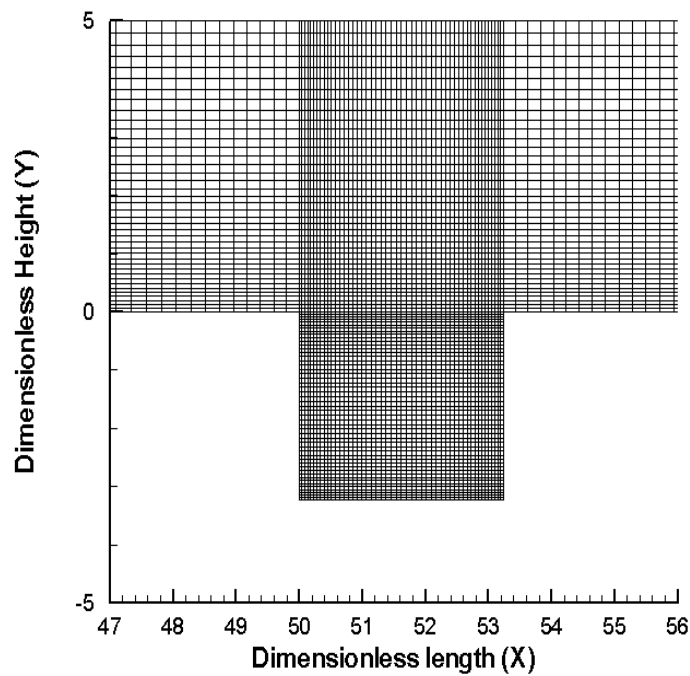


Figure 4.21 - A Drawing illustrating the cell distribution.



(a)



(b)

(a) The standard mesh for the gap configuration with $L/H = 1$ and 10-degree angle of attack, (b) A magnified view of region R5.

SOURCE: Author Production.

5 COMPUTATIONAL RESULTS AND DISCUSSIONS

Having computed flowfield properties over a wide range of simulation parameters, the attention is turned now to the analysis of the results. In doing so, the purpose of this Chapter is to discuss and to compare differences in the flowfield structure as well as in the aerodynamic surface quantities due to variations on cavity L/H ratio and on the angle of attack α .

5.1 Flowfield Structure

In order to present the DSMC results coherently, this section focuses on the calculations of the primary properties obtained from DSMC simulations. The primary properties of particular interest in this thesis are velocity, density, pressure and kinetic temperatures.

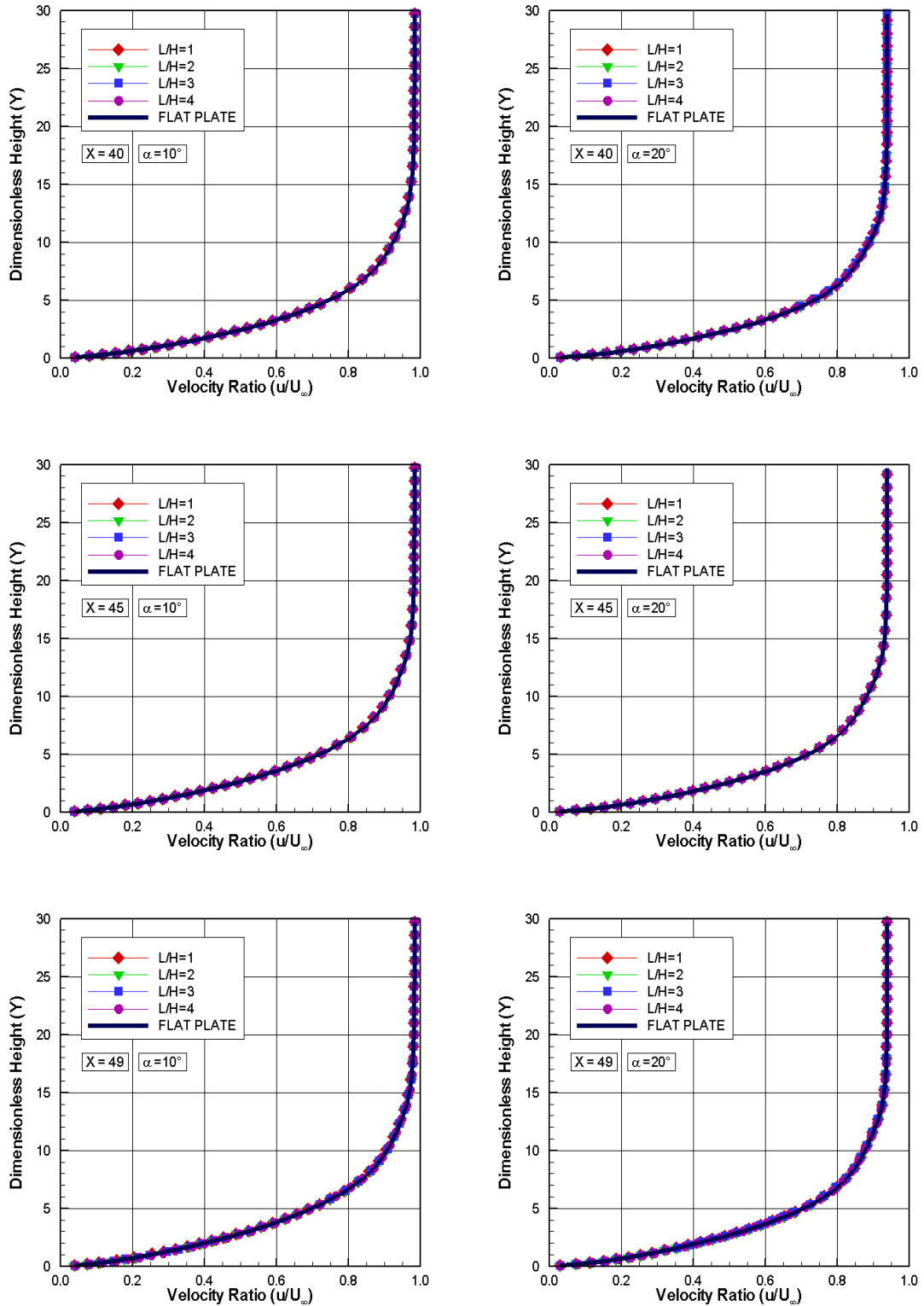
5.1.1 Velocity Field

Tangential velocity profiles for three sections along the cavity upstream surface, surface S1, are illustrated in Figure 5.1, parameterized by the cavity L/H ratio. In this set of plots, left- and right-column plots correspond to angle of attack of 10 and 20 degrees, respectively. Results for angle of attack of 15 degrees are intermediate, and they are not shown in this figure. In addition, the tangential velocity u is normalized by the freestream velocity U_∞ , X and Y stand, respectively, for the length x and the height y normalized by the mean free path λ_∞ . As a base of comparison, the tangential velocity profile for a flat plate without cavity is present in the same plots.

According to Figure 5.1, it is clearly seen that tangential velocity profiles for the cavities are identical to those for flat plates with the correspondent angle of attack α , indicating that the presence of cavities did not affect the flowfield upstream, for the condition investigated in this work. In addition, of particular interest is the magnitude of velocity at $Y=0$ for section X shown. It is also seen that the velocity ratio is not zero at the wall. There is a slip velocity, a characteristic of a rarefied flow. As a result, the condition $u/U_\infty = 0$, no-slip velocity, does not apply in a rarefied flow. It should be also observed that the tangential velocity $u \rightarrow U_\infty$ as $Y \rightarrow \infty$. Therefore, because of the flow incidence, U_∞ varies as a function of the angle of attack, $u \rightarrow U_\infty \cos\alpha$ as $Y \rightarrow \infty$. As a result U_∞ decreases with increasing the angle of attack, as shown in the plots.

As a base of comparison, it becomes instructive to examine the differences in the

Figure 5.1 - Tangential velocity ratio (u/U_∞) profiles for three sections along surface S1 parameterized by the cavity L/H ratio. Left and right columns correspond to angle of attack α of 10 and 20 degrees, respectively.



tangential velocity profiles due the angle-of-attack effect. In this fashion, Figure 5.2 displays the tangential velocity profiles for the same three sections along surface S1, parameterized by the angle of attack α . In this set of plots, left- and right-column plots correspond to cavity L/H ratio of 1 and 4, respectively. Result for L/H ratio of 2 and 3 are intermediate, and they will not be shown. It should be mentioned in this context that results for zero-degree angle of attack in these plots were obtained earlier by Palharini (PALHARINI, 2010).

On examining Figure 5.2, it is apparent that the flow decelerates as the angle of attack increases. By increasing the angle of attack, the body geometry changes aerodynamically from a sharp body to a blunt body for the oncoming flow. As a result, the geometry becomes less streamlined. In addition, as expected, by increasing the angle of attack, $u/U_\infty < 1$ as $Y \rightarrow \infty$, i.e., as Y tends to the outer border of the computational domain, since the tangential velocity u tends to $U_\infty \cos\alpha$.

Another interesting characteristic in these plots is the similarity of the velocity profiles along the body surface. This is an indication that the velocity profiles may be expressed in terms of functions that, in appropriate coordinates, may be independent of one of the coordinate directions. However, no attempts have been done to find such functions.

In the following, tangential velocity profiles along three sections on the cavity floor, surface S3, are demonstrated in Figure 5.3, parameterized by the cavity L/H ratio. In this group of plots, left- and right-column plots correspond to angle of attack of 10 and 20 degrees, respectively. In addition X'_L represents the distance $(x - L_u)$ normalized by the cavity length L , and Y_H stands for the height y normalized by the cavity height H . In this framework, sections X'_L of 0.25, 0.50 and 0.75 correspond, respectively, to sections located close to the cavity backward face, in the middle of the cavity, and at the vicinity of the cavity forward face.

Based on this group of plots, it is observed that the tangential velocity ratio is negative at the bottom of the cavity, at section $Y_H = -1$, it increases in the upward direction, and becomes positive at the top of the cavity, at section $Y_H = 0$. Outside of the cavity, the tangential velocity ratio continues to increase, as shown in Figure 5.4, up to reach the maximum value close to the upper boundary of the computational domain. In addition, it is also observed that, by increasing the angle of attack from 10 to 20 degrees, tangential velocity ratio becomes more negative close to the cavity bottom surface, and the station where the velocity changes from negative to positive values occurs closer to the top of the cavity, for the cavity L/H ratio investigated.

Figure 5.2 - Tangential velocity ratio (u/U_∞) profiles for three sections along surface S1 parameterized by the angle of attack. Left and right columns correspond to cavity L/H ratio of 1 and 4, respectively.

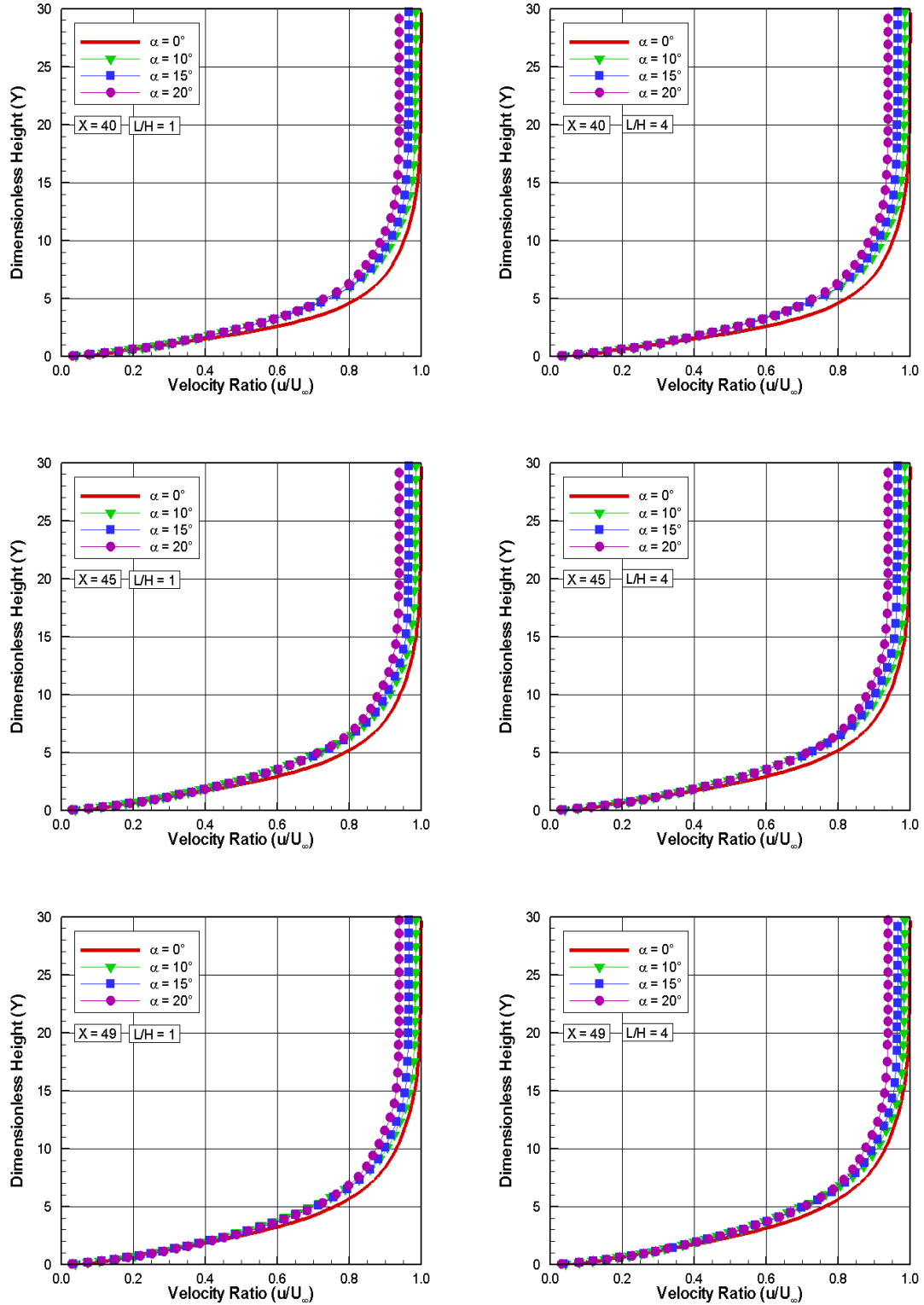


Figure 5.3 - Tangential velocity ratio (u/U_∞) profiles for three sections along surface S3 parameterized by the cavity L/H ratio. Left and right columns correspond to angle of attack α of 10 and 20 degrees, respectively.

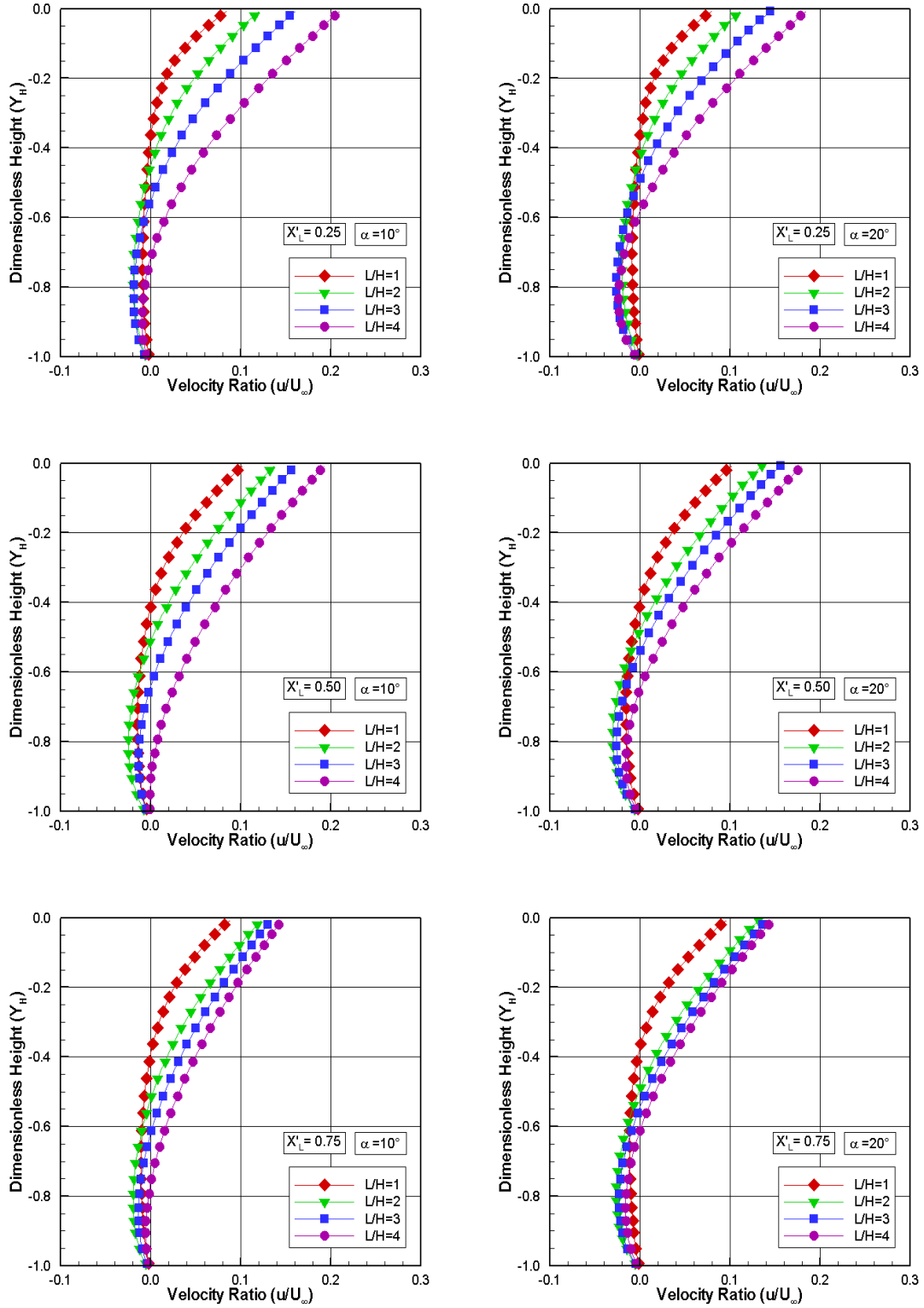


Figure 5.4 - Tangential velocity ratio (u/U_∞) profiles for three sections along surface S3 outside the cavity parameterized by the cavity L/H ratio. Left and right columns correspond to angle of attack α of 10 and 20 degrees, respectively.

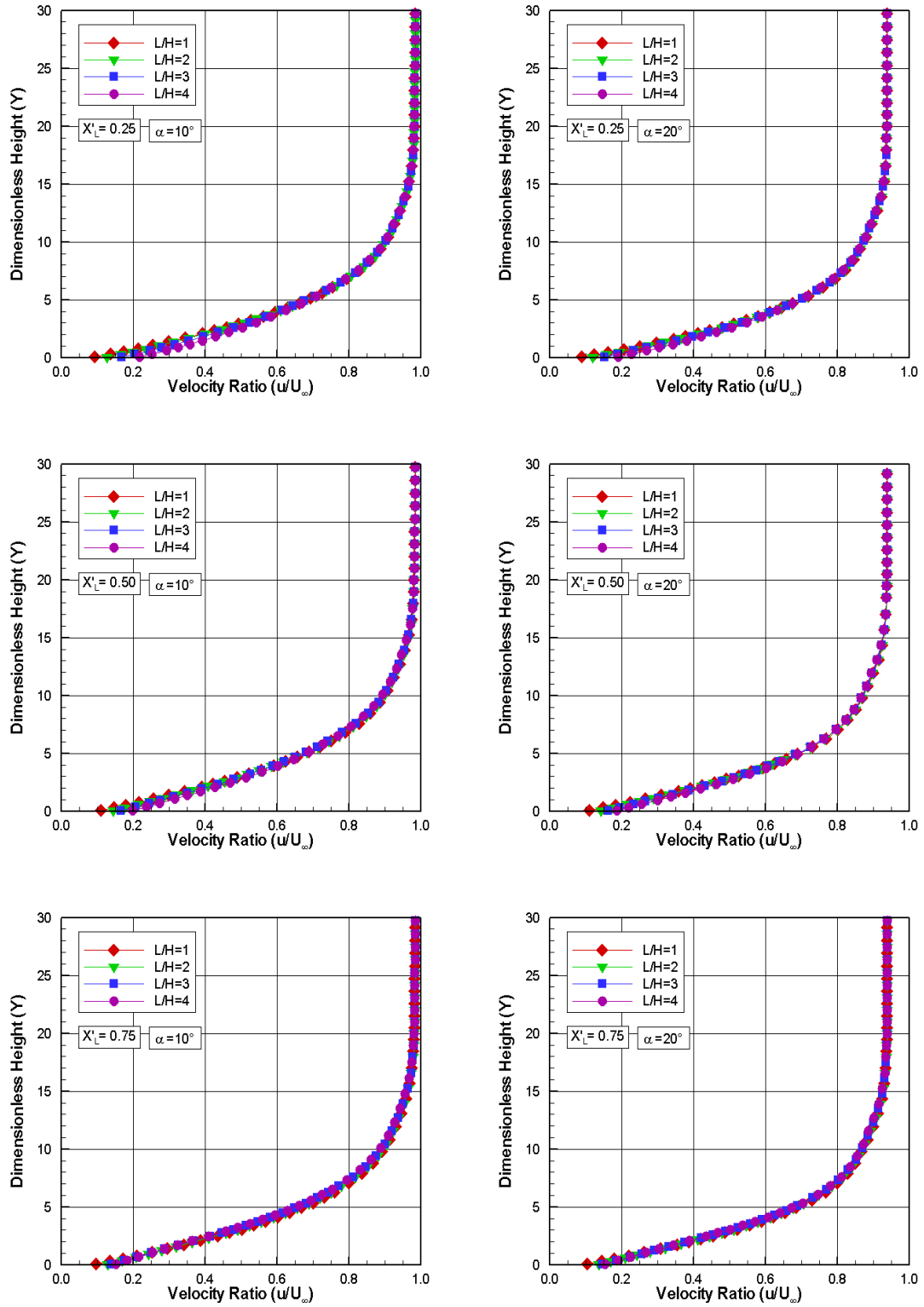
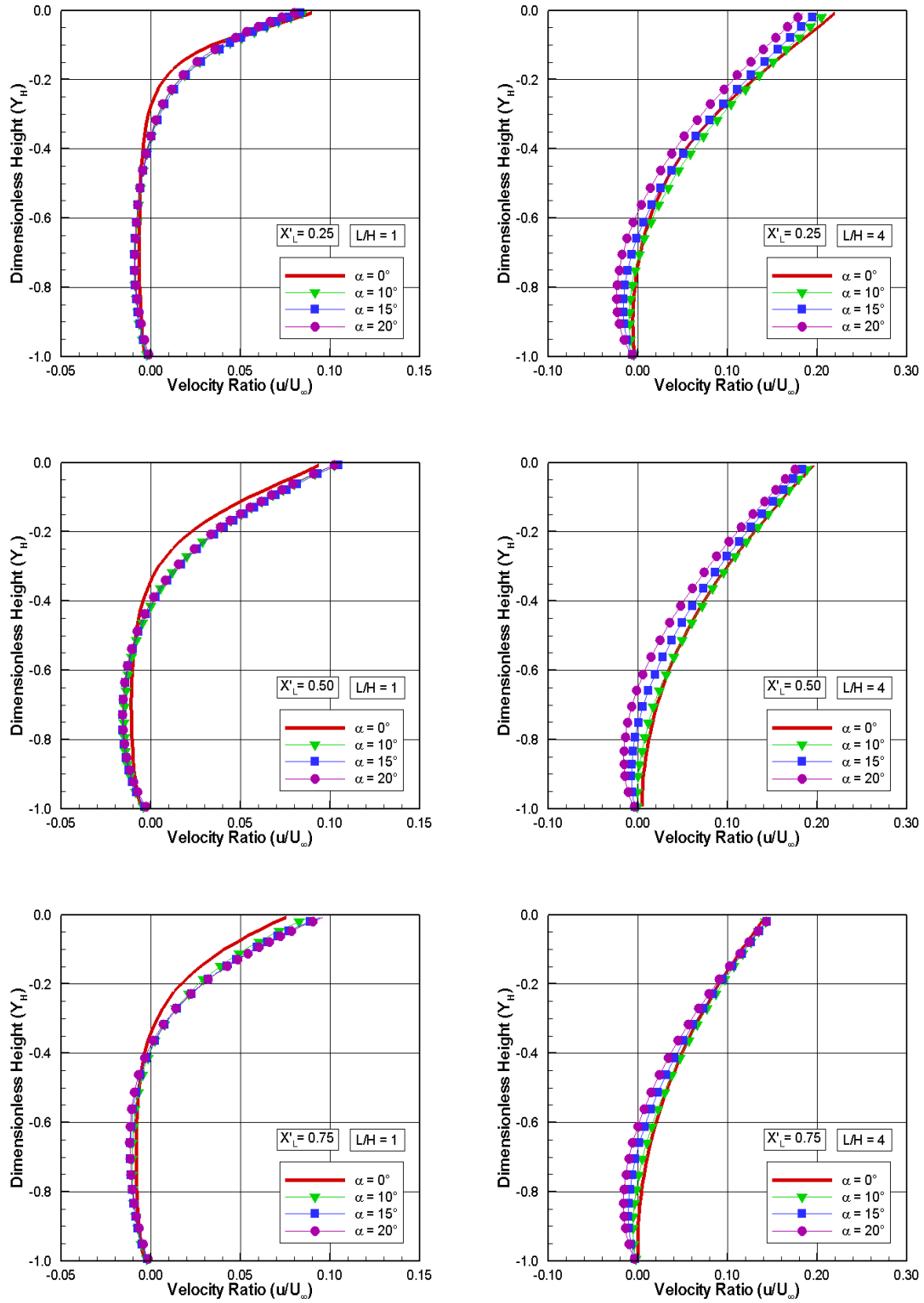


Figure 5.5 - Tangential velocity ratio (u/U_∞) profiles for three sections along surface S3 parameterized by the angle of attack α . Left and right columns correspond to cavity L/H ratio of 1 and 4, respectively.



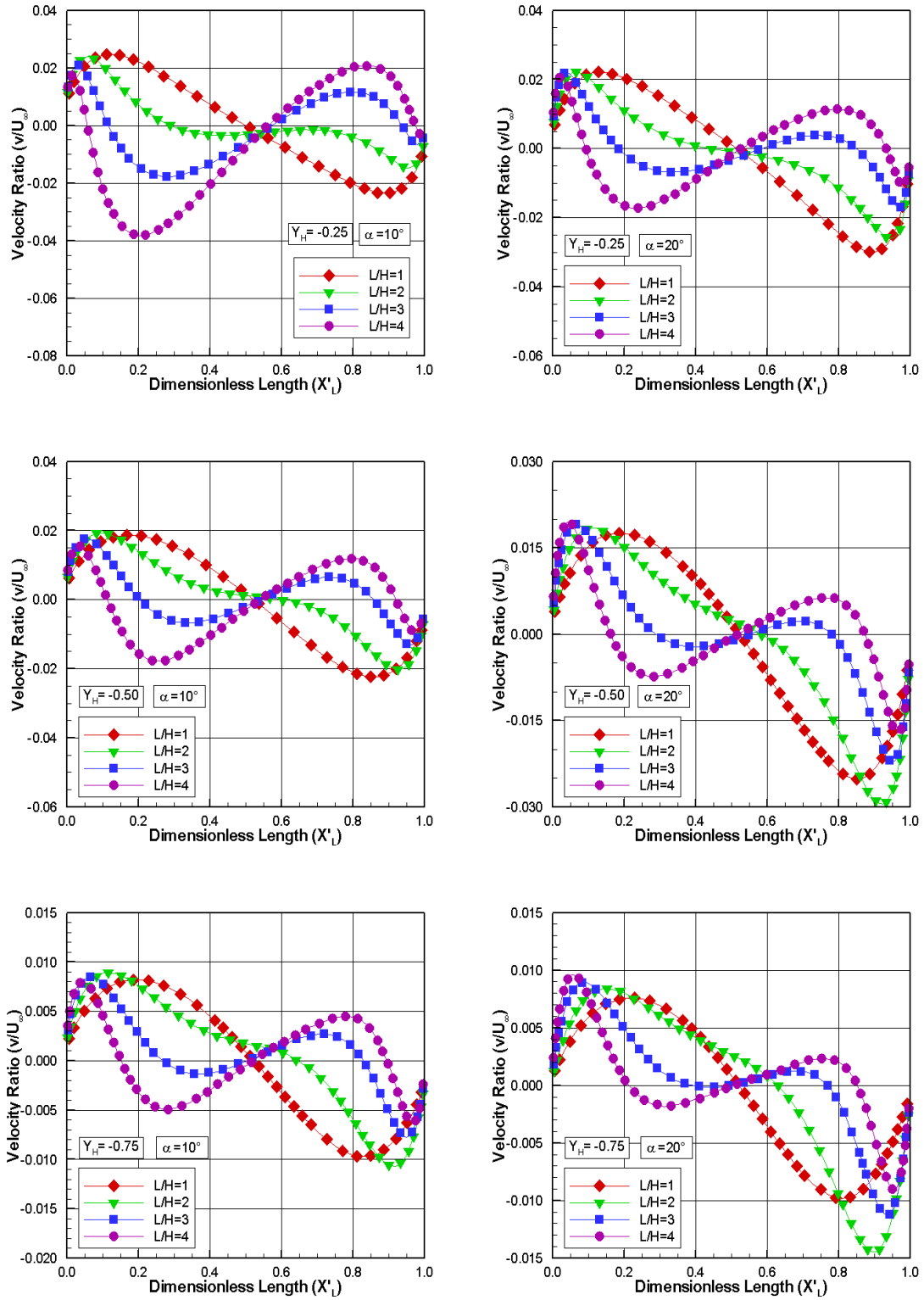
Still referring to this group of plots, it is seen that, for section $X'_L = 0.25$, the location (station Y_H) where tangential velocity ratios changes from negative to positive values is close to the top of the cavity in comparison to that for section $X'_L = 0.75$. Therefore, the separated boundary layer increases with increasing L/H ratio as well as with increasing the angle of attack α .

An understanding of the angle of attack effect on the tangential velocity inside the cavity can be gained by analyzing Figure 5.5. This figure displays the tangential velocity ratio for three sections along the cavity floor parameterized by the angle of attack α . In these plots, left and right columns corresponds to cavity L/H ratio of 1 and 4, respectively.

On examining Figure 5.5, it is quite apparent that tangential velocity is very low inside the cavity as compared to the freestream velocity. The maximum value takes place at the top of the cavity. For the cavity L/H ratio of 1, the tangential velocity ratio u/U_∞ slightly increases with the angle of attack rise in the up-most portion of the cavity. In contrast, for the cavity L/H ratio of 4, u/U_∞ slightly decreases with increasing the angle of attack. For comparison purpose, at section $X'_L = 0.25$ and zero-degree angle of attack, the tangential velocity ratio changes from positive to negative values at section Y_H of -0.2886, -0.4070, -0.5311 and -0.7665 for L/H ratio of 1, 2, 3, and 4, respectively. On the other hand, at section $X'_L = 0.25$ and 20-degree angle of attack, the velocity ratio changes from positive to negative values at section Y_H of -0.3641, -0.4280, -0.4918, and -0.5826, for L/H ratio of 1, 2, 3, and 4, respectively.

Normal velocity profiles inside the cavity are depicted in Figure 5.6 for three transversal sections as a function of the streamwise distance X'_L , parameterized by the cavity L/H ratio. In this set of diagrams, the normal velocity v is normalized by the freestream velocity U_∞ . In addition, the three sections correspond to transversal sections defined by the dimensionless height Y_H of -0.25, -0.50 and -0.75. Again, left- and right-column plots correspond to angle of attack of 10 and 20 degrees, respectively. According to this sets of plots, near the cavity backward face, $X'_L < 0.2$, the normal velocity profiles basically present positive values for the L/H cases investigated, meaning that the flow is moving upward. In contrast, at the vicinity of the forward face, $X'_L > 0.8$, the normal velocity profiles present negative values for $L/H < 3$, indicating that the flow is moving downward. Therefore, based on these two opposite behaviors for the normal velocity ratio, it may be recognized that there is a region of clockwise circulation flow.

Figure 5.6 - Normal velocity ratio (v/U_∞) profiles inside the cavity for three transversal sections as a function of the dimensionless length X'_L . Left and right columns correspond to angle of attack α of 10 and 20 degrees, respectively.



In what follows, Figures 5.7 and 5.8 reveal more clearly the angle-of-attack effects on the normal velocity profiles. In these figures, normal velocity ratio, v/U_∞ , is presented as a function of the streamwise distance X'_L , parameterized by the angle of attack α . It may be recognized from these plots that the effect of the angle of attack on the normal velocity depends on the cavity L/H ratio. In general, normal velocity increases, in absolute value, with increasing the angle of attack. In addition, this increase is more significant at the vicinity of the cavity forward face than that close to the cavity backward face. The reason for that is because the flow experiences an expansion at the vicinity of the cavity backward face and a compression at the vicinity of the cavity forward face.

Having a clear qualitative picture of the flow patterns in terms of tangential and normal velocities inside the cavities, it becomes instructive to highlight the effects of the L/H ratio and angle of attack α on the recirculation region within the cavities. In this fashion, streamlines trace inside the cavities are demonstrated in Figures 5.9, 5.10 and 5.11 for angle of attack of 10, 15 and 20 degrees, respectively. It is important to recall that streamline traces inside the cavities for zero-degree angle of attack, investigated by Palharini (PALHARINI, 2010), were displayed in Figure 1.5 in the introduction section.

On examining this set of plots, it is clearly noticed that the flow structure within the cavities is characterized by the appearance of recirculation regions. For L/H ratio of 1 and 2, streamlines patterns inside the cavities show that the flow structure is characterized by a primary vortex system regardless of the angle of attack investigated. For L/H ratio of 2, it is also noticed that the vortex core approached the cavity forward face. In addition, for these two cases, the vortex fills the entire cavity, and the flow behavior is similar to that observed for zero-degree angle of attack investigated earlier by Palharini (PALHARINI, 2010). Moreover, the flow behavior is also similar to that observed in an “open cavity” ($1 < L/H < 10$) in the continuum flow regime, as defined in Chapter 1.

Still examining this set of plots, for L/H ratio of 3, it is observed a different flow structure, i.e., two vortices are formed inside the cavities, one close to the backward face and another one to the cavity forward face. It is perhaps worth noting that, at least at first sight, these two vortices reduce to just one by increasing the angle of attack, for the conditions investigated. Also, it should be remarked that the external stream does not reach the bottom surface of the cavity. Finally, for L/H ratio of 4 and 10-degree angle of attack, the circulation region is well defined and similar to

Figure 5.7 - Normal velocity ratio (v/U_∞) profiles inside the cavity for three transversal sections as a function of the dimensionless length X'_L . Left and right columns correspond to cavity L/H ratio of 1 and 2, respectively.

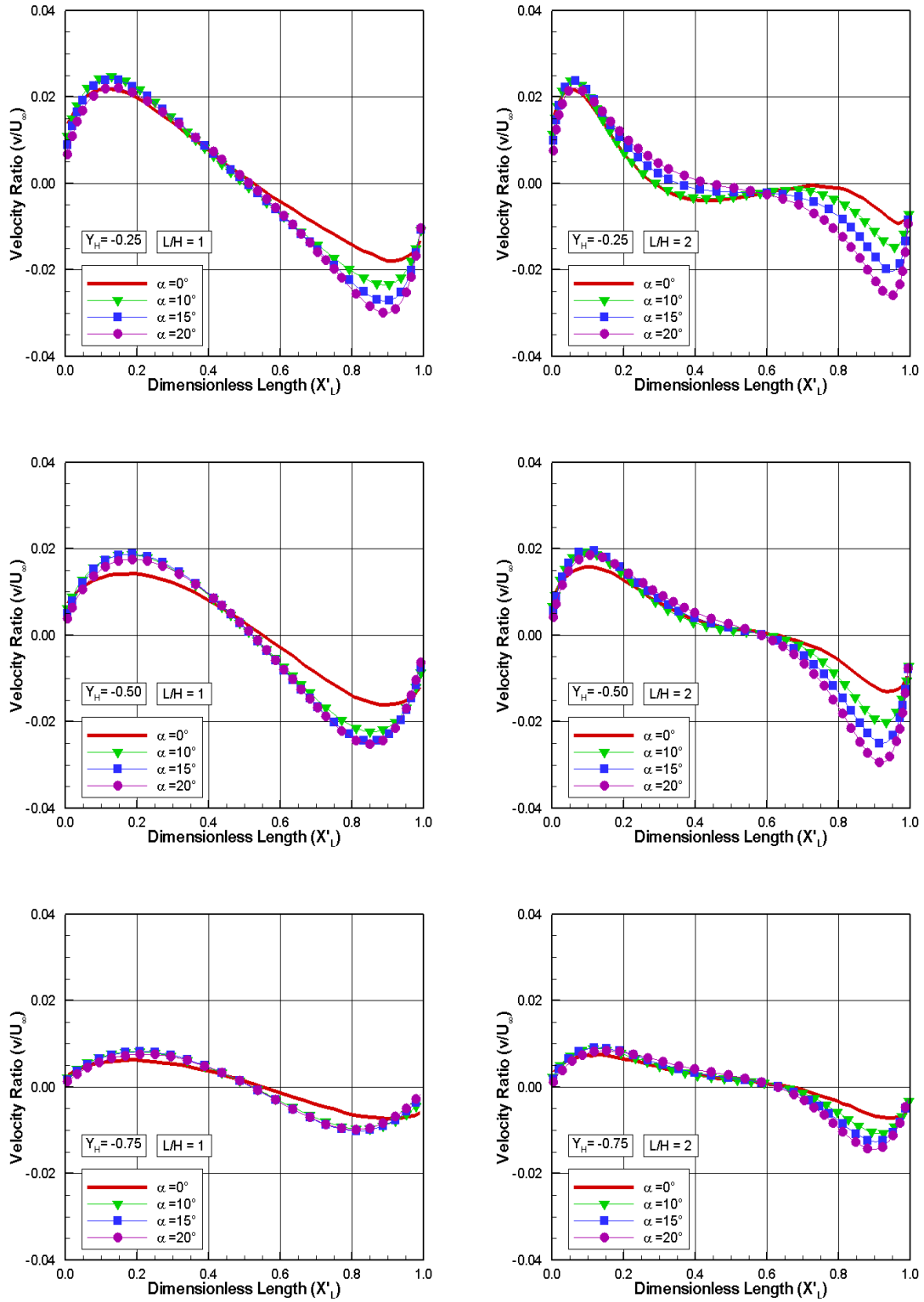


Figure 5.8 - Normal velocity ratio (v/U_∞) profiles inside the cavity for three transversal sections as a function of the dimensionless length X'_L . Left and right columns correspond to cavity L/H ratio of 3 and 4, respectively.

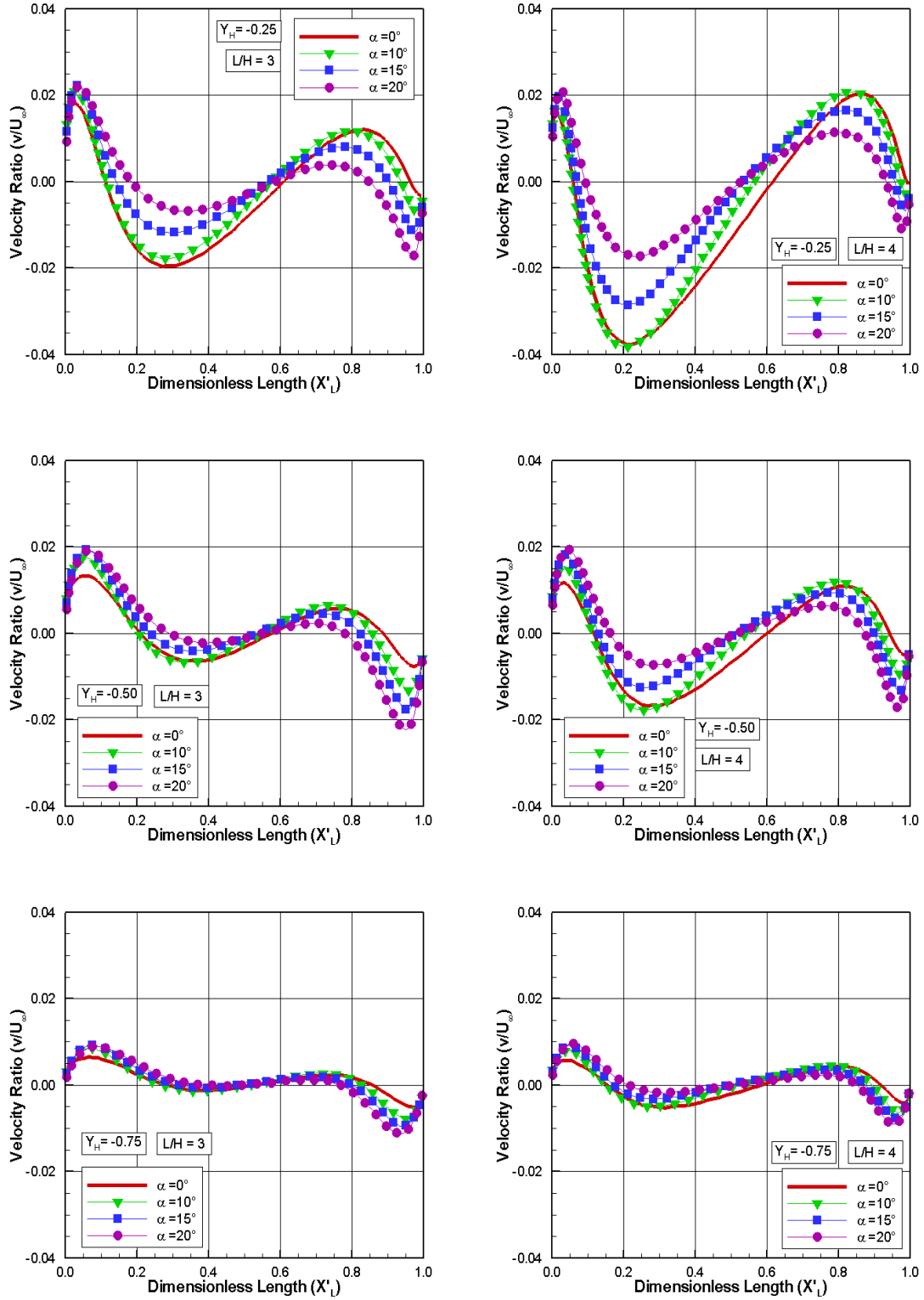


Figure 5.9 - Distribution of streamline traces inside the cavities for L/H ratio of 1, 2, 3, and 4 with 10-degree angle of attack.

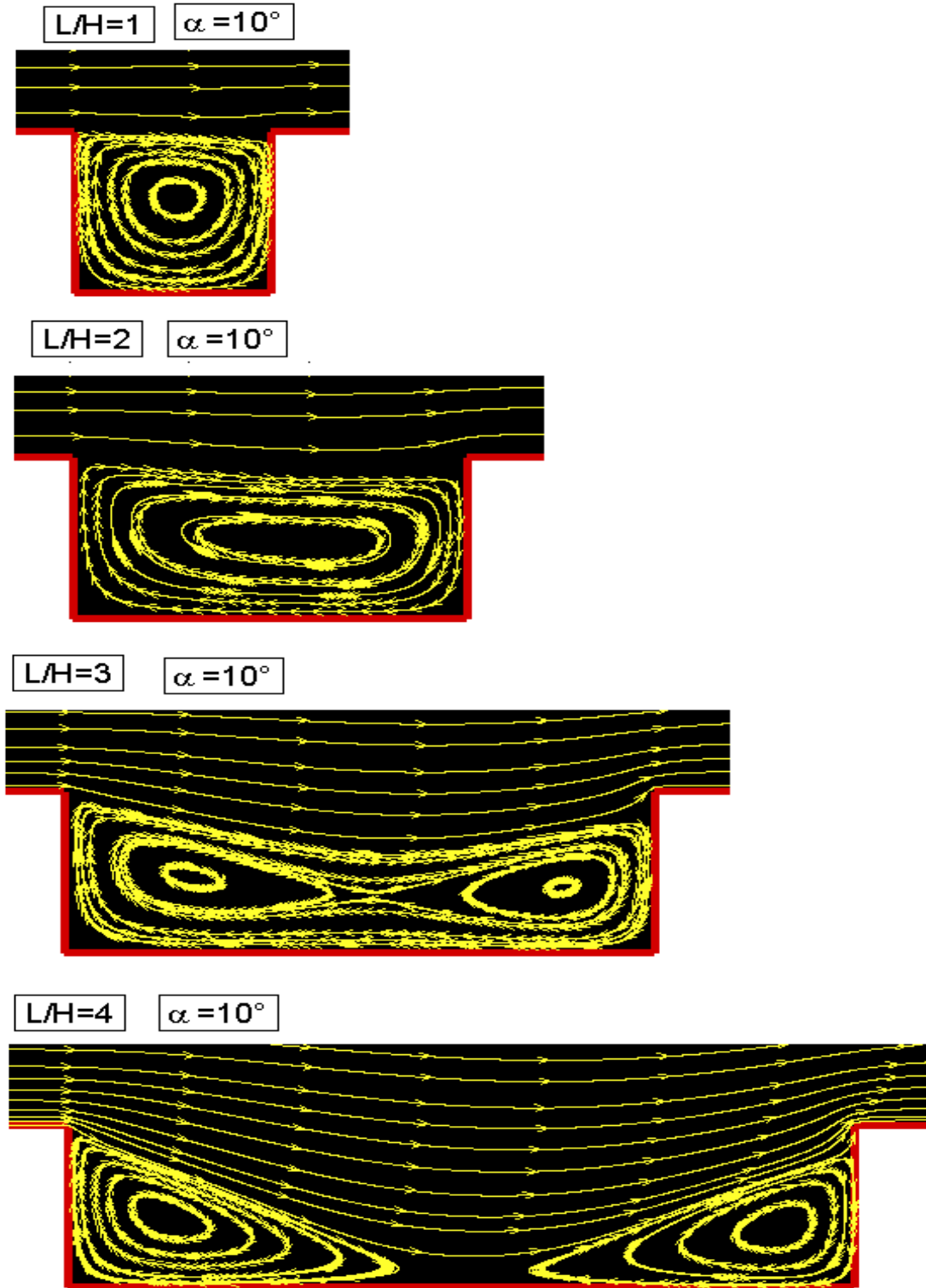


Figure 5.10 - Distribution of streamline traces inside the cavities for L/H ratio of 1, 2, 3, and 4 with 15-degree angle of attack.

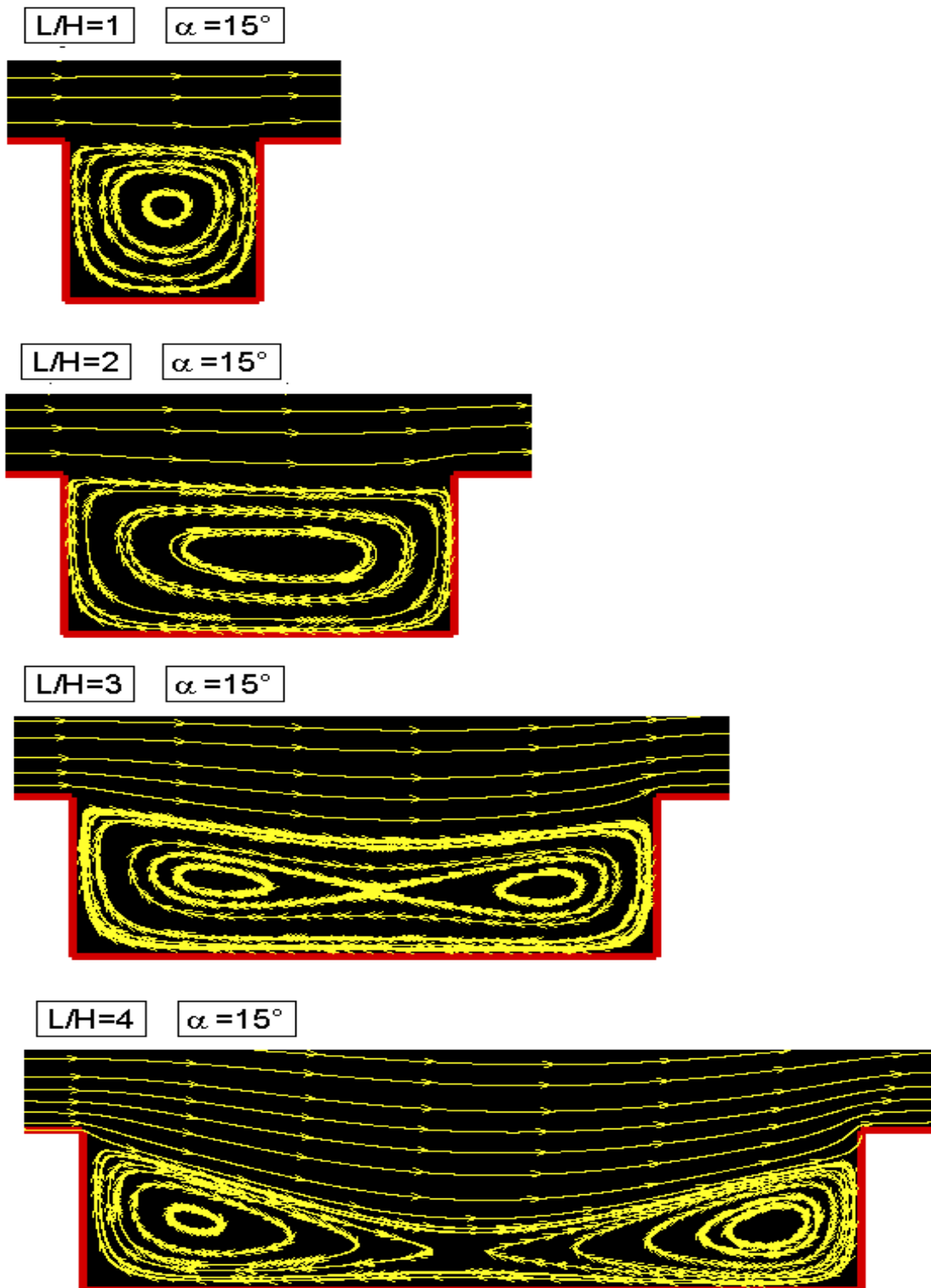
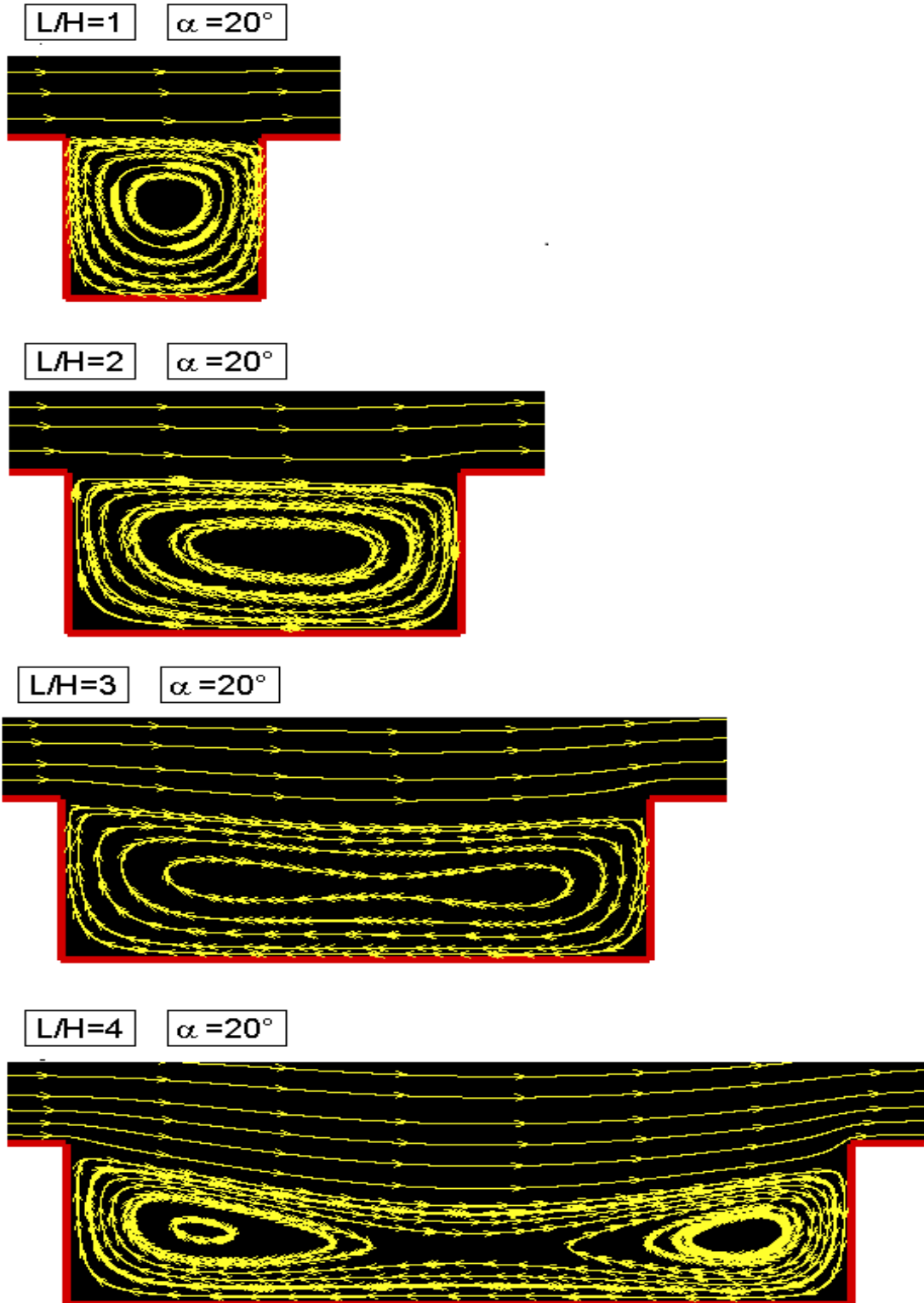


Figure 5.11 - Distribution of streamline traces inside the cavities for L/H ratio of 1, 2, 3, and 4 with 20-degree angle of attack.



that for zero-degree angle of attack (PALHARINI, 2010). Furthermore, for this case, the external stream reaches the bottom surface. This flow topology is similar to that observed for a “closed cavity” in the continuum flow regime, defined by $L/H > 14$. Nevertheless, by increasing the angle of attack, the external stream does not reach the bottom surface anymore, as observed for the $L/H < 4$, and the flow topology changes from “closed cavity” to “open cavity” .

In the results that follow, tangential velocity profiles for three sections along the cavity downstream surface, surface S5, are exhibited in Figure 5.12 parameterized by the cavity L/H ratio. In this set of plots, X_L'' stands for the distance $(x - L_u - L)$ normalized by the cavity downstream length L_d . Again, left- and right-column plots correspond to angle of attack of 10 and 20 degrees, respectively. In addition, for comparison purpose, the tangential velocity ratio profiles for the flat-plate case are presented in the same plots.

According to Figure 5.12, it is seen that tangential velocity profiles for the cavities are identical to those for flat plates with the correspondent angle of attack, indicating that the presence of cavities did not affect the flowfield far downstream, for the conditions investigated in this work. This domain of influence is confined in a small region close to the cavity corners. In addition, similar to the tangential velocity profiles on surface S1, the tangential velocity ratio is not zero at the wall, there is a slip velocity, a characteristic of a rarefied flow.

Tangential velocity profiles for the same three sections along surface S5 are demonstrated in Figure 5.13, parameterized by the angle of attack α . Based on these plots, no significant effects are noticed in the tangential velocity profiles in these sections due to variations on the angle of attack. However, as expected, by increasing the angle of attack, $u/U_\infty < 1$ as $Y \rightarrow \infty$, i.e., as Y tends to the other border of the computational domain, since the tangential velocity u tends to $U_\infty \cos\alpha$.

Finally, having a clear qualitative picture of the flow patterns in the cavities, it becomes instructive to present the distribution of the Mach number along with streamline traces inside the cavities. In doing so, Figures 5.14, 5.15 and 5.16 illustrate the distribution of Mach number along with streamline traces for angle of attack of 10, 15 and 20 degrees, respectively.

Figure 5.12 - Tangential velocity ratio (u/U_∞) profiles for three sections along surface S5 parameterized by the L/H ratio. Left and right columns correspond to angle of attack α of 10 and 20 degrees, respectively.

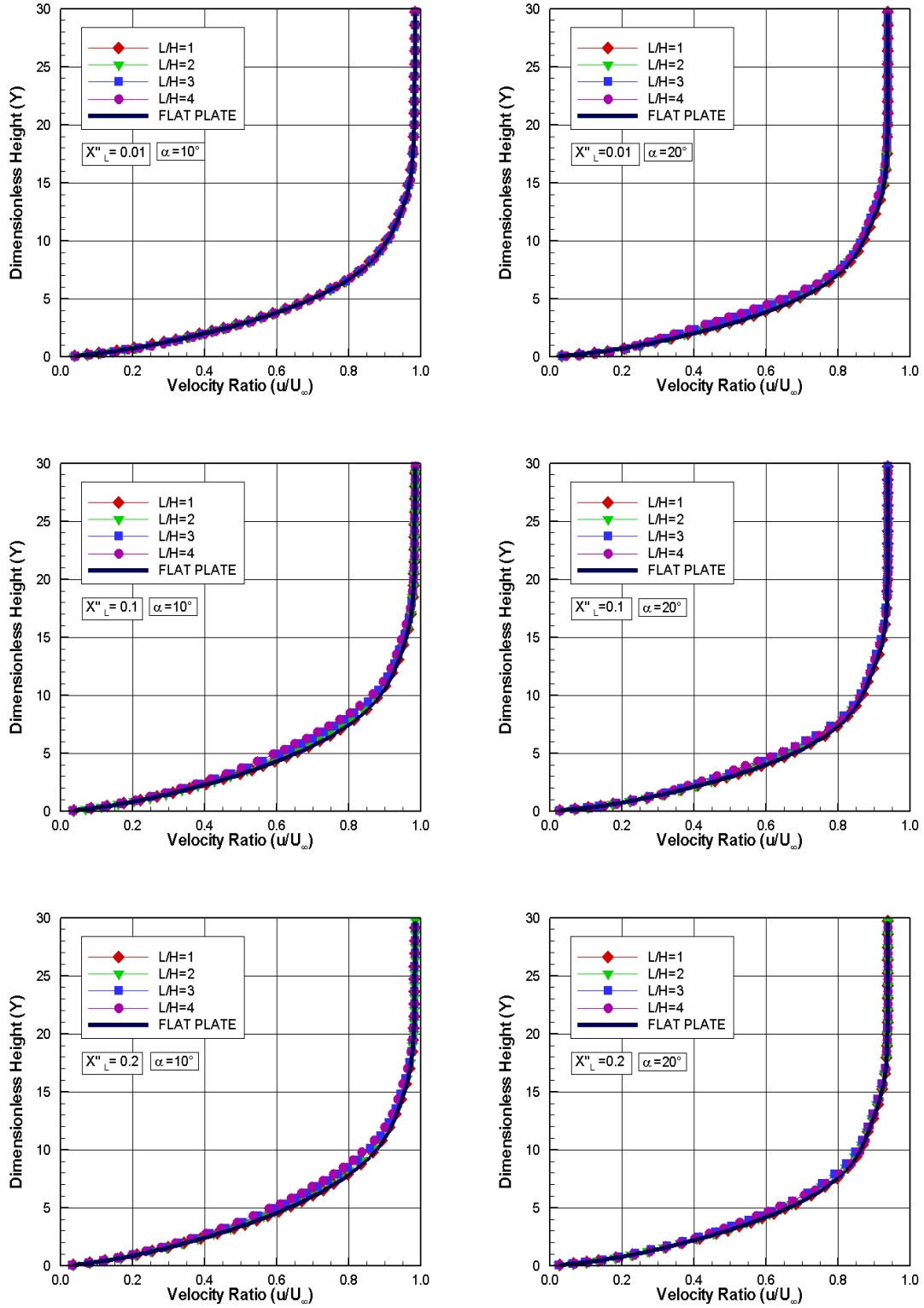


Figure 5.13 - Tangential velocity ratio (u/U_∞) profiles for three sections along surface S5 parameterized by the angle of attack α . Left and right columns correspond to cavity L/H ratio of 1 and 4, respectively.

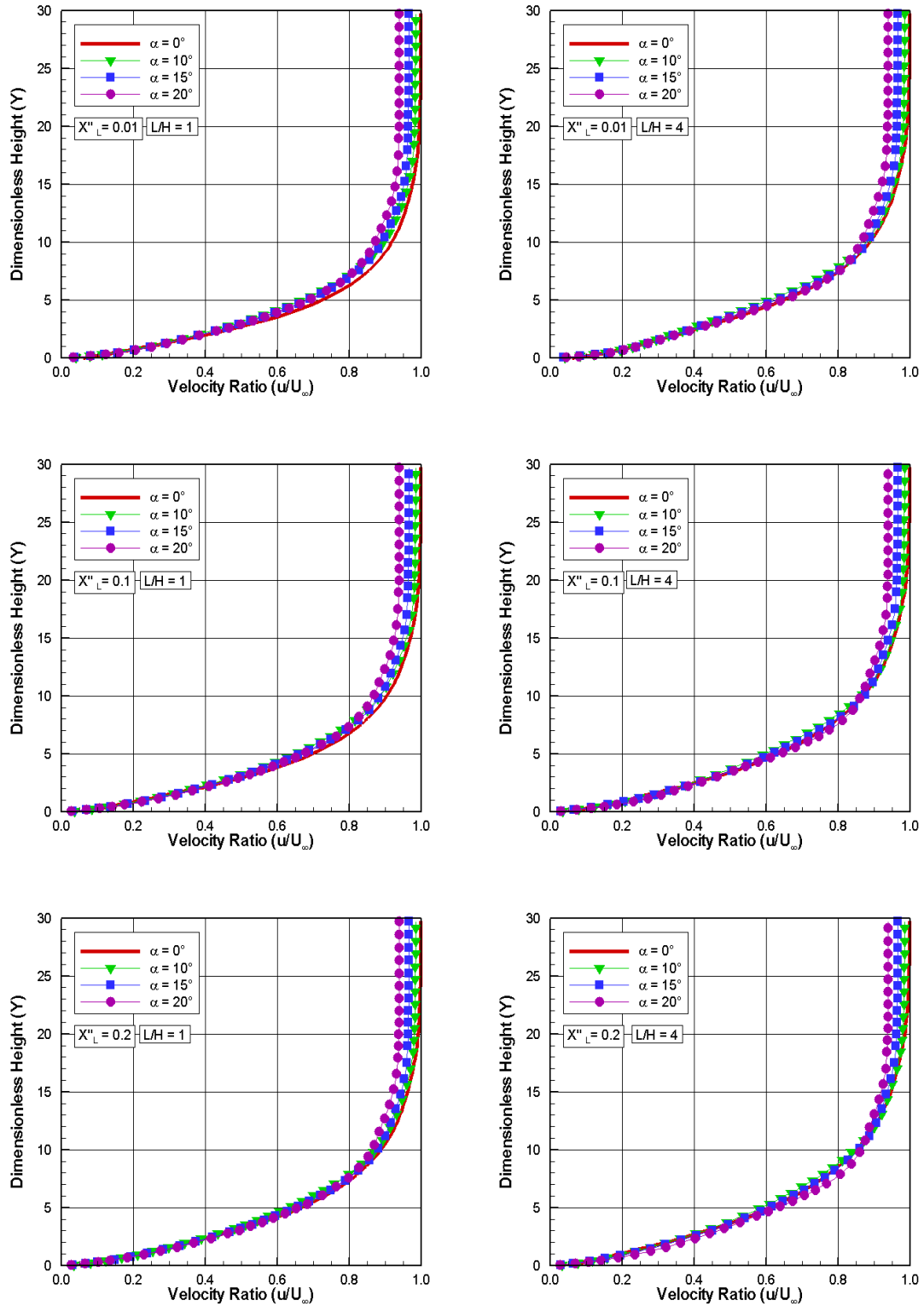


Figure 5.14 - Distribution of Mach number along with streamline traces inside the cavity for L/H ratio of 1 (top), 2, 3, and 4 (bottom), with angle of attack $\alpha = 10^\circ$ degrees.

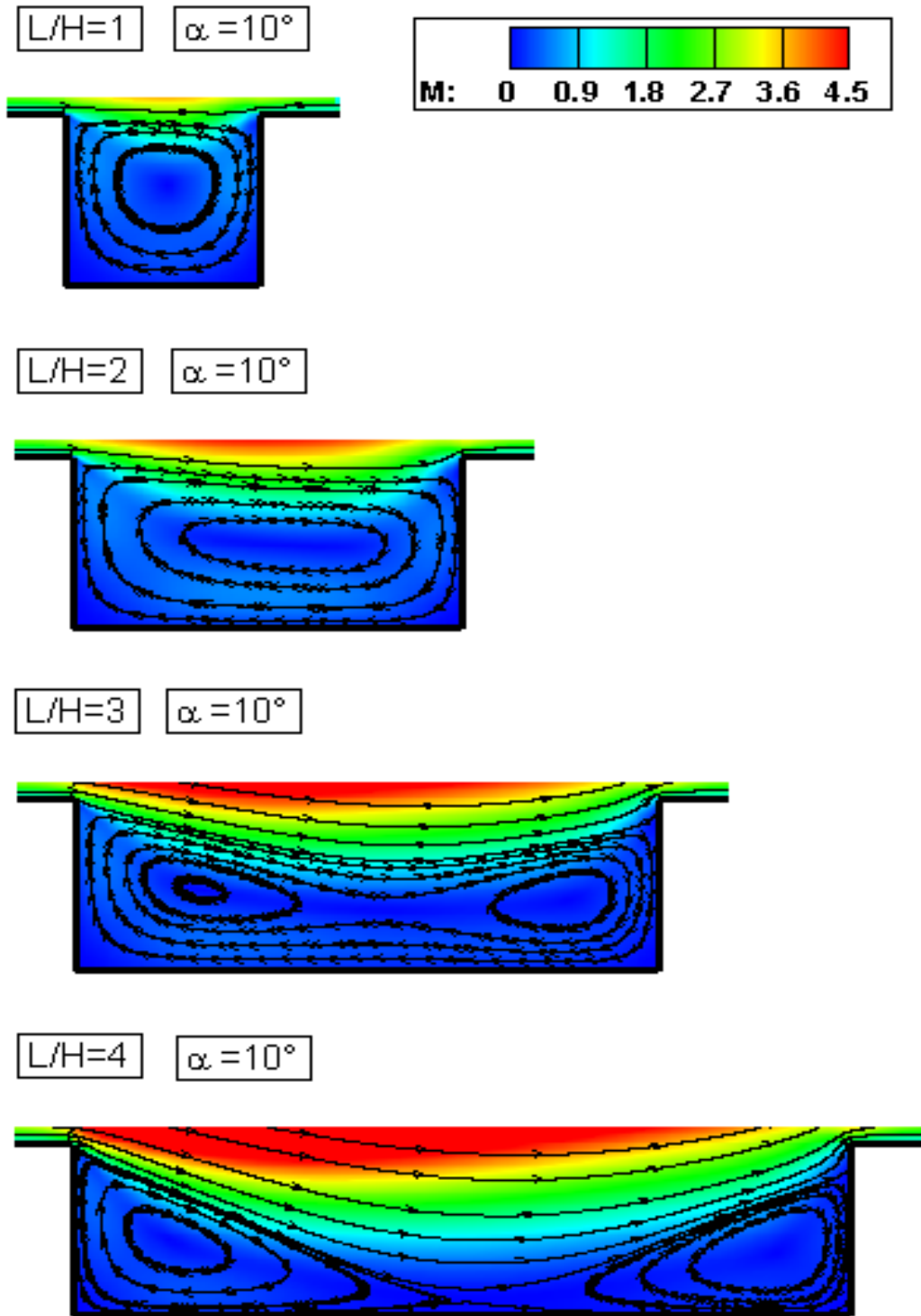


Figure 5.15 - Distribution of Mach number along with streamline traces inside the cavity for L/H ratio of 1 (top), 2, 3, and 4 (bottom), with angle of attack $\alpha = 15$ degrees.

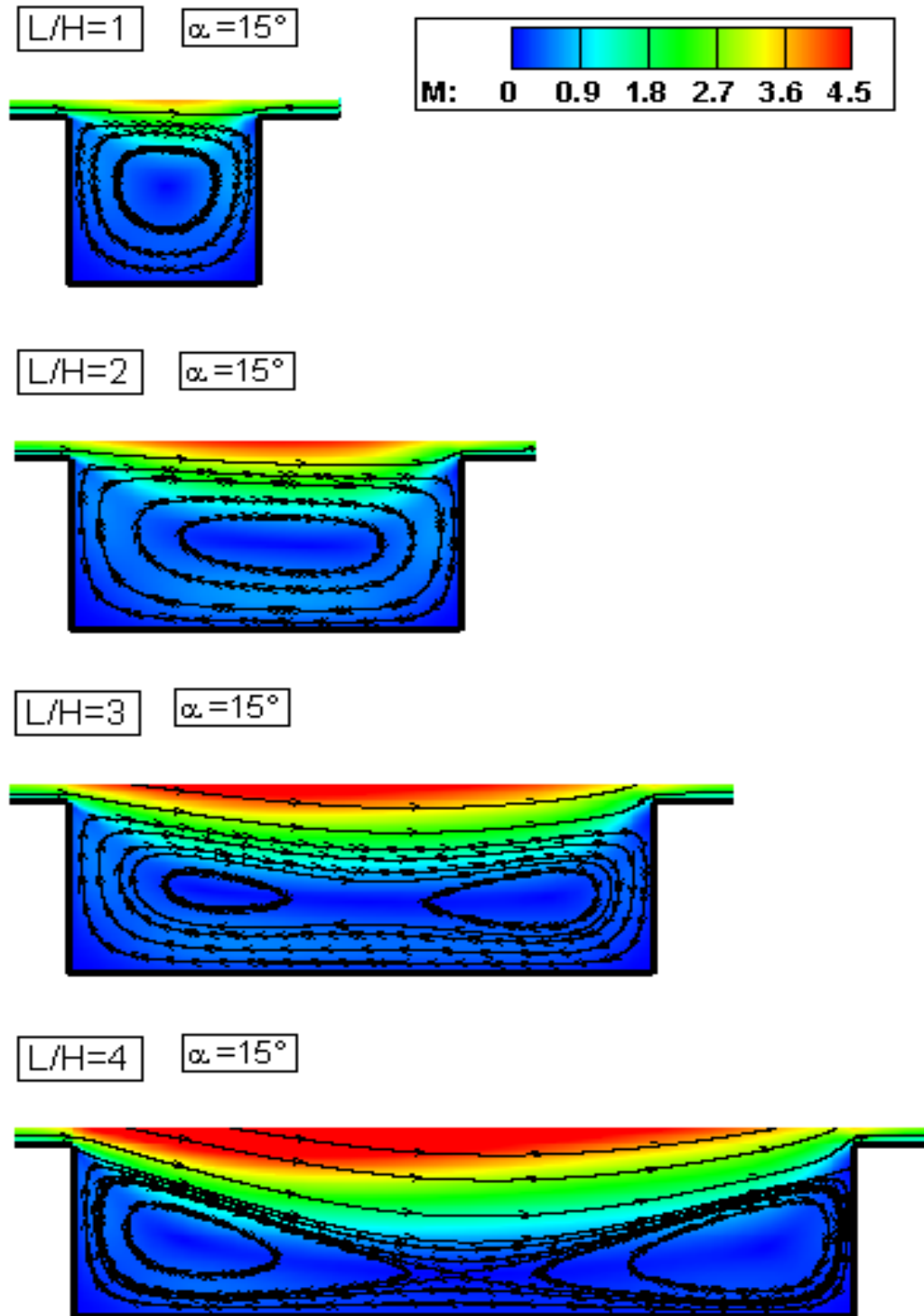
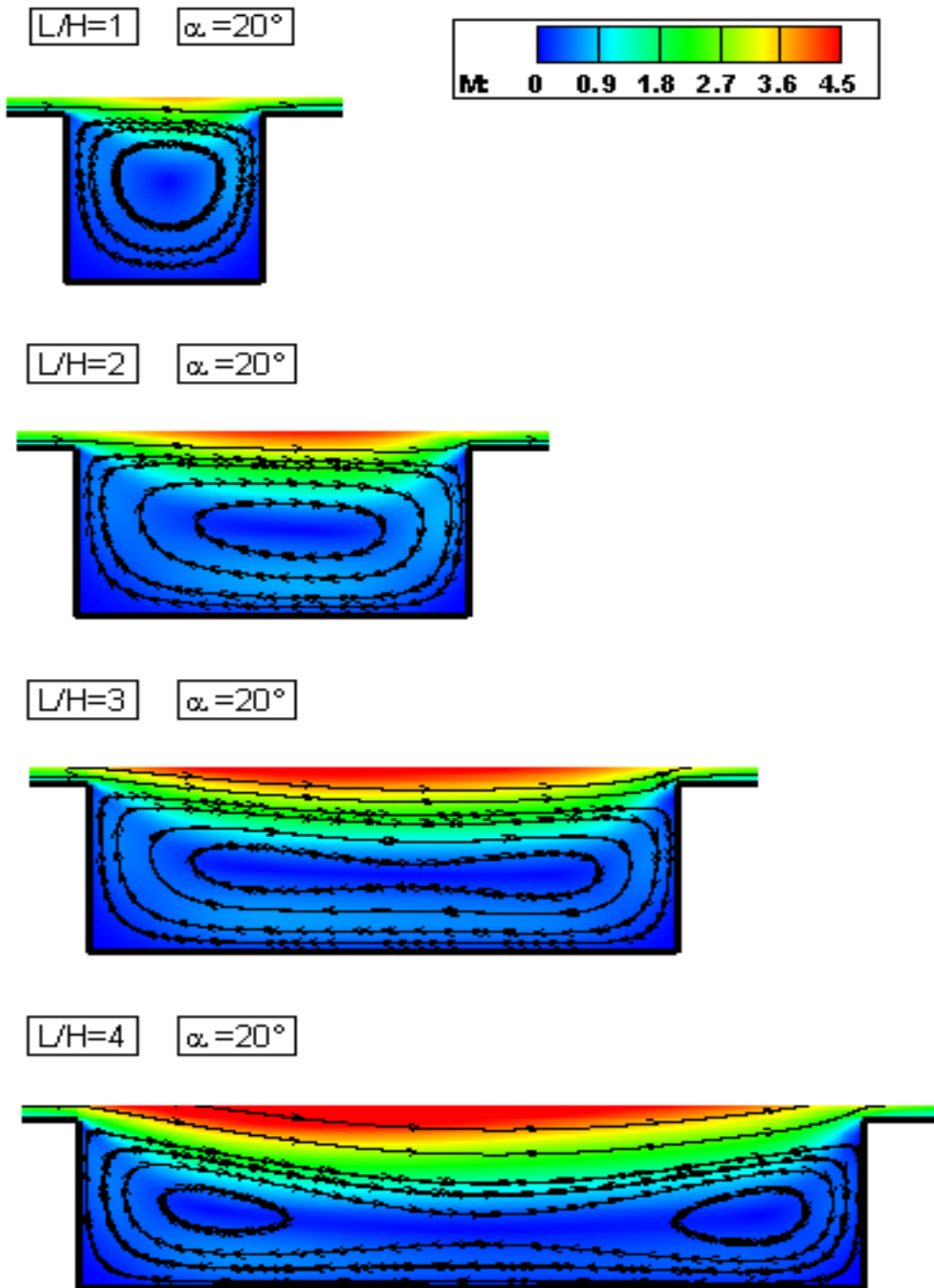


Figure 5.16 - Distribution of Mach number along with streamline traces inside the cavity for L/H ratio of 1 (top), 2, 3, and 4 (bottom), with angle of attack $\alpha = 20$ degrees.



5.1.2 Density Field

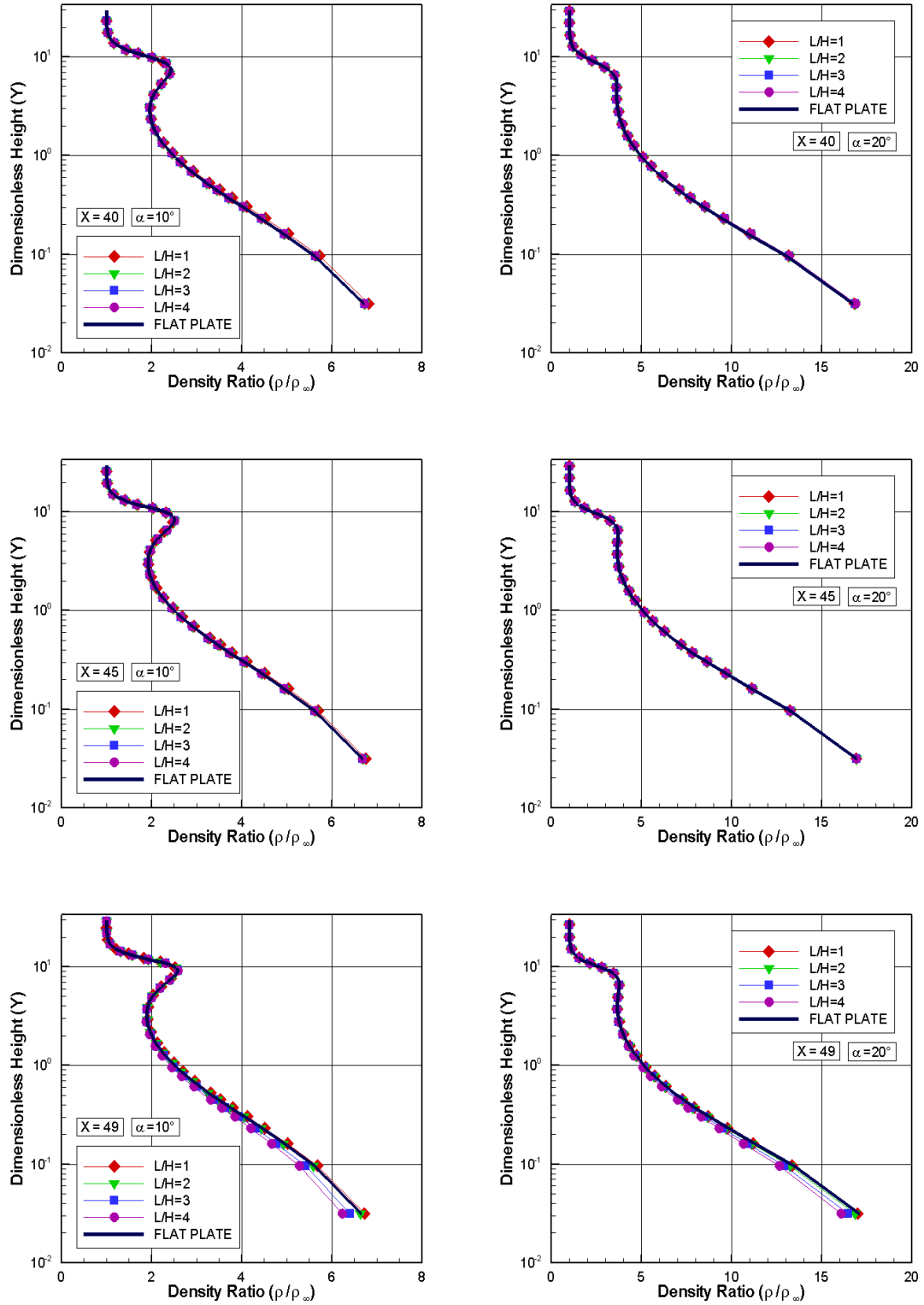
Effects on the density profiles due to changes on L/H ratio for three sections along cavity upstream surface, surface S1, are illustrated in Figure 5.17. In this set of plots, the density ρ is normalized by the freestream density ρ_∞ . Also, X and Y stand, respectively, for the length x and the height y normalized by the mean free path λ_∞ . In addition, left- and right-column plots correspond to angle of attack of 10 and 20 degrees, respectively. Again, results for 15-degree angle of attack are intermediate, and they are not shown in these plots. Furthermore, as a base of comparison, density ratio profiles for the flat-plate case are presented in the same plots.

Based on Figure 5.17, it is noticed that, similar to tangential velocity profiles, density ratio profiles for the cavity L/H ratio and angle of attack α investigated are basically identical to those for the flat-plate cases for sections $X \leq 45$, indicating that the presence of the cavity does not influence the flowfield far upstream the cavity. However, at the vicinity of the cavity, for section $X = 49$, density ratio profiles for the cavities are slightly different from those for the flat-plate cases close to the wall, indicating that the presence of the cavity is still felt at least one mean free path upstream the cavities.

The influence of the angle of attack α on the density ratio for the three sections along surface S1 is demonstrated in Figure 5.18 for cavity L/H ratio of 1 and 4. Results for L/H of 2 and 3 are intermediate, and they will not be shown. In addition, for comparison purpose, results for zero-degree angle of attack obtained by Palharini (PALHARINI, 2010) are presented in this set of plots. According to these plots, it is clearly seen that density ratio increases significantly with increasing the angle of attack α . The reason for that is because, for the oncoming freestream molecules, the body is changing from an aerodynamic sharp body to a blunt body with increasing the angle of attack.

Still referring to Figure 5.18, it is observed that the density ratio undergoes significant changes in the direction perpendicular to the surface. The density ratio is high adjacent to the wall, $Y \approx 0$, and rapidly decreases to a minimum value inside a layer of thickness around two to three freestream mean free paths. For instance, for the case of zero-degree angle of attack, the density ratio is less than one. It means that the density ρ is smaller than the freestream density ρ_∞ . This behavior, the gas near the body surface be much denser and cooler (see next sections) than the gas in the rest of the boundary layer, is observed when the body surface is very much colder

Figure 5.17 - Density ratio (ρ/ρ_∞) profiles for three sections along surface S1 parameterized by the cavity L/H ratio. Left and right columns correspond to angle of attack α of 10 and 20 degrees, respectively.



than the stagnation temperature of the oncoming gas. Afterwards, as Y increases, the density ratio increases significantly inside the shock wave, reaching a maximum value that depends on the angle of attack α . After that, the density decreases and reaches the freestream density value as $Y \rightarrow \infty$.

Density profiles for three sections X'_L along the cavity floor are displayed in Figure 5.19, parameterized by the cavity L/H ratio. In this group of plots, again, Y_H stands for the height y normalized by the cavity height H . The three sections X'_L of 0.25, 0.50, and 0.75 correspond, respectively, to a section close to the cavity backward face, in the middle of the cavity, and at the vicinity of the cavity forward face. In addition, left- and right-column diagrams correspond to density ratio for angle of attack α of 10 and 20 degrees, respectively.

According to this group of plots, it is quite apparent that density ratio profiles present a similar pattern for the three sections X'_L as well as for the angle of attack range investigated. It is observed that the density ratio inside the cavity increases from the top of the cavity, $Y_H = 0$, to the bottom of the cavity, $Y_H = -1$, for the L/H ratio investigated. In addition, it is also observed that, at section $X'_L = 0.25$, density ratio decreases with increasing the L/H ratio. In contrast, at section $X'_L = 0.75$, density ratio increases with increasing the L/H ratio. By increasing the L/H ratio, the flow penetrates more deeply inside the cavity since the flow experiences an expansion at the corner of the cavity backward face. As a result, a recirculation zone is formed, characterized by a zone of low density. Conversely, at the corner of the cavity forward face, the flow experiences a compression. Consequently, density is well above the freestream density. Also, at the bottom of the cavity, density ratio increases significantly with increasing the angle of attack α . This is an expected behavior in the sense that more molecules enter into the cavity with increasing the angle of attack α .

In the following, density ratio profiles outside the cavity, for the same three sections X'_L on surface S3, are displayed in Figure 5.20, parameterized by the cavity L/H ratio. Based on these plots, it is noticed that density ratio profiles follow the same trend of those observed on the cavity upstream surface in the sense that density ratio is high at $Y \approx 0$, then decreases to a minimum value inside a layer of thickness around two to three freestream mean free paths, $2 < Y < 3$. Afterwards, as Y increases, the density ratio increases significantly inside the shock wave, reaching a maximum value that depends on the angle of attack α . After that, the density decreases and reaches the freestream density value as $Y \rightarrow \infty$.

Figure 5.18 - Density ratio (ρ/ρ_∞) profiles for three sections along surface S1 parameterized by the angle of attack α . Left and right columns correspond to cavity L/H ratio of 1 and 4, respectively.

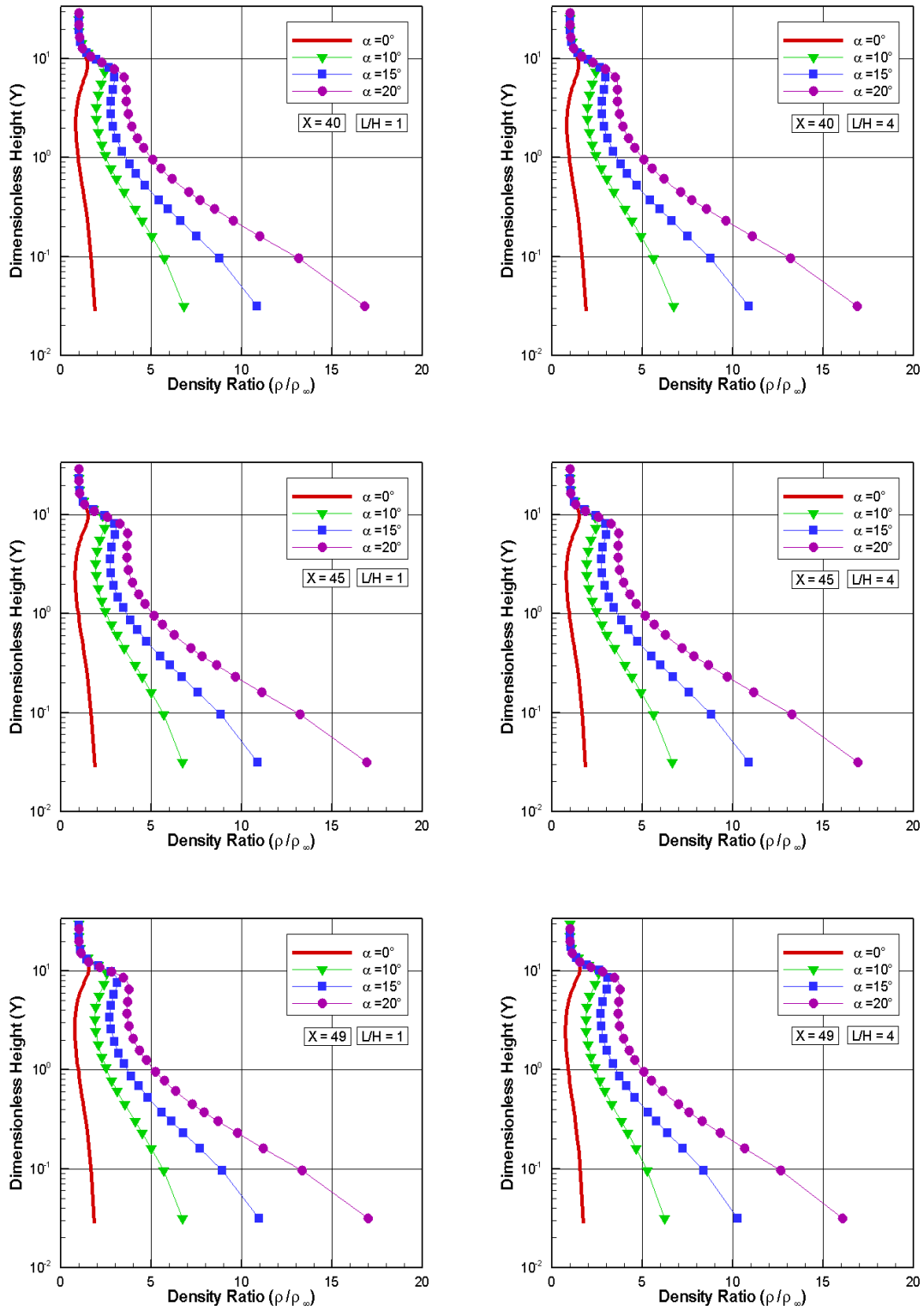


Figure 5.19 - Density ratio (ρ/ρ_∞) profiles for three sections along surface S3 parameterized by the cavity L/H ratio. Left and right columns correspond to angle of attack α of 10 and 20 degrees, respectively.

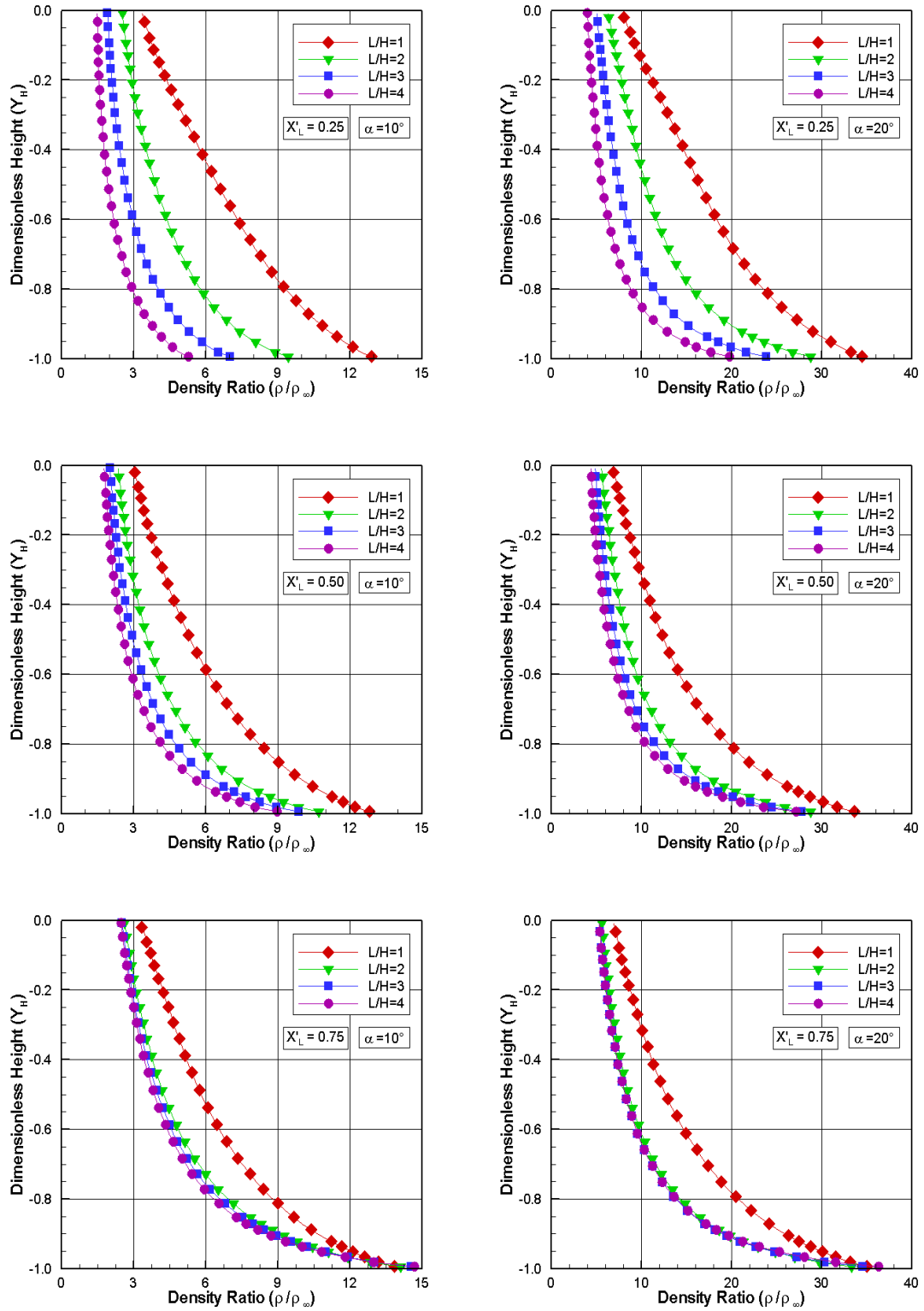
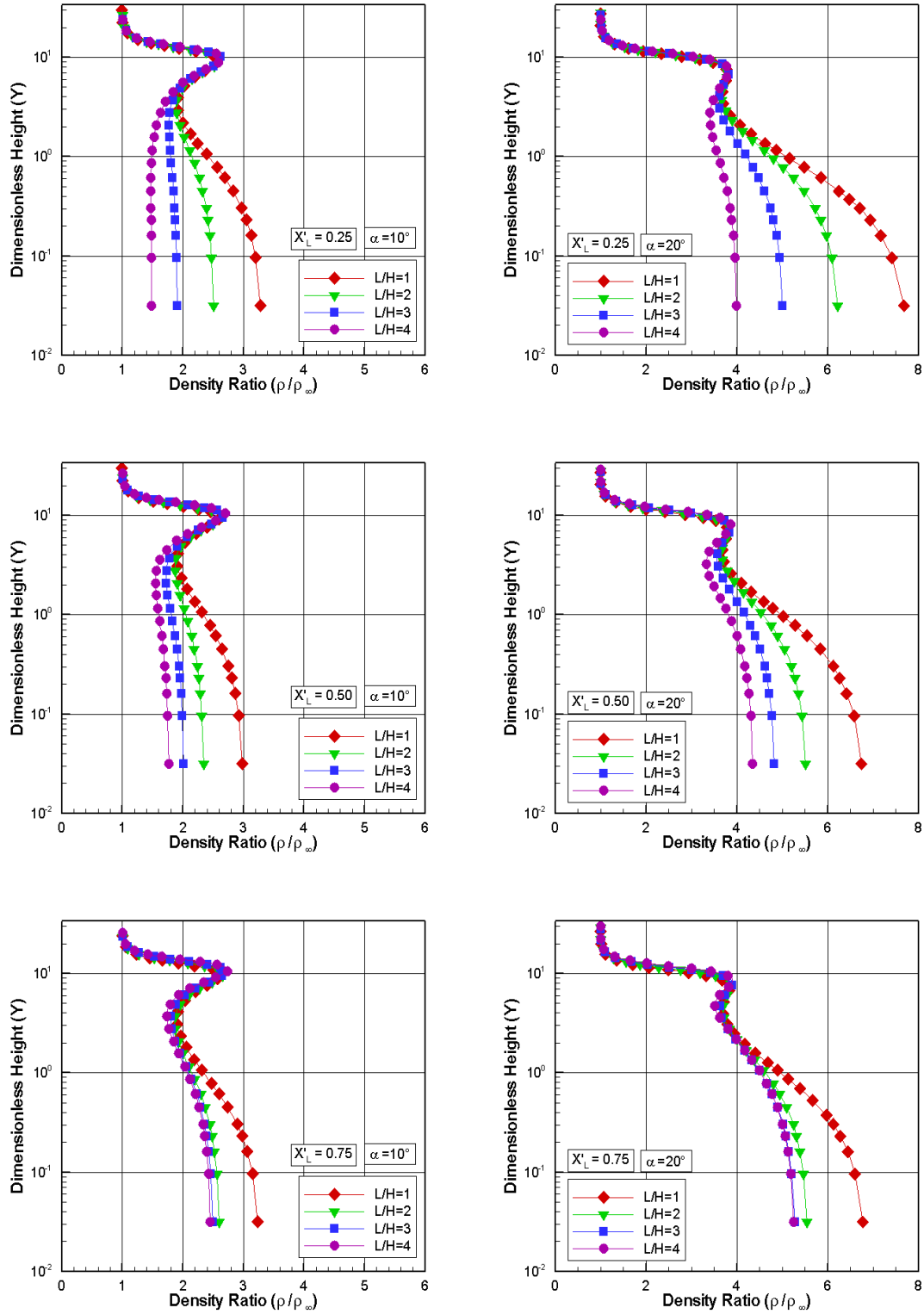


Figure 5.20 - Density ratio (ρ/ρ_∞) profiles for three sections along surface S3 outside the cavity parameterized by the cavity L/H ratio. Left and right columns correspond to angle of attack α of 10 and 20 degrees, respectively.



The sensitive of the density ratio due to changes on the angle of attack α , for the same three sections X'_L inside the cavity, is exhibited in Figure 5.21 for cavity L/H ratio of 1 and 4. Again, for comparison purpose, results for zero-degree angle of attack, obtained by Palharini (PALHARINI, 2010), are shown in this group of plots. It is recognized from this set of plots that density ratio increases significantly with increasing the angle of attack as compared to the case for zero-degree angle of incidence. As mentioned earlier, the amount of molecules entering into the cavity increases with increasing the angle of attack. Nevertheless, due to the flow structure inside the cavity, this increase in the density ratio depends on the cavity L/H ratio. As a base of comparison, for 20-degree angle of attack and L/H of 1, ρ/ρ_∞ reaches maximum values around 34 at section X'_L of 0.25, 0.50, and 0.75. On the other hand, for 20-degree angle of attack and L/H of 4, ρ/ρ_∞ reaches maximum values around 20, 28, and 38 at section X'_L of 0.25, 0.50, and 0.75, respectively.

Density profiles for three sections along the cavity downstream surface, surface S5, are exhibited in Figure 5.22 parameterized by the cavity L/H ratio. In this set of plots, similar to the velocity field analysis, X''_L stands for the distance $(x - L_u - L)$ normalized by the cavity downstream length L_d . In addition, left- and right-column plots correspond to angle of attack of 10 and 20 degrees, respectively. Again, as a base of comparison, density ratio profiles for the flat-plate case are presented in the same plots.

On examining Figure 5.22, it is seen that density profiles is affected by the presence of the cavity downstream along surface S5. The domain of this effect depends on the cavity L/H ratio as well as on the angle of attack α . It is notice that the downstream disturbance region increases with increasing the angle of attack, for the conditions investigated. In attempting to access such angle-of-attack effect, Figure 5.23 displays the density ratio profiles, parameterized by the angle of attack α , for sections X''_L of 0.01, 0.1 and 0.2. These sections correspond, respectively, to a distance $0.01L_d$, $0.1L_d$ and $0.2L_d$ along surface S5.

In the results that follow, in an effort to emphasize points of interest related to the density field, Figures 5.24, 5.25 and 5.26 display the distribution of density ratio, ρ/ρ_∞ , along with streamline traces inside the cavity. This family of plots covers all the cases investigated for cavity L/H ratio and angle of attack α . According to these plots, it is seen that maximum values for density ratio take place close to the surface-S3/surface-S4 junction.

Figure 5.21 - Density ratio (ρ/ρ_∞) profiles for three sections along surface S3 parameterized by the angle of attack α . Left and right columns correspond to cavity L/H ratio of 1 and 4, respectively.

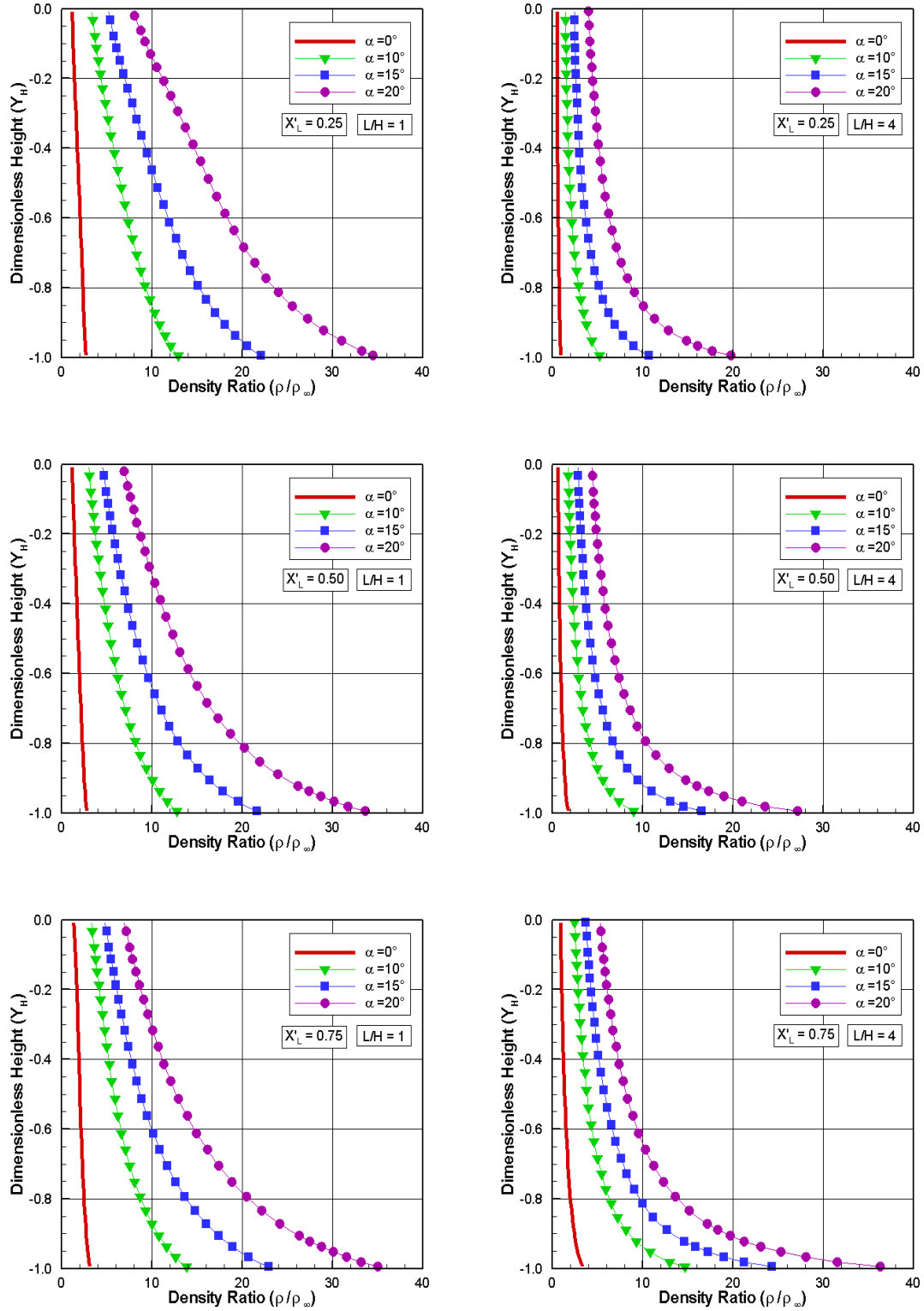


Figure 5.22 - Density ratio (ρ/ρ_∞) profiles for three sections along surface S5 parameterized by the L/H ratio. Left and right columns correspond to angle of attack α of 10 and 20 degrees, respectively.

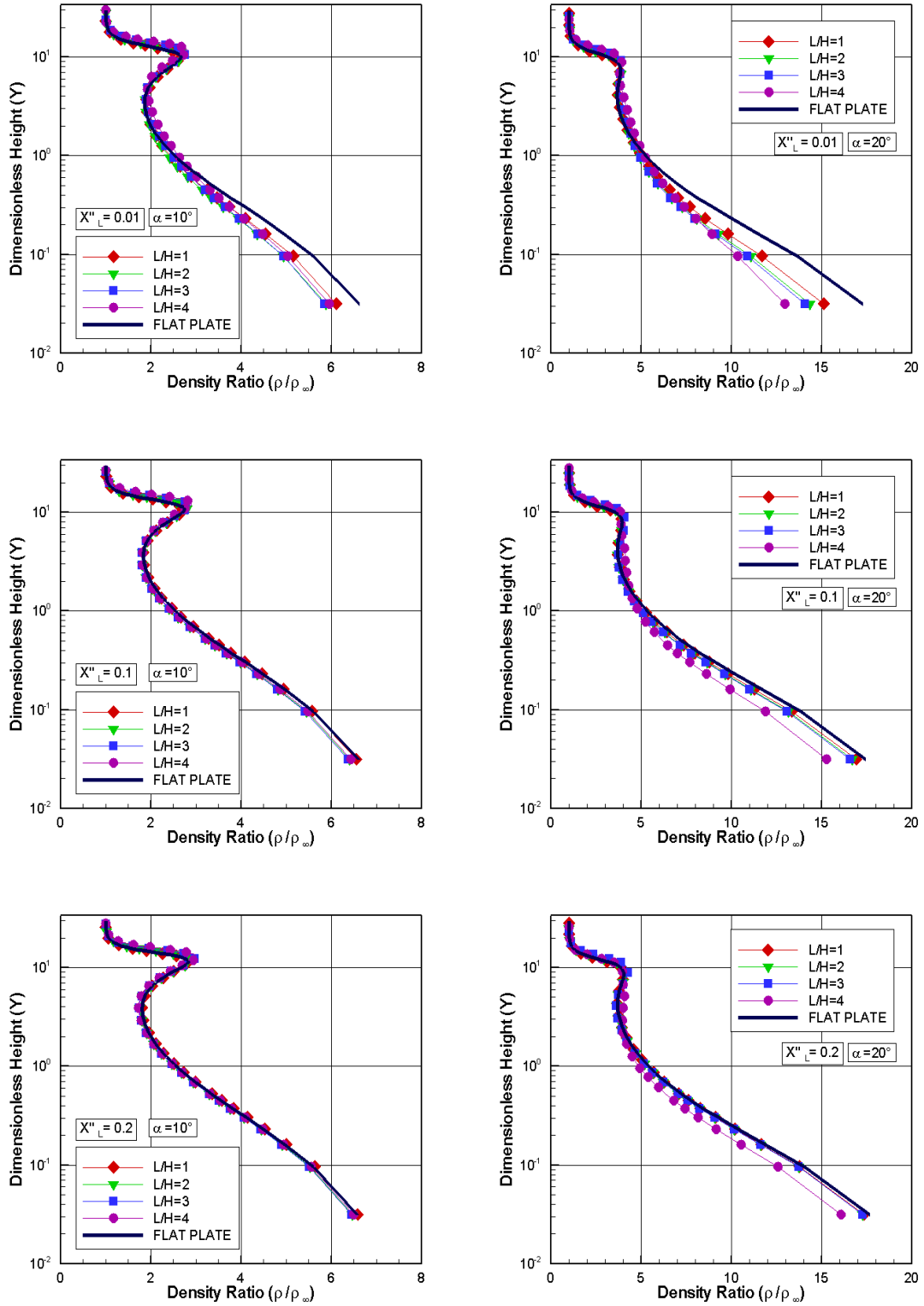


Figure 5.23 - Density ratio (ρ/ρ_∞) profiles for three sections along surface S5 parameterized by the angle of attack α . Left and right columns correspond to cavity L/H ratio of 1 and 4, respectively.

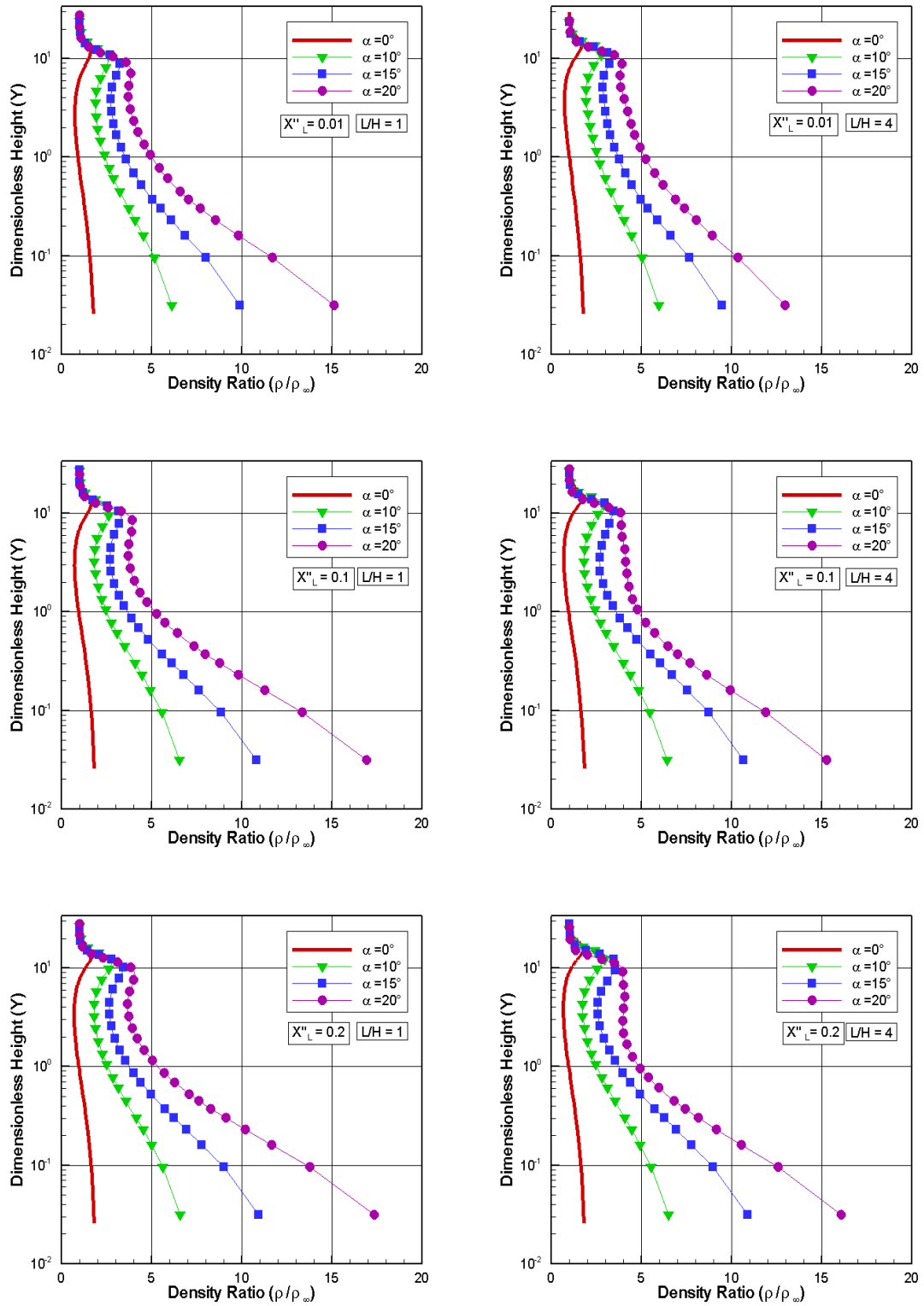


Figure 5.24 - Distribution of density ratio (ρ/ρ_∞) along with streamline traces inside the cavity for L/H ratio of 1 (top), 2, 3, and 4 (bottom), with angle of attack $\alpha = 10$ degrees.

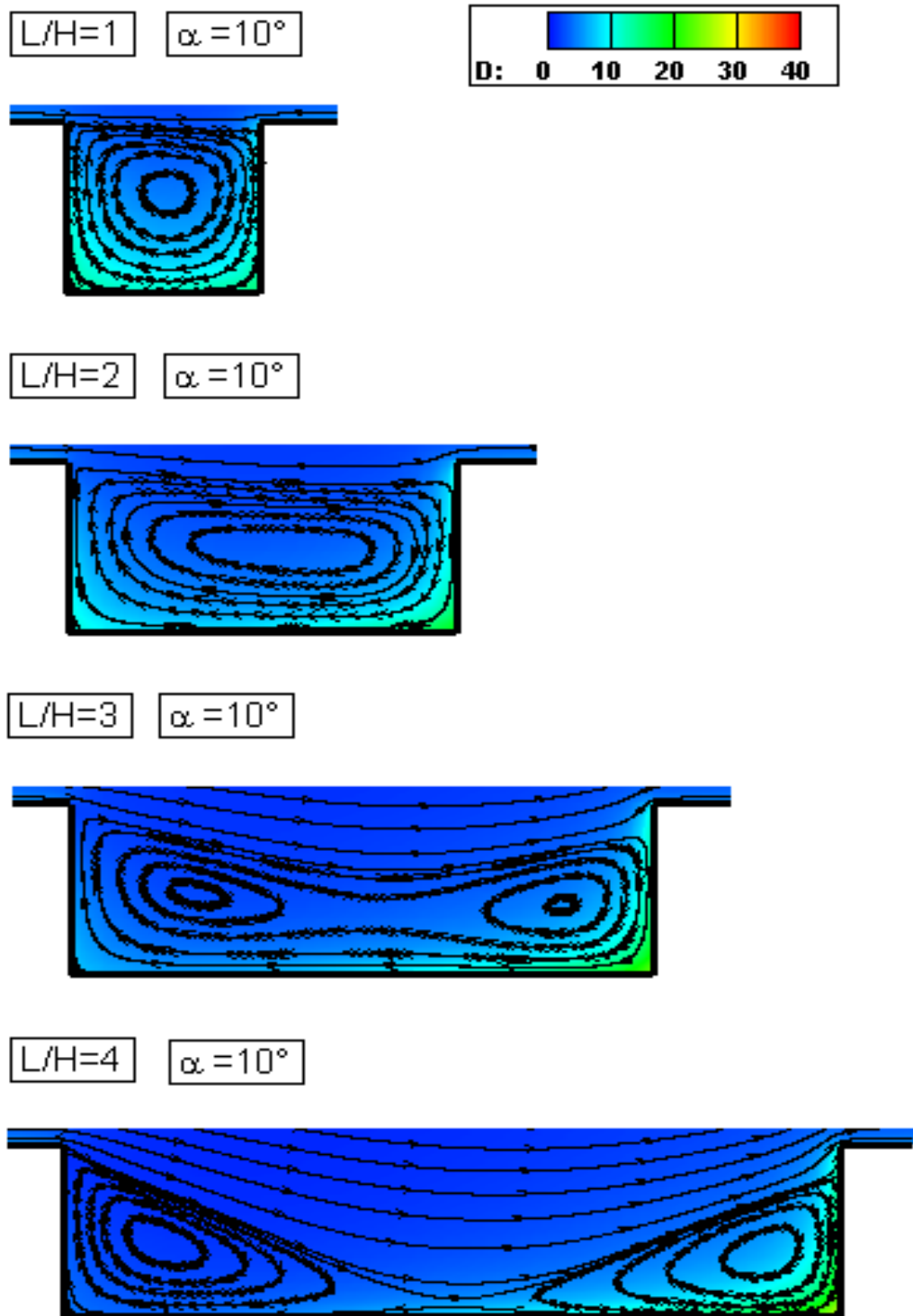


Figure 5.25 - Distribution of density ratio (ρ/ρ_∞) along with streamline traces inside the cavity for L/H ratio of 1 (top), 2, 3, and 4 (bottom), with angle of attack $\alpha = 15$ degrees.

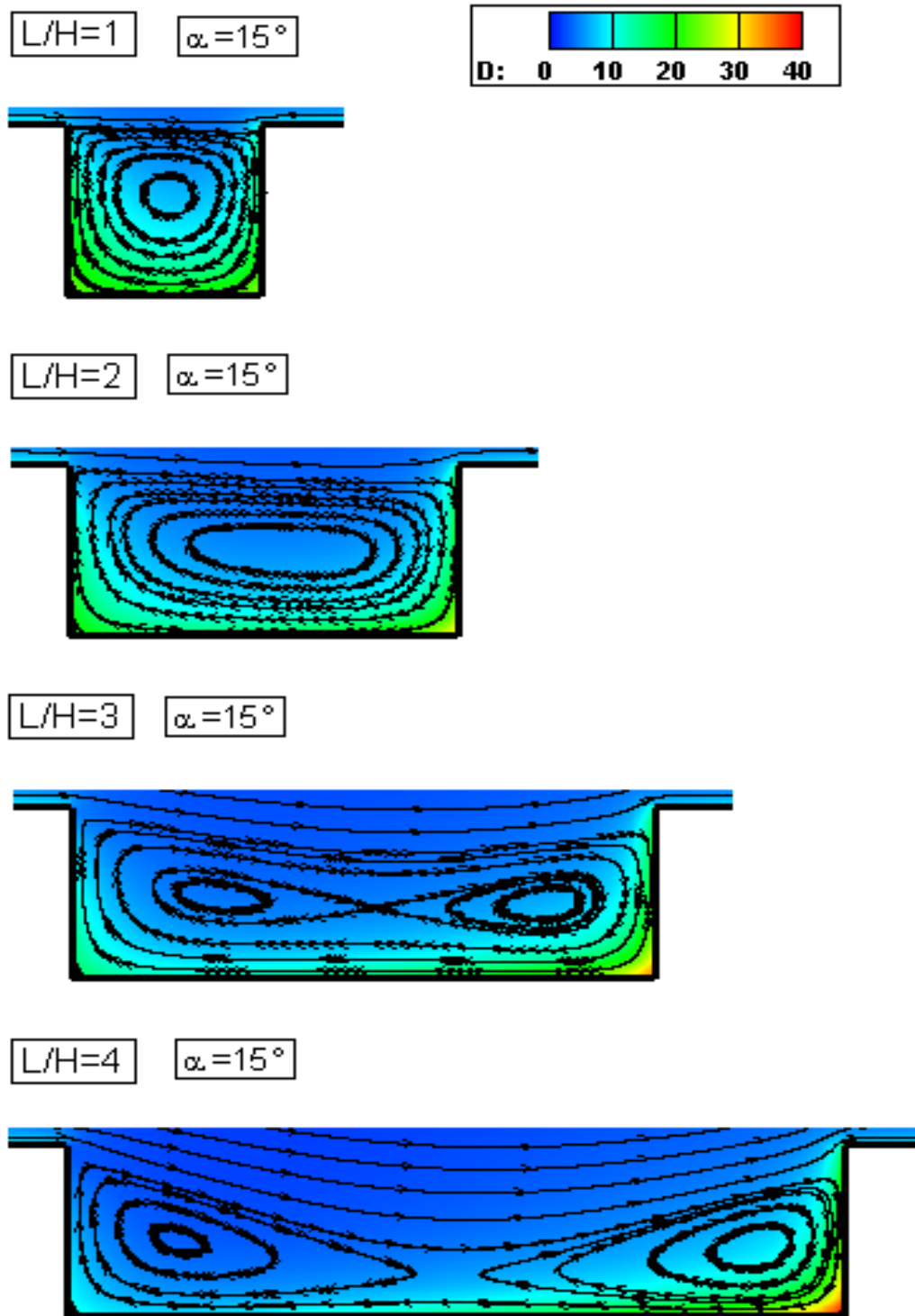
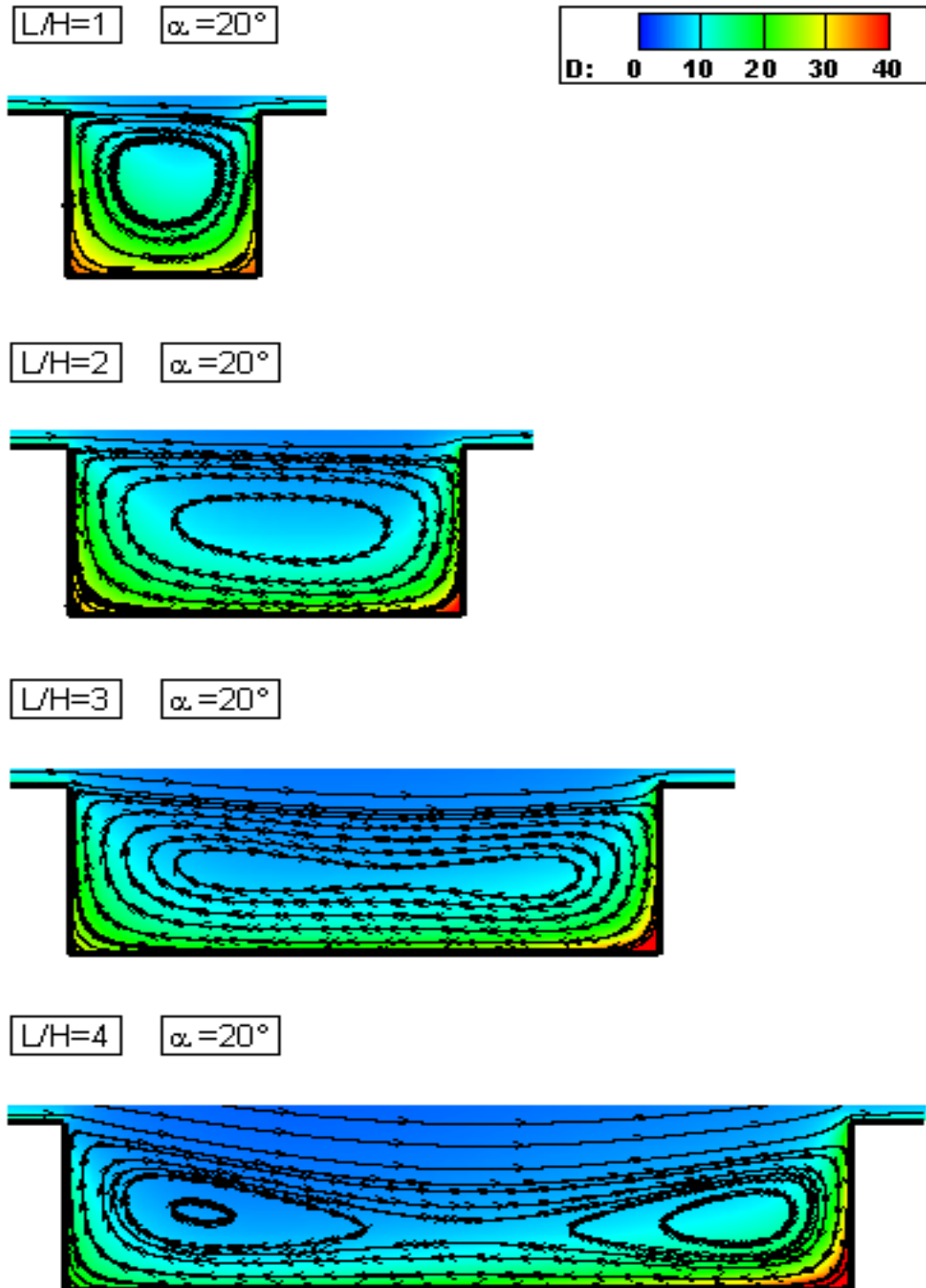


Figure 5.26 - Distribution of density ratio (ρ/ρ_∞) along with streamline traces inside the cavity for L/H ratio of 1 (top), 2, 3, and 4 (bottom), with angle of attack $\alpha = 20$ degrees.



5.1.3 Pressure Field

The influence of the L/H ratio on pressure profiles for three sections along cavity upstream surface, X of 40, 45, and 49, is exhibited in Figure 5.27 as a function of the dimensionless height Y . In this set of diagrams, pressure p is normalized by the freestream pressure p_∞ , X and Y are dimensionless length and height, respectively, as defined previously in the density profiles. Moreover, for comparative purpose, pressure ratio profiles for the flat-plate case are also exhibited in the same diagrams.

On examining Figure 5.27, it is observed that, similar to tangential velocity and density profiles, pressure ratio profiles for the cavity L/H ratio and angle of attack α investigated are basically identical to those for the flat-plate cases, indicating that the presence of the cavity does not affect the flowfield far upstream the cavity, section X of 40 and 45. However, for section $X = 49$, pressure ratio profiles are slightly different from that for the flat-plate case in the shock layer, region defined by $0 < Y < 3$, indicating that the presence of the cavity is felt at least a few mean free paths upstream the cavity position. Beyond this small region, as $Y \rightarrow \infty$, the pressure ratio continues to increase to a maximum value inside the shock wave that formed at the sharp leading edge of the flat plate. After that, the pressure dramatically decreases, outside the shock wave, and reaches the freestream pressure value at the outer boundary of the computational domain.

As a base of comparison, it becomes instructive to examine differences in the pressure ratio due to the angle-of-attack effect. In this fashion, Figure 5.28 illustrates the pressure ratio profiles for cavity L/H ratio of 1 and 4, at the same three sections along surface S1. In addition, once more, results for zero-degree angle of attack obtained by Palharini (PALHARINI, 2010) are presented in this set of plots for comparison purpose. According to this set of plots, it is clearly noticed that pressure ratio increases significantly with increasing the angle of attack α . This is an expected behavior since the body is changing from an aerodynamic sharp body to a blunt one, for the oncoming freestream molecules, with increasing the angle of attack. As a base of comparison, the pressure ratio increased one order of magnitude as the angle of attack increased from 0 to 20 degrees. Moreover, it is also noticed that, at the vicinity of the cavity position, at station $X = 49$, the pressure ratio slightly decreases as compared to the other two stations. The reason for that is because the flow experiences an expansion at the cavity corner.

The impact on the pressure ratio due to variations on the cavity L/H ratio for three sections X'_L along the cavity floor, surface S3, are demonstrated in Figure 5.29. In

Figure 5.27 - Pressure ratio (p/p_∞) profiles for three sections along surface S1 parameterized by the cavity L/H ratio. Left and right columns correspond to angle of attack α of 10 and 20 degrees, respectively.

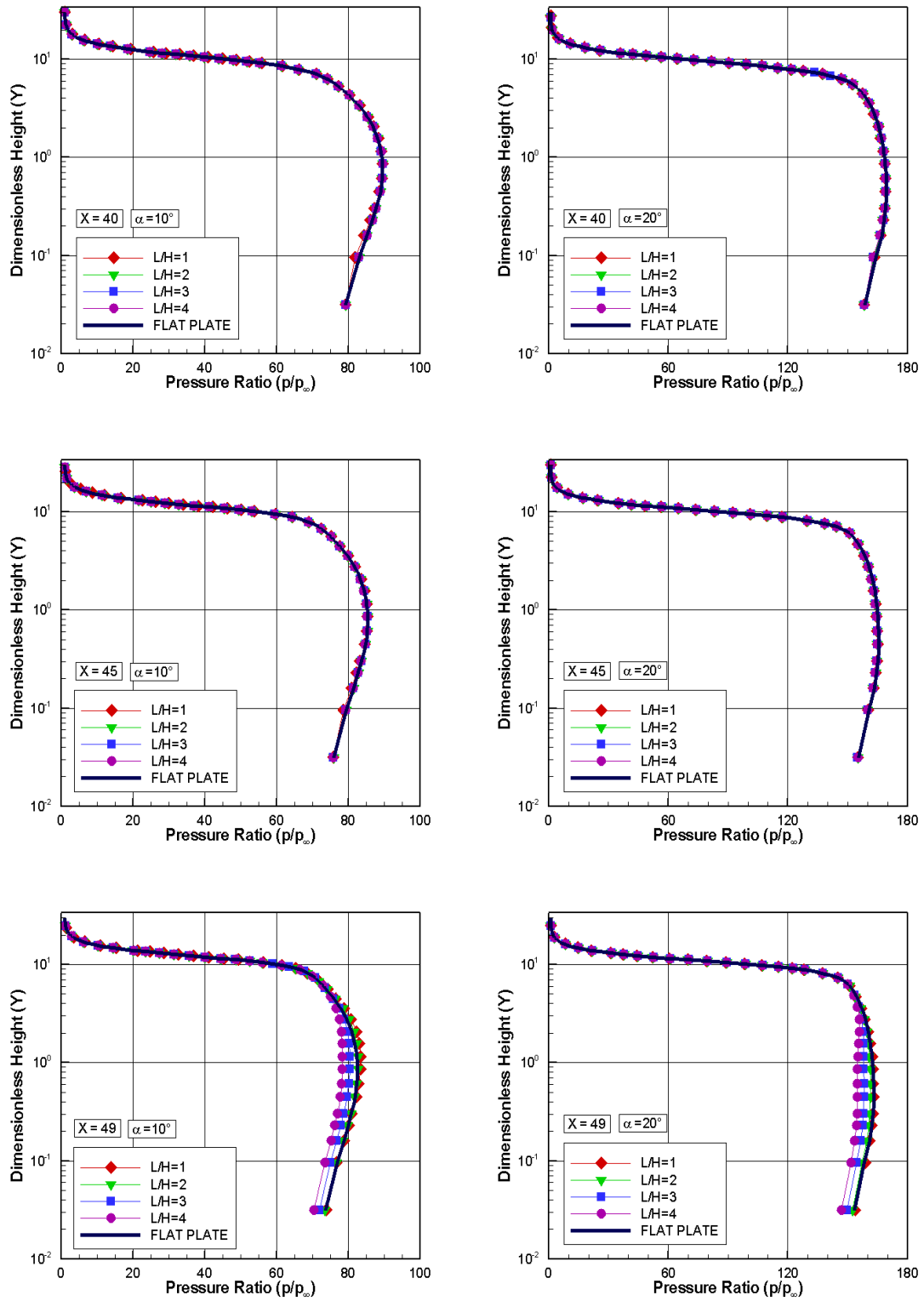


Figure 5.28 - Pressure ratio (p/p_∞) profiles for three sections along surface S1 parameterized by the angle of attack α . Left and right columns correspond to cavity L/H ratio of 1 and 4, respectively.

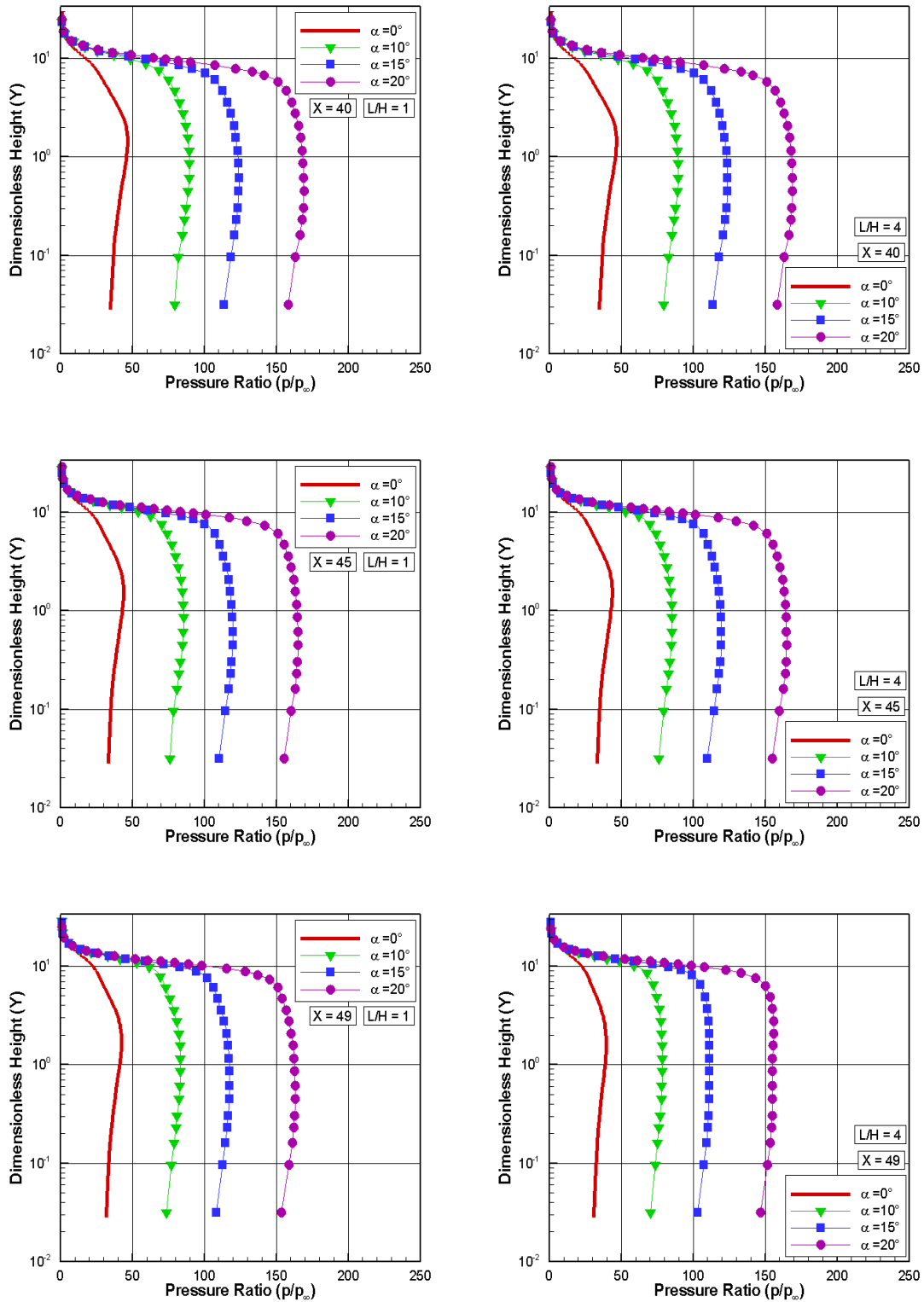
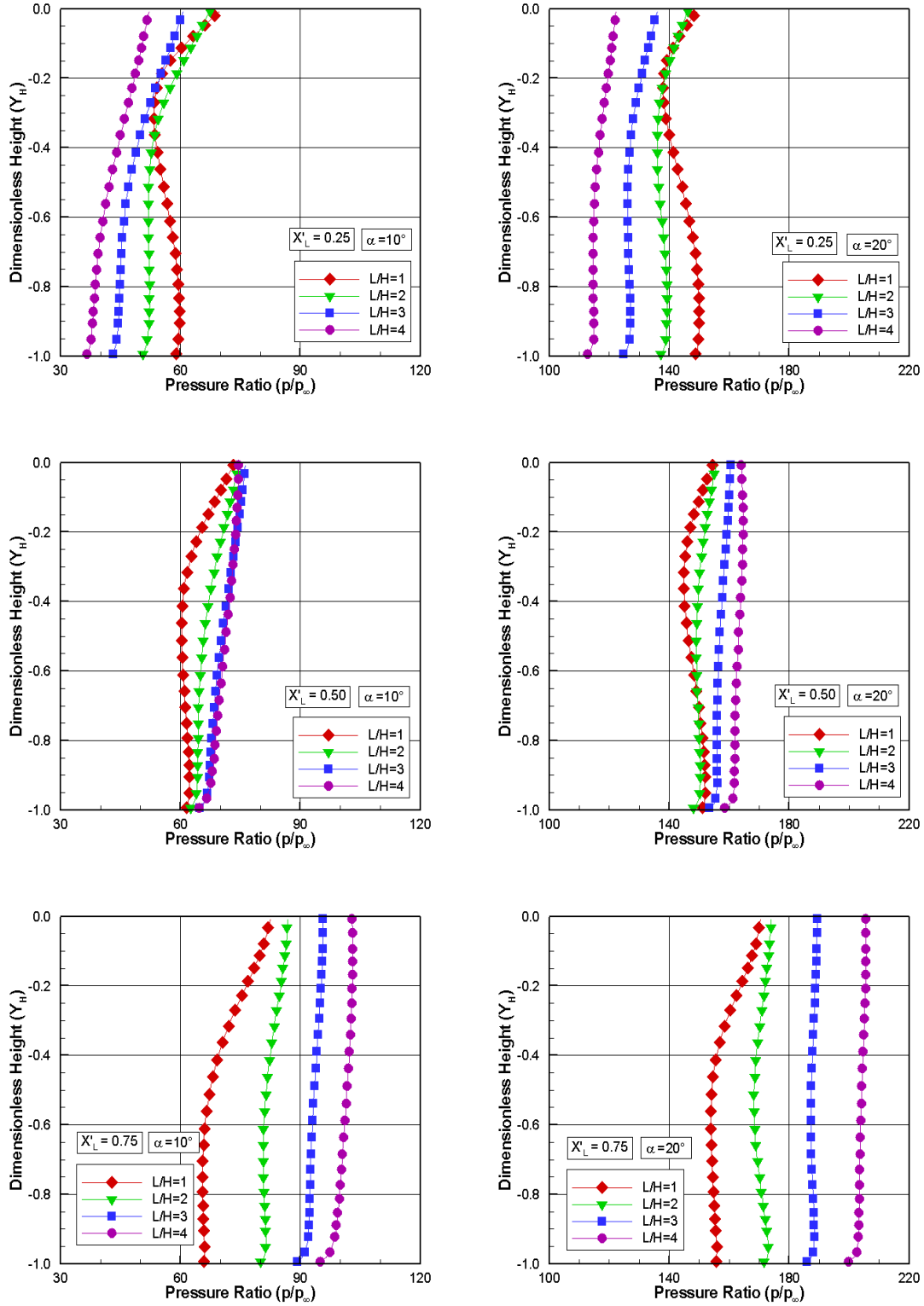


Figure 5.29 - Pressure ratio (p/p_∞) profiles for three sections along surface S3 parameterized by the cavity L/H ratio. Left and right columns correspond to angle of attack α of 10 and 20 degrees, respectively.



this group of plots, again, left- and right-column diagrams correspond to density ratio for angle of attack α of 10 and 20 degrees, respectively.

It may be recognized from Figure 5.29 that pressure ratio profiles inside the cavity are affected not only by the cavity L/H ratio but also by the angle of attack α . It is observed that pressure ratio for the $L/H = 1$ case presents a similar behavior for three sections X'_L , i.e., it presents a high value at the top of the cavity, $Y = 0$, and decreases up to the bottom, $Y = -1$. However, as the L/H ratio increases from 1 to 4, the pressure ratio decreases close to the cavity backward face, $X'_L = 0.25$, and increases at the vicinity of the cavity backward face, $X'_L = 0.75$, as compared to the pressure ratio for the $L/H = 1$ case. By increasing the L/H ratio, the flow topology inside the cavity changes from that for an “open cavity” to that of a “closed cavity”, as shown in Figures 5.14, 5.15, and 5.16. As discussed earlier, the flow experiences an expansion close to the cavity backward face and a compression close to the cavity forward face. Moreover, by increasing the angle of attack from 10 to 20, these effects on the pressure ratio are more significant.

Proceeding in a manner analogous to the density earlier treatment, Figure 5.30 exhibits the pressure ratio profiles outside the cavities for the same three sections X'_L . According to this figure, major differences in the pressure ratio take place inside the shock layer.

In order to account for the angle-of-attack effects, Figure 5.31 illustrates the dependence of the density ratio on the angle of attack α , for the same three sections X'_L inside the cavity. In this set of plots, left- and right-column plots correspond to cavity L/H ratio of 1 and 4, respectively. Also, a matter of comparison, results for zero-degree angle of attack, obtained by Palharini (PALHARINI, 2010), are shown in this group of plots. It is recognized from this set of plots that pressure ratio increases significantly with increasing the angle of attack as compared to the case for zero-degree angle of incidence. In general, pressure ratio increased one order of magnitude as the angle of attack increased from 0 to 20 degrees. Furthermore, it is worth noting that, for section $X'_L = 0.25$, pressure ratio decreased as the cavity L/H ratio increased from 1 to 4. Conversely, for section $X'_L = 0.75$, pressure ratio increased as the cavity L/H ratio increased from 1 to 4.

The consequence on the pressure ratio due to variations in the cavity L/H ratio, for three sections X''_L along the cavity downstream surface, surface S5, is demonstrated in Figure 5.32. In this set of plots X''_L represents the distance $(X - L_u - L)$ normalized by the cavity downstream length L_d . Again, left- and right-column plots corresponds

Figure 5.30 - Pressure ratio (p/p_∞) profiles for three sections along surface S3 outside the cavity parameterized by the cavity L/H ratio. Left and right columns correspond to angle of attack α of 10 and 20 degrees, respectively.

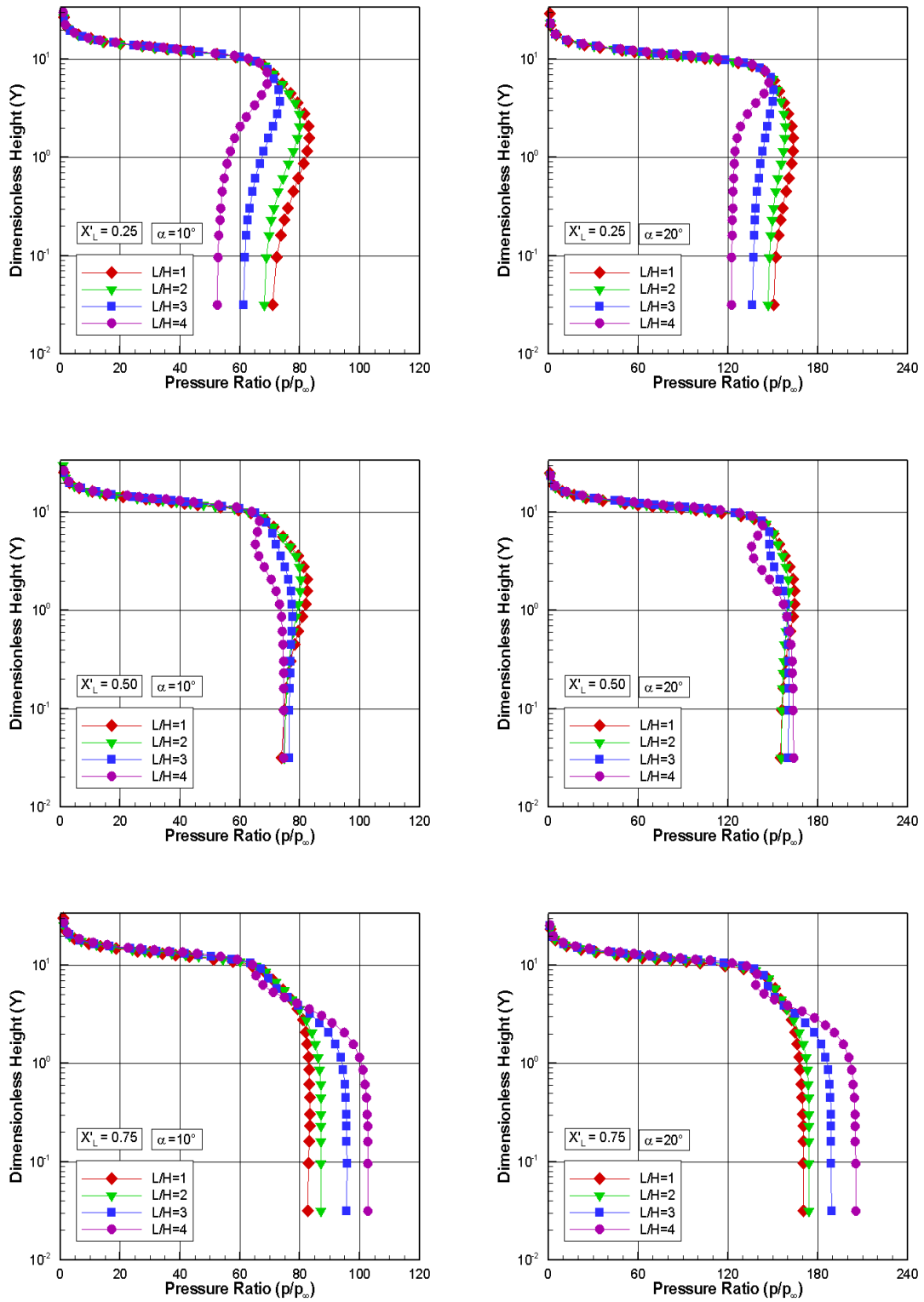


Figure 5.31 - Pressure ratio (p/p_∞) profiles for three sections along surface S3 parameterized by the angle of attack α . Left and right columns correspond to cavity L/H ratio of 1 and 4, respectively.

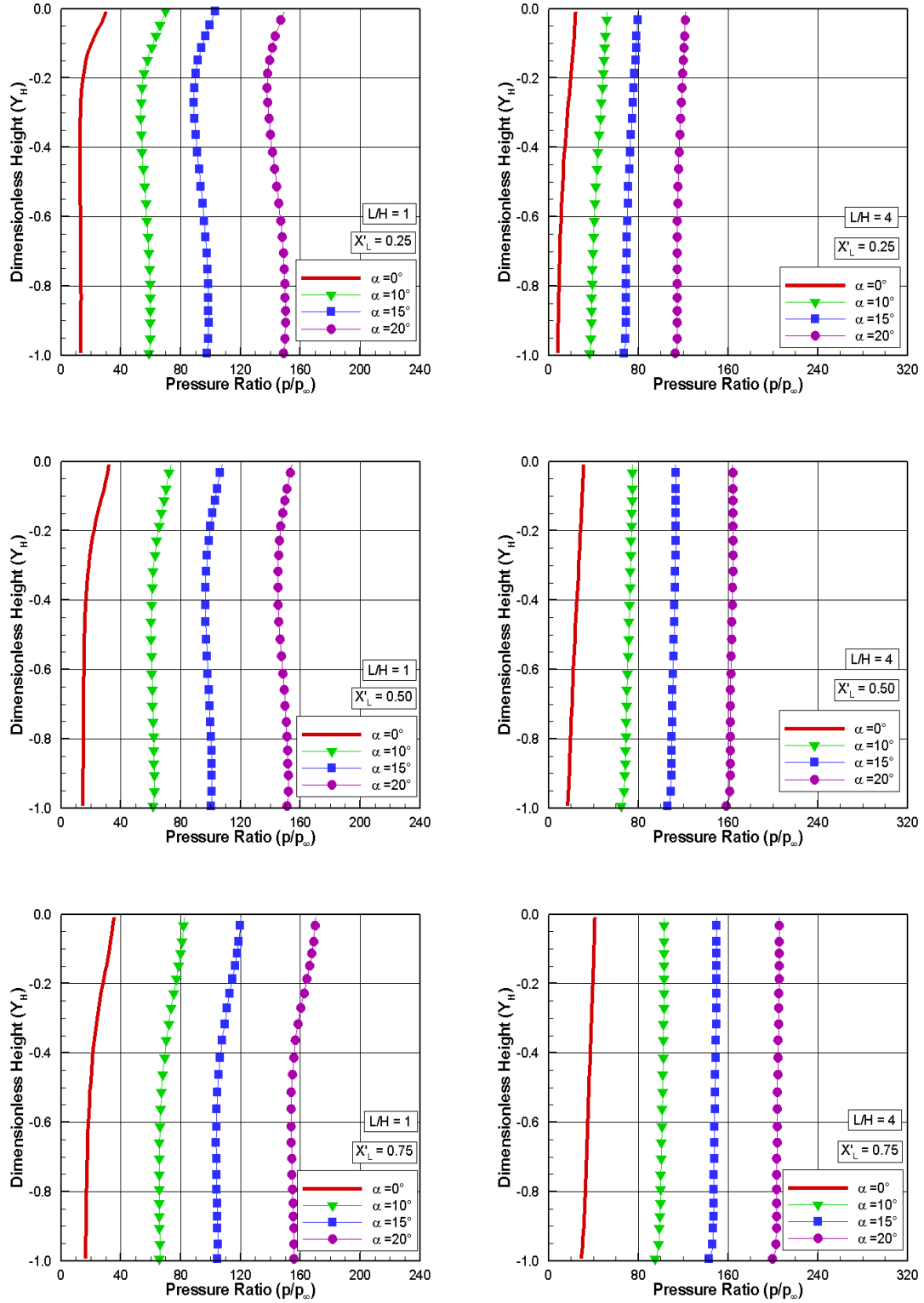
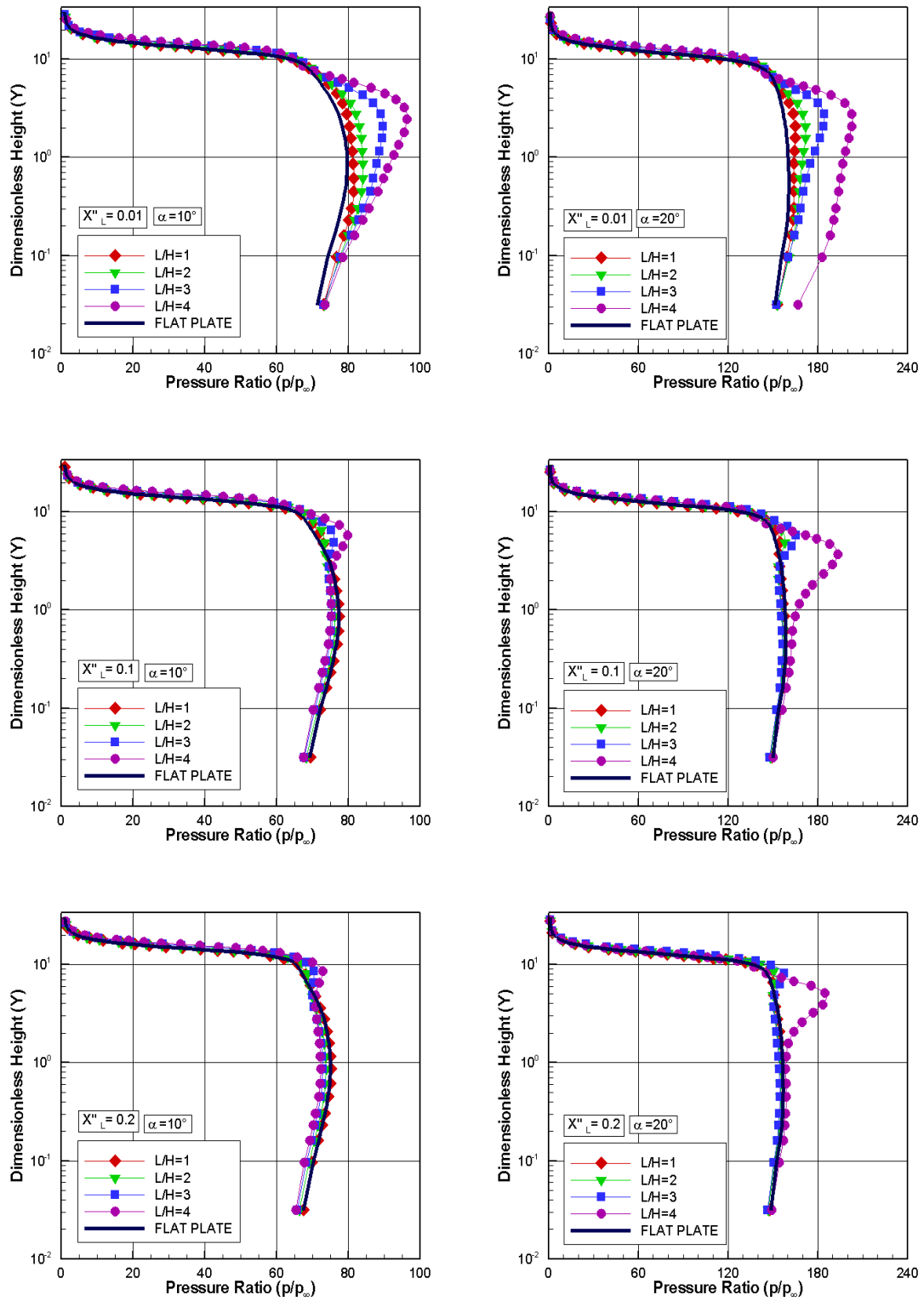


Figure 5.32 - Pressure ratio (p/p_∞) profiles for three sections along surface S5 parameterized by the L/H ratio. Left and right columns correspond to angle of attack α of 10 and 20 degrees, respectively.



to angle of attack of 10 and 20 degrees, respectively. Based on this set of plots, it is clearly seen that pressure ratio profiles follow a similar behavior as compared to those presented along the cavity upstream surface, surface S1. They differ from those for the flat-plate case in the shock layer at the vicinity of the cavity corner, i.e., at station $X_L'' = 0.01$. In this small region, the pressure ratio for the L/H ratio and angle of attack investigated is larger than that for the flat-plate case.

In what follows, in order to gain some insight into the pressure field behavior, Figures 5.33, 5.34, and 5.35 displays the distribution of pressure ratio, p/p_∞ , along with streamline traces inside the cavity. This family of plots covers all the cases investigated for cavity L/H ratio and angle of attack α . According to these plots, it is seen that maximum values for pressure ratio take place close to the cavity corner, at surface-S4/surface-S5 junction. It is also seen that, in this region, pressure p is two orders of magnitude larger than the freestream pressure p_∞ , for the majority of the cases. It should be remarked that this pressure ratio is higher than that observed at the bottom of the cavities, for the L/H ratio and angle of attack α investigated. As a result, it may be inferred in passing that particular attention should be paid to the cavity forward face in terms of the pressure loads, since the vicinity of the corner represents a zone of strong compression.

5.1.4 Kinetic Temperature Field

In a diatomic or polyatomic gas in complete thermodynamic equilibrium, the translational temperature is equal to the temperature related to the internal modes, i.e., rotational, vibrational, or electronic temperatures, and it is identified as thermodynamic temperature. Conversely, in a thermodynamic non-equilibrium gas, an overall temperature is defined as the weighted mean of the translational and internal temperatures (BIRD, 1994) as being,

$$T_O = \frac{\zeta_T T_T + \zeta_R T_R + \zeta_V T_V}{\zeta_T + \zeta_R + \zeta_V} \quad (5.1)$$

where T and ζ stand for the temperature and the degree of freedom, respectively, and subscripts T , R and V refer to translation, rotation and vibration, respectively.

Translational, rotational, and vibrational temperatures are obtained to each cell in the computational domain by the following equations,

Figure 5.33 - Distribution of pressure ratio (p/p_∞) along with streamline traces inside the cavity for L/H ratio of 1 (top), 2, 3, and 4 (bottom), with angle of attack $\alpha = 15$ degrees.

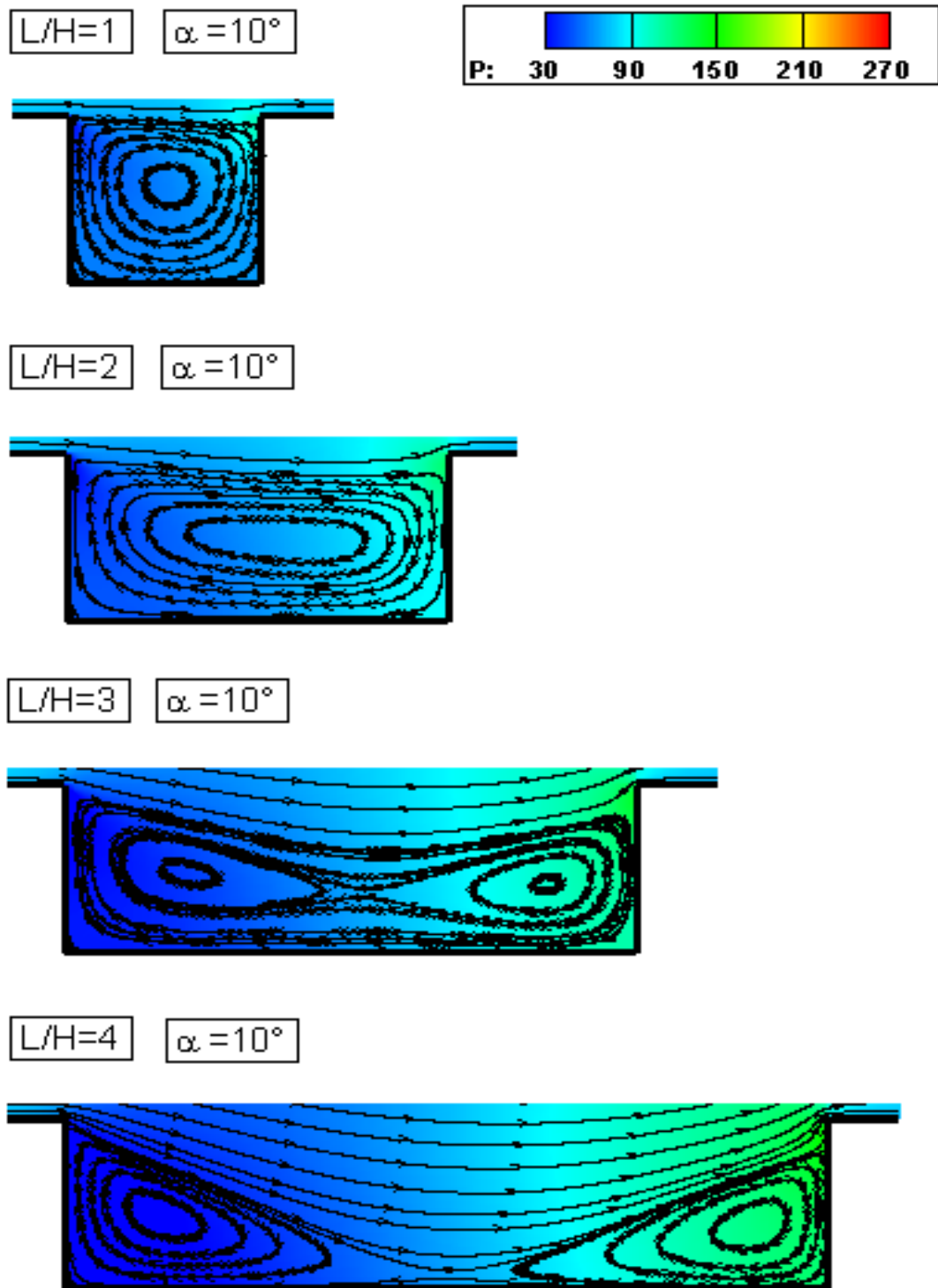


Figure 5.34 - Distribution of pressure ratio (p/p_∞) along with streamline traces inside the cavity for L/H ratio of 1 (top), 2, 3, and 4 (bottom), with angle of attack $\alpha = 10$ degrees.

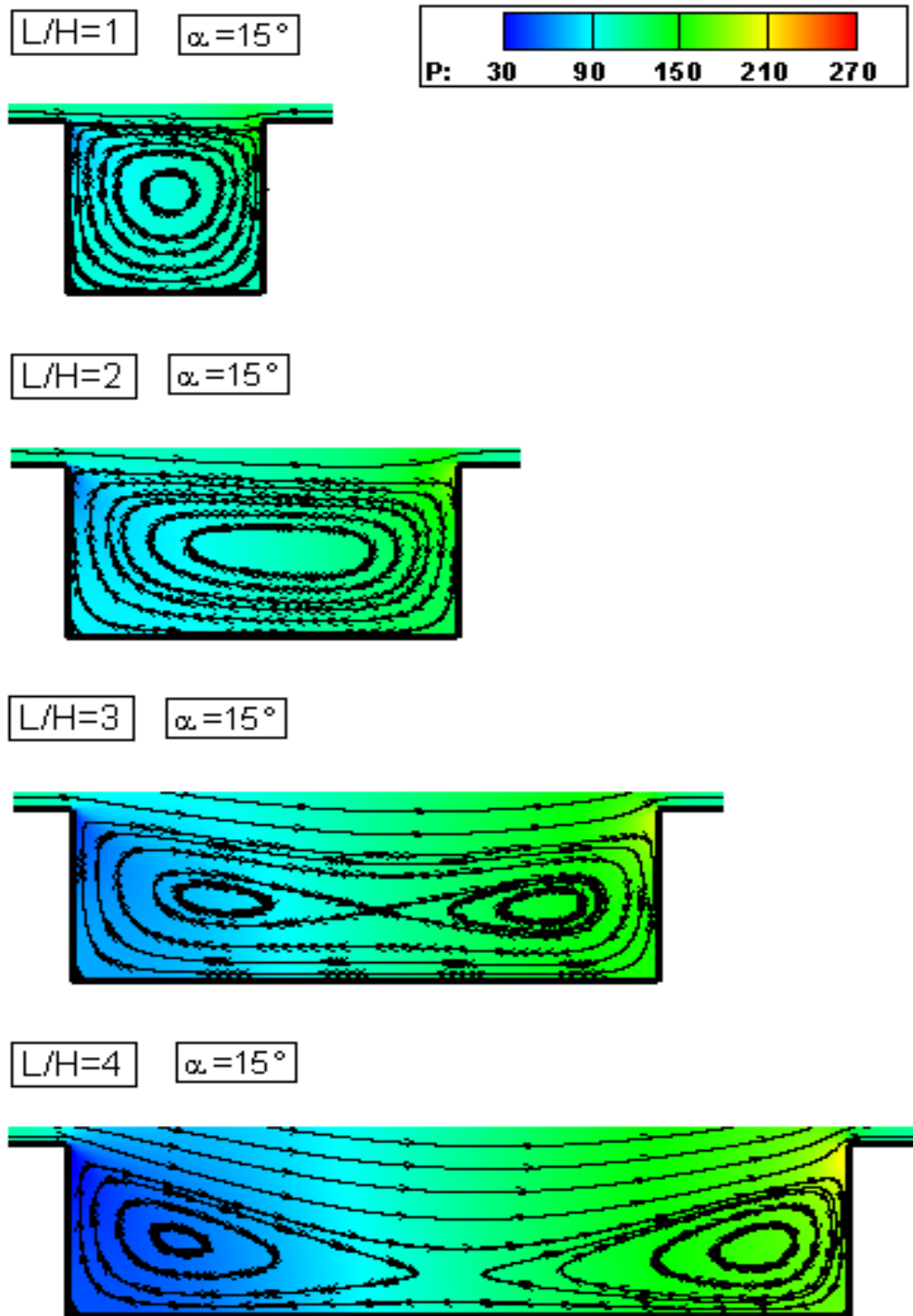
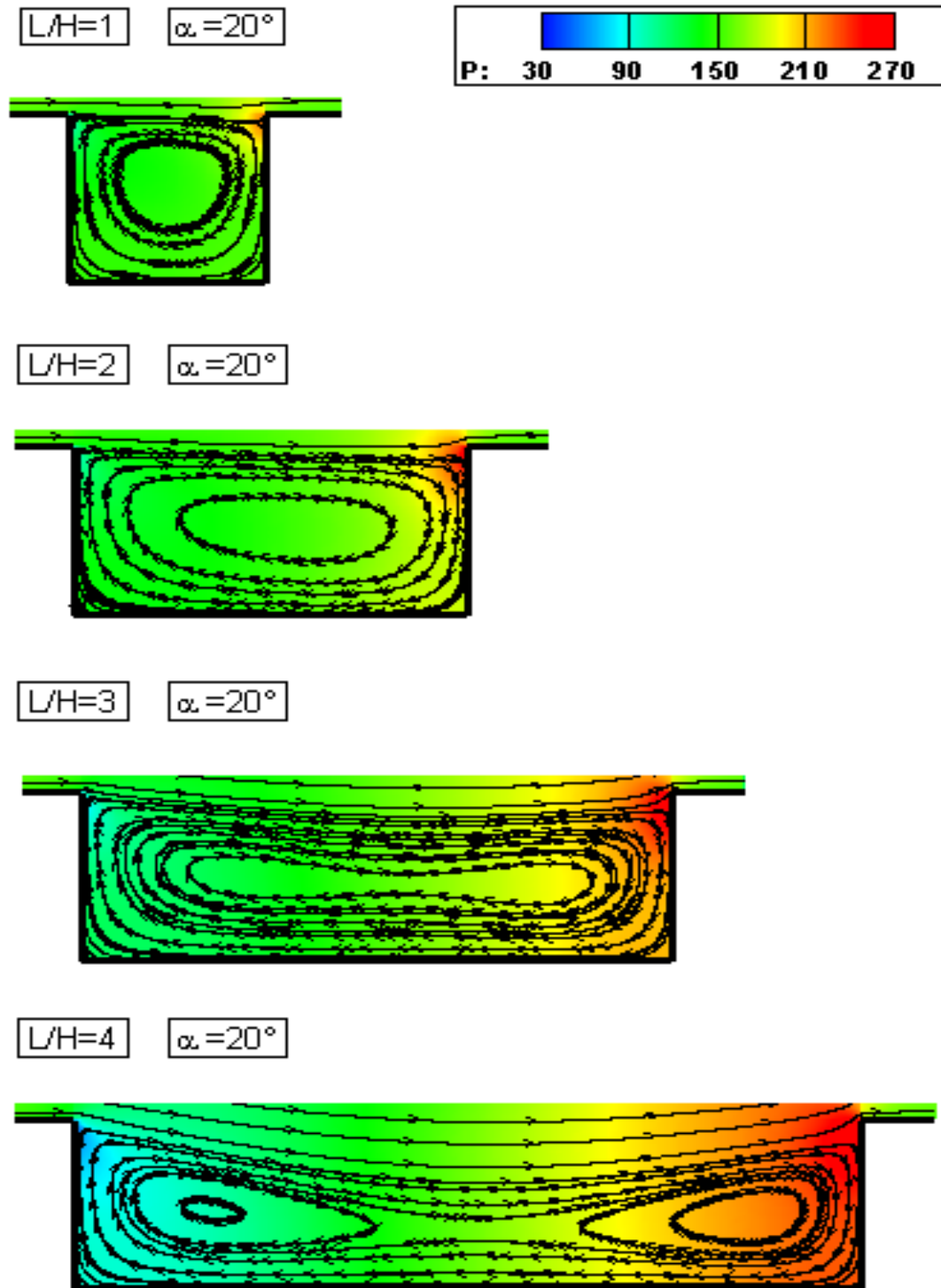


Figure 5.35 - Distribution of pressure ratio (p/p_∞) along with streamline traces inside the cavity for L/H ratio of 1 (top), 2, 3, and 4 (bottom), with angle of attack $\alpha = 20$ degrees.



$$T_T = \frac{1}{3k} \sum_{j=1}^N \frac{(m\mathbf{c}'^2)_j}{N} \quad (5.2)$$

$$T_R = \frac{2 \bar{\varepsilon}_R}{k \zeta_R} \quad (5.3)$$

$$T_V = \frac{\Theta_V}{\ln \left(1 + \frac{k\Theta_V}{\bar{\varepsilon}_V} \right)} \quad (5.4)$$

where k is the Boltzmann constant, Θ_V is the characteristic temperature of vibration, $\bar{\varepsilon}_R$ and $\bar{\varepsilon}_V$ are, respectively, rotation and vibration average energies in each cell.

Under the aforementioned definitions, the sensitive of the kinetic temperature due to changes on the L/H ratio and angle of attack α is demonstrated in Figure 5.36 for three sections along cavity upstream surface, X of 40, 45, and 49. In this set of diagrams, kinetic temperature ratio stands for the translational temperature T_T , rotational temperature T_R , vibrational temperature T_V , and overall temperature T_O normalized by the freestream temperature T_∞ . In addition, filled and empty symbols correspond to temperature ratio profiles for L/H of 1 and 4, respectively. Results for L/H of 2 and 3 are intermediate, and they will not be shown.

On examining Figure 5.36, it is quite apparent that thermodynamic non-equilibrium occurs outside the cavities, as shown by the lack of equilibrium between the translational and internal kinetic temperatures. Thermal non-equilibrium occurs when the temperatures associated with the translational, rotational, and vibrational modes of a polyatomic gas are different. In this context, the overall temperature, defined by Equation 5.1, is equivalent to the thermodynamic temperature only under thermal equilibrium conditions. In addition, the ideal gas equation of state does not apply to this temperature in a non-equilibrium situation.

Still examining Figure 5.36, it is firmly established that, by visual inspection, no significant changes are observed in the temperature ratio profiles due to variations on the L/H ratio, since L/H of 1 and 4 represent, respectively, the smallest and the largest values investigated. In addition, the kinetic temperature ratio is basically identical to that for the flat-plate case, indicating that the presence of the cavity does not influence the flowfield immediately upstream the cavity, section $X = 49$. This behavior is in contrast to that observed for the density and pressure profiles.

Figure 5.36 - Kinetic temperature ratio (T/T_∞) profiles for three sections along surface S1 parameterized by the cavity L/H ratio. Left and right columns correspond to angle of attack α of 10 and 20 degrees, respectively.

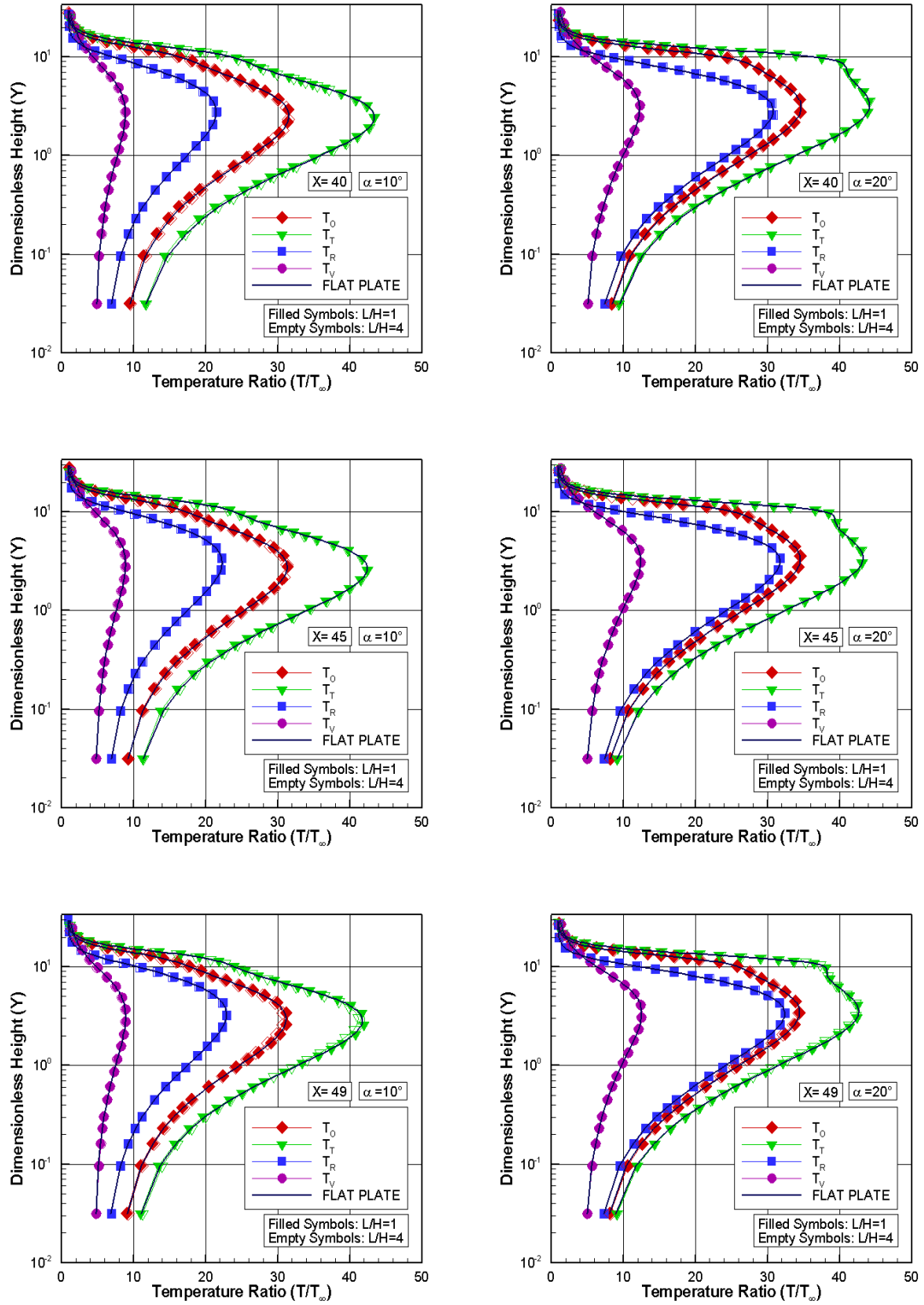
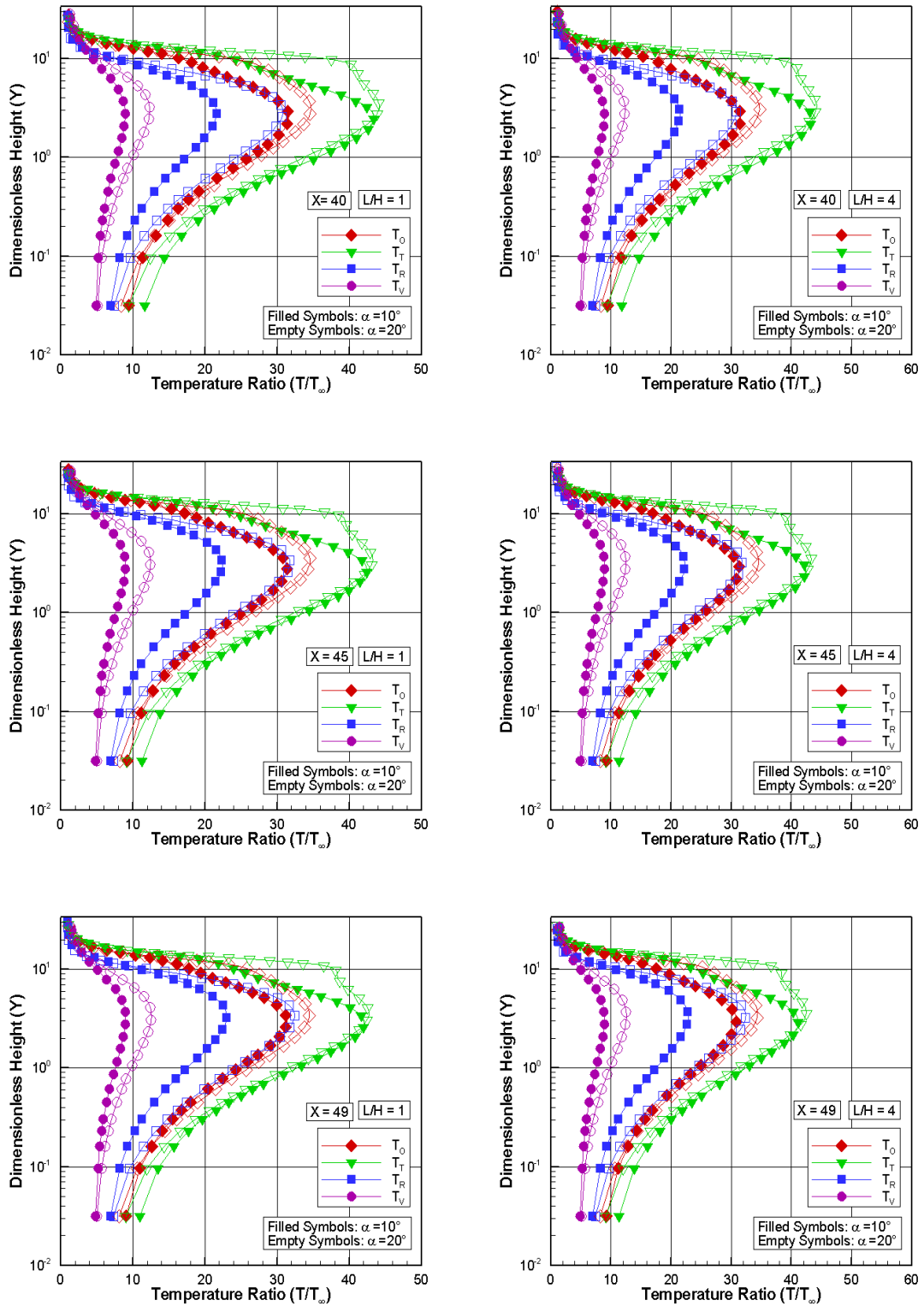


Figure 5.37 - Kinetic temperature ratio (T/T_∞) profiles for three sections along surface S1 parameterized by the angle of attack α . Left and right columns correspond to cavity L/H ratio of 1 and 4, respectively.



Of particular interest in Figure 5.36 is the behavior of the temperature ratio profiles in the body off direction. It is seen that, in the undisturbed freestream far from the flat-plate surface, $Y \rightarrow \infty$, the translational and internal kinetic temperatures have the same value and are equal to the thermodynamic temperature. Approaching the flat-plate surface, $Y \approx 3$, the translational kinetic temperature rises to well above the rotational and vibrational temperatures and reaches a maximum value that is basically the same for the angle of attack range investigated. Since a large number of collisions is necessary to excite the vibration mode of the molecules, from the ground state to the upper state, the vibrational temperature is seen to increase much more slowly than rotational temperature. Still further toward the flat-plate surface, $Y \approx 0$, the translational kinetic temperature decreases, and reaches a constant value on the wall that is above the wall temperature T_w ($\approx 4T_\infty$), resulting in a temperature jump as defined in continuum formulation (GRUPTA et al., 1985). Furthermore, the difference between translational temperature and internal temperatures at the vicinity of the flat-plate surface also indicates that the thermodynamic equilibrium is not achieved in the boundary layer.

Proceeding in a manner analogous to the earlier treatment to velocity, density, and pressure profiles, Figure 5.37 displays the impact of the angle of attack on the kinetic temperature ratio for the three sections on the cavity upstream surface, surface S1. Based on this group of plots, it is noticed that kinetic temperature ratio increases inside the shock layer with increasing the angle of attack for the range investigated.

In order to assess the overall behavior of the kinetic temperature ratio profiles inside the cavities, Figure 5.38 illustrates the kinetic temperature ratio profiles for three sections, X'_L of 0.25, 0.50, and 0.75. In this set of plots, left- and right-column plots correspond to density ratio for angle of attack α of 10 and 20 degrees, respectively. In addition, filled and empty symbols stand for cavity L/H ratio of 1 and 4, respectively. Results for L/H ratio of 2 and 3 are intermediate, and they will not be shown.

According to this set of plots, it is observed that the kinetic temperature ratio T/T_∞ decreases from the top of the cavity and basically reaches a minimum value on the cavity bottom surface, which corresponds to the wall temperature T_w ($\approx 4T_\infty$). At the bottom surface, it is seen that the flow is in thermal equilibrium, once the rotation and vibration temperatures are equal to the translational temperature. It is important to recall that, the density increased at the vicinity of the gap bottom surface, as shown in Figure 5.19. As a result, the local mean free path decreased and the mean collision frequency increased and, therefore, the flow reached the thermal

equilibrium.

Kinetic temperature profiles for three sections along the cavity downstream surface, surface S5, are displayed in Figure 5.39 for cavity L/H ratio of 1 and 4. In this set of plots, X_L'' stands for the distance $(x - L_u - L)$ normalized by the cavity downstream length L_d . In addition, left- and right-column plots correspond to angle of attack of 10 and 20 degrees, respectively. Again, as a base of comparison, kinetic temperature ratio profiles for the flat-plate case are presented in the same plots.

According to Figure 5.39, it is seen that kinetic temperature profiles is affected by the presence of the cavity downstream along surface S5. The domain of this effect depends on the cavity L/H ratio as well as on the angle of attack α . It is also seen that the downstream disturbance region increases with increasing the angle of attack, for the conditions investigated. In attempting to access such angle-of-attack effect, Figure 5.40 illustrates the kinetic temperature ratio profiles, parameterized by the angle of attack α , for the same three sections, i.e., X_L'' of 0.01, 0.1 and 0.2. It may be recognized from this plots that the effect of the angle of attack is more pronounced in the shock layer, similar to that observed for the other primary properties.

In the following, it proves helpful to present the distribution of kinetic temperature inside the cavities. In doing so, Figs. 5.41, 5.42, and 5.43 displays the distribution of overall temperature ratio, T_O/T_∞ , along with streamline traces for the entire range of L/H ratio and angle of attack α investigated. According to these plots, the distribution of overall temperature inside the cavities is similar one to each other with decreasing the cavity L/H ratio. In addition, the same behavior is observed as the angle of attack increases from 10 to 20 degrees.

Figure 5.38 - Kinetic temperature ratio (T/T_∞) profiles for three sections along surface S3 parameterized by the cavity L/H ratio. Left and right columns correspond to angle of attack α of 10 and 20 degrees, respectively.

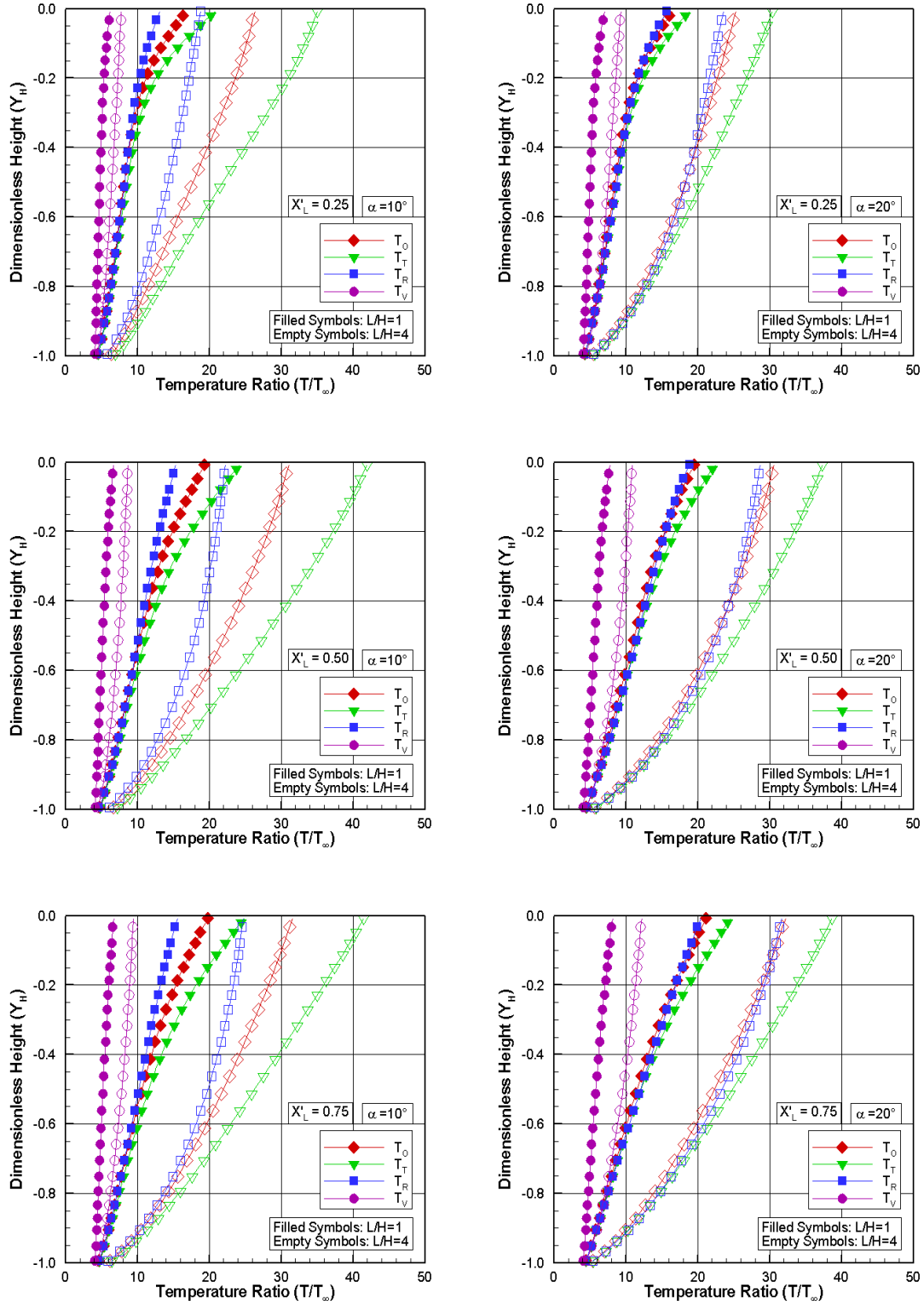


Figure 5.39 - Kinetic temperature ratio (T/T_∞) profiles for three sections along surface S5 parameterized by the L/H ratio. Left and right columns correspond to angle of attack α of 10 and 20 degrees, respectively.

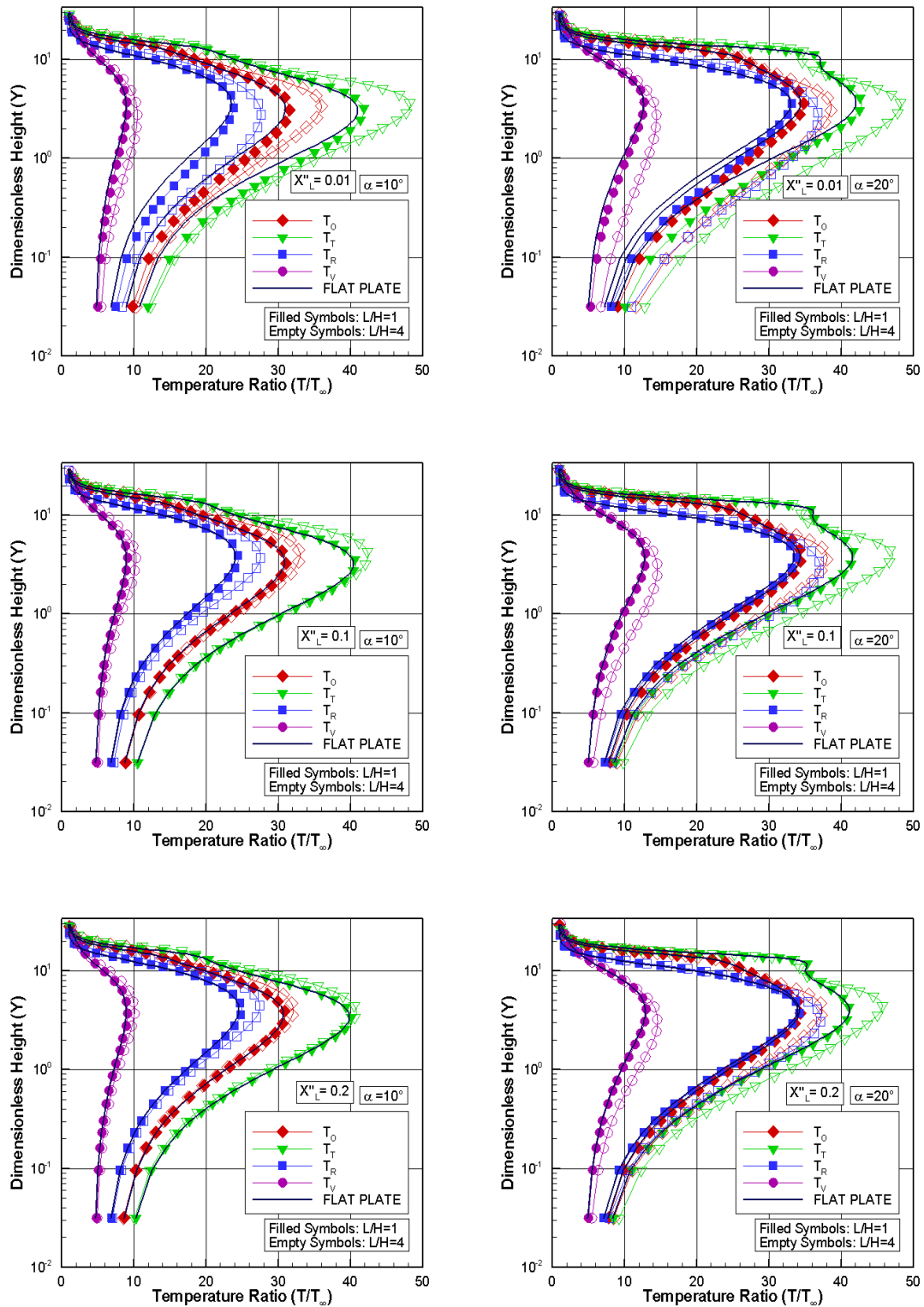


Figure 5.40 - Kinetic temperature ratio (T/T_∞) profiles for three sections along surface S5 parameterized by the angle of attack α . Left and right columns correspond to cavity L/H ratio of 1 and 4, respectively.

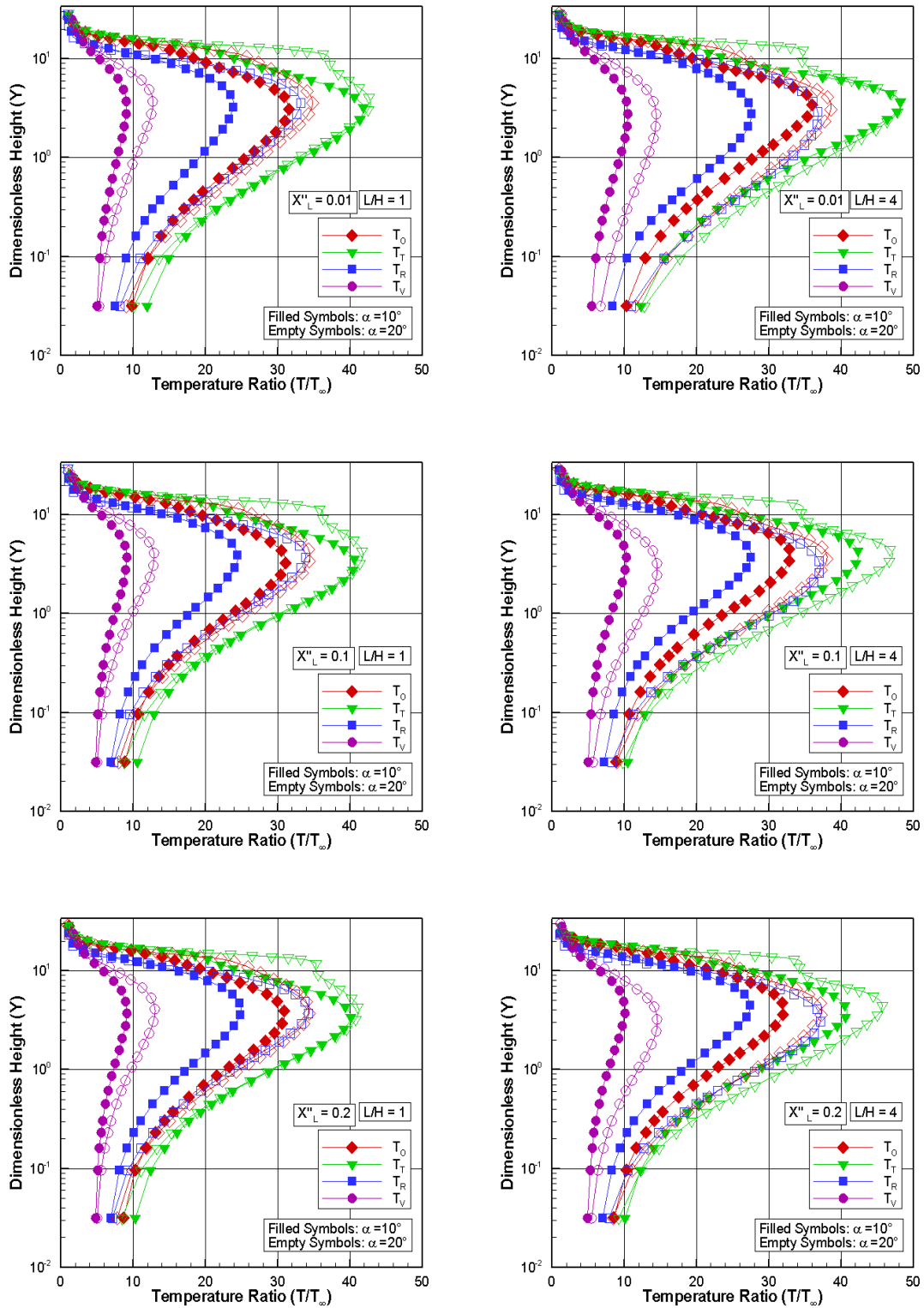


Figure 5.41 - Distribution of overall temperature ratio (T/T_∞) along with streamline traces inside the cavity for L/H ratio of 1 (top), 2, 3 and 4 (bottom), with angle of attack $\alpha = 10^\circ$.

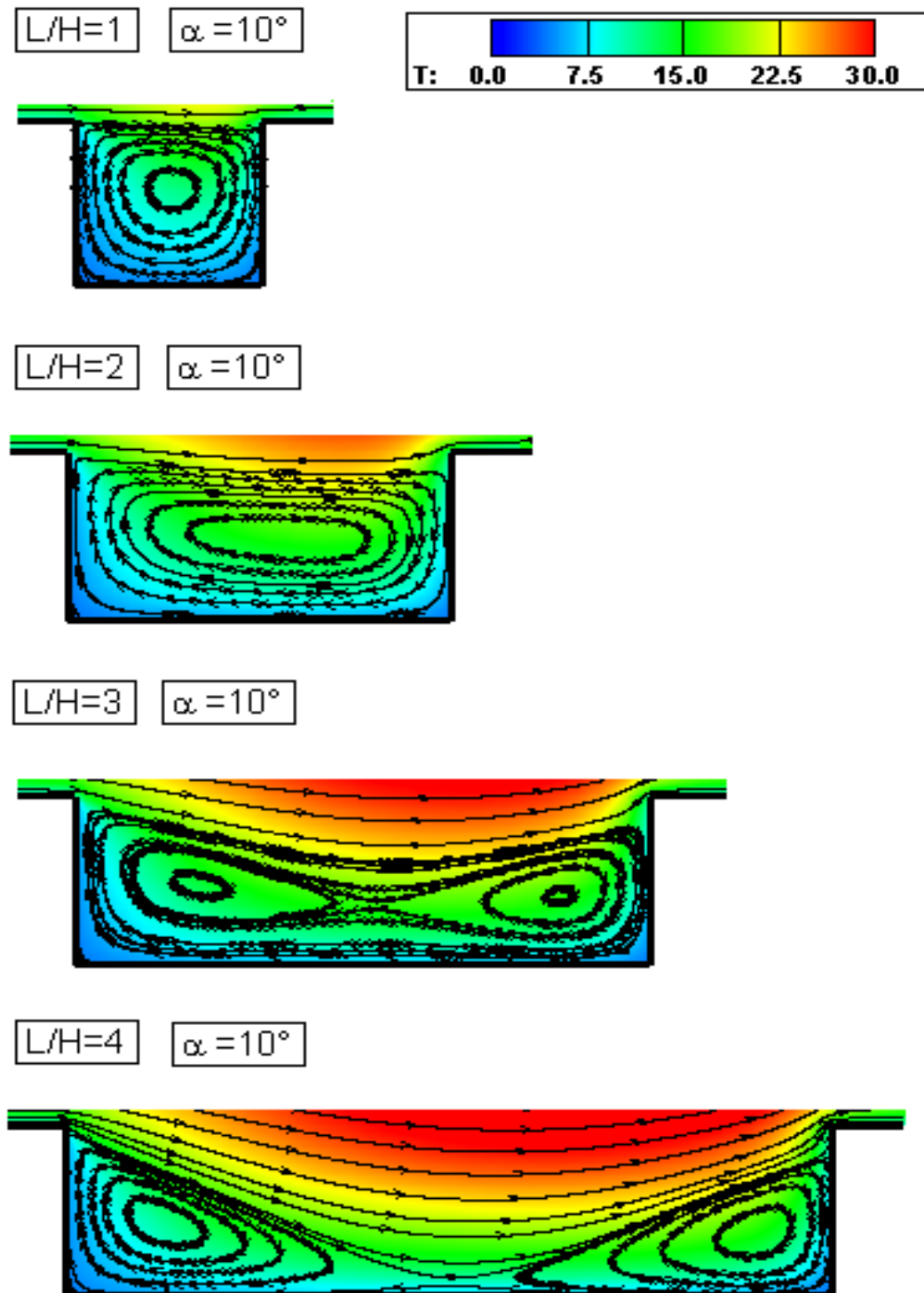


Figure 5.42 - Distribution of overall temperature ratio (T/T_∞) along with streamline traces inside the cavity for L/H ratio of 1 (top), 2, 3 and 4 (bottom), with angle of attack $\alpha = 15$ degrees.

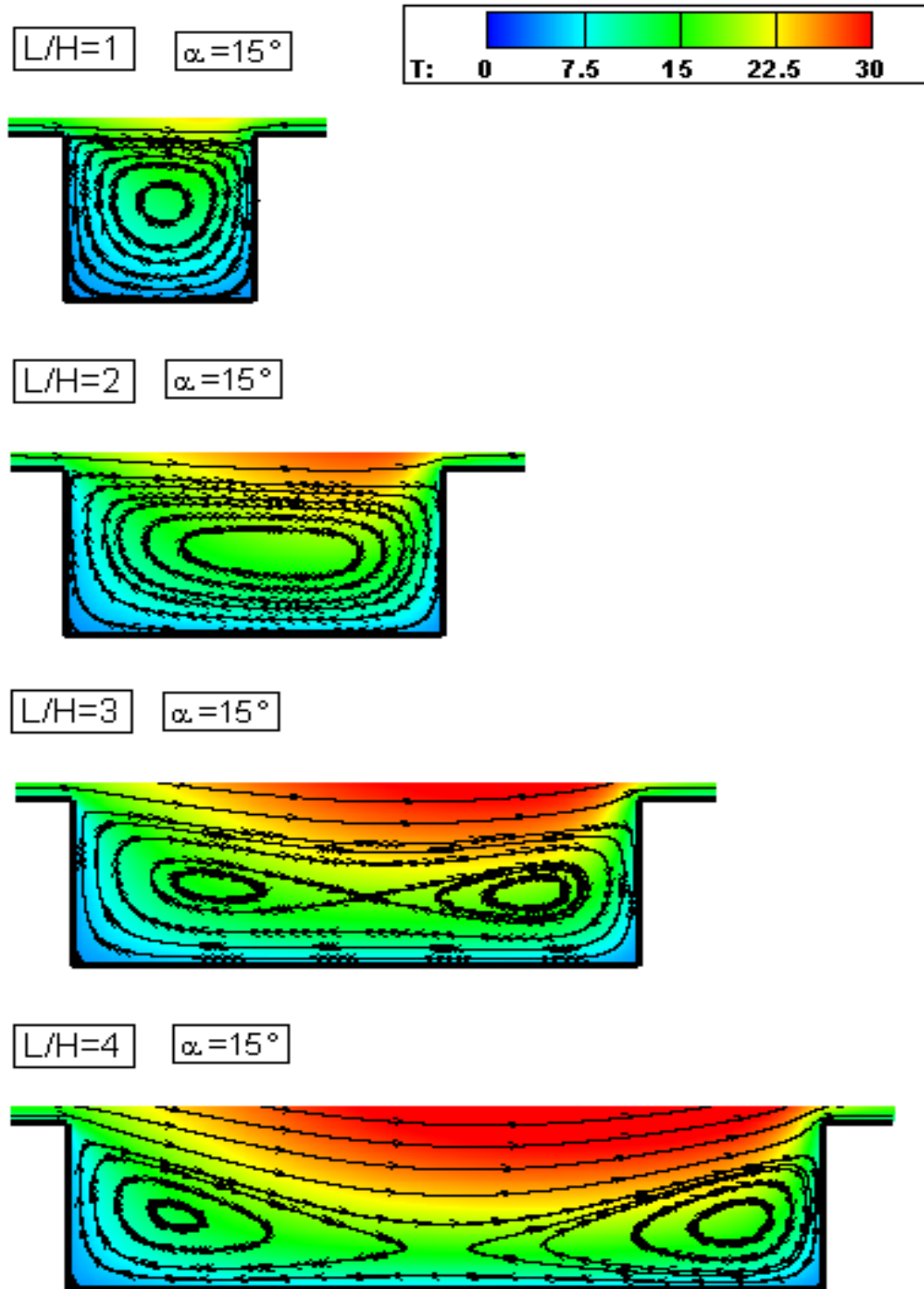
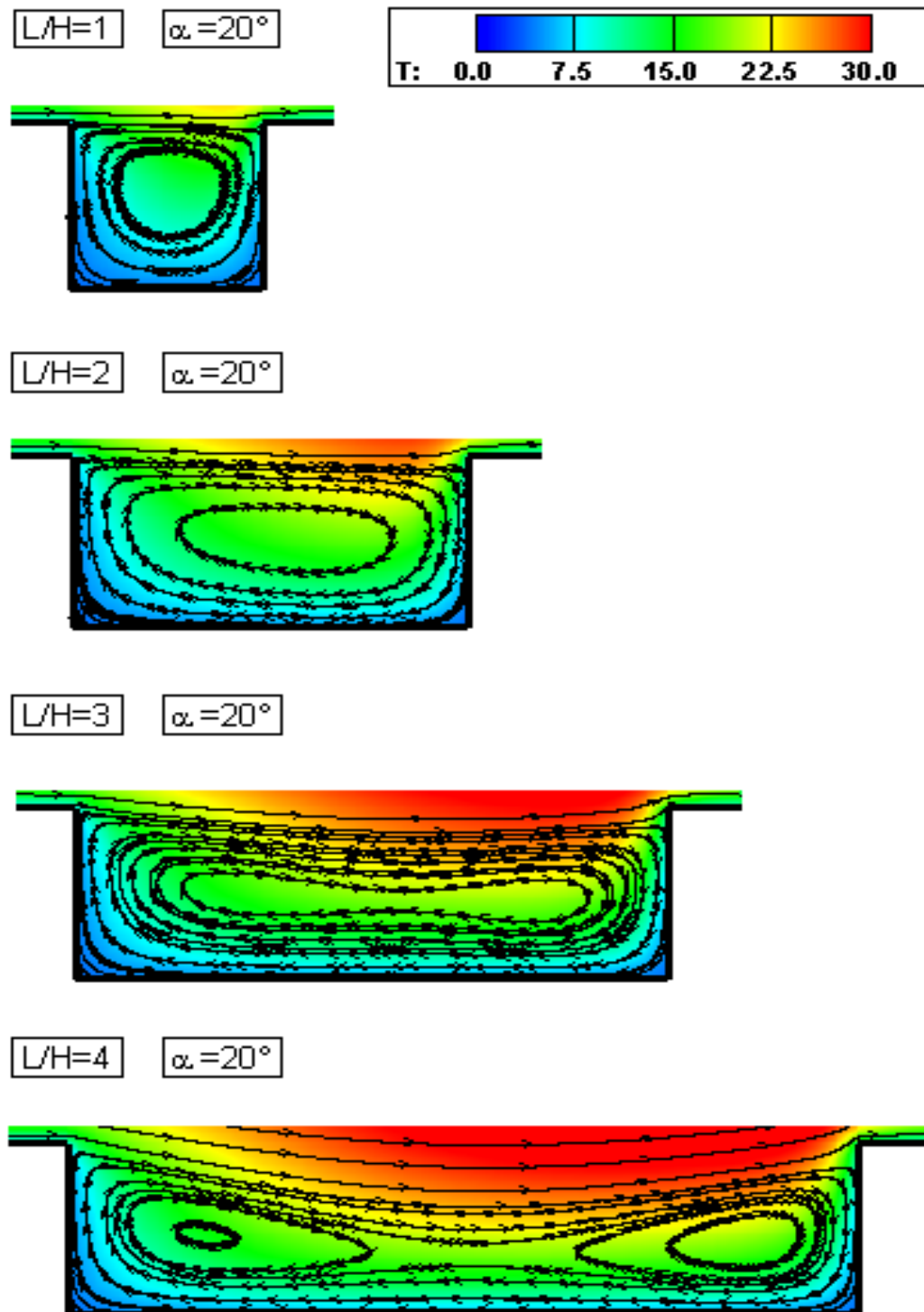


Figure 5.43 - Distribution of overall temperature ratio (T/T_∞) along with streamline traces inside the cavity for L/H ratio of 1 (top), 2, 3 and 4 (bottom), with angle of attack $\alpha = 20^\circ$.



5.2 Aerodynamics Surface Quantities

In order to present the DSMC results coherently, this section focuses on the comparison of the aerodynamics surface quantities due to variations on the cavity L/H ratio and on the angle of attack α , expressed in coefficient form. The aerodynamics surface quantities of particular interest in the present work are the number flux, heat transfer, pressure and skin friction.

5.2.1 Number Flux

Effects of the cavity L/H ratio on the number flux are illustrated in Figures 5.44 and 5.45 for angle of attack of 10 and 20 degrees, respectively. In this group of plots, left-column plots refer to the distribution of the number flux along the cavity upstream and downstream surfaces, i.e., surfaces S1 and S5, while right-column plots correspond to the distribution on the surfaces inside the cavity, i.e., surfaces S2, S3, and S4. Results for angle of attack of 15 degrees are intermediate, and they are not shown in this group of plots. In addition, N_f represents the number flux N normalized by $n_\infty U_\infty$, where n_∞ is the freestream number density and U_∞ is the freestream velocity, X is the length x normalized by the freestream mean free path λ_∞ , X'_L is the distance $(x - L_u)$ normalized by the cavity length L , and Y_H represent the height y normalized by the cavity height H . Furthermore, as a base of comparison, the number flux distribution for the flat-plate case is also illustrated in this group of plots.

On examining first the left-column plots, it is noticed that the number flux behavior to the surfaces outside the cavity basically follows that presented by the flat-plate case for the L/H ratio investigated in this work. Except close to the cavity position, no upstream disturbance is caused by the presence of the cavity. However, close to the upstream cavity corner, i.e., the surface-S1/surface-S2 junction, there is a decrease in the number flux due to the flow expansion around the upstream corner. A magnified view of this behavior is shown in detail in the middle plot. It is seen that the upstream disturbance increases with increasing the cavity L/H ratio.

Still referring to the left-column plots, along surface S5, appreciable changes, as compared to the flat-plate case, are observed in the number flux distribution at the vicinity of the cavity shoulder, i.e., at the surface-S4/surface-S5 junction. These changes depend on the cavity L/H ratio as well as on the angle of attack α . Another feature that deserves attention is the significant drop in the number flux at the end of surface S5. This reduction is due to vacuum condition used as the boundary

Figure 5.44 - Dimensionless number flux (N_f) distribution along the cavity surfaces parameterized by the cavity L/H ratio for 10-degree angle of attack.

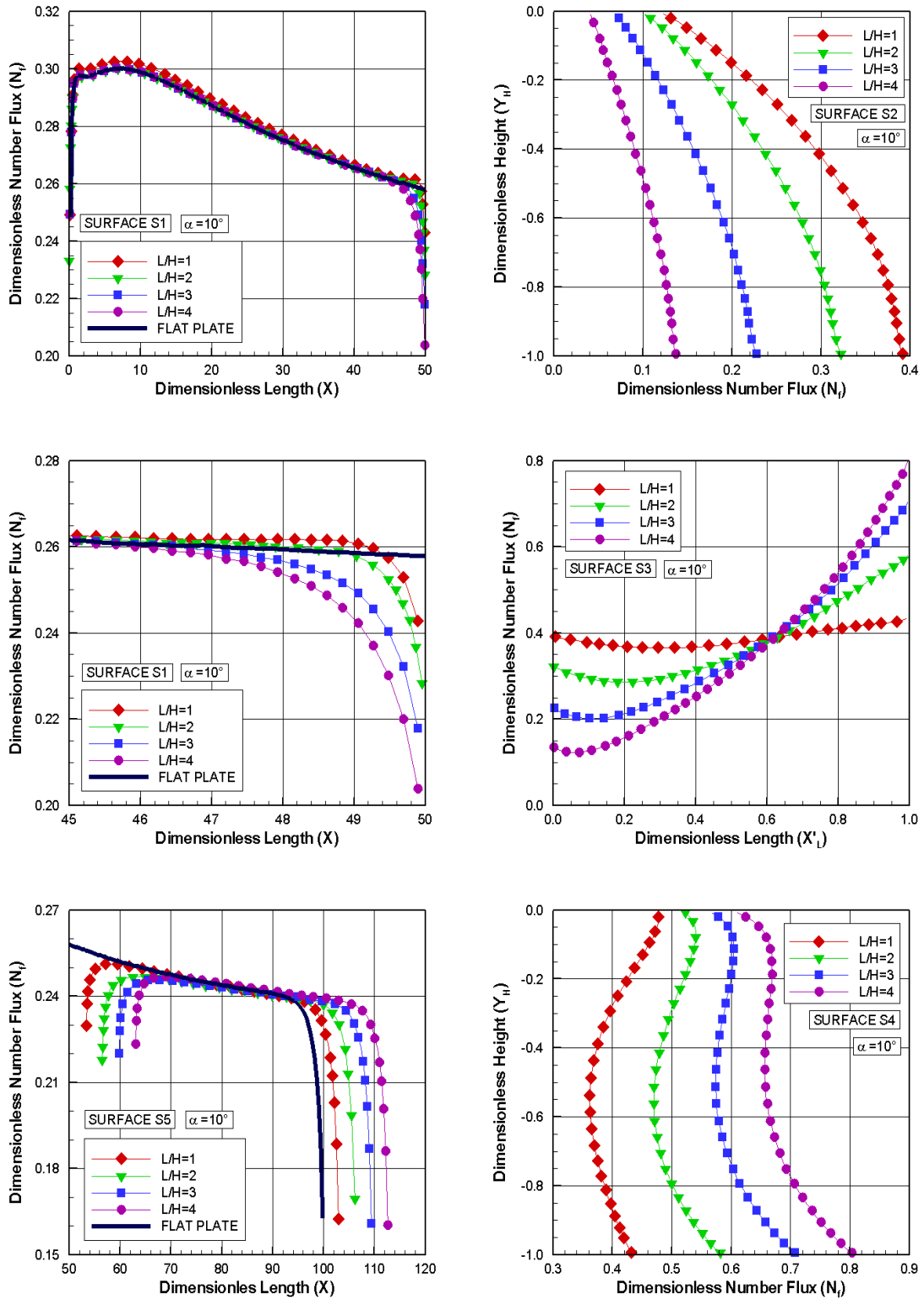
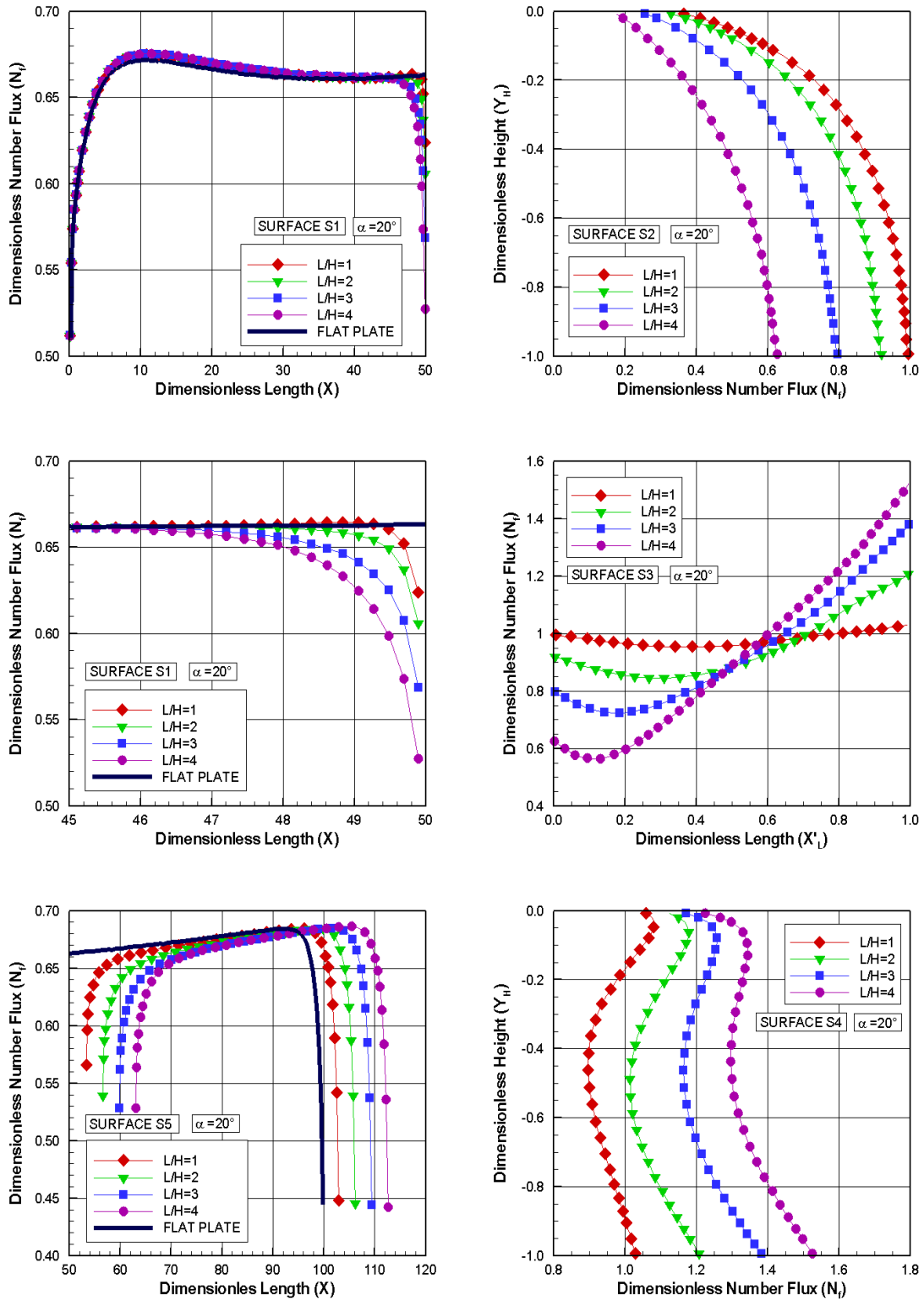


Figure 5.45 - Dimensionless number flux (N_f) distribution along the cavity surfaces parameterized by the cavity L/H ratio for 20-degree angle of attack.



condition at the end of the computational domain, as explained in Chapter 3. It should be also remarked that the total length of the flat plate is equal to $100\lambda_\infty$.

Turning next to right-column plots, for the backward face, surface S2, the number flux is low at the cavity shoulder, surface-S1/surface-S2 junction, it increases gradually along the surface up to the corner at the bottom surface, surface S3, where it reaches the maximum value. In addition, this maximum value decreases with increasing the cavity L/H ratio and increases significantly with increasing the angle of attack α . Along the cavity floor, surface S3, the number flux behavior also relies on L/H ratio and on the angle of attack α . It is observed that the number flux decreases at the vicinity of the surface S2 and increases at the vicinity of surface S4 with increasing the L/H ratio and with increasing the angle of attack α . Finally, along the forward face, surface S4, N_f basically increases from the corner, at the top surface, up to the bottom of the cavity, except for the $L/H = 1$ case. In addition, it is also observed that the number flux to the forward face, surface S4, increases with increasing L/H ratio, in contrast to that behavior observed for surface S2. In fact, this is an expected behavior in the sense that it is directly related to the flow recirculation inside the cavities, as pointed out earlier. Due to the clockwise flow recirculation, at the vicinity of the surface S4, density is higher than that close to the surfaces S2 and S3. Therefore, a larger flux of molecules colliding to this surface is expected.

In order to examine the differences in the number flux distribution due the angle-of-attack effect, Figures 5.46 and 5.47 illustrate the distribution of the number flux along the cavity surfaces, parameterized by the angle of attack, for cavity L/H ratio of 1 and 4, respectively. Results for the other cavity L/H ratio are intermediate, and they will not be shown in this set of plots. In addition, results obtained early by Palharini (PALHARINI, 2010) for zero-degree angle of attack are shown in this set of plots.

Based on these plots, it is clearly noticed that the number flux increases significantly with increasing the angle of attack. This is an expected behavior in the sense that density increases inside the cavities with the angle-of-attack rise, for the L/H ratio investigated. In addition, as the angle of attack increases from 0 to 20 degrees, the body geometry changes aerodynamically from a sharp body to a blunt body for the oncoming flow. As a result, the geometry becomes less streamlined and the collision frequency of the molecules with the surfaces increases. Therefore, the number flux to the cavity surfaces increases.

Figure 5.46 - Dimensionless number flux (N_f) distribution along the cavity surfaces parameterized by the angle of attack α for the L/H ratio of 1.

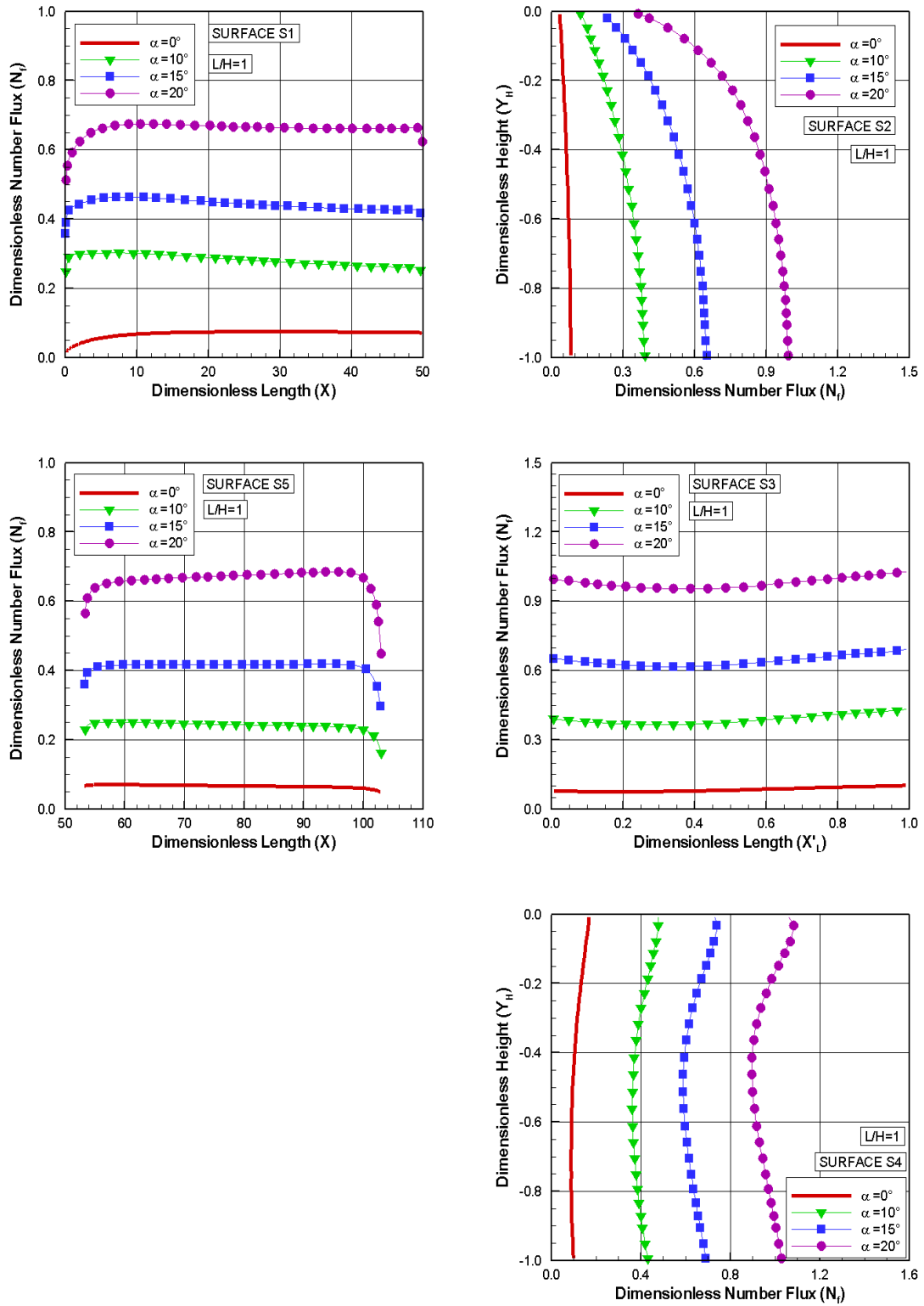
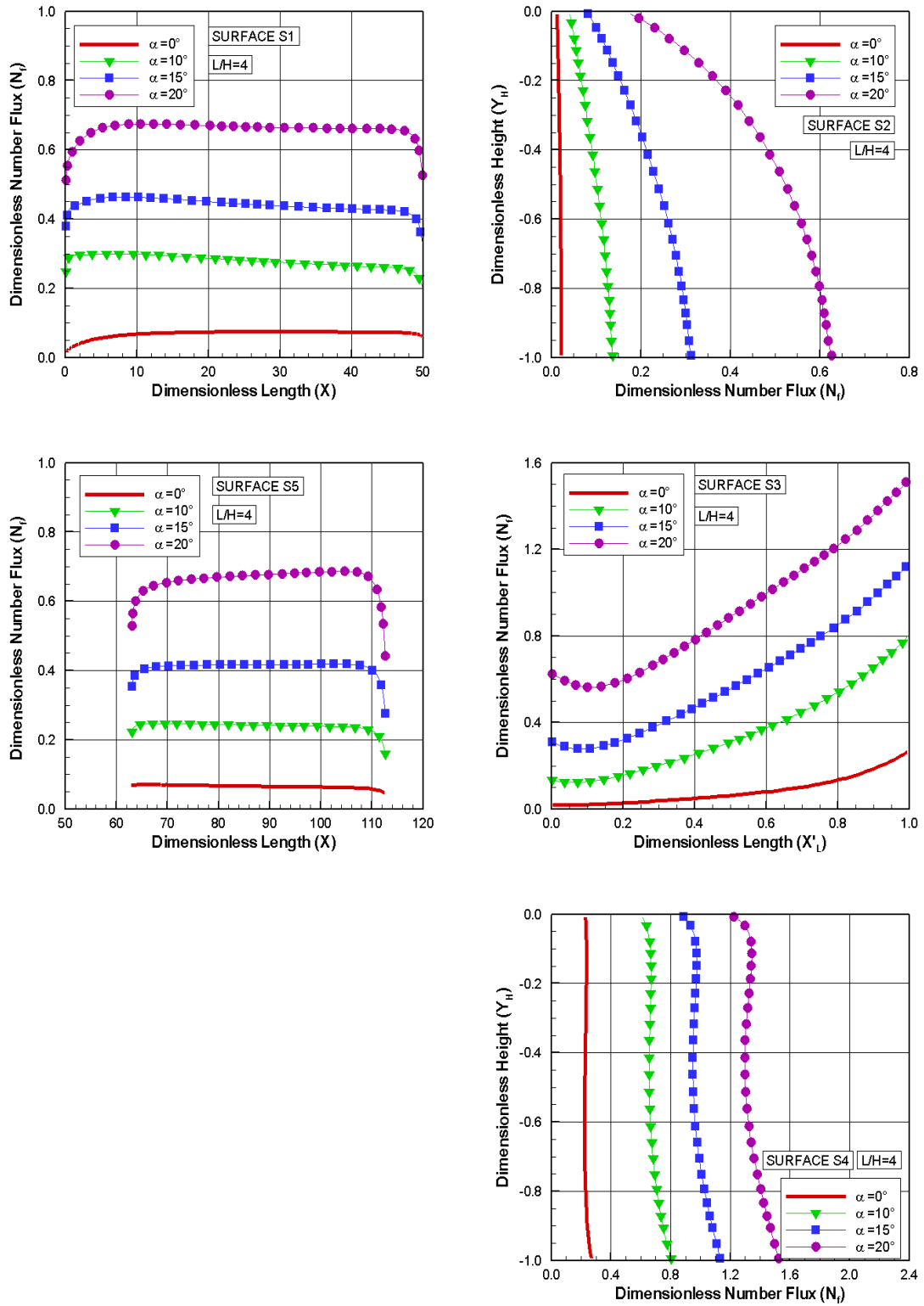


Figure 5.47 - Dimensionless number flux (N_f) distribution along the cavity surfaces parameterized by the angle of attack α for the L/H ratio of 4.



5.2.2 Heat Transfer Coefficient

The heat transfer coefficient is defined by,

$$C_h = \frac{q_w}{\frac{1}{2}\rho_\infty U_\infty^3} \quad (5.5)$$

where q_w is the net heat flux, ρ_∞ is the freestream density and U_∞ is the freestream velocity.

The net heat flux q_w to the cavity surface is calculated by the net energy flux of the molecules impinging on the surface. A flux is considered as positive when it is directed toward the surface. In this manner, the net heat flux q_w is related to the sum of the translation, rotation and vibration energies of both incident and reflected molecules as follows,

$$q_w = q_i - q_r = \frac{F_N}{A\Delta t} \left\{ \sum_{j=1}^N \left[\frac{1}{2}m_j c_j^2 + e_{rj} + e_{vj} \right]_i - \left[\frac{1}{2}m_j c_j^2 + e_{rj} + e_{vj} \right]_r \right\} \quad (5.6)$$

where F_N is the number of real molecules represented by a single simulated molecule, Δt is the time step, A stands for the surface area, N is the number of molecules colliding with the surface by unit time and area, m is the mass of the molecules, c is the velocity of the molecules, e_R and e_V are the rotational and vibrational energies, respectively. Subscripts i and r refer to incident and reflect molecules.

The cavity L/H ratio effect on the heat transfer coefficient along all surfaces is demonstrated in Figs. 5.48 and 5.49 for angle of attack of 10 and 20 degrees, respectively. Based on the left-column plots, the value of C_h along surface S1 starts from a peak value at the leading edge and decreases monotonically downstream along the body surface, for the conditions investigated. This peak value increases with increasing the angle of attack α . In addition, no upstream effect is observed on the heat transfer coefficient along surface S1 far from the cavity position, since the heat transfer coefficient for the flat plate with a cavity is basically the same as that of the flat-plate case, i.e., a flat plate without a cavity. However, at the vicinity of the cavity position, station $X = 50$, the heat transfer coefficient is smaller than that for the flat-plate case with increasing the L/H ratio. Conversely, along surface S5, it is clearly seen that the heat transfer coefficient C_h is larger than that for the flat-plate case, especially at the vicinity of the cavity downstream corner, defined by

Figure 5.48 - Heat transfer coefficient (C_h) distribution along the cavity surfaces parameterized by the cavity L/H ratio for for 10-degree angle of attack.

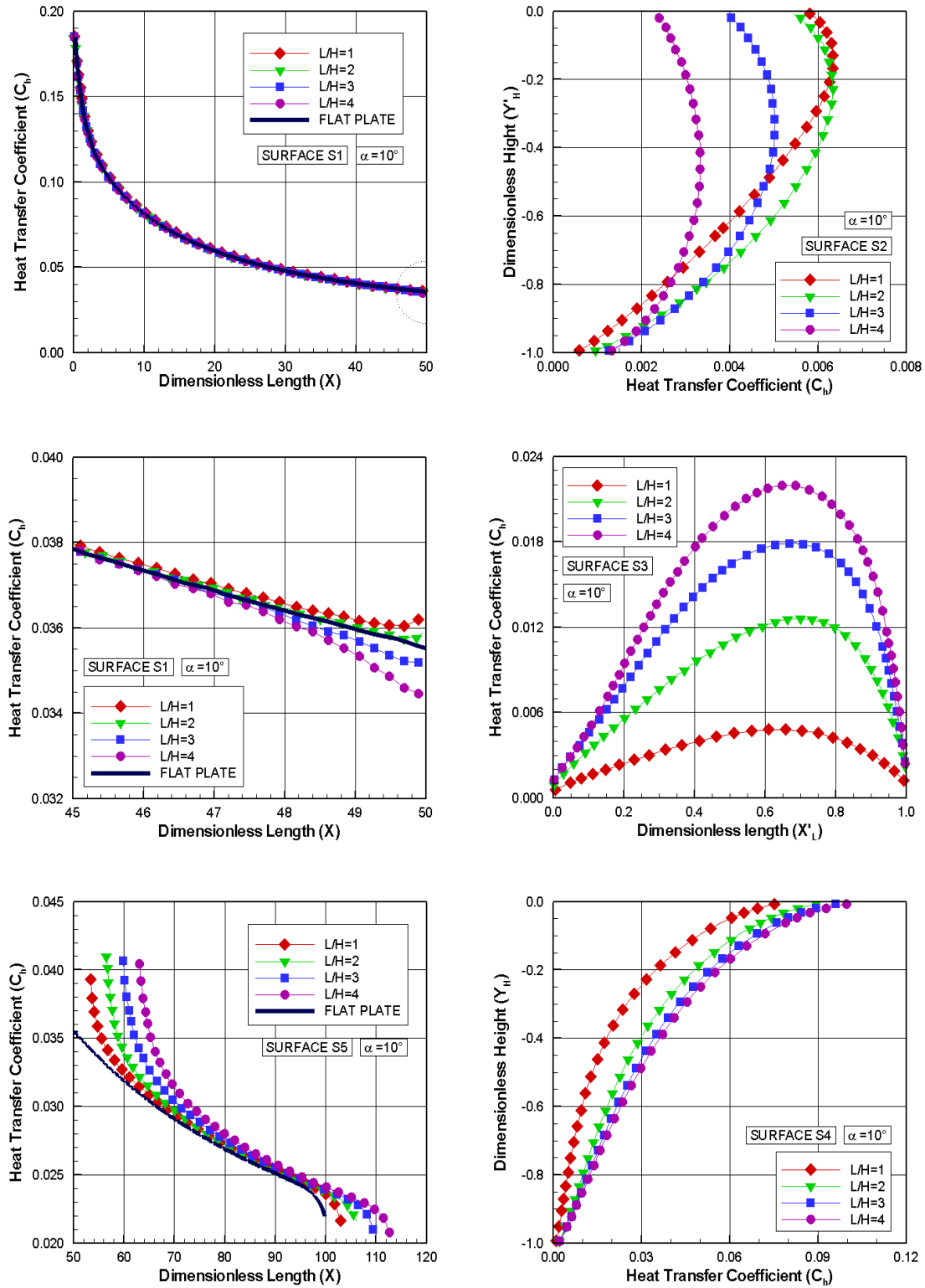
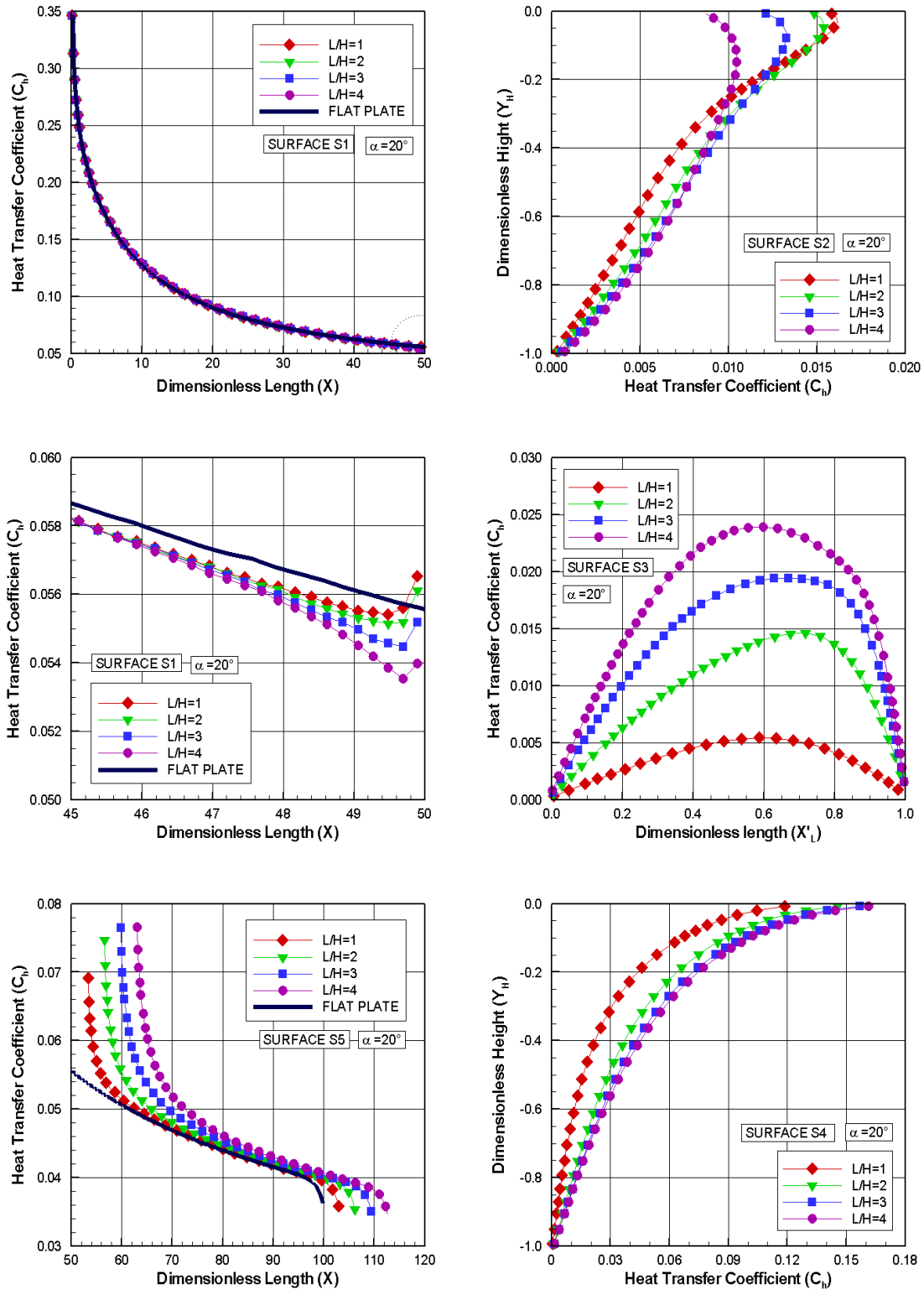


Figure 5.49 - Heat transfer coefficient (C_h) distribution along the cavity surfaces parameterized by the cavity L/H ratio for for 20-degree angle of attack.



the surface-S4/surface-S5 junction. Again, this peak value increases with increasing the angle of attack α . Finally, as the flow moves downstream along surface S5, the heat transfer coefficient C_h recovers the value observed for the flat-plate case.

Focusing on the right-column plots, for backward surface, surface S2, the heat transfer coefficient C_h presents high values close to the shoulder, $Y_H = 0$. Then, it increases and reaches maximum values along the upper half part of the surface. Afterwards, it decreases and reaches low values at the concave corner, surface-S2/surface-S3 junction, $Y_H = -1$. In addition, it is observed that the section Y_H where the heat transfer coefficient achieves the maximum values depends on the cavity L/H ratio and the angle of attack α . This behavior is related to the flow topology inside the cavity, since it changes not only with the cavity L/H ratio but also with the angle of attack α .

Still focusing on the right-column plots, particular attention is paid to the behavior of the heat transfer coefficient at the upper and lower corners on surface S2. At section $Y_H = 0$, the heat transfer coefficient decreases with increasing the cavity L/H ratio. Conversely, at section $Y_H = -1$, the heat transfer coefficient increases with increasing the cavity L/H ratio. In the following, for the cavity floor, surface S3, the heat transfer coefficient presents very low values at both concave corners, and maximum values around section $X_L \approx 0.7$. It is also observed that the maximum value for the heat transfer coefficient increases with increasing the cavity L/H ratio as well as increasing the angle of attack α . Furthermore, maximum values for heat transfer on the cavity floor are at least one order of magnitude smaller than the peak values observed in surface S1. Then, along the forward face, surface S4, the heat transfer coefficient present the minimum value at the concave corner, surface-S3/surface-S4 junction, and increases upstream along the surface up to the convex corner, surface-S4/surface-S5 junction.

In the following, a critical assessment of the angle-of-attack effects is provided by Figures 5.50 and 5.51. This group of plots displays the distribution of the heat transfer coefficient C_h along the five cavity surfaces, parameterized by the angle of attack α , for gap L/H ratio of 1 and 4, respectively. For comparison purpose, results obtained early by Palharini (PALHARINI, 2010) for zero-degree angle of attack are shown in the same plots.

According to this group of plots, for zero-degree angle of attack, the maximum value for heat transfer coefficient along surface S1 is $C_h = 0.029$, which takes place at section $X = 8.8$, for the cavity L/H ratio investigated. Inside the cavity, peak

Figure 5.50 - Heat transfer coefficient (C_h) distribution along the cavity surfaces parameterized by the angle of attack α for the cavity L/H ratio of 1.

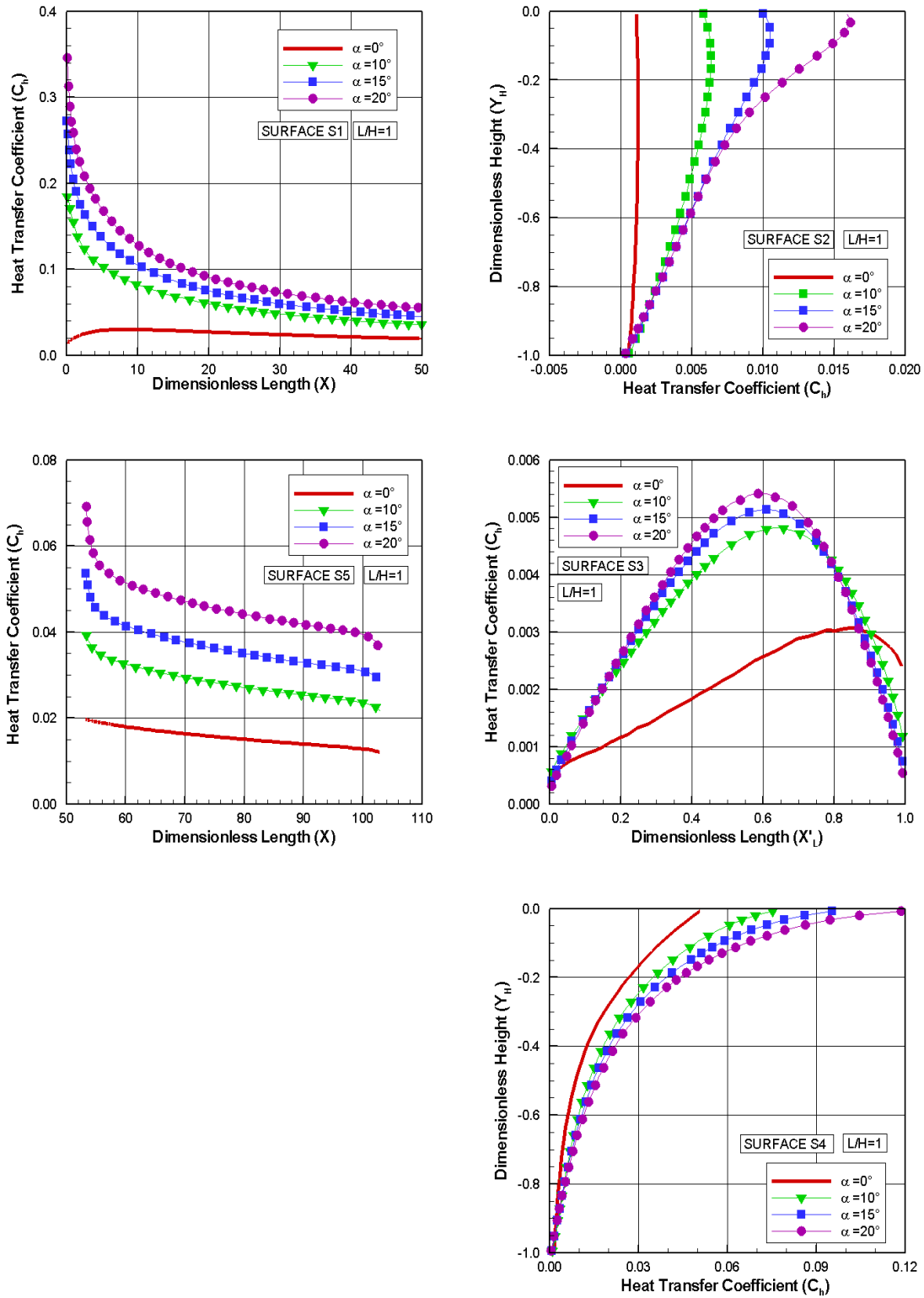
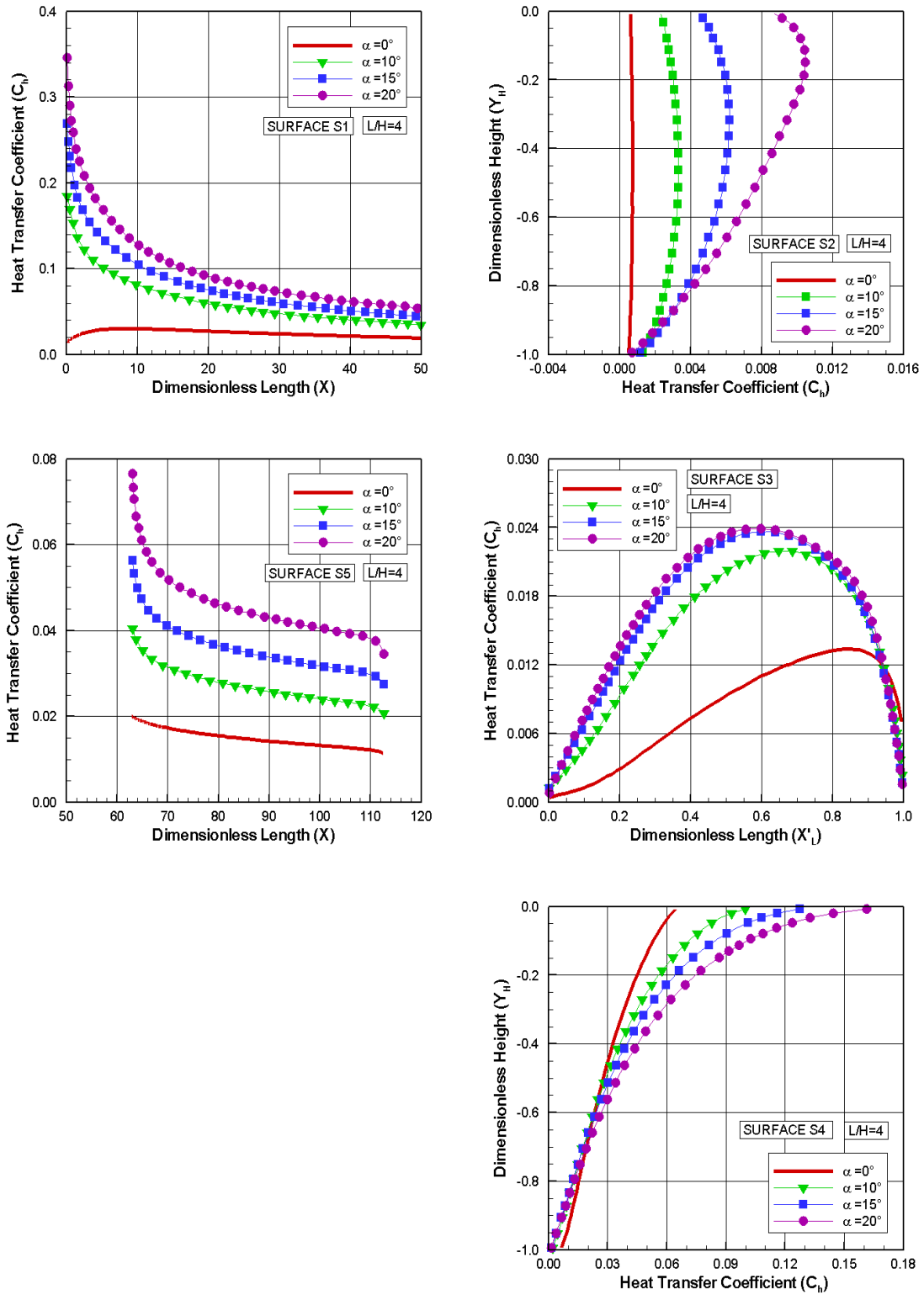


Figure 5.51 - Heat transfer coefficient (C_h) distribution along the cavity surfaces parameterized by the angle of attack α for the cavity L/H ratio of 4.



values for the heat transfer coefficient take place along surface S4, C_h is 0.049 and 0.064 for the cavity L/H ratio of 1 and 4, respectively. Therefore, for zero-degree angle of attack, the maximum values for the heat transfer coefficient to surface S4 are larger than that to surface S1. As a result, the presence of the cavity on the surface of a hypersonic vehicle may not be ignored. On the other hand, for a cavity at incidence, peak values for C_h on surface S1 take place at the flat-plate leading edge, and they are 0.184, 0.268 and 0.345 for angle of attack of 10, 15 and 20 degrees, respectively, for the conditions investigated. In addition, along surface S4, maximum values for C_h are observed for cavity L/H ratio of 4, and they are 0.099, 0.127 and 0.163 for angle of attack of 10, 15 and 20 degrees, respectively. Therefore, for angle of attack in the range of 10 to 20 degrees, maximum values for the heat transfer coefficient to surface S4 are smaller than that to surface S1. Consequently, in the design of a hypersonic vehicle at incidence, the presence of a cavity may be ignored in terms of heat flux to the vehicle surface, for the conditions investigated.

5.2.3 Pressure Coefficient

The pressure coefficient C_p is defined by,

$$C_p = \frac{p_w - p_\infty}{\frac{1}{2}\rho_\infty U_\infty^2} \quad (5.7)$$

where p_w is the wall pressure.

The wall pressure p_w on the cavity surface is calculated by the sum of the normal momentum fluxes of both incident and reflected molecules at each time step as follows,

$$p_w = p_i - p_r = \frac{F_N}{A\Delta t} \sum_{j=1}^N \{[(mv)_j]_i - [(mv)_j]_r\} \quad (5.8)$$

where v is the velocity component of the molecule in the surface normal direction.

The impact on pressure coefficient distribution due to changes on the cavity L/H ratio is illustrated in Figures 5.52 and 5.53 for angle of attack of 10 and 20 degrees, respectively. Again, left-column plots refer to the pressure coefficient distribution along the upstream and downstream surface, i.e., surfaces S1 and S5, while right-column plots correspond to the C_p distribution along surfaces inside the cavity, i.e.,

surfaces S2, S3 and S4.

Referring to the left-column plots in these figures, it is seen that the pressure coefficient distribution follows the same trend as that presented by the number flux in the sense that, along surfaces S1 and S5, the pressure coefficient presents the same behavior for the flat-plate case, except at the vicinity of the cavity shoulders. At the vicinity of these shoulders, a significant drop is observed due to the flow expansion around these shoulders. Moreover, this pressure decrease is associated with the reduction in the number flux, as shown in Figures 5.44 and 5.45.

Turning to the right-column plots in these figures, it is noticed that the pressure coefficient C_p along the cavity backward surface, surface S2, basically increases from the top to the bottom corner, reaching the maximum value at the surface-S2/surface-S3 junction. It is also noticed that pressure coefficient C_p decreases with increasing the cavity L/H ratio. In what follows, for the cavity floor, surface S3, the pressure coefficient C_p increases along the surface, and reaches maximum values at the concave corner, at the surface-S3/surface-S4 junction. Of particular interest is the impact of the cavity L/H ratio in the pressure coefficient along surface S3. It is seen that, close to the backward face, C_p decreases with increasing the cavity L/H ratio. In contrast, close to the forward face, C_p increases with increasing the cavity L/H ratio. Finally, along the cavity forward face, surface S4, the pressure coefficient behavior is in contrast to that observed along surface S2 in the sense that C_p presents the lower value at section $Y_H = -1$, and increases upward along the surface, reaching the maximum value at the shoulder, $Y_H = 0$.

It is noteworthy that the pressure coefficient behavior along the cavity surfaces is directly related to the flow topology inside the cavity. As shown in Figures 5.9 to 5.11, the flow inside the cavity is characterized by a clockwise recirculation region for the cavity L/H ratio of 1 and 2. Conversely, for the cavity L/H of 3 and 4, the flow is characterized by two vortex systems at the vicinity of the surfaces S2 and S4. In addition, the flow experiences an expansion close to surface S2, and a compression close to surface S4.

Proceeding in a manner analogous to number flux, Figures 5.54 and 5.55 display the pressure coefficient distribution along all cavity surfaces, parameterized by the angle of attack α , for cavity L/H ratio of 1 and 4, respectively. Based on this set of plots, it is clearly seen that pressure coefficient C_p increases significantly with increasing the angle of attack. As a base of comparison, for zero-degree angle of attack, the maximum value for C_p is around 0.039 at station $X = 23.9$ along surface S1, in-

Figure 5.52 - Pressure coefficient C_p distribution along the cavity surfaces parameterized by the L/H ratio for 10-degree angle of attack.

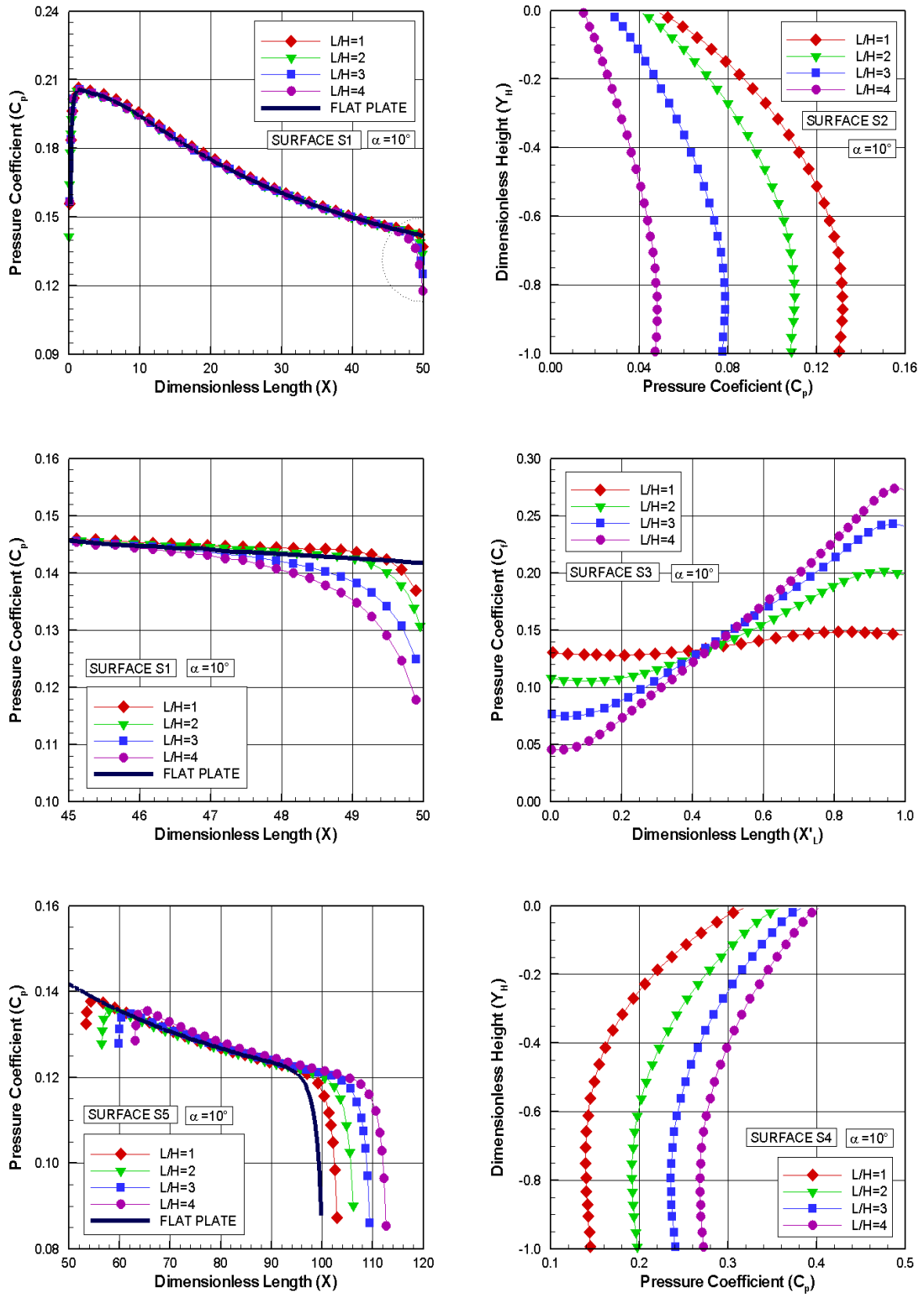


Figure 5.53 - Pressure coefficient C_p distribution along the cavity surfaces parameterized by the L/H ratio for 20-degree angle of attack.

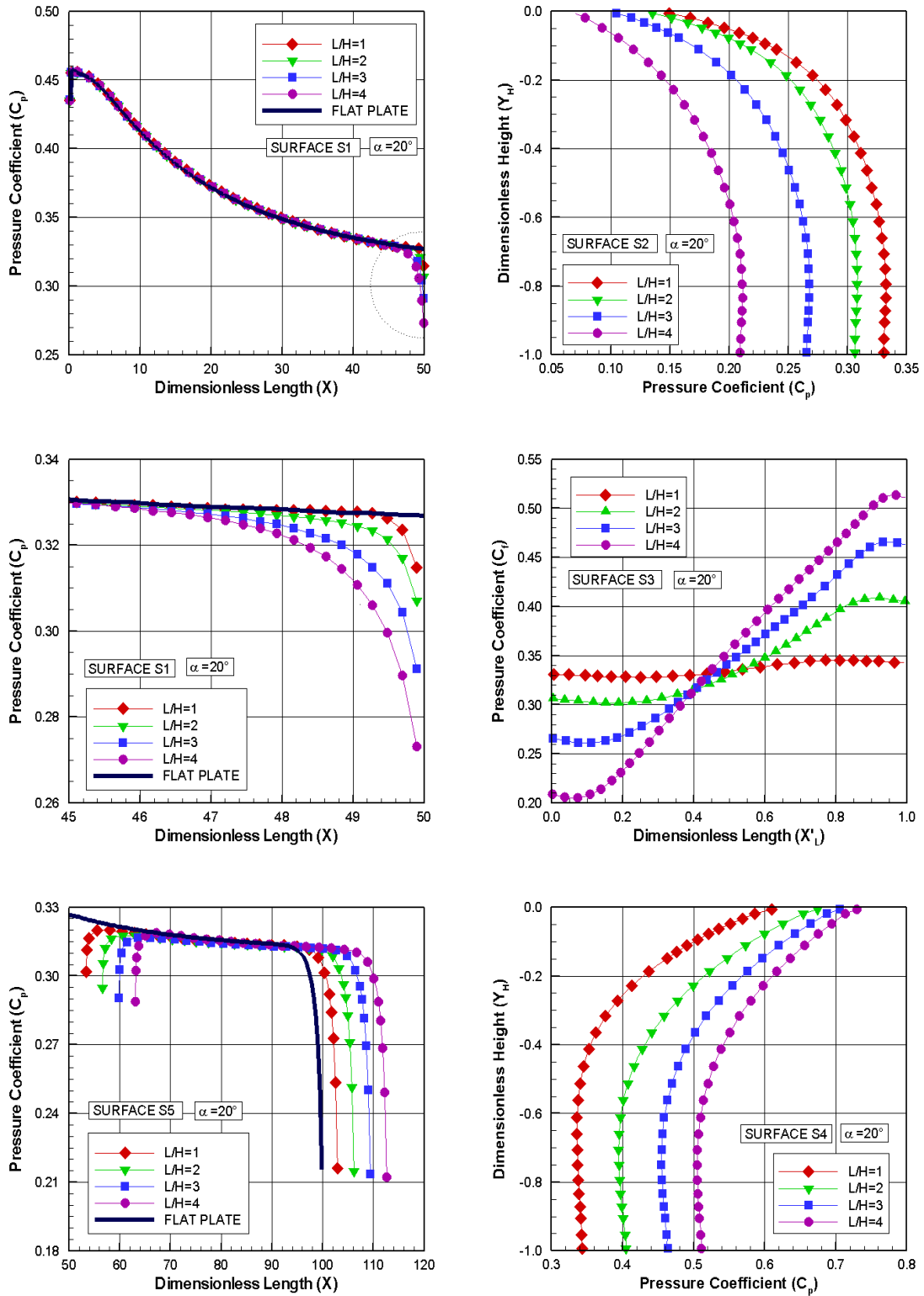


Figure 5.54 - Pressure coefficient (C_p) distribution along the cavity surfaces parameterized by the angle of attack α for the cavity L/H ratio of 1.

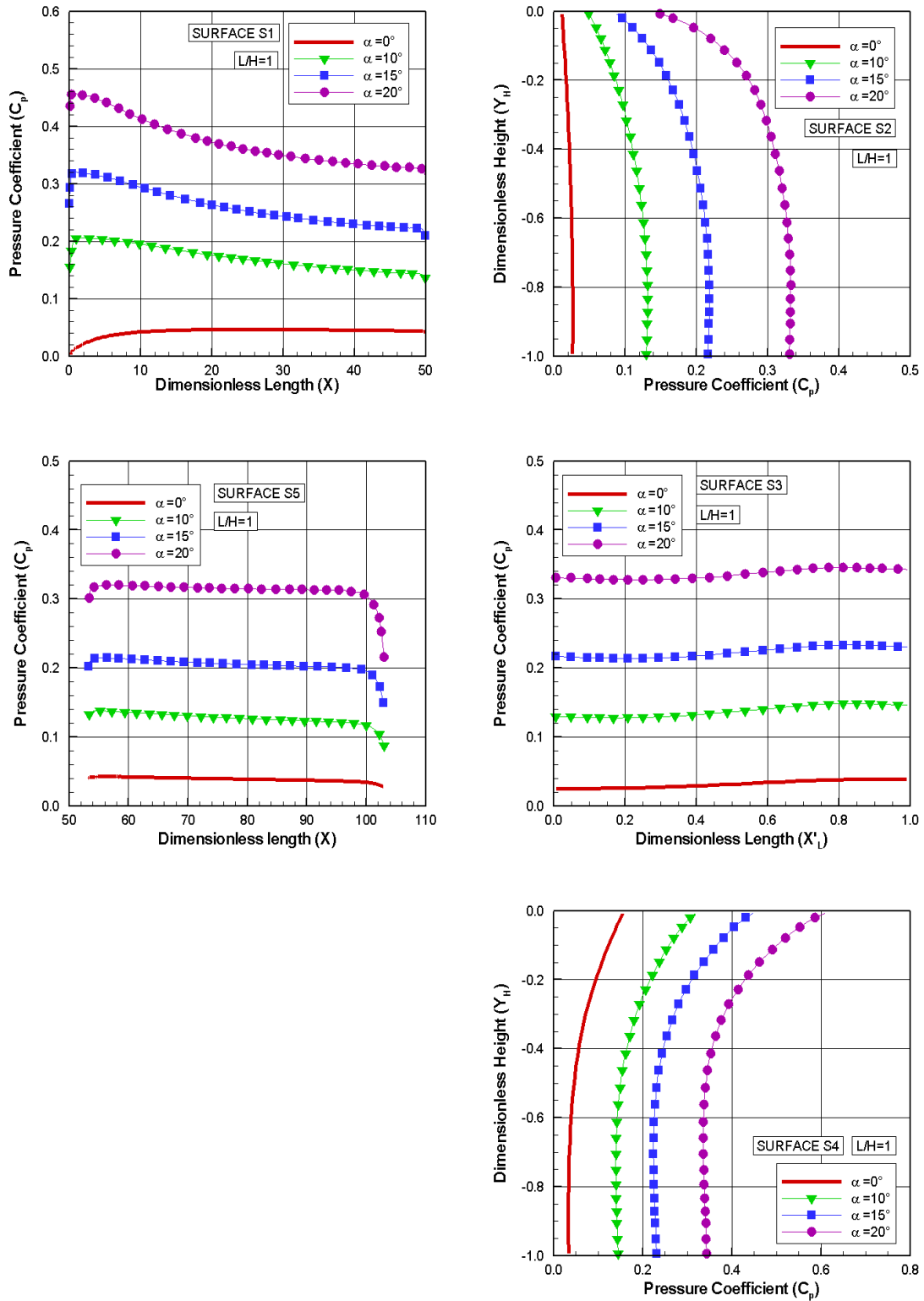
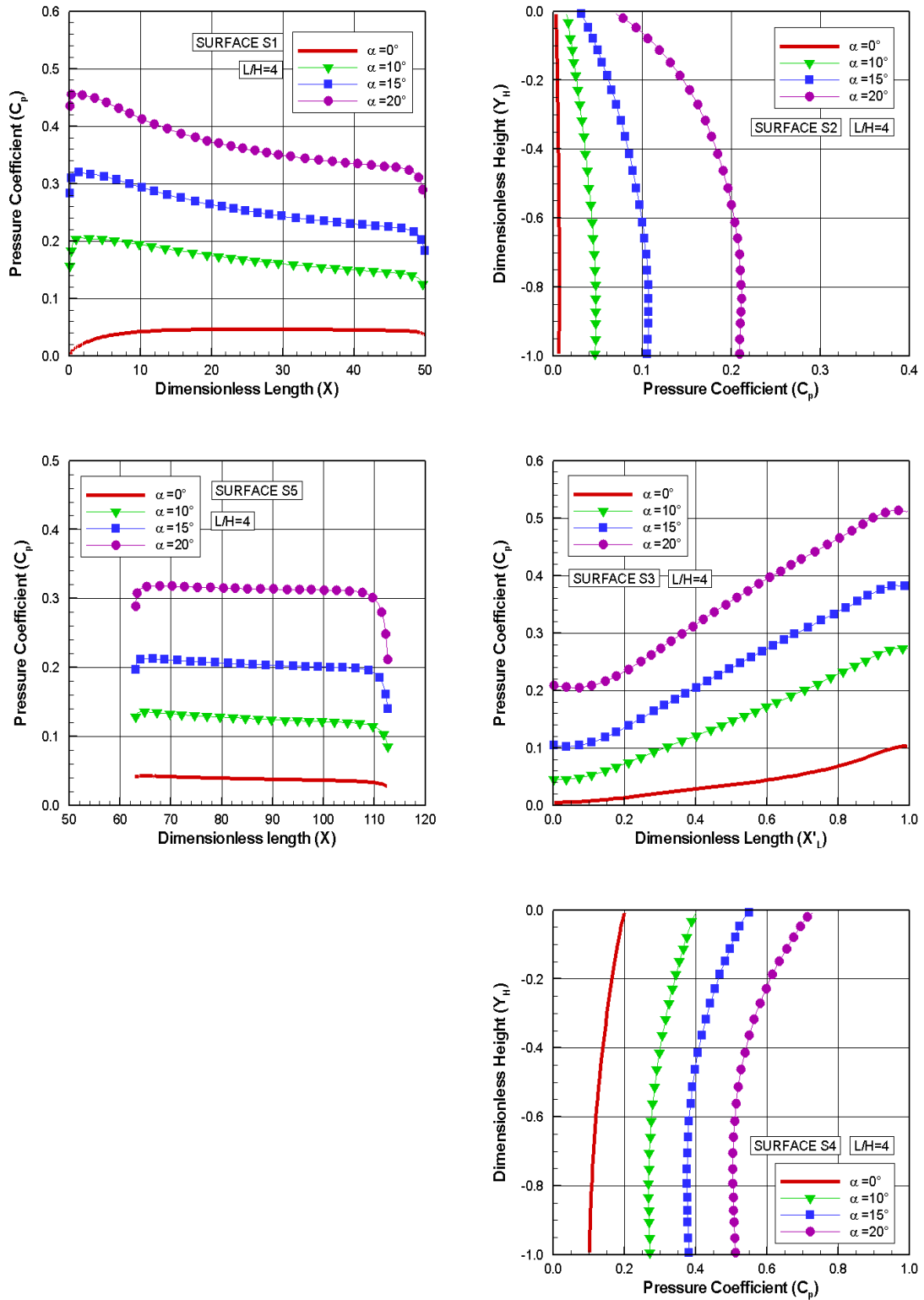


Figure 5.55 - Pressure coefficient (C_p) distribution along the cavity surfaces parameterized by the angle of attack α for the cavity L/H ratio of 4.



dependently of the L/H ratio. In contrast, this maximum value increases to 0.205, 0.320, and 0.457, at station X of 1.02, 0.95 and 0.78, for angle of attack of 10, 15 and 20 degrees, respectively. It is also seen that the maximum value approaches the leading edge of the plate with increasing the angle of attack. As mentioned earlier, with increasing the angle of attack, the body geometry changes aerodynamically from a sharp body to a blunt body for the oncoming flow. As a result, the geometry becomes less streamlined and the collision frequency of the molecules with the surfaces increases, therefore, pressure coefficient increases.

In the following, it proves instructive to compare the maximum values for the pressure coefficient observed in the cavities with that for a flat plate without a cavity, for the corresponding angle of attack α . For comparative purpose, for a cavity L/H ratio of 4, the peak values for C_p is around 0.199, 0.401, 0.547 and 0.725, for angle of attack of 0, 10, 15 and 20 degrees, observed at the cavity corner, surface-S4/surface-S5 junction, for the conditions investigated. For the flat-plate cases, the maximum value for C_p is around 0.0392, 0.205, 0.320 and 0.458, at station X of 23.90, 1.39, 0.88 and 0.48 along surface S1, for angle of attack of 0, 10, 15 and 20 degrees, respectively. Therefore, the C_p peak values for the cavities are around 5.07, 1.95, 1.71, and 1.58 times larger than the peak values for a smooth surface at 0, 10, 15, and 20 degrees of incidence, respectively. Consequently, the presence of the cavities on the vehicle surface can not be ignored.

5.2.4 Skin Friction Coefficient

The skin friction coefficient is defined as follows,

$$C_f = \frac{\tau_w}{\frac{1}{2}\rho_\infty U_\infty^2} \quad (5.9)$$

where τ_w is the shear stress.

The shear stress τ_w on the cavity surface is calculated by the sum of the tangential momentum fluxes of both incident and reflect molecules impinging on the surface at each time step as follows,

$$\tau_w = \tau_i - \tau_r = \frac{F_N}{A\Delta t} \sum_{j=1}^N [(mu)_j]_i + [(mu)_j]_r \quad (5.10)$$

where u is the velocity component of the molecule in the surface tangential direction and subscripts i and r refers to the incident and reflect molecules, respectively.

In the present work, diffusion reflection was adopted as the gas-surface interaction model. For this model, the reflected molecules have a tangential momentum equal to zero, since the molecules essentially lose, on average, their tangential velocity components. In this fashion, the net tangential momentum flux is defined by,

$$\tau_w = \tau_i = \frac{F_N}{A\Delta t} \sum_{j=1}^N [(mu)_j]_i \quad (5.11)$$

The dependence of the skin friction coefficient along all cavity surfaces due to variations on the cavity L/H ratio is demonstrated in Figures 5.56 and 5.57 for angle of attack of 10 and 20 degrees, respectively. Again, in these figures, the left-column plots correspond to the skin friction coefficient distribution along surfaces outside the cavity, surfaces S1 and S5, and the right-column plots refer to the skin friction coefficient distribution along surfaces inside the cavity, i.e., surfaces S2, S3 and S4.

According to the left-column plots, along surface S1, it is noted that the C_f starts from the maximum value near the leading edge and decreases downstream along the surface. This maximum value at the leading edge increases with increasing the angle of attack α , for the conditions investigated. In addition, it is also noted that the skin friction coefficient distribution along surface S1 is basically the same to that of the flat-plate case, except at the vicinity of the cavity corner. At the vicinity of the cavity corner, the skin friction coefficient slightly increases with increasing the cavity L/H ratio, as shown in the magnified view, in the middle plot. Along surface S5, it is seen that the skin friction coefficient is similar to that for the flat-plate case, except close to the cavity downstream corner, i.e., surface-S4/surface-S5 junction, where the skin friction is larger than that for the flat-plate case. It is important to remark that this behavior for the skin friction coefficient at the vicinity of the upstream and downstream cavity corner is in contrast to that observed for the pressure coefficient and heat transfer coefficient, where they decreased with increasing the cavity L/H ratio.

Turning to the right-column plots in these figures, for backward face, surface S2, the skin friction coefficient C_f presents the maximum value at the vicinity of the cavity shoulder. Then, it decreases downward along the surface and reaches the minimum value at the bottom corner, surface-S2/surface-S3 junction. It is seen that, along

Figure 5.56 - Skin friction coefficient (C_f) distribution along the cavity surfaces parameterized by the cavity L/H ratio for 10-degree angle of attack.

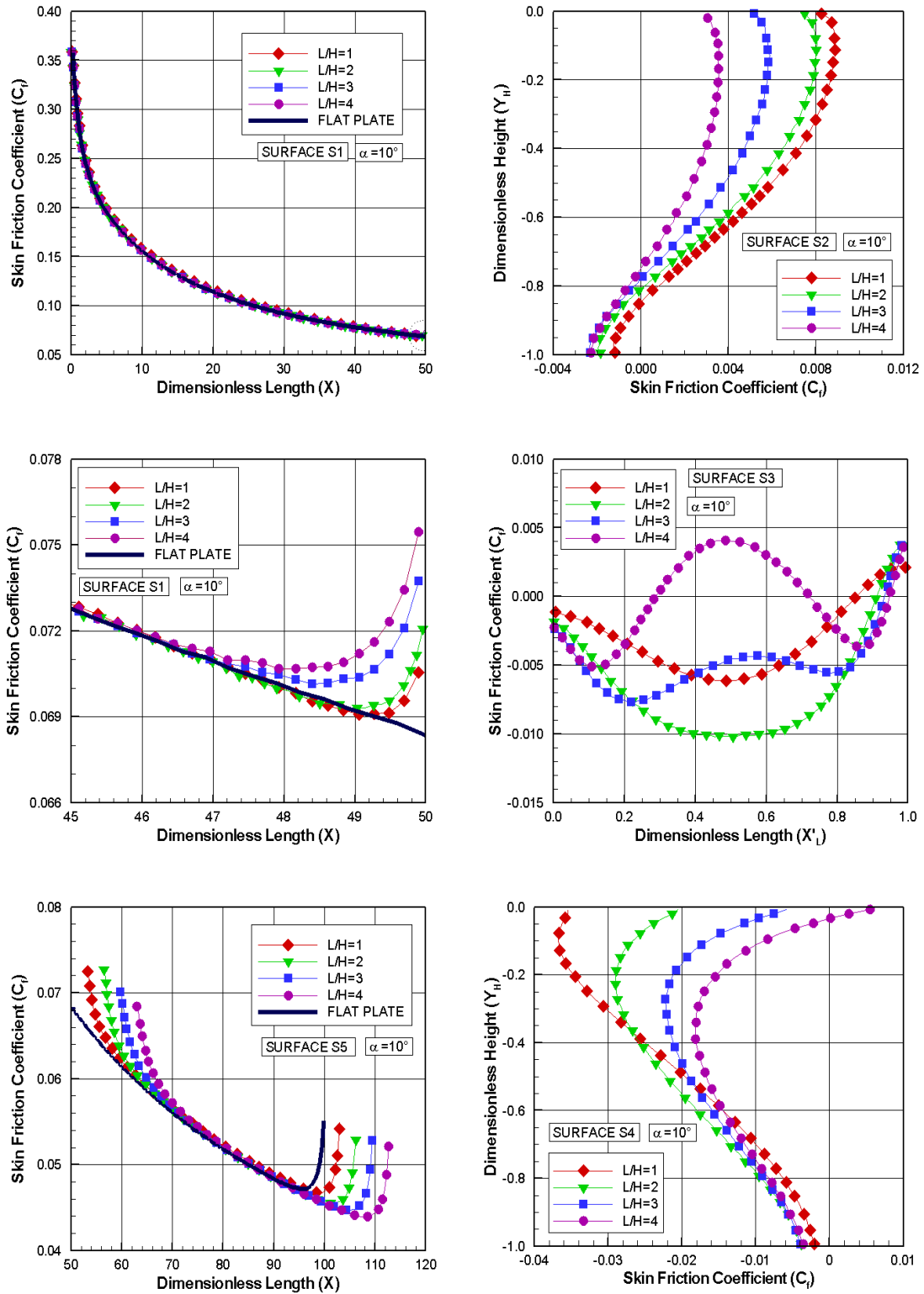
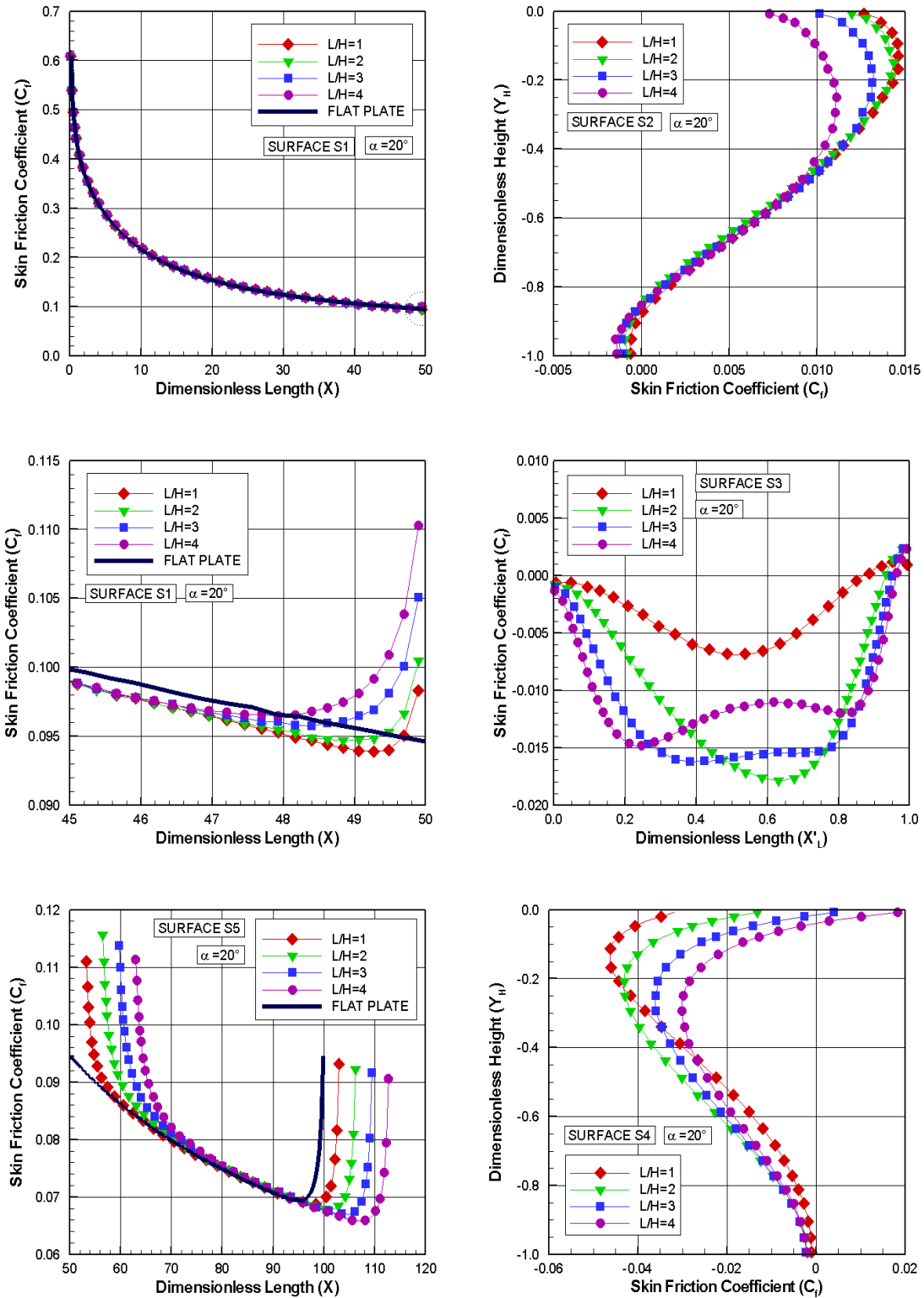


Figure 5.57 - Skin friction coefficient (C_f) distribution along the cavity surfaces parameterized by the cavity L/H ratio for 20-degree angle of attack.



surface S2, the skin friction decreases with increasing the cavity L/H ratio. In what follows, for the cavity floor, surface S3, the skin friction coefficient is negative at the vicinity of the surface-S2/surface-S3 junction and becomes positive at the vicinity of the surface-S3/surface-S4 junction. In addition, along the surface S3, the skin friction coefficient behavior depends not only on the cavity L/H ratio but also on the angle of attack. This behavior is related to the flowfield structure inside the cavity. As was shown earlier, it is seen a flowfield structure identified not only by an “open” cavity but also by a “closed” cavity. Afterwards, along the forward face, surface S4, the skin friction coefficient starts from a low value around zero at the vicinity of the surface-S3/surface-S4 junction and decreases negatively up to a minimum value in the upper portion of the cavity. Then it increases up to top of the cavity.

In the results that follow, it is instructive to examine the impact of the angle-of-attack on the skin friction coefficient. In doing so, Figures 5.56 and 5.57 exhibit the distribution of the skin friction coefficient C_f along the cavity surfaces, parameterized by the angle of attack α , for cavity L/H ratio of 1 and 4, respectively. Again, left-column plots refer to the skin friction coefficient distribution along surfaces S1 and S5, and the right-column plots present C_f to surfaces inside the cavity, i.e., surfaces S2, S3 and S4, respectively. In addition, as a matter of comparison, results obtained early by Palharini (PALHARINI, 2010) for zero-degree angle of attack are shown in the same plots.

According to this group of plots, it is quite apparent that skin friction coefficient C_f increases significantly with increasing the angle of attack. For comparison purpose, for zero-degree angle of attack, the maximum value of C_f is around 0.063 at station $X = 8.02$ from the leading edge, along surface S1, independently of the cavity L/H ratio. Conversely, this maximum value increases to 0.351, 0.477 and 0.574, at the leading edge of surface S1, for angle of attack of 10, 15, and 20 degrees respectively. On the other hand, for surfaces inside the cavity, it may be recognized that skin friction coefficient is at least one order of magnitude smaller than the maximum value observed on surface S1, for the conditions investigated.

Figure 5.58 - Skin friction coefficient (C_f) distribution along the cavity surfaces parameterized by the angle of attack α for the cavity L/H ratio of 1.

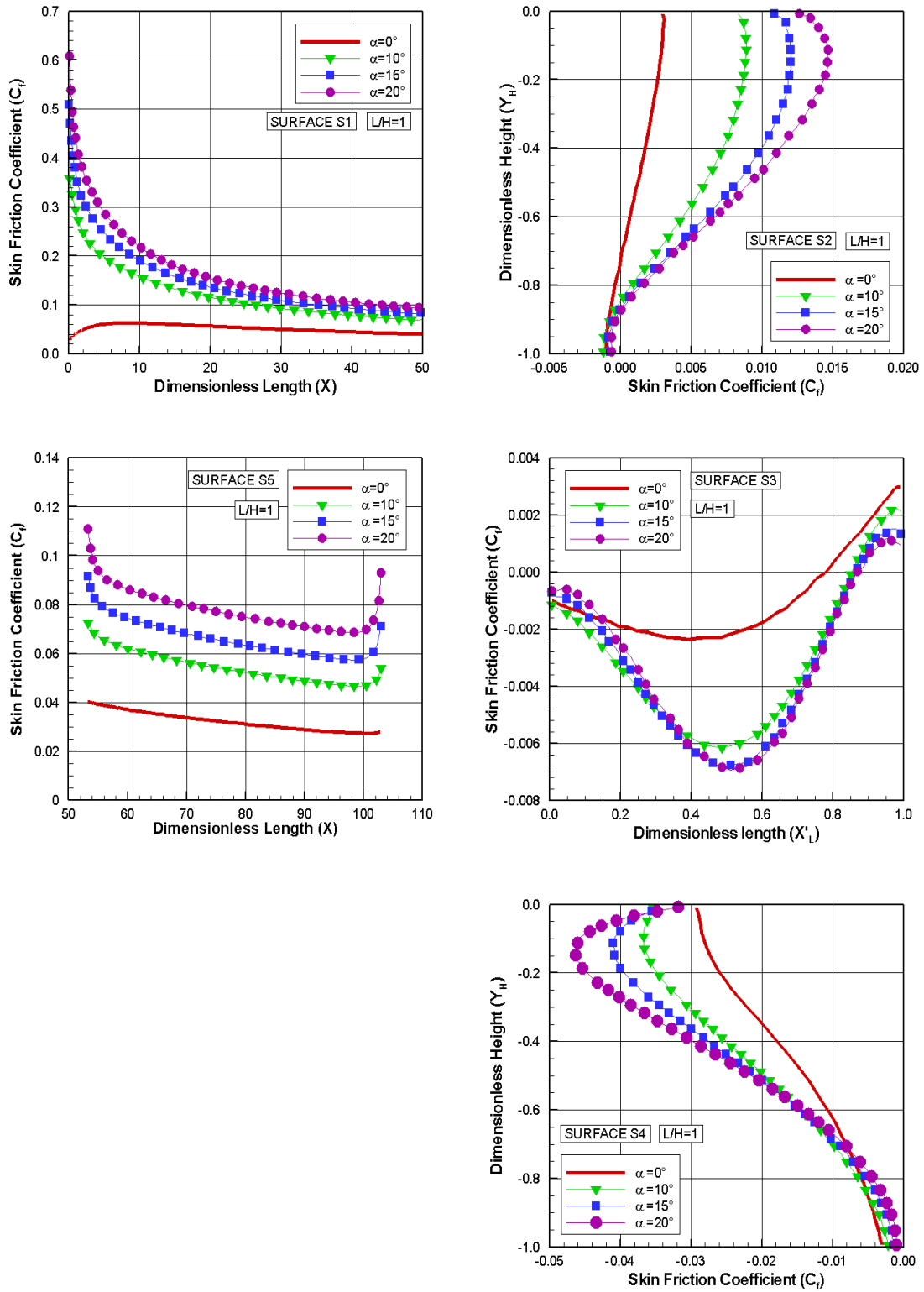
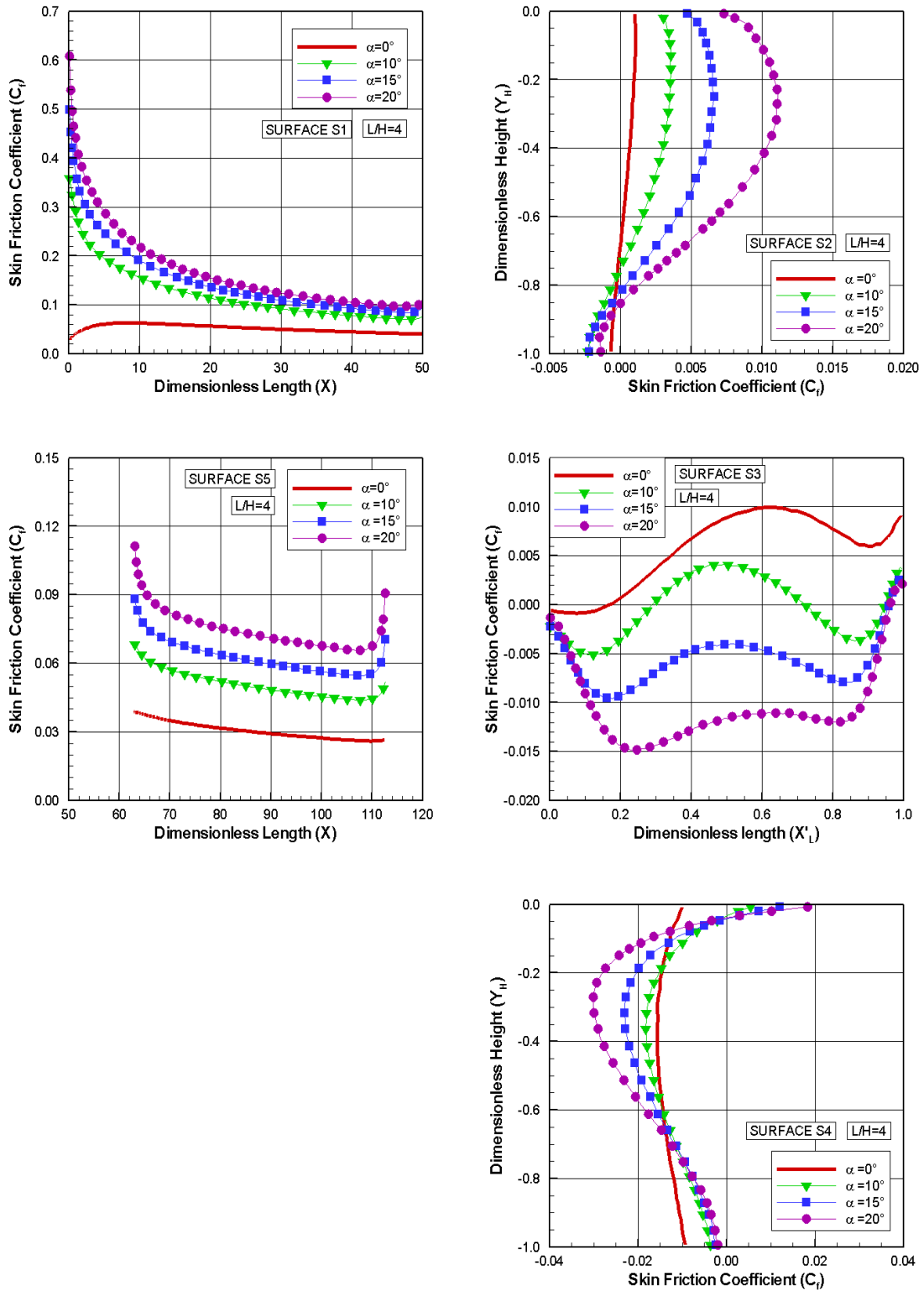


Figure 5.59 - Skin friction coefficient (C_f) distribution along the cavity surfaces parameterized by the angle of attack α for the cavity L/H ratio of 4.



6 CONCLUSIONS

6.1 Concluding Remarks

The study described in this dissertation was undertaken with the objective to investigate the impact of discontinuities present on hypersonic space vehicles. In pursuit of this goal, computational simulations of a low-density hypersonic flow over a cavity have been performed by using the Direct Simulation Monte Carlo method. The simulations provided information about the nature of the flowfield structure and the aerodynamic surface properties on the cavity resulting from variations in the length-to-depth (L/H) ratio and variations in the angle of attack. A description of the flowfield properties, such as velocity, density, pressure and temperature, and aerodynamics surface quantities, such as, number flux, heat transfer, pressure and skin friction, were obtained by a numerical method that properly account for non-equilibrium effects in the transition flow regime. Results for cavities defined by L/H ratio of 1, 2, 3 and 4, and flow with angle of attack of 10, 15 and 20 degrees, were compared to those of a flat plate without a cavity with zero-degree angle of incidence.

It was observed that the cavity L/H ratio did not disturb significantly the primary flowfield properties far upstream and far downstream along the surface outside of the cavity, as compared to the freestream mean free path, and the domain of influence along the upstream and downstream surfaces was confined close to the cavity corners, for the conditions investigated. Conversely, significant changes in the primary flowfield properties were observed inside the cavity with increasing the angle of attack of the oncoming flow.

It was also observed that the flow topology inside the cavity with incidence is slightly different from that for zero-degree angle of incidence for the L/H ratio investigated. For $L/H = 1$ and 2 cases, the flow structure was characterized by a primary vortex system, with the recirculation region filling the entire cavities, similar to that for the zero-degree angle of incidence. For $L/H = 3$ and 4 cases, the recirculation region was characterized by a system of two vortices. However, a feature of particular interest was observed for the $L/H = 4$ case. For 10-degree angle of incidence, the external flow reached the bottom of the cavity. This flow topology corresponds to that of a “closed cavity”, usually observed in the continuum flow regime for $L/H > 14$. Nevertheless, for 15- and 20-degree angle of incidence, the external stream did not reach the bottom of the cavity. In this case, the flow topology corresponds to that of an “open cavity”, usually observed in the continuum flow regime for $1 < L/H < 10$. Therefore, the behavior for $L/H = 3$ and 4 cases is in contrast to that for zero-degree

angle of incidence. In addition, even at incidence, the cavity flow topology observed here in a rarefied environment differs from that usually observed in the continuum flow regime, as showed in Chapter 1.

Also of great significance in this study was the heat flux to and forces, due to pressure and shear stress, acting on the cavity surface. Results showed that both, heat flux and forces, depended on the L/H ratio and on the angle of attack α , for the range investigated. It was found that the maximum values for the heat transfer, pressure and skin friction coefficients inside the cavity took place on the cavity forward face. Maximum values for pressure coefficient are around 5.07, 1.95, 1.71, and 1.58 times larger than the peak values for a smooth surface at 0, 10, 15, and 20 degrees of incidence, respectively. It was also found that maximum values for heat transfer coefficient inside the cavities increased with increasing the angle of attack α . Nevertheless, it was observed that these maximum values are smaller than those observed in a flat-plate without a cavity for the corresponding angle of attack. As a result, in terms of heat flux, the presence of the cavities on the vehicle surface can be ignored in the vehicle design. Conversely, in terms of pressure, the presence of the cavities on the vehicle surface can not be ignored in the vehicle design.

6.2 Future Work

This present work has described an investigation of a low-density hypersonic cavity flow at incidence in order to simulate discontinuities present on a surface of hypersonic vehicles. Although this investigation has taken into account a representative range for the L/H ratio and angle of attack α , improvements to a realistic investigation on surface discontinuities are still desirable.

In the present work, chemical reactions were not considered. In realistic situations, the flow may experience chemical reactions, such as dissociation or, even though, recombination of the molecules. In this way, the implementation of chemical reactions may provide more insight into the sensitivity of the aerothermodynamics surface quantities.

Finally, the impact of a large range of angle of attack, the Mach number effect, as well as geometrical effect, i.e., blunt leading edge, different length for the distance L_u in front of the cavity or different geometric combinations, seems to be important.

REFERENCES

- ABE, T. Rarefied gas flow analysis by direct simulation Monte Carlo method in body-fitted coordinate system. **Journal of Computational Physics.**, v. 83, p. 424–432, 1989. 45
- _____. Generalized scheme of the no-time-counter scheme for the DSMC in rarefied gas flow analysis. **Computers Fluids.**, v. 22, n. 2, p. 253–257, 1993. 23, 28
- AKIRA, S. **Introduction to practice of molecular simulation.** [S.l.]: Elsevier Inc., 2011. 18
- ALDER, B. J.; WAINWRIGHT, T. E. Studies in molecular dynamics. **Journal of Chemical and Physics.**, v. 27, p. 1208–1209, 1957. 18
- _____. Molecular dynamics by electronic computers. **Transport Processes in Statistical Mechanics.**, v. 27, p. 97–131, 1958. Ed. I. Prigogine, New York, Interscience. 18
- ALEXANDER, F. J.; GARCIA, A. J.; ALDER, B. J. A consistent Boltzmann algorithm. **Physical Review Letter.**, v. 74, n. 26, p. 5212–5215, 1995. 19
- _____. Cell size dependence of transport coefficients in stochastic particle algorithms. **Physics of Fluids.**, v. 10, n. 6, p. 1540–1542, 1998. 20
- _____. Erratum: Cell size dependence of transport coefficients in stochastic particle algorithms. **Physical of Fluids.**, v. 12, n. 3, p. 731, 2000. 20, 46
- ATVARS, K.; KNOWLES, K.; RITCHIE, S. A.; LAWSON, N. J. Experimental and computational investigation of an “open” transonic cavity flow. **Journal of Aerospace Engineering.**, p. 357–368, 2009. 9
- BABOVSKY, H.; GROPENGREISSER, F.; NEUNZERT, H.; STRUCKMEIER, J.; WIESEN, B. Low-discrepancy method for the Boltzmann equation. **AIAA: Progress in Astronautics and Aeronautics.**, v. 118, p. 85–99, 1989. 45
- BAGANOFF, D.; MCDONALD, J. A collision-selection rule for particle simulation method suited to vector computers. **Physics of Fluids A - Fluid Dynamics.**, v. 2, n. 7, p. 1248–1259, 1990. 29
- BERGEMANN, F.; BOYD, I. D. New discrete vibrational energy model for the direct simulation Monte Carlo. In: SHIZGAL B. D.; WEAVER, D. P. (Ed.).

- Rarefied gas dynamics: Theory and simulation.** [S.l.]: AIAA Progress in Astronautics and Aeronautics, 1994. p. 174–183. 35
- BERRY, S. A.; HORVATH, T. J. Discrete-roughness transition for hypersonic flight vehicles. **Journal of spacecraft and rockets.**, AIAA, v. 45, p. 216–227, 2008. 1, 2
- BERTRAM, M. H.; WIGGS, M. M. Effect of surface distortions on the heat transfer to a wing at hypersonic speeds. **AIAA Journal**, v. 1, n. 6, p. 1313–1319, 1963. 1, 6, 7
- BERTRAN, M. H.; WEINSTEIN, L. M.; CARY JR., A. M.; ARRINGTON, J. P. Heat transfer to wavy wall in hypersonic flow. **AIAA Journal**, v. 5, n. 10, p. 1767–1967, 1967. 1, 6
- BIRD, G. A. Molecular gas dynamics. **Annual Review of Fluid Mechanics.**, 1976. [S.l.]: Clarendon Press, Oxford. 18, 19, 23, 28, 29, 45
- _____. Rarefied gas dynamics: Monte Carlo simulation in a engineering context. **AIAA Journal.**, v. 74, n. PART I, p. 239–253, 1981. 25
- _____. Definition of mean free path for real gases. **Physics of Fluids.**, v. 26, n. 11, p. 3222–3223, 1983. 41
- _____. Low-density aerothermodynamics. **Progress in Astronautics and Aeronautics**, v. 103, 1986. 16
- _____. Direct simulation of high-vorticity gas flow. **Physics of Fluids.**, v. 30, n. 2, p. 364–366, 1987. 20, 23
- _____. Perception of numerical method in rarefied gas dynamics. In: MUNTZ, E. P.; WEAVER, D. P.; CAPBELL, D. H. (Ed.). **Rarefied gas dynamics: Theoretical and computational techniques.** [S.l.]: AIAA Progress in Astronautics and Aeronautics, 1989. p. 211–226. (The 16th International Symposium on Rarefied Gas Dynamics (KGD16) was held July 10-16, 1988 at the Pasadena Convention Center, Pasadena, CA.). 23, 28, 40
- _____. **Molecular gas dynamics and the direct simulation of gas flows.** New York: Oxford University Press Inc., 1994. 458 p. ISBN 0-19-856195-4. 18, 19, 20, 21, 24, 28, 29, 33, 35, 40, 41, 42, 45, 46, 53, 119
- _____. **The DS2G program user 's guide.** Sidney, AU: G.A.B. Consulting Pty Ltd., 1999. 47

_____. A comparison of collision energy-based and temperature-based procedures in DSMC. In: INTERNATIONAL SYMPOSIUM ON RAREFIED GAS DYNAMICS, 26. **Proceedings...** Kyoto, Japan: Edited by T.Abe, 2008. v. 1084, p. 245–250. 40

_____. The DSMC method, version 1.1. 2013. 18, 19

BORGNAKKE, C.; LARSEN, P. Stistical collision model for Monte Carlo simulation of a polyatomic gas mixture. **Journal of Computational Physics.**, v. 18, p. 405–420, 1975. 34, 40

BOYD, I. D. Analysis of rotational nonequilibrium in standing shock waves of nitrogen. **AIAA Journal.**, v. 28, n. 11, p. 1997–1999, 1990. 34, 40

_____. Monte Carlo study of vibrational relaxation process. In: INTERNATIONAL SYMPOSIUM ON RAREFIED GAS DYNAMICS., 17. **Proceedings...** Germany: Ed. A. E. Beylch Aachen, 1990. p. 792–799. 35

_____. Rotational and vibrational relaxation nonequilibrium effects in rarefied hypersonic flow. **Journal of Thermophysics and Heat Transfer.**, v. 4, n. 4, p. 478–484, 1990. 34

_____. Rotational-translational energy transfer in rarefied nonequilibrium flows. **Physics of Fluids A - Fluid Dynamics.**, v. 2, n. 3, p. 447–452, 1990. 34

_____. Analysis of vibrational-translational energy transfer using the direct simulation Monte Carlo method. **Physics of Fluids A - Fluid Dynamics.**, v. 3, n. 7, p. 1785–1791, 1991. 35

BOYD, I. D.; CHEN, G.; CANDLER, G. V. Prediction failure of the continuum fluid equations in the transition hypersonic flows. **Physics of Fluids**, v. 7, n. 1, p. 210–219, 1995. 17

BURNETT, D. The distribution of molecular velocities and the mean motion in a non-uniform gas. In: LONDON MATHEMATICAL SOCIETY. **Proceedings...** Germany, 1936. v. 40, n. 2, p. 382–435. 17

CERCIGNANI, C. The Boltzmann equation and its applications. **Springer-Verlag**, 1988. 18, 40

CHAPMAN, S.; COWLING, T. G. **The mathematical theory of non-uniform gases.** Cambridge, UK: Cambridge University press., 1970. 17

CHENG, H. K.; EMMANUEL, G. Perspective on hypersonic nonequilibrium flows. **AIAA Journal.**, v. 33, n. 3, p. 385–400, 1995. 18

COMEAX, K. A.; MACCORMACK, R. W.; CHAPMAN, D. R. An analysis of the Burnett equations based on the second law of thermodynamics. In: AIAA AEROSPACE SCIENCE MEETING AND EXHIBIT, 33rd. **Proceedings...** [S.l.]: AIAA, 1995. 17, 18

DAZZI, F. **Shuttle orbiter thermal protection system (Tiles)**. 2005.

Available from:

<<https://www.flickr.com/photos/checco/219912733/in/photostream/>>.

Access in: April 01 2010. 2

DIETRICH, S. Efficient computation of particle movement in 3-D DSMC calculations on structured body-fitted grids. In: INTERNATIONAL SYMPOSIUM ON RAREFIED GAS DYNAMICS, 17. **Proceedings...** Aachen, Germany: Edited by ED.A.E.Beylich, 1990. p. 745–752. 21

DOGRA, V. K.; MOSS, J. N.; PRICE, J. M. Rarefied flow past a flat plate at incidence. In: MUNTZ, E. P.; WEAVER, D. P.; CAPBELL, D. H. (Ed.). **Rarefied gas dynamics: Theoretical and computational techniques**. [S.l.]: AIAA Progress in Astronautics and Aeronautics, 1989. p. 567–581. (The 16th International Symposium on Rarefied Gas Dynamics (KGD16) was held July 10-16, 1988 at the Pasadena Convention Center, Pasadena, CA.). xxi, 48, 49, 50, 58, 59

DOMINIK, M.; JÜRIG, H. **AB Initio Molecular Dynamics: Basic theory and advanced methods**. New York, U.S.A.: Cambridge University Press, 2009. 578 p. ISBN 978-1-107-66353-4. 18

ESTEVE, M. J.; REULET, P.; MILLAN, P. Flow field characterisation within a rectangular cavity. In: INTERNATIONAL SYMPOSIUM ON APPLICATIONS OF LASER TECHNIQUES TO FLUID MECHANICS., 10. **Proceedings...** [S.l.], 2000. 6, 8, 9

EVERHART, J. L.; ALTER, S. J.; MERSKI, N. R.; WOOD, W. A.; PRABHU, R. K. Pressure gradient effects on hypersonic flow heating. In: AIAA AEROSPACE SCIENCES MEETING AND EXHIBIT, 44. **Proceedings...** Reno, Nevada, U.S.A.: AIAA, 2006. p. 0185. 1, 5, 6, 8, 10

EVERHART, J. L.; BERGER, K. T.; BEY, K. S.; MERSKI, N. R.; WOOD, W. A. **Cavity Heating Experiments Supporting Shuttle Columbia Accident**

Investigation. Hampton, Virginia, U.S.A., 2011. 106p. Technical Reports, NASA TM 2011-214528. Available from: <<https://ntrs.nasa.gov/archive/nasa/casi.ntrs.nasa.gov/20110011174.pdf>>.

Access in: May 09, 2011. 3

FALLAVOLLITA, M.; BAGANOFF, D.; MCDONALD, J. Reduction of simulation cost and error for particle simulations of rarefied flow. **Journal of Computational Physics.**, v. 109, n. 1, p. 30–36, 1993. 46

FISCKO, K. A.; CHAPMAN, D. R. Hypersonic shock structure with Burnett terms in the viscous stress and heat transfer. In: THERMOPHYSICS, PLASMADYNAMICS AND LASERS CONFERENCE, 23. **Proceedings...** San Antonio, CA, U.S.A.: AIAA, 1988. p. 2733. 17

_____. Comparison of Burnett, super-Burnett and Monte Carlo solutions for hypersonic shock structure, rarefied gas dynamics: Theoretical and computational techniques. **AIAA Progress in Astronautics and Aeronautics.**, v. 118, p. 374–395, 1989. AIAA Paper 88-2733. 17

FRENKEL, D.; SMIT, B. Understanding molecular simulation from algorithms to applications. v. 1, 2009. Computational Science Series. 18

GAD-EL-HAK, M. The fluid mechanics of microdevices the freeman scholar lecture. **Journal of Fluids Engineering.**, v. 121, n. 5, p. 5–33, 1999. 6

GAI, S.; MILTHORPE, J. Hypersonic high-enthalpy flow over a blunt-stepped cone. In: INTERNATIONAL SYMPOSIUM ON SHOCK WAVES, 20. **Proceedings...** California, U.S.A.: Edited by Sturtevant, B. and Shepherd, J.E and Hornung, H.G, v.1, 1995. p. 234–244. 5, 6

GROTOWSKY, I. M. G.; BALLMANN, J. Numerical investigation of hypersonic step-flows. **Shock Waves**, v. 10, p. 57–72, 2000. 6

GRUPTA, R. N.; SCOTT, C. D.; MOSS, J. N. Surface-slip equations for low Reynolds number multicomponent air flow. **Progress in astronautics and aeronautics.**, 1985. 126

HAHN, M. Experimental investigation of separated flow over a cavity at hypersonic speed. **AIAA Journal**, v. 7, n. 6, p. 1092–1098, 1969. 1, 6

HAIBO, L.; WEIQIANG, L. Aerodynamic investigation of hypersonic vehicle with forward-facing cavity. **Applied mechanics and materials.**, Trans Tech Publications., v. 18, p. 41–47, 2012. 1

_____. Investigation of thermal protection system by forward-facing cavity and opposing jet combinatorial configuration. **Chinese journal of aeronautics.**, Elsevier, v. 26, n. 2, p. 287–293, 2013. 1

HARVEY, J. K. Perception of numerical method in rarefied gas dynamics. In: MOSS, J. N.; SCOTT, C. D. (Ed.). **Rarefied gas dynamics: Thermophysical aspect of re-entry flows.** Washington DC, U.S.A.: AIAA Progress in Astronautics and Aeronautics, 1986. v. 103, p. 25–43. (The 20th thermophysics conference was held June 19-21, 1985, Williamsburg, Virginia, U.S.A). 19

_____. A review of a validation exercise on the use of the DSMC method to compute viscous/inviscid interaction in hypersonic flow. In: AIAA THERMOPHYSICS CONFERENCE, 36. **Proceedings...** Orlando, Florida, U.S.A.: AIAA, 2003. 19

HARVEY, J. K.; GALLIS, M. A. Review of code validation studies in high-speed low-density flows. **Journal os Spacecraft and Rockets**, v. 37(1), p. 8–20, 2000. 19

HASH, D. B.; HASSAN, H. Direct simulation with vibration-dissociation coupling. **Journal of Thermophysics and Heat Transfer.**, v. 7, n. 4, p. 680–686, 1993. 35

HASH, D. B.; MOSS, J. N.; HASSAN, H. A. A direct simulation of diatomic gases using the generalized hard sphere model. **Journal of Themophysics and Heat Transfer.**, v. 8, n. 4, p. 758–764, 1993. 28

HASSAN, H. A.; HASH, D. B. A generalized hard-sphere model for Monte Carlo simulation. **Physics of Fluids A - Fluid Dynamics.**, v. 5, n. 3, p. 738–744, 1993. 28

HAVILAND, J. K. The solution of two molecular flow problems by the Monte Carlo method. **Methods in Computational Physics.**, v. 4, p. 109–209, 1965. 18

HAVILAND, J. K.; LAVIN, M. L. Application of Monte Carlo method to heat transfer in rarefied gases. **Physics of Fluids**, v. 5, p. 1399–1405, 1962. 18

HINDERSKS, M.; RADESPIEL, R. Investigation of hypersonic gap flow of a reentry nose cap with consideration of fluid structure interaction. In: AIAA AEROSPACE SCIENCES MEETING AND EXHIBIT., 44. **Proceedings...** Orlando, Florida, U.S.A.: AIAA, 2006. p. 0188. 1, 6

HOLDEN, M. S.; WADHAMS, T. P. A review of a experimental studies for DSMC an Navier-Stokes code validation in laminar regions of shock/shock and shock/boundary layer interaction including real gas effects in hypervelocity flows. In: AIAA THERMOPHYSICS CONFERENCE., 36. **Proceedings...** Orlando, Florida, U.S.A.: AIAA, 2003. 19

HOZUMI, K.; KOYAMA, T.; HIRABAYASHI, N. Experimental study on hypersonic heating characteristics of cavity wake flow. In: INTERNATIONAL CONGRESS OF THE AERONAUTICAL SCIENCES, 24. **Proceedings...** Yokohama, Japan: AIAA, 2004. 6

HUANG, W.; WANG, Z. G.; JIN, L.; LIU, J. Effect of cavity location on combustion flow field of integrated hypersonic vehicle in near space. **Journal of visualization.**, Springer, v. 14, n. 4, p. 339–351, 2011. 1

JACKSON, A. P.; HILLIER, R.; SOLTANI, S. Experimental and computational study of laminar cavity flows at hypersonic speeds. **Journal of Fluid Mechanics**, v. 427, p. 329–358, 2001. 6

KANNENBERG, K. C.; BOYD, I. Strategies for efficient particle resolution in the direct simulation Monte Carlo method. **Journal of Computational Physics.**, v. 157, p. 727–745, 2000. 46

KEON-YOUNG, Y.; AGARWAL, R. K.; BALAKRISHNAN, R. Beyond Navier-Stokes: Burnett equations for flows in the continuum-transition regime. **Physics of Fluids.**, v. 13, n. 10, p. 3061–3086, 2001. 17

KOURA, K.; MATSUMOTO, H. Variable soft sphere molecular model for inverse-power-law of Leonard-Jones potential. **Physics of Fluids.**, v. 3, n. 10, p. 12459–2465, 1991. 23, 28

_____. Variable soft sphere molecular model for air species. **Physics of Fluids.**, v. 4, n. 5, p. 1083–1085, 1992. 28

KUNC, J.; HASSAN, H. A.; HASH, D. B. The GHS interaction model for strong attractive potentials. **Physics of Fluids.**, v. 7, n. 3, p. 1173–1175, 1995. 28

LADA, C.; KONTIS, K. Experimental studies on transitional and closed cavity configurations including flow control. **Journal of Aircraft.**, v. 47, n. 2, p. 723–730, 2010. 9

- LAUX, M. Optimization and parallelization of the DSMC method on unstructured grids. In: AIAA THERMOPHYSICS CONFERENCE, 32. **Proceedings...** Atlanta, U.S.A., 1997. p. 23–25. 21
- LEE, C. J. Unique determination of solutions to the Burnett equations. **AIAA Journal.**, v. 32, n. 4, p. 985–990, 1994. 17
- LEE, G.; CHANDRA, S. Numerical analysis of heat transfer enhancement from surfaces with cavities. In: AIAA AEROSPACE SCIENCES MEETING AND EXHIBIT, 44. **Proceedings...** Reno, Nevada, U.S.A: AIAA, 2006. p. 0186. 6
- LENGRAND, J.; ALLÉGRE, J.; CHPOUN, A.; RAFFIN, M. Rarefied hypersonic flow over a sharp flat plate: Numerical and experimental results. In: INTERNATIONAL SYMPOSIUM ON RAREFIED GAS DYNAMICS., 18. **Proceedings...** Vancouver, British Columbia, Canada., 1992. v. 160, p. 276–284. xxi, 48, 49, 58, 60, 61
- LIU, N.; YIN-KWEENG, E. The impact of the-step size in the application of the direct simulation Monte Carlo method to ultra thin gas film lubrication. **Journal of Micromechanics and Microengineering.**, v. 12, p. 5667–573, 2002. 21
- LUMPKIN, F. E.; HASS, B. L.; BOYD, I. D. Resolution of differences between collision number definitions and continuum simulations. **Physics of Fluids A - Fluid Dynamics.**, v. 3, n. 9, p. 2282–2284, 1991. 35
- LUMPKIN III, F. E.; CHAPMAN, D. R. Accuracy of the Burnett equations for hypersonic real gas flows. **Journal of Thermophysics and Heat Transfer.**, v. 6, n. 3, p. 419–425, 1992. 17
- MEIBURG, E. Comparison of the molecular dynamics method and the direct simulation Monte Carlo technique for flows around simple geometries. **Physics of Fluids.**, v. 29, n. 10, p. 3107–3113, 1986. 20
- MIZZI, S.; EMERSON, D. R.; STEFANOV, S. K.; BARBER, R. W.; REESE, J. M. Effects of rarefaction on cavity flow in the slip regime. **Journal of Computational and Theoretical Nanoscience.**, v. 4, n. 4, p. 817–822, 2007. 6
- MORGENSTERN JR., A.; CHOKANI, N. Hypersonic flow past open cavities. **AIAA Journal**, v. 32, n. 12, p. 2387–2393, 1994. 1, 6, 7
- MOSS, J. N.; PRICE, J. M.; DOGRA, V. K.; HASH, D. B. Comparison of DSMC and experimental results for hypersonic external flows. In: AIAA

THERMOPHYSICS CONFERENCE, 30. **Proceedings...** San Diego, CA, U.S.A.: AIAA, 1995. p. AIAA paper 95-2028. 19

NANBU, K. Theoretical basis of the direct simulation Monte Carlo method. In: INTERNATIONAL SYMPOSIUM ON RAREFIED GAS DYNAMICS, 15. **Proceedings...** Grado, Italy, 1986. p. 369-383. 23, 28

NANCE, R.; WILMOTH, R. G.; HASSAN, H. A. Comparison of grid-definition schemes for Monte Carlo simulations. **Journal of Thermophysics and Heat Transfer.**, v. 11, n. 2, p. 296-303, 1997. 21, 45

NARIS, S.; VALOUGEORGIS, D. The driven cavity flow over the whole range of the Knudsen number. **Physics of Fluids**, v. 17, n. 097106, 2005. 6

NATIONAL AERONAUTICS AND SPACE ADMINISTRATION NASA. **Desert Layover for Shuttle Discovery**. 2009. Available from: <https://www.nasa.gov/sites/default/files/images/386229main_ED09-0253-15_full.jpg>. Access in: September 22th 2009. 2

NESTLER, D. E. An experimental study of hypersonic cavity flow. **AIAA Journal**, v. 19, n. 3, p. 195-196, 1982. 1, 6

NESTLER, D. E.; SAYDAH, A. R.; AUXER, W. L. Heat transfer to steps and cavities in hypersonic turbulent flow. **AIAA Journal**, v. 7, n. 7, p. 1368-1370, 1969. 1, 6, 7

NICOLL, K. M. A study of laminar hypersonic cavity flows. **AIAA Journal.**, v. 2, n. 9, p. 1535-1541, 1964. 6, 7

OHMACHI, Y.; SUSUKI, K. Study on hypersonic flow over flat plate with channels. In: AIAA APPLIED AERODYNAMICS CONFERENCE., 29. **Proceedings...** Honolulu, Hawaii, U.S.A.: AIAA, 2011. p. 1-10. 6, 8

OLYNICK, D. P.; MOSS, J. N.; HASSAN, H. A. Grid generation and adaptation for direct simulation Monte Carlo method. **Journal of Thermophysics and Heat Transfer.**, v. 3, n. 4, p. 368-373, 1989. 45

ORAN, E. S.; OH, C. K.; CYBYK, B. Z. DIRECT SIMULATION MONTE CARLO: Recent advances and applications. **Annual Review of Fluid Mechanics.**, v. 30, p. 403-441, 1998. 22

PALHARINI, R. C. **Numerical investigation of aerothermodynamic in a reentry vehicle with surface discontinuity-like cavity**. 2010. 155 p.

(sid.inpe.br/mtc-m19/2010/10.07.02.39-TDI). Master's Degree (Master's Degree in Engineering and Space Technology) — Instituto Nacional de Pesquisas Espaciais (INPE), São José dos Campos, 2010. Available from:

<<http://urlib.net/8JMKD3MGP7W/38CL3PB>>. Access in: 2010. 6, 9, 11, 37, 43, 79, 86, 92, 98, 104, 111, 115, 137, 143, 156

PALHARINI, R. C.; SANTOS, W. F. length-to-depth ratio effects on flowfield structure of low-density hypersonic cavity flow. In: AIAA THERMOPHYSICS CONFERENCE., 42. **Proceedings...** Honolulu, Hawaii, U.S.A.: AIAA, 2011. p. 1–13. 39

PALMER, G. E.; PULSONETTI, M.; WOOD, W. A.; ALTER, S.; GNOFFO, P.; TANG, C. Computational assessment of thermal protection system damage experienced during sts-118. **Journal of Spacecraft and Rockets**, v. 46, n. 6, p. 1110–1116, 2009. 3, 4

RAULT, D. F. G. Aerodynamic of the shuttle orbiter at high altitude. **Journal of Spacecraft and Rockets.**, v. 31, n. 6, p. 944–952, 1994. 45

RIEFFEL, M. A. A method for estimating the computational requirements of DSMC simulations. **Journal of Computational Physics.**, v. 149, p. 95–113, 1999. 47

ROWLEY, C. W.; WILLIAMS, D. R. Dynamics control of high-reynolds-number flow over open cavities. **Annual Review of Fluids Mechanics**, v. 38, p. 251–276, 2006. 6

SARAVANAN, S.; JAGADEESH, G.; REDDY, K. P. J. Investigation of missile-shaped body with forward-facing cavity at Mach 8. **Journal of spacecraft and rockets.**, AIAA, v. 46, p. 577–591, 2009. 1

SCIENCE MUSEUM LONDON / SCIENCE AND SOCIETY PICTURE LIBRARY. **Silica Space Shuttle thermal protection (TPS) tile, c 1980.** 1986. Available from: <<http://www.scienceandsociety.co.uk/results.asp?image=10309930&itemw=4&itemf=0003&itemstep=1&itemx=4>>. Access in: 1986. 2

SCOTT, C. D.; MARAIA, R. J. Gap heating with pressure gradients. In: AIAA THERMOPHYSICS CONFERENCE., 14. **Proceedings...** Orlando, Florida, U.S.A.: AIAA, 1979. p. 1043. 1

SHANKAR, P. N.; DESHPANDE, M. D. Fluid mechanics in the driven cavity. **Anual Review of Fluid Mechanics.**, v. 32, p. 93–136, 2000. 6

SHU, C.; MAO, X.; CHEW, Y. Particle number per cell and scaling factor effect on accuracy of DSMC simulation of micro flows. **International Journal of Numerical Methods for Heat and Fluid Flows.**, v. 15, n. 8, p. 827–841, 2005. 47

SILTON, S. I.; GOLDSTEIN, D. B. Ablation onset in unsteady hypersonic flow about nose tip with cavity. **Journal of thermophysics and heat transfer.**, AIAA, v. 14, n. 3, p. 421–434, 2000. 1

SOLTANI, S.; HILLIER, R. An experimental and computational study of hypersonic cavity flows. In: AEROSPACE SCIENCES MEETING AND EXHIBIT., 32. **Proceedings...** Reno, Nevada, U.S.A.: AIAA, 1994. p. 1–14. 9

TANNEHILL, J. C.; EISLER, G. R. Numerical computation of the hypersonic leading edge problem using the Burnett equations. **Physics of Fluids.**, v. 19, n. 1, p. 09–15, 1976. 17

THE BOEING COMPANY. **Second Boeing-built X-37B orbital test vehicle completes first flight.** 2010. Available from:

<http://www.boeingimages.com/archive/>

[Second-20Boeing-built-X-37B-Orbital-Test-Vehicle-Completes-first-flight-2F3XC5POZNI.html](http://www.boeingimages.com/archive/Second-20Boeing-built-X-37B-Orbital-Test-Vehicle-Completes-first-flight-2F3XC5POZNI.html)>. Access in: april 22th 2010. 2

THOMPSON, R. A.; LESSARD, V.; JENTINK, T.; ZOBY, E. V. Analysis of compression pad cavities for the Orion heatshield. In: AIAA AEROSPACE SCIENCES MEETING INCLUDING THE NEW HORIZONS FORUM AND AEROSPACE EXPOSITION., 47. **Proceedings...** Orlando, Florida, U.S.A.: AIAA, 2009. p. 1–14. 1, 9

TOKUMASU, T.; MATSUMOTO, Y. Dynamic molecular collision (DMC) model for rarefied gas flow simulations by the DSMC method. **Physics of Fluids.**, v. 11, n. 7, p. 1907–1920, 1999. 49

TSUBOI, N.; MATSUMOTO, Y.; YAMAGUCHI, H. Direct simulation Monte Carlo method on rarefied hypersonic flow around flat plates. **Journal of Spacecraft and Rockets.**, v. 41, n. 3, p. 397–405, 2004. 48, 49, 50, 58, 60, 61, 63

USAMI, M.; NAKAYAMA, T. Intermolecular collision scheme of DSMC taking molecular locations within a cell into account. In: INTERNATIONAL

SYMPOSIUM ON RAREFIED GAS DYNAMICS., 23. **Proceedings...** Whistler, British Columbia, Canada: AIP conference proceedings, 2003. v. 663, p. 374–384. 21

WEINSTEIN, I.; AVERY, D. E.; CHAPMAN, A. J. **Aerodynamic heating to the gaps and surfaces of simulated reusable-surface-insulation tile arrays in turbulent flow at Mach 6.6.** Hampton, Virginia, U.S.A., 1975. 51p.

Technical Memorandum, NASA TM X-3225. Available from: <<https://ntrs.nasa.gov/archive/nasa/casi.ntrs.nasa.gov/19760004291.pdf>>.

Access in: Nov 18, 1995. 5

WILMOTH, R. G.; LEBEAU, G. J.; CARLSON, A. DSMC grid methodologies for computing low-density, hypersonic flows about reusable launch vehicles. In: AIAA THERMOPHYSICS CONFERENCE, 31. **Proceedings...** Louisiana, U.S.A.: Edited by AIAA Paper, 1996. p. 1812. 21, 45

XUE, H.; FAN, Q.; SHU, C. Prediction of micro-channel flows using direct simulation Monte Carlo. **Probabilistic Engineering Mechanics.**, Elsevier, v. 15, n. 2, p. 213–219, 2000. 20

YEN, S. M. Monte Carlo solutions of nonlinear Boltzmann equation for problems of heat transfer in rarefied gases. **International Journal of Heat and Mass Transfer.**, v. 14, p. 1865–1865, 1971. 18

_____. Numerical solution of the nonlinear Boltzmann equation for nonequilibrium gas flow problems. **Annual Review of Fluid Mechanics.**, v. 16, p. 67–97, 1984. 18

ZDANSKI, P. S. B.; ORTEGA, M. A.; FICO(JR)., N. G. C. R. Heat transfer on shallow cavities: Aspect ratio and Reynolds number influence. In: APPLIED AERODYNAMICS CONFERENCE AND EXHIBIT, 22. **Proceedings...** Providence, Rhode Island, U.S.A.: AIAA, 2004. p. 4961. 6

ZHAO, W.; CHEN, W.; AGARWAL, R. K. Formulation of a new set of simplified conventional burnett equations for computation of rarefied hypersonic flows. **Aerospace Sciences and Technology.**, v. 38, p. 64–75, 2014. 17

ZHONG, X.; MCCORMACK, R. W.; CHAPMAN, D. R. Stabilization of the Burnett equations and application to hypersonic flows. **AIAA Journal.**, v. 31, n. 6, p. 1036–1043, 1993. 17

PUBLICAÇÕES TÉCNICO-CIENTÍFICAS EDITADAS PELO INPE

Teses e Dissertações (TDI)

Teses e Dissertações apresentadas nos Cursos de Pós-Graduação do INPE.

Manuais Técnicos (MAN)

São publicações de caráter técnico que incluem normas, procedimentos, instruções e orientações.

Notas Técnico-Científicas (NTC)

Incluem resultados preliminares de pesquisa, descrição de equipamentos, descrição e ou documentação de programas de computador, descrição de sistemas e experimentos, apresentação de testes, dados, atlas, e documentação de projetos de engenharia.

Relatórios de Pesquisa (RPQ)

Reportam resultados ou progressos de pesquisas tanto de natureza técnica quanto científica, cujo nível seja compatível com o de uma publicação em periódico nacional ou internacional.

Propostas e Relatórios de Projetos (PRP)

São propostas de projetos técnico-científicos e relatórios de acompanhamento de projetos, atividades e convênios.

Publicações Didáticas (PUD)

Incluem apostilas, notas de aula e manuais didáticos.

Publicações Seriadas

São os seriados técnico-científicos: boletins, periódicos, anuários e anais de eventos (simpósios e congressos). Constam destas publicações o Internacional Standard Serial Number (ISSN), que é um código único e definitivo para identificação de títulos de seriados.

Programas de Computador (PDC)

São a seqüência de instruções ou códigos, expressos em uma linguagem de programação compilada ou interpretada, a ser executada por um computador para alcançar um determinado objetivo. Aceitam-se tanto programas fonte quanto os executáveis.

Pré-publicações (PRE)

Todos os artigos publicados em periódicos, anais e como capítulos de livros.